DISSERTATION

PERFORMANCE OF STEEL STRUCTURES SUBJECTED TO FIRE FOLLOWING EARTHQUAKE

Submitted by

Mehrdad Memari

Department of Civil and Environmental Engineering

In partial fulfillment of requirements

For the Degree of Doctor of Philosophy

Colorado State University

Fort Collins, Colorado

Summer 2016

Doctoral Committee:

Advisor: Hussam N. Mahmoud

Todd M. Bandhauer
Bruce R. Ellingwood
Paul R. Hyliger
John W. van de Lindt

ABSTRACT

PERFORMANCE OF STEEL STRUCTURES SUBJECTED TO FIRE FOLLOWING EARTHQUAKE

Fires following earthquakes are considered sequential hazards that may occur in metropolitans with moderate-to-highly seismicity. The potential for fire ignition is elevated by various factors including damage to active and passive fire protections following a strong ground motion. In addition, damage imposed by an earthquake to transportation networks, water supply, and communication systems, could hinder the response of fire departments to the post-earthquake fire events. In addition, the simultaneous ignitions – caused by strong earthquake – might turn to mass conflagrations in the shaken area, which could lead to catastrophic scenarios including structural collapse, hazardous materials release, loss of life, and the inability to provide the emergency medical need. This has been demonstrated through various historical events including the fires following the 1906 San Francisco earthquake and the 1995 Kobe earthquakes, among others, making fire following earthquake the most dominant contributor to earthquake-induced losses in properties and lives in the United States and Japan in the last century.

From a design perspective, current performance-based earthquake design philosophy allows certain degrees of damage in the structural and non-structural members of steel-framed buildings during the earthquake. The cumulative structural damages, caused by the earthquake, can reduce the load-bearing capacity of structural members in a typical steel building. In addition, potential damage to active and passive fire protections following an earthquake leaves the steel material exposed to elevated temperatures in the case of post-earthquake fire events.

The combined damage to steel members and components following an earthquake combined with damage to fire protection systems can increase the vulnerability of steel buildings to withstand fire following seismic events. Therefore, there is a pressing need to quantify the performance of steel structures under fire following earthquake in moderate-to-high seismic regions.

The aim of the study is to assess the performance of steel structural members and systems under the cascading hazards of earthquake and fire. The research commences with evaluation of the stability of hot-rolled W-shape steel columns subjected to the earthquake-induced lateral deformations followed by fire loads. Based on the stability analyses, equations are proposed to predict the elastic and inelastic buckling stresses in steel columns exposed to the fire following earthquake, considering a wide variety of variables. The performance of three steel moment-resisting frames – with 3, 9, and 20 stories – with reduced beam section connections is assessed under multi-story fires following a suite of earthquake records. The response of structural components – beams, columns, and critical connection details – is investigated to evaluate the demand and system-level instability under fire following earthquake. Next, a performance-based framework is established for probabilistic assessment of steel structural members and systems under the combined events of earthquake and fire. A stochastic model of the effective random variables is utilized for conducting the probabilistic performance-based analysis. This framework allows structural engineers to generate fragility of steel columns and frames under multiple-hazard of earthquake and fire.

The results demonstrate that instability can be a major concern in steel structures, both on the member and system levels, under the sequential events and highlights the need to develop provisions for the design of steel structures subjected to fire following earthquake. Furthermore, a suite of recommendations is proposed for future studies based on findings in this dissertation.

ACKNOWLEDGEMENT

I wish to express my sincere thanks and gratefulness to my advisor, Professor Hussam Mahmoud, who has supported me academically and emotionally throughout the entire of my Ph.D. studies. His technical guidance, encouragement, and patience always motivated me to overcome difficult moments during my Ph.D. research at Colorado State University (CSU). I was very fortunate to have him as my advisor and older brother. All his generous supports are greatly appreciated. God bless him and his family.

I want to thank Professor Bruce Ellingwood for his constructive technical inputs, comments, and suggestions on my articles and performance-based analysis. I also thank him for serving as my doctoral committee member. My gratitude thanks go to the rest of my Ph.D. committee members, Professor John van de Lindt, Professor Paul Heyliger, and Professor Todd Bandhauer for their guidance and supports throughout my Ph.D. studies. I would also like to acknowledge the financial supports and teaching opportunity (in summer 2014) provided by Department of Civil and Environmental Engineering at Colorado State University (CSU). I also thank all my friends for their supports.

Finally, I would like to extend my heartfelt thanks to my parents, Dariush, and Iran. I dedicate my Ph.D. dissertation to them who are my inspiration to keep working hard for my dreams. I would also like to express my special thanks to my siblings, Fattaneh, Afshin, Homayoun, and Zahra for being always supportive. I also thank Shahram, Fatemeh, and Ali for their persistent encouragements. I would like to bring here the name of my lovely nieces and nephews, Kimia, Roshanak, Hossein, and Amirali. God bless all my lovely family members.

TABLE OF CONTENTS

LIST OF TABLES

LIST OF FIGURES

Chapter 1. Introduction

1.1. Motivation

Fire following earthquake is a cascading hazard initiated by large magnitude earthquakes in metropolitan areas characterized by moderate-to-high seismic activities. The multiple simultaneous ignitions caused by earthquake can result in mass conflagrations in the shaken area. Post-earthquake fires may lead to substantial damages to civil infrastructures and human fatalities during and/or after a large earthquake. For instance, it was reported that fire following the 1906 San Francisco earthquake caused 80% of the total damage (Scawthorn, 2008). Furthermore, fire following the 1923 Tokyo earthquake resulted in significant number of fatalities to a total 140,000 people (Scawthorn, 2008).

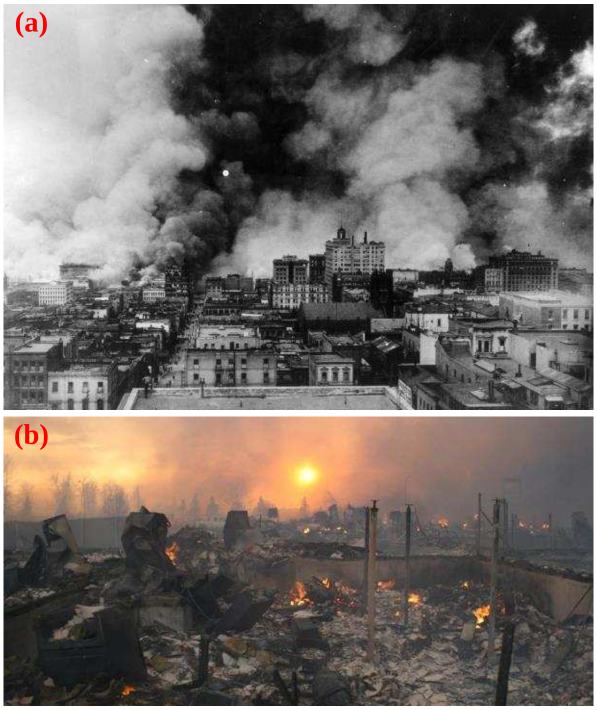

Figure 1.1 (a) A mass conflagration in city of San Francisco after the 1906 San Francisco earthquake (b) burnt remains of fire following the 1995 Kobe earthquake, photographers unknown.

Damages sustained by both active and passive fire protection systems in steel frame buildings during past earthquakes have been highly variable and can be substantial. This damage may result in unprotected steel frame being directly exposed to the elevated temperatures when post-earthquake fire ignition reaches flashover state. The potential for structural fire damage is further aggravated by the fact that current seismic design philosophy permits a certain degree of damage in the structures during an earthquake, making the structural systems more vulnerable when exposed to the additional demands from fire hazard after an earthquake event. In addition to structural damage, the ability of emergency response personnel to respond to the fire following a seismic event is hindered due to the earthquake-induced impairment to transportation, water supply, and communication systems as well as the existence of numerous fires.

The combined issues mentioned above can lead to catastrophic scenarios including structural collapse, hazardous materials release, loss of life, and the inability to provide emergency medical need. Even if no fire develops immediately after an earthquake, the modern performance-based design philosophy creates a need for understanding the effects of earthquake-induced damage on fire resistance of steel structured buildings. The performance of a structure that has been damaged by an earthquake must be assessed for the potential subsequent fire-induced demands. In summary, there is a pressing need to understand and quantify the response of steel structural members and frames under cascade hazard of earthquake and fire in moderate-to-high seismic regions.

1.2. Objectives

This study aims to evaluate the performance of steel structural members and systems under the cascading hazard of earthquake and fire using both deterministic and probabilistic approaches. The main focus of the investigation is on evaluating stability of steel columns subjected to lateral sway caused by earthquake and elevated temperatures due to fire in deterministic and probabilistic manners. This is realized through (1) the use of a newly devised nonlinear flexibility-based formulation, (2) the use of commercially-developed numerical finite element models, and (3) the use of a newly developed performance-based framework, which utilizes both the flexibility based method as well as the numerical finite element models.

The proposed flexibility-based formulation allows for the integration of a wide variety of variables in stability analysis of steel columns, including uniform or non-uniform longitudinal temperature profiles, various boundary conditions, among many others. In addition to using the proposed formulation for evaluating column stability, an equation is developed to predict Euler elastic buckling of W-shape steel columns in case of non-uniform longitudinal temperature distributions. Moreover, equations are proposed to estimate inelastic buckling of steel columns subjected to various levels of lateral sway and non-uniform longitudinal temperature profiles.

The numerical finite element models, developed using the commercial software ABAQUS (Simula, 2010), are utilized to evaluate the performance of steel moment resisting frames (MRFs), varying in height, with reduced beam section (RBS) connection under multi-story fire scenarios following time-history dynamic analysis of the frames under a suite of earthquake records. This includes assessment of system performance based on inter-story drift ratios (IDRs), interaction of axial force and bending moment in beams and columns, system instability of, and local response of RBS connections to post-earthquake fires. The numerical finite element models of the frames comprise of models with only line elements that are discretized at the beam-column joint to represent RBS connections as well as multi-resolution models that comprise of line element and detailed 3-D models of the RBS connections. The reason for choosing to investigate the response of RBS connections under fire following earthquake is because they have been extensively used in MRFs following the 1994 Northridge and the 1995 Kobe earthquakes to mitigate the brittle fractures that were observed in moment-resisting connections during these two earthquakes. However, studies on the performance of MRFs with RBS connections under the combined hazards of earthquake and fire are lacking.

A performance-based framework is established for probabilistic assessment of steel columns under fire following earthquakes. This framework allows structural design engineers to predict probability of instability in steel columns under determined level of lateral sway and design fire load. This is realized through first introducing a methodology for fire hazard modeling followed by stochastic modeling of the hazard, thermal properties of spray-applied fire resistive material, and applied mechanical loads. A Monte Carlo simulation technique is used to run a large number of deterministic analyses to obtain probability of failure in steel columns under various levels of lateral sway and design fire load. This probabilistic analysis will result in the development of fragility surfaces for individual structural columns subjected to the cascade hazards of earthquake and fire.

Reliability of structural systems under fire following earthquake is also considered in the present study. A scenario-based analysis framework is devised to evaluate probability of collapse in structural systems under the combined events. This is performed using Monte Carlo Simulations to define a large set of post-earthquake fire scenarios. The IDRs at the conclusion of all finite element simulations of the MRFs are combined with fragility analysis of steel columns to obtain collapse fragility of MRFs for the given fire scenario produced using Monte Carlo simulations.

1.3. Scope

In this study, the performance of steel structural members and systems subjected to multiple hazards of earthquake and fire is evaluated using deterministic and probabilistic approaches as illustrated in Figure 1.2.

The member-level deterministic analysis, conducted using the flexibility-based formulation, is utilized to evaluate instability of W-shape steel columns subjected to cascading load scenario of lateral sway and elevated temperatures. This analysis results in newly proposed equations for predicting inelastic buckling of steel columns under various levels of lateral sway and non-uniform longitudinal temperature distributions. As shown in Figure 1.2, the resulting equations are used in deterministic stability analysis of 2D structural systems under multi-story fire following earthquake. The deterministic analysis on the member- and system-level are crucial for proper understanding of the response of steel columns, girders, connections, and systems as a whole under the combined seismic and fire loadings. While the deterministic analysis provides valuable information regarding various aspects of structural response, such approach is not sufficient to assess performance of structural members and systems in accordance with modern performance-based design approach. It is worth noting that the developed equations using the deterministic analyses informs the probabilistic simulations through understanding the response sensitivity to various design parameters, which are altered in the probabilistic simulations.

A member-level probabilistic analysis is developed to evaluate fragility of steel columns subjected to cascading loading of lateral sway and fire. A strength-based limit state is defined to meet stability requirements of steel columns under fire following earthquake loading scenario. Monte Carlo simulation is implemented to run a large set of deterministic analysis to obtain fragility of steel columns subjected to various levels of IDR and design fire loads. Once the fragilities for a single column are developed, it is essential to combine the results to obtain fragility of a structural system subjected to fire following earthquake. This is conducted using a scenario-based Monte Carlo simulation. The fragility of the structural system will be based on global collapse limit state defined by instability in steel columns in one or more story levels.

As indicated above, in this study instability of one or more steel columns in a 2D frame is defined as a limit state for developing fragilities. However, in an actual 3D structural system buckling of a column or more in a 2D lateral resisting frame might not have an impact on the overall integrity of the structure in terms of the potential for lateral or vertical collapse. Indeed, modeling structural collapse where the structure is allowed to fail all the way to the ground is critical for proper assessment of failure. This, however, was not done in this study and therefore it is important to view the results presented in this dissertation in the proper context.

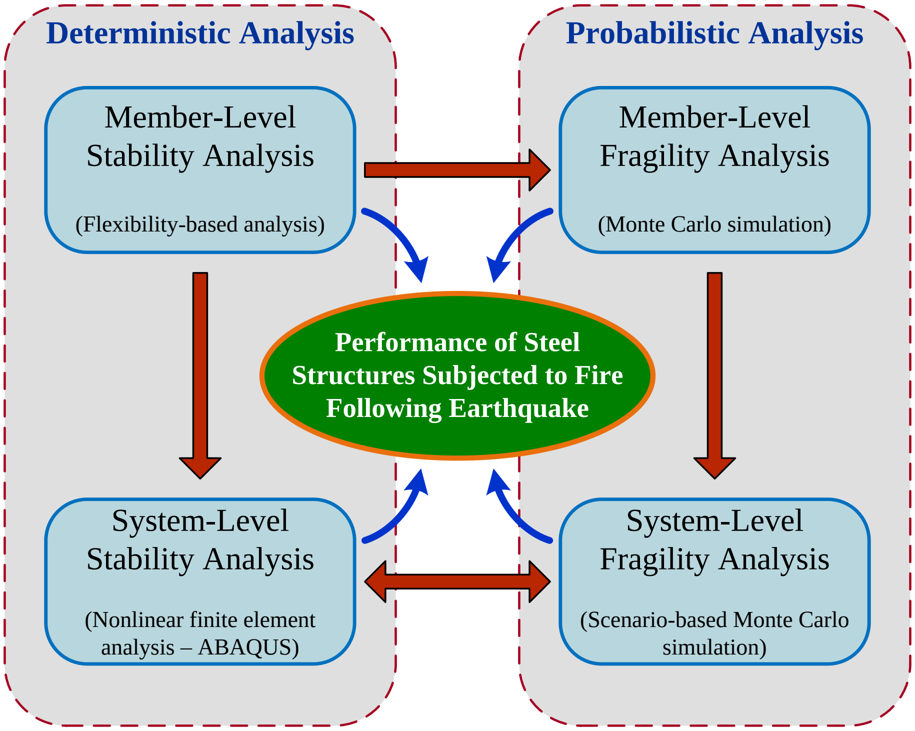

Figure 1.2 The framework of present study.

1.4. Research significance

The lack of design provisions on performance of steel structures subjected to fire following earthquake is a direct result of the very limited research being conducted on that subject. Therefore, this study attempts to develop rigorous deterministic and probabilistic performance-based approach for analysis and design of steel structures subjected to fire following earthquake on the member and system-levels.

Stability analysis of steel columns subjected to various levels of IDRs and non-uniform longitudinal temperature distribution and the resulting design equations are key elements in this study. The developed formulation and the resulting equations can be utilized by researchers and engineering for predicting inelastic buckling of steel columns under combined lateral sway caused by earthquake and elevated temperatures due to fire loads.

Although nonlinear static pushover analysis was predominantly utilized in previous studies on fire following earthquake of steel frames (Della Corte et al., 2003, Faggiano et al., 2007), utilizing nonlinear time-history analysis prior to the fire allows for proper capturing of stiffness and strength degradation in the system and will result in better representation of system condition prior to fire loading. In the present study the performance of steel MRFs with RBS connections is evaluated under a suite of ground motions then subjected to realistic fire curves that including both heating and cooling phases of fire using multi-resolution modeling technique. The multi-resolution models comprise of 3D continuum elements to represent the connection at the location of interest and line element for the remainder of the model. The 3D detailed model of the connection allows for capturing the localized demand on critical details such as the reduced section of the beams and weld access holes. The use of line elements serves two purposes – (1) allows for capturing of evaluation of the system level response of the frames and

(2) serves as a mean of providing natural and realistic boundary conditions for the 3D connection models such that accurate prediction of their response can be made.

A framework for performance-based fire following earthquake (PBFFE) is proposed also in the present study and is used to obtain fragility of steel columns subjected to different levels of IDRs and fire design loads. The instability limit state resulting from lateral sway and fire loading is chosen in developing steel columns fragilities for steel columns.

A scenario-based probability analysis is also developed to obtain fragility of structural systems subjected to fire following earthquake. In doing so, four damage measures representing instability of a column in a story are chosen for fragility development. This will allow structural engineers to determine probability of exceedance of various damage measures in structural systems under various post-earthquake fire scenarios. The significance of the present study can be summarized as follows:

Significance 1: Developing an efficient flexibility-based finite element tool to evaluate instability of steel columns with any level of IDRs while subjected to either uniform or non-uniform temperature profiles.

Significance 2: Proposing new design equations for inelastic buckling of columns under the combined demands of IDR and fire design loads.

Significance 3: Investigating the performance of steel MRFs with RBS connections subjected to fire following earthquake.

Significance 4: Implementing multi-resolution modeling technique in numerical finite element analysis to accurately capture the localized behavior of the connections as well as the global system response.

Significance 5: Developing a framework for performance-based fire following earthquake (PBFFE) engineering.

Significance 6: Developing fragility for steel columns subjected to lateral drift and fire loads considering member instability as a limit state.

Significance 7: Proposing a scenario-based framework to obtain fragility of steel structural systems exposed to post-earthquake fire loading.

1.5. Organization of dissertation

The present dissertation is outlined in 7 chapters to address the objectives of the study according to the highlighted scope. Chapter 2 provides background review of current knowledge on the cascading hazards of interest. This chapter mainly starts by providing an overview of post-earthquake ignition models available in literature. It continues by highlighting significant historical fire following earthquake events. It is then follows by a discussion on the response of steel structural systems at elevated temperatures according to historical fire events. Temperature-dependent material properties are presented in the next section based on American and European standards. The fire exposure models available in the literature are reviewed as well and their advantages and/or disadvantages. The previous studies on performance of steel structures under fire following earthquake are then briefly discussed to understand current level of knowledge and identify gaps pertaining to these cascading hazards. At the end of Chapter 2, existing structural fire design codes are highlighted.

In Chapter 3, a flexibility-based framework is devised for analyzing stability of steel columns subjected to demands imposed by IDR followed by fire loads. A non-linear finite element approach is proposed to assess the stability of W-shape steel columns under this multi-hazard loading scenario. Few case studies are conducted to evaluate the response of steel columns various levels of IDRs under either uniform or non-uniform longitudinal temperature distributions. Following the case studies, an equation is developed and proposed to calculate Euler elastic buckling of columns with non-uniform longitudinal temperature profiles. An equation is also proposed to determine inelastic buckling of steel columns under the two cascading hazards.

Chapter 4 pertains to conducting non-linear time-history analyses on low-, medium-, and high rise steel moment resisting frames (MRFs) under fire following earthquake. Specifically, nonlinear dynamic time-history and thermal-mechanical analyses are implemented to simulate ground motions and post-earthquake fires, respectively. This analysis provides a realistic representation of the expected seismic and fire demands. A multi-resolution analysis framework is developed to analyze detailed response of reduced beam section (RBS) connection under the cascading hazard of earthquake and fire.

Chapter 5 introduces a probabilistic framework to evaluate performance of steel structures subjected to combined hazards of earthquake and fire given uncertainties in hazards, thermal properties of passive fire protection, and applied mechanical loads. The framework can provide means by which structural design engineers could assess alternative design scenarios and select the preferred design option based on a desired probability of failure. Monte Carlo simulations are implemented to obtain fragility of steel structural members and systems subjected to the multi-hazard loading scenario of fire following earthquake.

In Chapter 6, a summary of current research is presented along with highlighting the most important findings of the study. The contribution of this research to the field of structural engineering is emphasized. Finally, a set of recommendations are made for future studies on the related topics.

Chapter 2. Background: Cascading hazard of earthquake and fire

2.1. Overview

Strong ground motions can cause severe damages to civil infrastructures and fatalities by shaking, landslide, liquefaction, tsunami, fire, and release of hazardous materials. Shaking is the predominant source of damage in majority of earthquakes. Although spread of fires following an earthquake in large urban area is relatively a rare cascading hazard, it can be the predominant source of damage due to urban characteristics, density, and meteorological conditions. Early fire following earthquake events such as the 1906 San Francisco earthquake in the U.S. and the 1923 Tokyo earthquake in Japan demonstrated the destructive potential of the combined hazards. More recently, fire following the 2009 Indonesia and 2010 Chile earthquakes was an indication of how important it is to quantify and mitigate the effect of the cascading hazards (Faggiano et al., 2010). The risk of human injuries and/or fatalities along with the potential for considerable damages to civil infrastructures and communities can be quite serious. The problem could be further worsened due to fire ignitions in multiple locations, inability of emergency personnel to respond to post-earthquake ignitions, impairment to transportation systems by rubbles and collapsed buildings induced by the earthquake, and damages to water supply and communication systems that are also induced by the earthquake (Della Corte et al., 2003). On the building level, the earthquake-induced damages to gravity and lateral load resisting systems can significantly reduce fire resistance of the system as a whole. This is particularly the case because current seismic design codes allow buildings to sustain a certain level of damages caused by strong ground motions. Hence, properly designed buildings for seismic actions can be significantly vulnerable under post-earthquake fire loads. Despite the potential threat, the cascading hazard of earthquake and fire has been given relatively minimal attention in the U.S. and worldwide.

This chapter provides a brief overview of post-earthquake fire hazard ignition models. Significant historical fires following earthquake events are reviewed and their consequences with respect to fatalities, damages to civil infrastructures, and costs of repair are highlighted. A few significant historical fires in steel framed buildings are examined in order to understand performance of steel structures subjected to elevated temperatures. Temperature-dependent properties of structural steel material are also reviewed since they have significant effects on the response of steel systems under elevated temperatures. Fire exposure models will be discussed in this chapter with detailed information regarding their characteristics. The past studies on response of steel structural systems under fire following earthquake are also reviewed along with current design standards for fire design of structures.

2.2. Post-earthquake fire ignition models

It is essential to model post-earthquake fire ignition in order to estimate potential locations of post-earthquake fires as well as their coincidence following an earthquake (Scawthorn, 2008). Most post-earthquake ignition models are actually based on regression analysis, which correlate ignition rate per unit area to earthquake intensity as the only independent variable. Diversity in datasets and variety in ignition sources present a challenge in modeling post-earthquake ignition. Therefore, available post-earthquake fire ignition models are only valid for dataset upon which they were built. Most of these models provide very close estimation of post-earthquake ignition in the range of historical dataset (Lee et al., 2008). Table 2.1 shows 5 post-earthquake ignition models with their characteristics including dataset from which they were developed, response variable, covariate, proposed equations, R-square of fitness, and the statistical model for the number of ignitions predicted. For instance, Ren and Xie (2004) estimated the ignition rate in particular building per area unit according to relative estimated fire risk.

Table 2.1 Post-earthquake fire ignition models.

Model	Data	Response variable (Y)	Covariate (X)	Equation	R^2	No. of ignitions predicted	Reference
HAZUS (1999)	10 US earthquakes between 1906 and 1989	Ignition per 106 sq. ft. of building floor area	PGA	Y=-0.025+0.59X-0.29X2	0.34	Poisson process	FEMA (2002)
Ren and Xie (2004)	US, Japan, and China earthquake between 1900 and 1996	Fire sites per 105 sq. m.	PGA	Y=-0.11749+1.3453X-0.8476X2	N/A	Y* (total building area)	Ren and Xie (2004)
Scawthorn et al. (2005)	California earthquakes between 1971 and 2005	Ignition per 103 SFED	MMI	Y=-0.61-0.185X+0.015X2	0.2	Poisson process	Scawthorn et al. (2005)
Scawthorn et al. (2005)	California earthquakes between 1971 and 2005	Ignition per 106 sq. ft. of building floor area	PGA	Y=0.028e4.16X	0.2	Poisson process	Scawthorn et al. (2005)
Zhao et al. (2006)	US, Japan, and China earthquakes in 20th century	No. of outbreaks per 105 sq. m. building floor area	PGA	Y=-0.0042+0.5985X	N/A	Poisson process	Zhao et al. (2006)

Scawthorn et al. (1981) and Scawthorn (1986) developed an integrated stochastic modeling approach for post-earthquake ignition, spread, and suppression. Scawthorn et al. (2005) also developed a probabilistic analysis framework for modeling of fire following earthquake in a large urban area as illustrated in Figure 2.1.

It is important to note that there has been significant progress toward modeling of fire following earthquake ignition in the last 50 years, particularly in the last 20 years, using computational simulation tools (Lee et al., 2008). However, the accuracy of such models still requires further improvements.

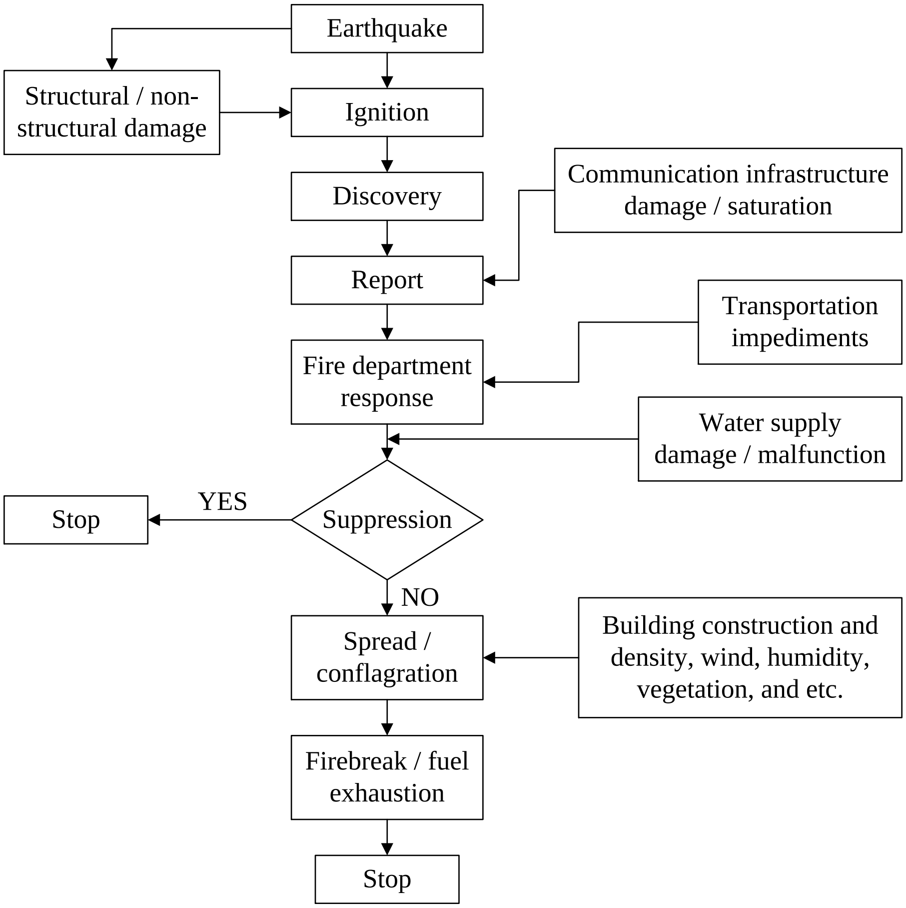

Figure 2.1 Fire following earthquake process (Scawthorn et al., 2005).

2.3. Historical post-earthquake fire events

This section briefly discusses some historical post-earthquake fire events in urban areas in the United States and other countries. The review of these historical post-earthquake fires demonstrates that this cascading hazard is a recurring event where multiple simultaneous fires following an earthquake with large magnitude could result in substantial losses. In the following sections, fire following the 1906 San Francisco, 1923 Tokyo, 1989 Loma Prieta, 1994 Northridge, and 1995 Kobe earthquakes will be reviewed.

2.3.1. The 1906 San Francisco earthquake

The 1906 San Francisco earthquake with magnitude of 8.3M_W was classified as the most devastating earthquake in U.S. history due to the subsequent fire that occurred, which has been classified as the largest urban fire known to occur in the U.S. The combination of the earthquake and the following urban fires caused approximately 3,000 deaths and $524 million (1906 US dollar) loss in properties (Eidinger, 2004). The combination of high winds in San Francisco bay area, earthquake-induced impairment to transportation, limitations in firefighter personnel, and lack of water supply resulted in 3 days of fire burning in city urban area. This caused severe damages to 28,000 buildings where 80% of damage was because of post-earthquake fires rather than the earthquake (Eidinger, 2004). Scawthorn (2006) reported data on 52 earthquake-induced fire ignitions in urban area of San Francisco, which were converted to a conflagration following earthquake, causing the vast majority of damages in this earthquake event.

Figure 2.2 (a) View of Sacramento Street, fire in background, following the 1906 San Francisco earthquake, photo by Arnold Genthe (b) destroyed buildings in vicinity of Post and Grand avenues after the 1906 San Francisco earthquake, photographer unknown.

2.3.2. The 1923 Tokyo earthquake

The largest conflagration in the world ever to occur was recorded following the 1923 Tokyo earthquake with magnitude 7.9M_W, which resulted in approximately 140,000 deaths. This earthquake created significant damages to 126,000 residential buildings and ruined 128,000 houses (Eidinger, 2004). High density of wood structures in Tokyo, dry meteorological conditions, and hot wind with high gusts – 21 (m/s) – resulted in 133 spread fires out of approximately 277 small fire incidents. The major conflagration kept burning approximately 447,000 residential houses for several days (Eidinger, 2004).

Figure 2.3 (a) Ginza district of Tokyo engulfed in flames after the 1923 Tokyo earthquake (b) burning of metropolitan police department at Marunouchi following the 1923 Tokyo earthquake, photographers unknown.

2.3.3. The 1989 Loma Prieta earthquake

The 1989 Loma Prieta earthquake with magnitude 7.1M_W resulted in substantial number of collapses of important structures such as San Francisco-Oakland Bay bridge, Cypress Street section of I-880 in Oakland, several buildings in Marina district of San Francisco, and many structures in Santa Cruz and some small towns (Eidinger, 2004). Reports indicate 62 deaths, 3,700 injuries, and more than 12,000 displaced. In addition, 18,000 residential buildings were significantly damaged, while 960 were destroyed (Eidinger, 2004). A total of 26 earthquake-induced fires occurred in the city of San Francisco, in which one of the major fire incidents took place in Marina district. This post-earthquake fire could become a major conflagration because of lack of water supply, severe liquefaction and damage to pipelines of Marina, and impairment in transportation system. The total loss was estimated at $6.0 billion.

Figure 2.4 (a) Fire consumes homes in the Marina District after the 1989 Loma Prieta earthquake in San Francisco (b) Fire flames in a residential district after the 1989 Loma Prieta earthquake (c) Fire erupts in the hard-hit Marina District of the city after the 1989 Loma Prieta earthquake, photographers unknown.

2.3.4. The 1994 Northridge earthquake

The 6.8M_W 1994 Northridge earthquake was a devastating ground motion in the late 20th century. Over 100 earthquake-induced fire ignitions took place, as reported, with no conversion into a conflagration. A total of 161 fires took place on the day of earthquake, in which 77 fire incidents were earthquake-induced as Los Angeles Fire Department (LAFD) reported. Other resources reported 110 earthquake-related fires where the majority of them (86%) were earthquake-induced structural fires, and more than 70% of which were in single- and multiple-residential buildings. Electrical arcing because of a short circuit and gas flame from an appliance were two major sources of ignition after earthquake.

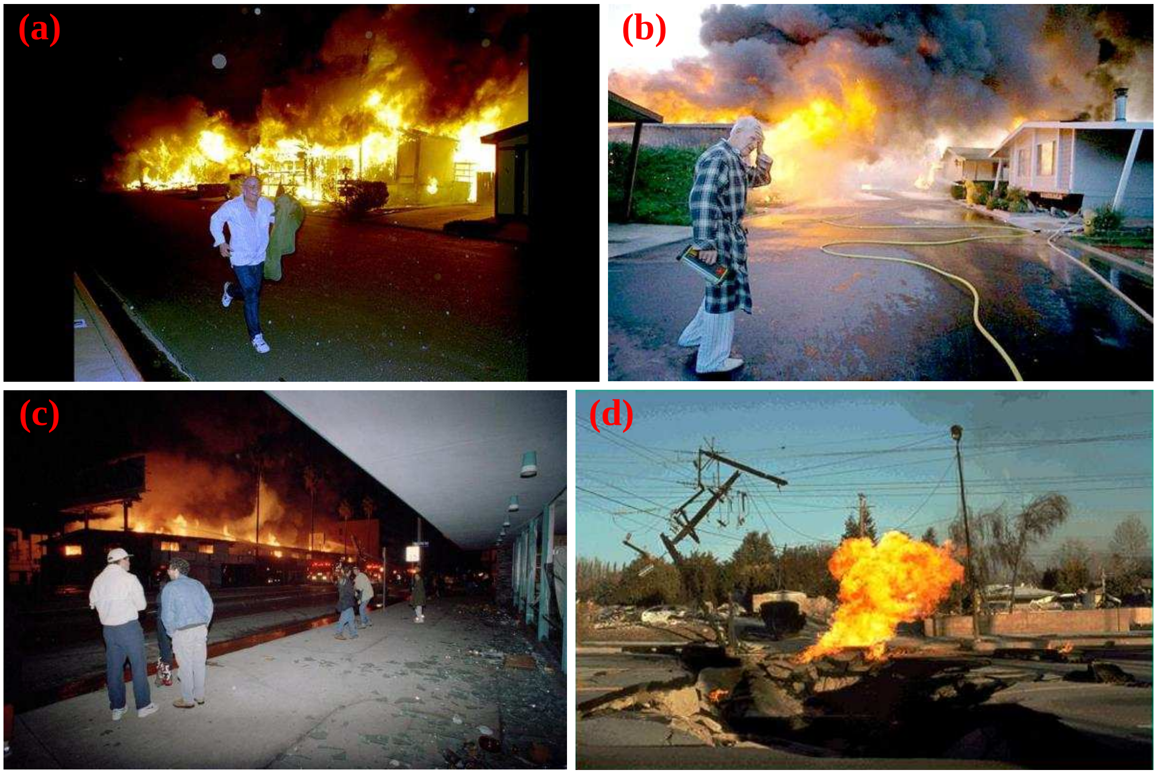

Figure 2.5 (a) Burning mobile homes in a neighborhood following the 1994 Northridge earthquake (b) fire and lateral spread caused by the 1994 Northridge earthquake (c) spectators watch a building burn amid glass shards and other rubble in the Sherman Oaks area of Los Angeles after the 1994 Northridge earthquake (d) a broken gas pipeline resulted in fire after the 1994 Northridge earthquake, photographers unknown.

2.3.5. The 1995 Kobe earthquake

The 1995 Kobe earthquake with magnitude of 6.9M_W shook an area of 400 square km with population of approximately 2 million people. More than 100 earthquake-induced fire incidents were started right after the conclusion of the ground motion and resulted in several conflagrations within 1-2 hours after the earthquake. These fire incidents mainly took place in the central part of the city with high concentration of low-rise residential-commercial wood constructed buildings. It has been reported that firefighting was hindered by a large traffic jam and collapsed buildings, which made many areas inaccessible to vehicles.

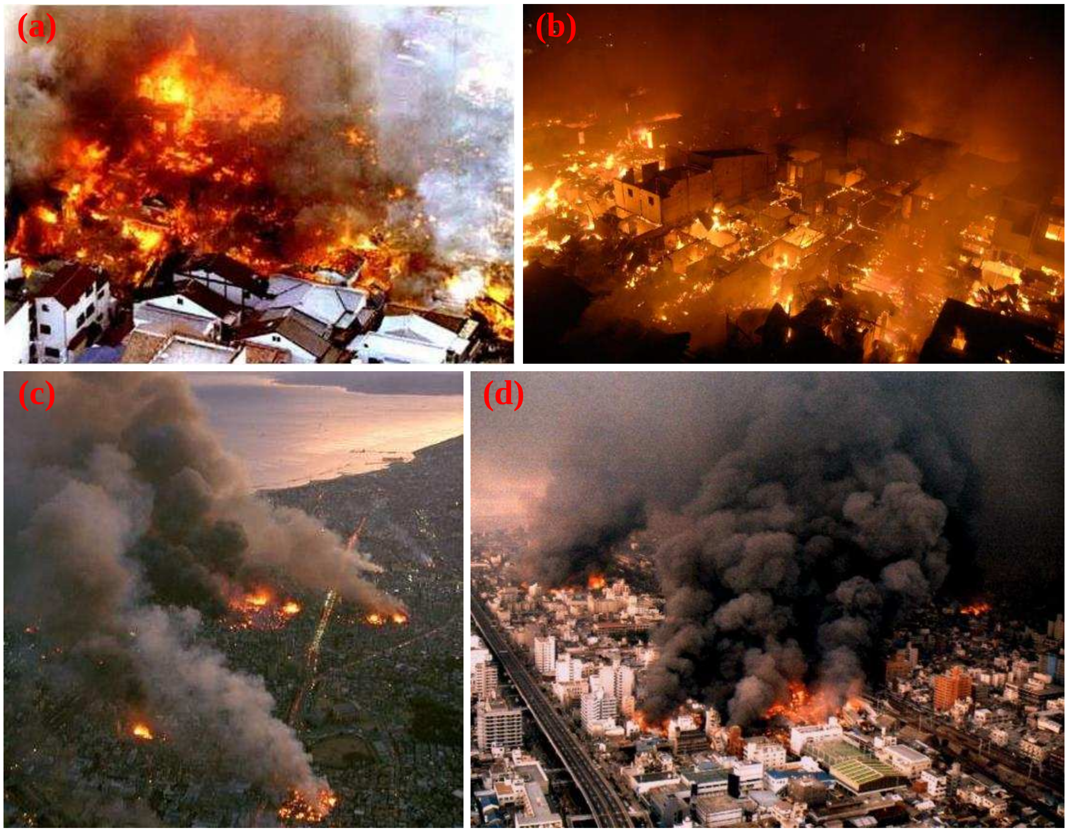

Figure 2.6 (a) Houses in flames as fire spreads through a city block following the 1995 Kobe earthquake (b) a mass conflagration in city of Kobe after the 1995 Kobe earthquake (c) simultaneous conflagrations after the 1995 Kobe earthquake (d) Black smoke rises from burning buildings on aerial view of Kobe following the 1995 Kobe earthquake, photographers unknown.

2.4. Significant historical fires

Although the focus of the present study is on performance of steel structures subjected to fire following earthquake, it will be worth to review performance of steel structures under only fire hazard. Although there are many historical building fires, e.g. One New York Plaza, First Interstate Bank, One Meridian Plaza, Alexis Nihon Plaza, among others., two cases are only discussed in this section because of their relevance and the important observations and lessons learned from these two cases. This includes the Broadgate phase 8 in London, UK, and Windsor

Building fire in Madrid, Spain. A large full-scale fire test was conducted in Cardington, UK, to assess the response of an 8-story steel building exposed to fire. The details of this fire test are not discussed here since they have been well-documented in the literature and are publically available. Furthermore, the details of the collapse of World Trade Center (WTC) building 7, which resulted from loss of structural integrity in one of the load transfer systems likely caused by fires on the 5th to 7th floors (FEMA 403, 2002), due to the 9/11 terrorist attack are not discussed in the present study since many reports provided comprehensive coverage of the event.

A 14-story steel building caught on fire during development of Broadgate project (Broadgate phase 8) in London, UK. The fire lasted for more than 4 hours and resulted in over 1000℃ temperature. No passive and active fire protections were installed in the stories that caught on fire since the building was under construction at the time of fire. Although, the structure was subjected to loads much less than the design loads, significant damage was observed in many of structural members and components. Permanent deflection was noted, as shown in Figure 2.7(a), to be larger than 500 mm in steel trusses and between 80 mm and 270 mm in composite beams. Significant local buckling was also observed in flanges and web of steel girders, which is an indication of high axial compressive demand due to thermal expansion. Furthermore, steel columns had large local buckling in flanges and web, as shown in Figure 7.2(b), along with shortening by approximately 100 mm.

Figure 2.7 (a) Large permanent deflections in composite beams and trusses and (b) significant local buckling in flanges and web of a steel column in Broadgate project (Broadgate phase 8) fire.

The 32-story Windsor building in Madrid, Spain, was engulfed by fire flames, while being renovated, from the 21st story to the 31st story as well as slightly to lower levels (Figure 2.8(a)). There was a significant structural damage at the top 10 stories since fire protections were not installed on the steel components during the renovation operation. Perimeter steel columns in these stories completely failed as shown in Figure 2.8(b); however, the reinforced concrete core of the building prevented a global system collapse. It was reported that partial collapse of the building was triggered by buckling of perimeter steel columns due to material deterioration at elevated temperatures combined with the axial demand caused by the fire. The number of buckled columns was increased due to the spread of fire to various stories. The instability of columns in one of the stories resulted in collapse of a waffle concrete slab on the slab of another lower story and propagation of collapse in a pancaking effect.

Figure 2.8 (a) Fire flames engulf top 10 stories of Windsor building in Madrid, Spain (b) partial collapse in top 10 stories.

In summary, Table 2.2 shows details of fires that occurred in 8 steel structures. Only World Trade Center (WTC) building 7 collapsed under elevated temperatures, while the remainder of the listed buildings experienced partial to no collapse. The most important conclusion from a brief review of fire events in steel buildings revealed that there is no global collapse in steel structures under only fire loads except WTC building 7. In fact, this shows the high potential of steel building to remain standing under fire hazard when designed according to the current prescriptive provisions. It is important to note, however, that full understanding of system performance and the potential for global collapse requires the utilization of analytical tools that can capture system response up to and including total failure. In general, historical events of steel buildings under fire have shown steel beams with temperatures higher than 1000℃ to undergo excessive deflections accompanied with associated catenary actions and have highlighted the vulnerability of steel columns under elevated temperature conditions. As an example, the partial collapse in upper stories of Windsor building in Madrid, Spain, was because of buckling of unprotected steel columns.

Table 2.2 Significant historical fires in steel structures.

Name of Building	Location	No. of Stories	Duration of Fire	Type of Structural Damges	Year
One New York Plaza	New York, USA	50	6-hour	Failure in bolted connections	1970
Alexis Nihon Plaza	Montreal, CA	15	13-hour	Collapse at 11th floor	1986
First Interstate Bank	Los Angeles, USA	62	3.5-hour	No collapse	1988
Broadgate Phase 8	London, UK	14	4.5-hour	No collapse	1990
Mercantile Insurance Building	Basingstoke, UK	12	---	No collapse	1991
One Meridian Plaza	Philadelphia, USA	38	19-hour	No collapse	1991
WTC 7	New York, USA	47	8-hour	Global collapse	2001
Windsor building	Madrid, Spain	32	20-hour	Partial collapse at top 10 stories	2005

2.5. Temperature-dependent constitutive model of structural steel

The recent move towards using advanced simulation tools in assessing performance of steel structures under fire hazard created an essential need to specify temperature-dependent properties of structural steel material in numerical models. Three important characteristics of structural steel material determine the response of steel structural system exposed to fire hazard, including thermal, deformational, and mechanical properties. These properties vary with temperature such that substantial levels of deteriorations in strength and stiffness occur as the temperature increases. It should be noted that available data in the literature on temperature-dependent properties of structural steel are based on limited number of experimental tests commonly conducted under controlled-heating fire phase. There is a noticeable variation between the available data sets due to variation in testing methodology, e.g. transient- versus steady-state approaches, force- versus displacement-controlled methods, and various heating rates. The noted variations are due to the lack of standard testing protocol for measuring temperature-dependent properties of structural steel.

A steel structural system under a real fire event is exposed to transient-state process with temperature and stress variation. Hence, transient-state testing approaches could result in more realistic predictions of material properties of structural steel at elevated temperature (Phan et al., 2010). Twilt (1991) indicated that the Eurocode 3 (CEN, 2005) temperature-dependent constitutive model have been originated based on transient-state testing protocol with a slow heating rate, while there is no such information on how the ASCE (1992) model has been established. In brief, this variation in temperature-dependent properties of structural steel creates a challenge for researchers and engineers in selecting the most reliable set of data for numerical simulations. The temperature-dependent constitutive models of structural steel material are reviewed according to ASCE (ASCE, 1992), Eurocode 3 (CEN, 2005), and AISC 360-10 (2010) standards in this section. In addition, features and variation of these three temperature-dependent constitutive models of structural steel are highlighted.

2.5.1. Mechanical properties

Temperature-dependent stress-strain relationship is required to analyze mechanical response of steel structural systems subjected to elevated temperatures. This includes modulus of elasticity, yield stress, proportional limit, and Poisson's ratio. The later parameter, Poisson's ratio, is usually considered independent from temperature change, and is taken as 0.3. However, tensile tests are usually conducted to measure strength (yield stress) and stiffness (modulus of elasticity) of structural steel at ambient and elevated temperatures. It is shown that both yield stress and modulus of elasticity decrease as temperature increases in accordance with Figure 2.9(a) and (b). This reduction is attributed to the fact that nucleus of atoms move apart in material structure due to increase in temperature. As a result, bonding of nucleus of atoms deteriorates and this results in reduction in yield stress and modulus of elasticity at elevated temperatures.

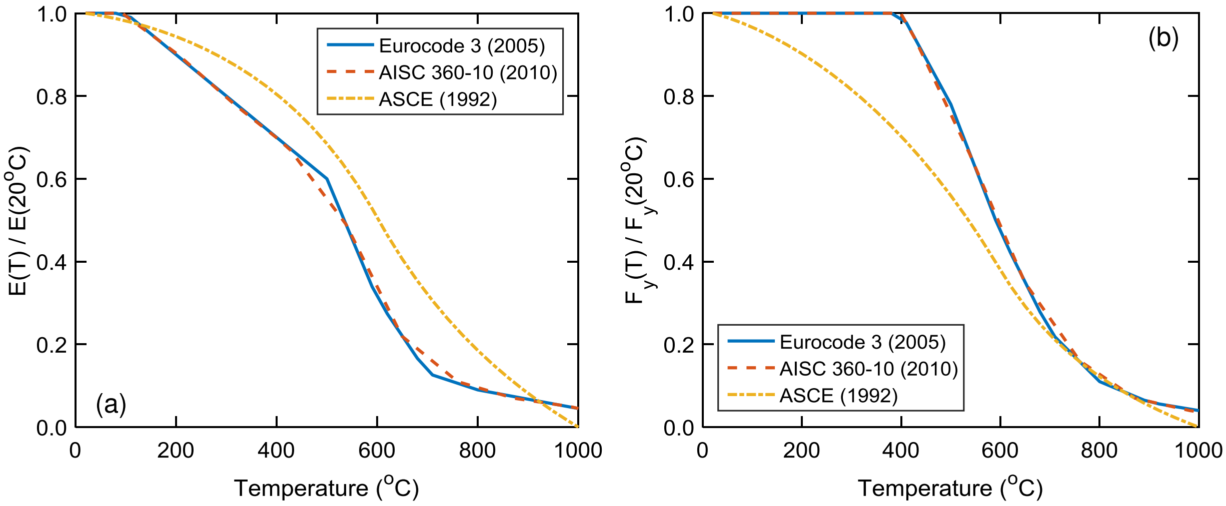

Figure 2.9 Deterioration models for (a) modulus of elasticity and (b) strength of structural steel at elevated temperatures.

A review of temperature-dependent mechanical properties of structural steel according to ASCE (1992) and Eurocode 3 (CEN, 2005) indicates a significant difference between both provisions, while AISC 360-10 (2010) addresses these properties similar to Eurocode 3 (CEN, 2005) with minimal difference, since they are both based on the same study, as shown in Figure 2.9(a) and (b). The difference between ASCE (1992) and Eurocode 3 (CEN, 2005) can be attributed to many parameters, e.g. testing protocol and/or testing at various heating rates. The

ASCE (1992) model predicts very rapid reduction in yield stress at elevated temperatures in comparison with Eurocode 3 (CEN, 2005). For example, the yield stress has no reduction prior 400°C in the Eurocode 3 (CEN, 2005) constitutive model (Figure 2.9(a)), while 30% reduction is observed at 400°C (Figure 2.9(a)) in accordance with the ASCE (1992) model. Nevertheless, the Eurocode 3 (CEN, 2005) model undergoes faster reduction in modulus of elasticity of structural steel than that of ASCE (1992) model at elevated temperatures. It is important to note that both the Eurocode 3 (CEN, 2005) and the AISC 360-10 (2010) constitutive models consider proportional limit along with yield stress in mechanical properties of structural steel at elevated temperatures, while the ASCE (1992) model does not incorporate it in the model. The proportional limit is defined as the end of the linear portion in a stress-strain relationship, where stress-strain relationship remains elastic but nonlinear beyond that point. Furthermore, the yield stress is the point where the material response becomes inelastic and nonlinear.

The concept of including proportional limit in the Eurocode 3 (CEN, 2005) model is to reflect viscoelastic behavior of structural steel material at elevated temperatures, which is recognized to have large impact on the behavior of steel columns at elevated temperature. This is because the material, beyond the proportional limit, exhibits larger strain at a particular level of stress compared to that in linear elastic behavior. Subsequently, incorporating proportional limit in the constitutive model of structural steel in Eurocode 3 (CEN, 2005) partially takes into account the inherent creep effects at elevated temperatures. Buchanan (2001) argues that inherent creep effects considered in the Eurocode 3 (CEN, 2005) constitutive model is a key parameter in attaining more flexible response of steel structures when subjected to elevated temperatures. Figure 2.10(a) shows deterioration of proportional limit in accordance with Eurocode 3 (CEN, 2005) and AISC 360-10 (2010) at elevated temperatures. A minimal difference is also observed between these two models. In addition, Figure 2.10(b) shows the stress-strain relationship for structural steel according to Eurocode 3 (CEN, 2005) at ambient, 200°C, 500°C, 800°C, and 1000°C. The inclusion of proportional limit in this constitutive model is clearly shown in Figure 2.10(b). It is also noted that the yield stress is defined as the stress corresponding to 0.2% of strain according to Eurocode 3 (CEN, 2005).

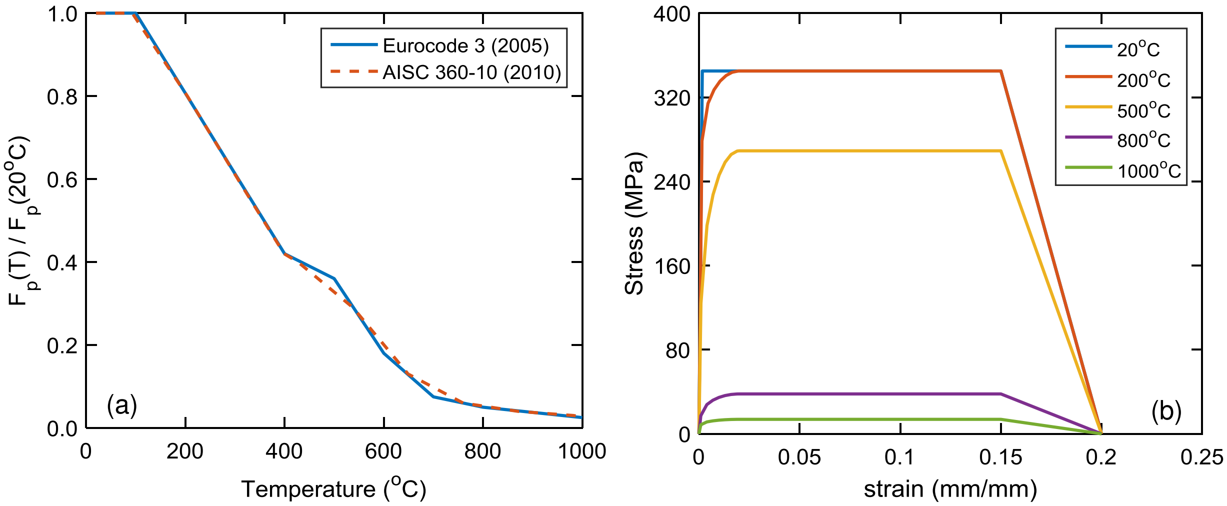

Figure 2.10 (a) Variation of proportional limit at elevated temperatures (b) Eurocode 3 (CEN, 2005) constitutive model considering variation of proportional limit, yield stress, and modulus of elasticity at elevated temperatures.

2.5.2. Thermal properties

Thermal conductivity, specific heat, and density are known as the most effective parameters in predicting heat propagation inside the body of structural steel material. While thermal conductivity and specific heat have temperature-dependent properties, the density of structural steel is assumed constant at 7850 (Kg/m^3) irrespective of temperature. Both Eurocode 3 (CEN, 2005) and ASCE (1992) stipulate empirical temperature-dependent relationship for these thermal parameters. Thermal conductivity is defined as the heat energy propagated per unit of time through a unit of surface area divided by the temperature gradient, which is the temperature difference divided by the distance between the two surfaces. The thermal conductivity of structural steel decreases linearly at elevated temperatures up to 800°C according to Eurocode 3 (CEN, 2005) as illustrated in Figure 2.11, after which it becomes constant. It should be noted that the ASCE (1992) model predicts less reduction in thermal conductivity in comparison to Eurocode 3 (CEN, 2005). The Eurocode 3 (CEN, 2005) predicts constant thermal conductivity starting at 800℃, and it turns to be constant approximately after 900°C in the ASCE (1992) model.

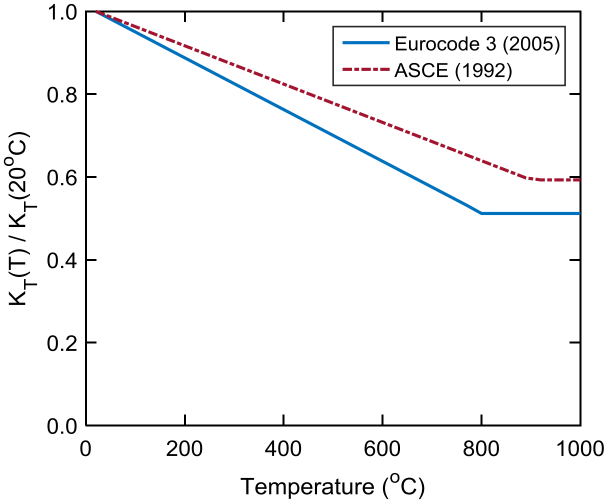

Figure 2.11 Variation of thermal conductivity of structural steel at elevated temperatures.

The specific heat is the amount of heat in calories required to increase the temperature of one gram of a substance by one degree of temperature in Celsius. The specific heat of structural steel material increases in a linear fashion at elevated temperatures prior to 700°C. This increase in specific heat is because atoms in structure of material move apart as the temperature rises; hence, they attain a higher level of energy. The big thorn in the specific heat around 750°C is because of a phase change in steel material such that the structure of the atoms is transformed from a face-centered cubic to a body-centered cubic. The significant amount of energy absorbed through this process results in a thorn at almost 750°C as shown in Figure 2.12.

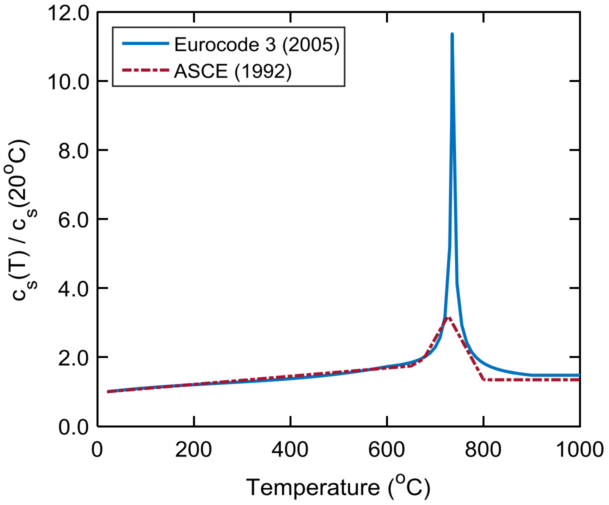

Figure 2.12 Variation of specific heat of structural steel at elevated temperatures.

2.5.3. Coefficient of thermal expansion

Thermal expansion or thermal strain is expressed as the deformational property of structural steel material at elevated temperatures. Thermal expansion is defined as material tendency to expand and/or retract due to temperature change. Eq. (2.1) determines the relationship between thermal expansion, $\alpha(T)$, and thermal strain, $\epsilon(T)$, as shown below:

$$\epsilon_T(T) = \alpha(T).\Delta T \tag{2.1}$$

where, ΔT is defined as temperature change.

The thermal expansion of structural steel increases with a linear trend at elevated temperatures prior to approximately 700°C according to both Eurocode 3 (CEN, 2005) and ASCE (1992). However, the Eurocode 3 (CEN, 2005) model shows a linear drop in thermal expansion between 750°C and 850°C, while the ASCE model provides a continuously increasing thermal expansion in this temperature range and beyond. The Eurocode 3 (CEN, 2005) model reflects again linear increase in thermal expansion beyond 850°C. The drop in thermal expansion between 750°C and 850°C is because of phase change in material structure. Figure 2.13 illustrates variation of thermal expansion in structural steel as a function of temperature.

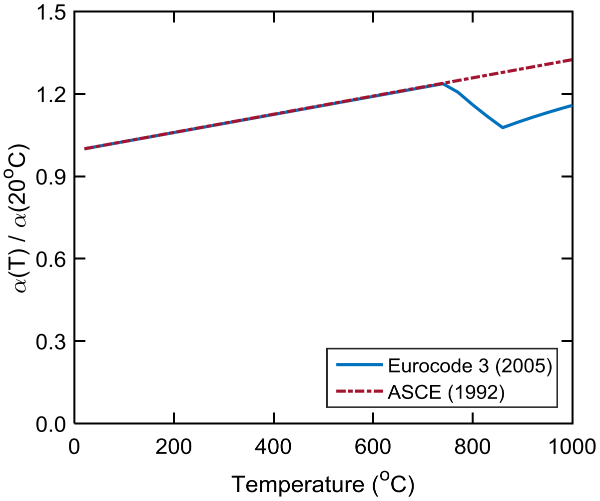

Figure 2.13 Variation of thermal expansion of structural steel at elevated temperatures.

In summary, different prediction of temperature-dependent thermal, mechanical, and deformational properties of structural steel by ASCE (1992) and Eurocode 3 (CEN, 2005) results in completely different structural response of steel frames to fire simulations. It is recognized that temperature-dependent properties of structural steel in accordance with the Eurocode 3 (CEN, 2005) model provide a more realistic fire response of steel structural components and systems than that of the ASCE (1992) model. Pending further verifications, this could be attributed to the fact that the temperature-dependent stress-strain relationship in the Eurocode 3 (CEN, 2005) model inherently takes into account high-temperature creep effects. This can also be because of transient-state testing protocol with a slow heating rate for extracting data at elevated temperatures.

2.6. Temperature-dependent damage of structural steel

An accurate prediction of the plastic deformation and failure of the steel elements essentially requires proper capturing of material damage. The Johnson-Cook damage model represents a cumulative-damage fracture model, which expresses fracture strain as a function of stress triaxiality (σ^*), strain rate ($\dot{\epsilon}^*$), and homologous temperature (T^*) (Johnson and Cook, 1985). Therefore, the Johnson-Cook ductile damage initiation criterion is viewed as an appropriate fracture model to use in the present study for σ^* less than or equal 1.5 as shown in Eq. (2.2), where $\sigma^* = \sigma_m/\bar{\sigma}$, in which σ_m is the average of the three normal stresses and $\bar{\sigma}$ is the von Mises equivalent stress as illustrated in Eq. (2.3).

$$\epsilon_f = [D_1 + D_2 . exp(D_3\sigma^*)][1 + D_4 . ln(\dot{\epsilon}^*)][1 + D_5 T^*] \tag{2.2}$$

$$\bar{\sigma} = \sqrt{\frac{1}{2}[(\sigma_1 - \sigma_2)^2 + (\sigma_2 - \sigma_3)^2 + (\sigma_3 - \sigma_1)^2]} \tag{2.3}$$

The strain rate ($\dot{\epsilon}^* = \dot{\epsilon}/\dot{\epsilon}_0$) is defined as dimensionless plastic strain at $\dot{\epsilon}_0 = 1.0\, s^{-1}$, where

$$\dot{\epsilon} = \sqrt{\frac{2}{9}[(\dot{\epsilon}_1 - \dot{\epsilon}_2)^2 + (\dot{\epsilon}_2 - \dot{\epsilon}_3)^2 + (\dot{\epsilon}_3 - \dot{\epsilon}_1)^2]} \tag{2.4}$$

and $\dot{\epsilon}_1$, $\dot{\epsilon}_2$, and $\dot{\epsilon}_3$ are principal strain rates. The homologous temperature is also defined as Eq. (2.4) shown below:

$$T^* = \begin{cases} 0 & T < T_t \\ \frac{T - T_t}{T_m - T_t} & T_t \le T \le T_m \\ 1 & T > T_m \end{cases} \tag{2.5}$$

where, T is temperature, T_m is melting temperature, and T_t is transition temperature defined as the one at or below which there is no temperature dependence on the expression of the damage strain $\dot{\epsilon}$. It is noted that the hydrostatic stress, σ_m, is the most effective parameter in fracture strain such that increase in hydrostatic stress causes rapid decrease in fracture strain. The effects of strain rate and temperature seem to be less important (Johnson and Cook, 1985). The five constants $D_1 - D_5$ are defined according to Johnson and Cook (1985). For σ^* greater than 1.5, a different relationship is used, in which fracture strain varies linearly with respect to stress triaxiality. A linear evolution of the damage variable with effective plastic displacement can be considered, which allows the effective plastic displacement to be specified at the point of full degradation of material. The schematic definition of temperature-dependent mechanical properties of material along with damage model is shown in Fig. 2.14. It is important to point out, however, that the Johnson-Cook model is very effective in simulating ductile failure under tensile loading. In cases where the failure is dominated by shear or a combined tension and shear demand, then inaccurate predictions can be expected. Recent work by Wen and Mahmoud (2015a and 2015b) resulted in the development of a new ductile fracture model that allowed for accurate prediction of fracture under the combined monotonic or cyclic tension and shear demands. The model is yet to be extended to account for the effect of temperature on the predicted fracture strain.

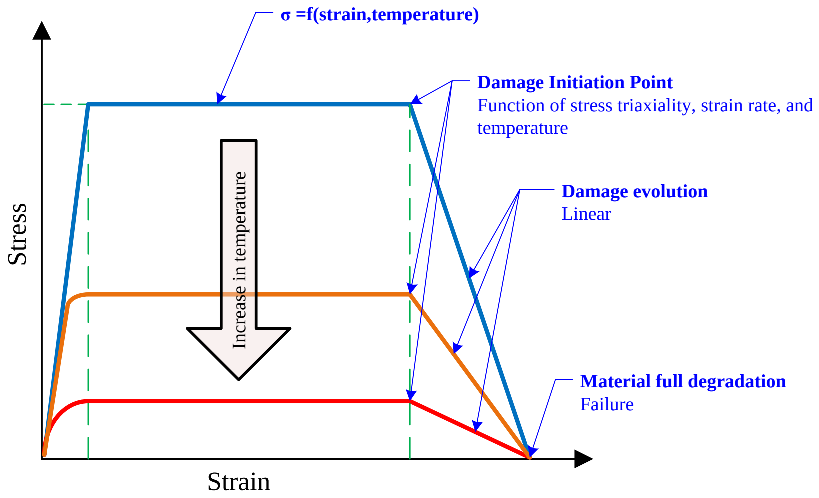

Figure 2.14 Schematic definition of temperature-dependent stress-strain relationship along with damage model at elevated temperatures.

2.7. Fire exposures

Fire ignition can be converted to flashover condition if sufficient fuel supply and ventilation are provided by the compartment, in which all combustible materials exposed to fire are ignited. After such point, the fire is considered fully developed (i.e. post-flashover) as illustrated in Figure 2.15. Structural fire engineers only consider the later phase of a fire event as temperature rises up significantly. The post-flashover phase of fire can cause significant deterioration in strength and stiffness of structural steel material. Consequently, post-flashover phase of a fire can increase the risk of partial and/or global collapse in a structural system.

The rate of heat release increases after flashover point such that it quickly reaches its maximum value based on available combustibles and ventilation in compartment. It is usually assumed that a compartment is fully involved in fire when the same temperature is simultaneously applied to the whole compartment. This is because time interval between the onset of flashover and maximum heat release can be usually ignored to simplify the design process. It is usually expected that flashover occurs when gas temperature reaches about 600℃ as fire flames touch the ceiling of a compartment. This section reviews available post-flashover fire curves used in structural fire engineering.

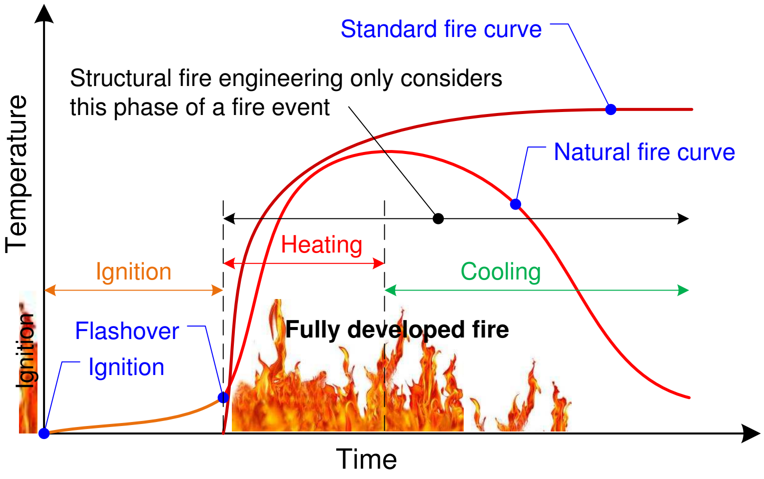

Figure 2.15 Typical time-temperature curve for fire in compartment.

2.7.1. Standard Fire Exposure

Fire is represented using time-temperature curves in experimental tests and numerical simulations. Standard fires are widely used to evaluate fire resistance ratings (FRR) of structural components and materials. Large-scale tests are commonly conducted to allow researchers to investigate the effects of thermal expansion, local damages, and large deformations in structural components. ASTM-E119 (2016) and ISO-834 (EC1, 2002) are discussed here in details as they represent the most common standard fire curves used in testing of structural components under elevated temperatures. These two standard fire curves are very similar with respect to gas temperature as a function of time as illustrated in Figure 2.16. It should be also noted that there are many other standard fire curves including NFPA 251 (NFPA 2006), UL 263 (UL 2003), Canadian Standard CAN/ULC-S101-04 (ULC 2004), British Standard BS 476, Parts 20-23 (BSI 1987), and Australian Standard AS 1530, Part 4 (SAA 1990), which will not be discussed here for sake of brevity.

The ASTM-E119 (2012) standard fire curve is defined by a set of discrete points in time-temperature coordinate system available in ASTM-E119 (2016) document. Further details can be found in ASTM-E119 (2016) for further details. The ISO-834 (EC1, 2002) represents gas temperature in a fire compartment as a function of time in accordance with Eq. (2.6) as shown below

$$T_g = 20 + 345\, log_{10}(8t + 1) \tag{2.6}$$

where, T_g is the gas temperature in compartment in degree Celsius and t is the time in minutes.

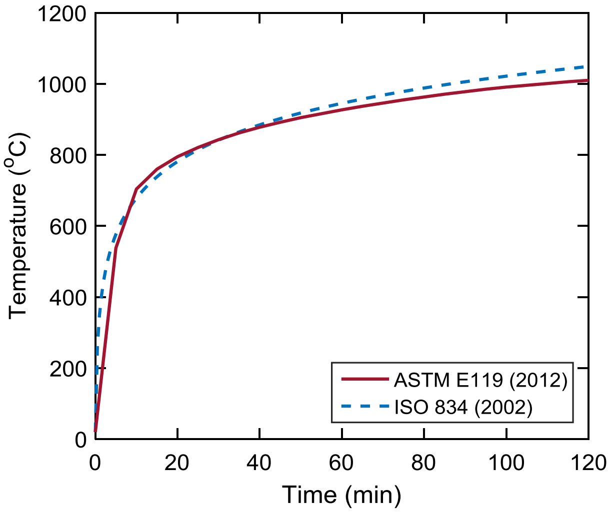

Figure 2.16 Comparison between ASTM E119-16 (2016)and ISO 834 (CEN, 2002) standard fire curves.

The ISO 834 (Eurocode 1, 2002) and ASTM E119 (2015) standard fire curves represent the heating phase only, in which the fuel supply is assumed to be inexhaustible, which is unrealistic. There are also two fire curves in EC1 (2002), including “external fire curve” and “hydrocarbon curve”. The external fire curve is used to test fire resistance of structural member located outside a burning compartment. The external fire curve is given by following equation, Eq. (2.7):

$$T_g = 660\,(1 - 0.687e^{-0.32t} - 0.313e^{-3.8t}) + 20 \tag{2.7}$$

where, Tg is the gas temperature near the member in degree Celsius, and t is the time in minutes. The hydrocarbon fire curve is used to test fire resistance of structural members located inside a fire compartment. This fire curve is represented by Eq. (2.8) below:

$$T_g = 1080\,(1 - 0.325e^{-0.167t} - 0.675e^{-2.5t}) + 20 \tag{2.8}$$

Where, Tg is the gas temperature in the fire compartment in degree Celsius, and t is the time in minutes.

2.7.2. Realistic Fire Exposure

Eurocode parametric fire curve allows for the generation of a time-temperature curve for any combination of ventilation condition, fuel load, opening factor, and wall lining material. This time-temperature curve can capture all three phases of a realistic fire, including heating ramp, followed by a cooling phase, and lastly a constant ambient temperature.

In the heating phase of the EC parametric fire curve, the temperature $\theta(°C)$ is a function of fictitious time t^* as shown in Eq. (2.9), where t^* is given by the product $\Gamma.t$ and Γ is a dimensionless parameter equal to $(O/b)^2/(0.04/1160)^2$, where O is an opening factor, b is the thermal absorptivity of surrounding surfaces of the compartment, and t is the time in hours (CEN, 2002).

$$\theta = 20 + 1325\left(1 - 0.324e^{-0.2t^*} - 0.204^{-1.7t^*} - 0.472e^{-19t^*}\right) \tag{2.9}$$

$$t^* = \Gamma.t \qquad (2.10)$$

$$\Gamma = (O/b)^2/(0.04/1160)^2 \tag{2.11}$$

$$b = \sqrt{\rho c \lambda} \tag{2.12}$$

$$O = \frac{A_v\sqrt{h_{eq}}}{A_t} \tag{2.13}$$

If Γ is assumed to be unity, the heating phase of fire curve approximates the ISO 834 standard fire curve (CEN, 2002) shown in Figure 2.16.

$$t_{max} = max\left\{0.2 \times 10^{-3}\frac{q_{t,d}}{O}, t_{lim}\right\} \tag{2.14}$$

The t_{lim} is considered 25, 20, and 15 minutes for slow, medium, and fast fire growth rates, respectively, according to Eurocode 1 (CEN, 2002). The time t_{max} given by t_{lim} is a fuel-controlled fire, and by $0.2 \times 10^{-3}\frac{q_{t,d}}{O}$ is a ventilation-controlled fire. The cooling phase of parametric fire curve is developed using Eq. (2.15) as below:

$$\theta = \begin{cases} \theta_{max} - 625(t^* - t^*_{max}.x) & for \quad t^*_{max} \leq 0.5 \\ \theta_{max} - 250(3 - t^*_{max})(t^* - t^*_{max}.x) & for \quad 0.5 < t^*_{max} < 2 \\ \theta_{max} - 250(t^* - t^*_{max}.x) & for \quad t^*_{max} \geq 2 \end{cases} \tag{2.15}$$

where, t^* is given by Eq. (2.16) as follow:

$$t^*_{max} = \frac{\left(0.2\times10^{-3}\frac{q_{t,d}}{O}\right)}{\Gamma} \tag{2.16}$$

$$x = 1.0 \; if \; t_{max} > t_{lim} \quad \text{or} \quad x = \frac{t_{lim}.\Gamma}{t^*_{max}} \quad if \;\; t_{max} = t_{lim} \tag{2.17}$$

The formulation of parametric fire curve allows flexibility in assuming a wide range of reasonable design values for the design fire load density ($q_{t,d}$), opening factor (O) and thermal absorptivity of surrounding surfaces of the compartment (b) for both open- and closed-plan buildings. For instance, in the case of an open-plan office building, $q_{t,d}$, O, and b may be assumed 130 MJ/m^2, 0.071 $m^{1/2}$, and 2030 $J/m^2s^{1/2}K$, respectively. In case of a closed-plan office building, these values can be assumed as 50 MJ/m^2, 0.027 $m^{1/2}$, and 783 $J/m^2s^{1/2}K$, respectively. The assumed combination of fire parameter values for the open- and closed-plan office buildings result in maximum temperature of 800°C in 22 minutes according to Eq.s (2.9-2.15), as illustrated in Figure 2.17. If t_{lim} is assumed to be 20 minutes for medium fire growth, the fire curve will be a ventilation-controlled fire (CEN, 2002).

The cooling phase is generated using Eq. (2.15), which ends prior to the ambient temperature phase. Finally, the ambient temperature at the end of the fire is assumed to terminate at 120 minutes.

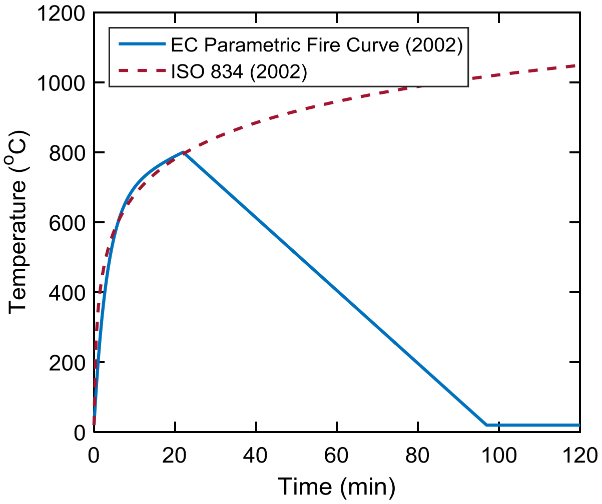

Figure 2.17 A comparison between ISO 834 (CEN, 2002) standard fire curve and Eurocode parametric fire curve (CEN, 2002) assuming Γ=1.0.

2.8. Response of steel structures subjected to fire following earthquake

To date, only limited number of studies have been conducted on the response of steel structures, both on the global and local scales, under post-earthquake fire scenarios. Della Corte et al. (2005) developed numerical models to investigate the performance of steel moment resisting frames (MRFs) subjected to fire following earthquake. Two different buildings were considered, one with perimeter moment resisting frames and the other with moment connections in all joints. The earthquake-induced damages in the buildings were represented by imposing a residual deformation (geometrical damage) and reducing the steel modulus of elasticity and yield strength (mechanical damage) in certain parts of the frames. The geometrical damage was defined as the maximum IDR ratio along the building height. The open-source computation environment, OpenSees (http://opensees.berkeley.edu/) was utilized to obtain the seismic response of the buildings using fiber beam-column element for capturing P-Δ effects. In addition, elastic-perfectly plastic hysteresis model was implemented. ISO-834 time-temperature curve was used for fire simulation considering uniform temperature distribution in fire compartment, which was located in the first floor of frames. In this study, thermal and mechanical properties of steel were adopted according to EC 3. SAFIR (Franssen et al. 2002) was also used to conduct post-earthquake fire simulations. The onset of system instability was defined as structural collapse. The fire effect was simulated using thermal-mechanical analysis. It was observed the seismic design philosophy can significantly affect the performance of steel MRFs under post-earthquake fires. It was recommended that fire safety codes should consider the location of buildings, seismic or non-seismic prone, as a basis for fire resistance provisions.

Faggiano et al. (2007) conducted a numerical study to identify a method for evaluating post-earthquake fire response of structures in terms of fire resistance and collapse mode. Four seismic performance levels were defined, including Fully Operational, Operational, Life Safe, and Near Collapse, according to SEAOC v2000. Nonlinear static pushover analysis was implemented to determine performance level of the structures under seismic demands. Following the seismic evaluation, performance of the system was evaluated under post-earthquake fire scenario using coupled thermal-mechanical analysis. In this study, four steel portal frames were analyzed considering variation in steel grades and span to height ratio. Commercial finite element software, ABAQUS v6.5 (2004), was used to run numerical simulations. Material temperature-dependent properties were adopted according to EC3. Furthermore, ISO-834 time-temperature curve was applied to the frames as fire loads. The results showed that fire resistance and collapse mechanisms of portal frames subjected to fire following earthquake are essentially the same as when the frames did not exceed the operational performance limit during the earthquake. A small reduction in fire resistance of portal frames was observed when the performance of the frames was at the life safety and near-collapse levels.

A study was conducted by Faggiano et al. (2010) to propose a performance-based design framework to evaluate robustness of steel framed structures subjected to fire following earthquake loading scenario. Four levels of seismic performance were chosen from FEMA 356 (2000), including Operational (O), Immediate Occupancy (IO), Life Safety (LS), and Collapse Prevention (CP). Furthermore, four levels of fire performance were introduced as Operational Fire (OF), Immediate Occupancy Fire (IOF), Life Safety Fire (LSF), and Collapse Prevention Fire (CPF). The proposed framework consisted of two main steps:

1) Identify damage state of structure in accordance with 4 seismic performance levels,

2) Determine performance of structure subjected to post-earthquake loads according to 4 fire performance levels

A two-story four-bay steel frame was selected for the study and consideration was given to variation in seismic performance levels and post-earthquake fire scenarios. In the study, EC 3 and EC 1 were implemented to model temperature-dependent material properties and ISO-834 fire load, respectively. That study included the identification of the seismic damage state and the determination of the residual bearing capabilities of the seismic damaged structures subjected to fire.

Braxtan and Pessiki (2011) conducted laboratory tests to investigate damage pattern in spray-applied fire-resistive material (SFRM) under cyclic loads in beam-to-column joint region of steel moment resisting connections. They also assessed bond of spray-applied fire-resistive material (SFRM) to the beam-column joint region of steel moment resisting connection. It was observed that the damage to the SFRM took place in the beam flanges at a certain level of story drift. Moreover, their supporting numerical analysis indicated that damage to the SFRM resulted in more heat penetration into the beam-column joint and an increase in temperature in the adjacent column. Later, Keller and Pessiki (2012) conducted numerical simulations to evaluate the effects of earthquake-induced damage to sprayed fire-resistive materials (SFRM) on the behavior of beam-column joints subjected to elevated temperatures, finding that earthquake-induced damage to SFRM caused a reduction in the rotational stiffness and flexural capacity of the beam-column joint subjected to compartment fires.

Pucinotti et al. (2011a) investigated the performance of steel-concrete composite full strength joints endowed with concrete filled tubes subjected to fire following earthquake. The authors proposed a multi-objective design approach to satisfy both seismic and fire demand, simultaneously. Pucinotti et al. (2011b) subsequently conducted numerical and experimental analyses to assess the performance of welded steel-concrete full-strength beam-column connections subjected to fire following earthquake. In the experiments, earthquake-induced damages were simulated by monotonic loads before exposing the specimens to fire. These tests indicated that such connections can survive damage following a design earthquake of 0.4g PGA.

2.9. Review of design standards and recommendations

Up till now, prescriptive approaches have been used to design of structures for fire loads in most of countries with the exception of some examples in the U.K., China, among others. Most of the current prescriptive fire design codes are required to meet two main objectives including life safety and property protection (Phan et al., 2010). The objective of life safety is mainly guaranteed by the design of active and passive fire protection systems. The key parameter in the design of passive fire protection is to achieve a particular fire-resistance ratings (FRR).

The ultimate goal in design of structures exposed to elevated temperatures, based on life safety objective, is to make sure fire resistance of structure is adequate for intensity of design fire loads (Phan et al., 2010). This requires meeting the following inequality:

$$Structural\ fire\ resistance\ \geq Intensity\ of\ fire\ hazard$$

where, structural fire resistance is defined as the ability of structure to survive under fire exposure with no partial or global collapse and/or avoid any fire spread to adjacent compartments. The structural fire resistance is then lumped in providing stability, integrity, and insulation. The stability pertains to the adequacy of structural members or systems under fire loads with respect to mechanical response, while integrity and insulation are intended to explain the ability of barriers to contain the fire and to prevent its spread to adjacent compartment (Phan et al., 2010). Intensity of fire hazard is a factor which illustrates how destructive fire is and/or temperature and forces developed in structural members during fire exposure, which can cause partial or global collapse (Phan et al., 2010). Three different approaches can be adopted to compare fire resistance and fire intensity including strength domain, temperature domain, and time domain. Table 2.3 illustrates these three different approaches.

Table 2.3 Three various methods to compare structural fire resistance and intensity of fire hazard (Phan et al., 2010).

Domain	**Unit**	**Structural fire resistance**	**Intensity of fire hazard**
Strength	kN / kN.m	Load capacity (strength/stability) at elevated temperatures	Applied load during fire
Temperature	°C	Temperature in steel causes failure	Maximum temperature in steel reached during the fire
Time	Minutes / hours	Time to failure (FRR)	Fire duration as calculated or specified by code

It is crucial to choose a clear strategy for structural fire design along with intensity of design fire during the design process. NIST (2010) recommends that the design of structural components and systems for elevated temperatures can be performed completely different than that for ambient temperature. This is because at the time of fire occurrence:

- The level of applied loads is less than that of design loads.

- Strength and stiffness of material is deteriorated due to elevated temperatures.
- Large axial demand is developed in structural members subjected to high temperatures.
- The global stability of system may be affected by associated large deformations in structural members.
- The low probability of fire occurrence enforces smaller factor of safety in structural fire design.

It is very likely that the level of applied loads at the time a fire event is much less than that of design loads at ambient temperature. Most design standards recommend the use of “arbitrary point-in-time” load for fire design of structural members, e.g. ASCE (2005) which proposes the design load combination as follow, Eq. (2.18) for fire conditions:

$$w = 1.2DL + 0.5LL \tag{2.18}$$

where, DL and LL are the design dead and live loads respectively according to ASCE (2005). Table 2.4 lists various load combinations for structural fire design in accordance with various standards and research studies.

Table 2.4 Dead and live load factors for structural fire design.

Reference	Factor of deal load	Factor of storage load	Factor for other live loads
Ellingwood and Corotis (1991)	1.0	0.5	0.5
New Zealand, SNZ (1992)	1.0	0.6	0.4
Eurocode, EC1 (1994)	1.0	0.9	0.5
ASCE (2005)	1.2	0.5	0.5

The analysis and design of structural systems exposed to fire can be performed in three levels of complication (Phan et al., 2010). These levels for analysis stage can be as following:

- Member-level analysis
- Subassembly-level of analysis
- System-level analysis

The three levels of design can be listed as below:

- Tabulated data
- Simplified calculation methods
- Advanced calculation methods

Table 2.5 (CEN, 2002) shows the applicability of the three design alternative methods for the various analysis approaches listed above.

Table 2.5 Applicable levels of analysis and design for fire conditions in accordance to Eurocode 2 (CEN, 2004).

		Design		
		Tabulated data	**Simplified calculation methods**	**Advanced calculation methods**
Analysis	Member-level	Yes (standard fire only)	Yes (standard and parametric fires)	Yes (parametric or real fires)
	Subassembly-level	No	Yes (standard and parametric fires)	Yes (parametric or real fires)
	System-level	No	No	Yes (parametric or real fires)

The structural fire design codes in the U.S. have not moved toward performance-based fire engineering (PBFE) as fast as performance-based earthquake engineering (PBEE) has. Most of existing building codes have prescriptive design methods for fire resistance ratings (FRR). The most updated standard in the U.S. is the joint ASCE/SFPE standard 29-05 (ASCE/SFPE, 2005), which proposes simple calculation methods to determine structural fire resistance. In addition, the AISC 360-10 (2010) provides information on thermal and mechanical properties of steel material at elevated temperatures as discussed previously. This standard also provides engineering approaches for analysis and strength-based design of steel structural members subjected to fire loads.

The Eurocode structural design codes can be classified as the most comprehensive standards in designing of structures under fire conditions. The fire design according to Eurocode needs to address the following steps throughout the design process:

- Design fire hazard (standard or realistic fire curves)
- Methods of verification
- Methods of structural analysis
- Mechanical and thermal properties of structural material
- Methods of structural design
- Details of construction

Figure 2.18 shows design flowchart in accordance with Eurocode 3 (CEN, 2005) for fire design of structures. As illustrated in the flowchart, it includes both prescriptive and performance-based fire design. Further details can be found in Eurocode 3 (CEN, 2005). Eurocode 3 (CEN, 2005) also provides extensive information regarding material properties at elevated temperature as discussed in section 2.5 of the present chapter.

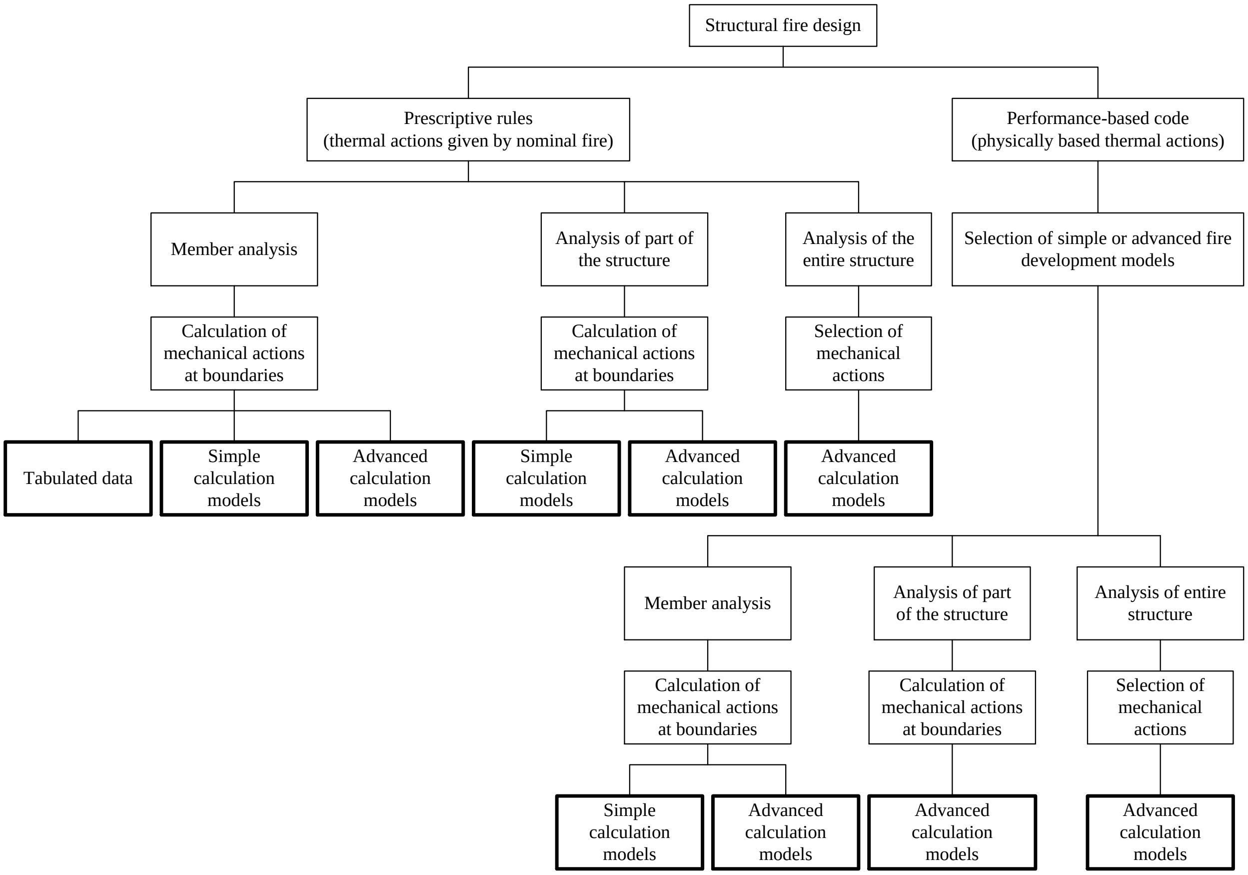

Figure 2.18 Structural fire design approaches according to Eurocode 3 (CEN, 2005).

2.10. Summary

This chapter briefly reviewed available literature in the structural fire and fire following earthquake. Here is a summary of topics discussed in this chapter:

- Post-earthquake fire ignition models: Most post-earthquake ignition models were built upon regression analysis that correlate ignition rate per unit area to the earthquake intensity. Diversity in datasets and variety in ignition sources created a challenge in modeling post-earthquake ignition.
- Significant historical fire following earthquakes: The review of historical post-earthquake fires revealed that fire following earthquake hazard is a recurring event where multiple simultaneous post-earthquake fires could result in substantial losses – e.g. fatalities,

damages to civil infrastructures. Fire following the 1906 San Francisco, 1923 Tokyo, 1989 Loma Prieta, 1994 Northridge, and 1995 Kobe earthquakes were also reviewed.

- Significant historical fires in steel framed buildings: Fire in the Broadgate building phase 8 in London, UK, and Windsor Building in Madrid, Spain were discussed because of their relevance and the important observations and lessons. The most important conclusion from a brief review of fire events in steel buildings revealed that there is no global collapse in steel structures under only fire loads except WTC building 7.
- Temperature-dependent properties of structural steel: It was recognized that three important characteristics of structural steel determine the response of steel framed buildings exposed to fire loads, including thermal, deformational, and mechanical properties. The temperature-dependent constitutive models of structural steel were reviewed according to ASCE (ASCE, 1992), Eurocode 3 (CEN, 2005), and AISC 360-10 (2010) standards. Features and variation of these three temperature-dependent constitutive models of structural steel were highlighted.
- Fire exposure models: Available post-flashover fire curves used in structural fire engineering were discussed with detailed information regarding their characteristics. Standard fire curves – American ASTM E119 (2016) and European ISO 834 (2002) – were compared. The details of parametric fire curve were also discussed along with its implementation in the present study.
- Response of steel structural systems subjected to fire following earthquake: The review of literature showed that only limited number of studies were conducted on the response of steel structures, both on the global and local scales, under post-earthquake fire

scenarios. A few of these studies were discussed in this chapter along with their assumptions and conclusions.

- Current design standards for fire design of structures: A brief review of fire design standards for steel structures indicated that prescriptive approaches have been used to design of structures for fire loads in most of countries with the exception of some examples in the U.K., China, among others. It was also realized that the Eurocode structural design codes can be classified as the most comprehensive standards in designing of structures under fire conditions.

Chapter 3. Stability of steel columns subjected to fire following earthquake

3.1. Overview

Assessing the stability of steel building frames exposed to fire conditions is challenging due to the need to consider elevated temperature properties of steel, non-uniform heating of structural members, and large deformational demands on the frames. This challenge is further intensified if the stability of the frame is also influenced by the lateral forces due to earthquake preceding the fire. Although there has been significant progress recently in simulating frame response using finite element methods, there is a need for computationally efficient tools that would minimize the modeling efforts and allow for accurate and rapid assessment so that a large number of simulations can be conducted. To this end, the present study develops an efficient framework for conducting stability analyses of steel columns subjected to demands imposed by lateral loading followed by fire. A non-linear flexibility-based finite element approach is proposed to assess the stability of W-shape steel columns under cascading hazard loading scenario of earthquake and fire. Results from the proposed formulation show good agreement with available strength design equations of steel columns at ambient and elevated temperatures. An equation is proposed to calculate the Euler elastic buckling stress in case of non-uniform longitudinal distribution of temperature. In addition, a set of equations and coefficients are proposed to predict the inelastic buckling stress in steel columns subjected to cascade loading of earthquake and fire. This computationally efficient finite element tool can be used to investigate the effect of a wide variety of variables on the stability of steel columns subjected to fire as well as fire following earthquakes.

3.2. Background

Significant progress has been made recently in the development of analytical, numerical, and experimental tools that can be used to evaluate the response of steel structural members and frames to fire loading. Despite this progress, many challenges to evaluating structural response under fire loading remain due to the significant geometrical nonlinearity and temperature-dependent material inelasticity that must be considered in the structural analysis. This is particularly the case when assessing the behavior of axially loaded members due to the presence of low or negative stiffness at the onset of instability. The stability of axially loaded members, particularly columns, under elevated temperatures, has been the focus of several previous studies (Franssen et all. 1998, Takagi and Deierlein 2007, Agarwal and Varma 2011) because columns are key components in resisting gravity loads in a building system.

A review of the literature indicates that many experimental studies have been conducted to investigate stability of isolated steel columns under elevated temperatures (e.g., Vandamme and Janss, 1981; Franssen et al., 1998; Ali and O'Connor, 2001). Extensive numerical studies also have been performed to assess the instability of isolated steel columns exposed to fire loads (e.g., Takagi and Deierlein, 2007; Tan and Yuan, 2009; Agarwal and Varma, 2011; and Agarwal, et al., 2014). Memari and Mahmoud (2014) and Memari et al. (2014) conducted non-linear finite element analyses to evaluate the performance of steel moment-resisting frames under fire and fire following earthquakes. These studies highlighted the importance of improving the understanding the behavior of steel columns subjected to non-uniform longitudinal temperature and lateral sway. The brief discussion below of two of the most recent and relevant studies on steel column buckling under fire (Takagi and Deierlein, 2007; Agarwal and Varma, 2011) will set the stage for introducing a new analytical model for evaluating the response of W-shape steel columns under the combined effect of lateral demand followed by fire loading.

Takagi and Deierlein (2007) evaluated the AISC Specification (AISC 360-05) and Eurocode 3 (CEN, 2005) provisions for design of isolated W-shape steel columns under elevated temperatures that were uniform along the length of columns. Numerical models of columns were developed, which accounted for residual stresses, local buckling, and inelasticity. Temperature-dependent material properties were adopted from Eurocode 3 (CEN, 2005). Initial geometric imperfections were also considered in the numerical models. It was concluded that the recommendation of the AISC 2005 Specification (AISC 360-05) to use the ambient temperature design equations in Chapter E for design of axial members under elevated temperatures, modifying only the material properties for elevated temperatures, was highly non-conservative. The outcome of this study was the design equation, eq. (A-4-2), for W-shape steel columns under uniform longitudinal temperature that currently appears in Appendix 4 of the AISC 2010 Specification (AISC 360-10).

Subsequently, Agarwal and Varma (2011) conducted finite element analyses to evaluate the effects of slenderness and rotational restraints on the buckling response of W-shaped steel columns at uniform elevated temperatures. Shell elements were used to create numerical models of columns because of their ability to capture local buckling and inelastic flexural-torsional buckling and to accommodate the specified residual stress distribution. Initial geometric imperfections, representing out-of-straightness, were included in the models as well as local imperfections. As with the earlier Takagi and Deierlein (2007) study, temperature-dependent stress-strain curves from Eurocode 3 (CEN, 2005) were implemented in the numerical models. This study resulted in new design equations for simply supported columns with uniform longitudinal temperature distribution and considering an equivalent bilinear material behavior. The effects of rotational restraints, provided by continuity with cooler columns above and below of column of interest in a structural frame, were also included in the proposed design equations.

The studies by Takagi and Deierlein (2007) and Agarwal et al. (2011) showed that the computational efforts associated with analyzing the stability of columns at elevated temperature were significant. To minimize these efforts, the two aforementioned studies introduced a number of assumptions and simplifications to reduce the number of analyses so that the computational effort for developing the design equations is minimized. For instance, these studies did not include the effects of non-uniform longitudinal temperature, various boundary conditions, and P-Δ effects. There remains a need for simple tools that can be utilized to evaluate the instability of columns under multiple demands and while accounting for the various material inelasticity and geometric nonlinearity features associated with column behavior under elevated temperature conditions.

Such tools are developed in this study, in which an analytical formulation is proposed for performing stability analysis of W-shape steel columns subjected to P-Δ effects and/or non-uniform longitudinal temperature profiles. Specifically, a non-linear flexibility-based finite element approach is developed that takes into account the residual stress distribution in steel hot-rolled W-shape sections, initial out-of-straightness and out-of-plumbness in steel members, temperature-dependent material properties, and specified boundary conditions. The results of the proposed approach are verified against comparison with previous studies. The results highlight the importance of details of the material modeling and P-Δ effects on the instability of steel columns exposed to either uniform or non-uniform longitudinal elevated temperature profiles. In addition, equation is proposed to predict the Euler elastic buckling stress in case of non-uniform distribution of temperature along with equations proposal to estimate the inelastic buckling stress in steel columns subjected to cascading hazard of earthquake and fire causing non-uniform longitudinal temperature distributions.

3.3. Analysis framework

The proposed flexibility-based approach to predict the geometrically nonlinear response of a beam-column element subjected to variable temperature distribution along its length and constant temperature throughout the cross section is based on Euler-Bernoulli beam theory, and is an extension of results obtained by Carol and Murcia (1989) and Memari and Attarnejad (2010). The flexural element, shown in Figure 3.1(a), is assumed to have a non-uniform longitudinal temperature distribution with T_i and T_j being the nodal temperatures at either end. Since the elastic modulus of steel is a function of temperature and degrades at elevated temperatures, the nodal temperature at each end of the element will result in temperature-dependent modulus of elasticity $E(T_i)$ and $E(T_j)$, as shown in Figure 3.1(a). In this study, a linear variation of temperature-dependent modulus of elasticity is assumed along the length of the element. The entire column can be divided into elements that are sufficiently short that the linear variation along each element allows the nonlinear variation along the entire length of the column to be captured. The modulus of elasticity along the length of the element, x, can therefore be written as:

$$E(x) = E(T_i)\left(1 + \frac{\zeta x}{L}\right) \tag{3.1.a}$$

$$\zeta = \frac{E(T_j)}{E(T_i)} - 1 \tag{3.1.b}$$

In the flexibility method, the equations of equilibrium are formulated on a stable and statically determinate structure. For the element shown in Figure 3.1(a), three nodal redundant actions - axial force at node i and bending moments at nodes i and j - are chosen. The resulting element is a simply supported beam-column. Figure 3.1(c) shows the deformed state of this element under applied external nodal actions. In accordance with the deformed state of the element, the kinematic equations (strain-displacement relationships) are developed written in the following matrix form:

$$\begin{bmatrix} -(u_j - u_i) \\ \frac{w_j - w_i}{L} - \theta_i \\ \theta_j - \frac{w_j - w_i}{L} \end{bmatrix} = \int_0^L \begin{bmatrix} 1 & 0 \\ 0 & 1 - \frac{x}{L} \\ 0 & \frac{x}{L} \end{bmatrix} \begin{bmatrix} \epsilon \\ \varphi \end{bmatrix} dx \tag{3.2.a}$$

$$\underline{\boldsymbol{u}} = \int_0^L \boldsymbol{\Omega}^T . \underline{\gamma} dx \tag{3.2.b}$$

where, ε and φ are the axial strain at the neutral axis of the cross section and curvature, respectively. Other variables in Eq. (3.2.a) are shown in Figure 3.1(b). The matrix form of the kinematic equations is written in a more compact form in Eq. (3.2.b), where, $\underline{\mathbf{u}}$ is a vector of relative displacements and rotations, $\underline{\boldsymbol{\gamma}}$ is a vector of strains. In addition, $\boldsymbol{\Omega}$ is a transformation matrix to convert strains into displacements and rotations.

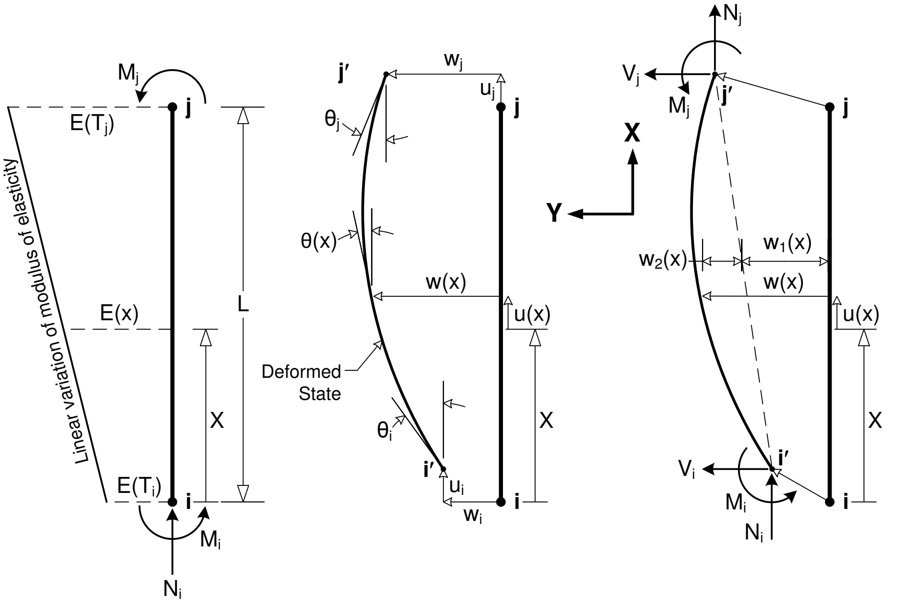

(a) (b) (c)

Figure 3.1 (a) Flexural element subjected to non-uniform longitudinal temperature and three applied external nodal forces (b) the deformed state of element with all nodal deformation variables (c) the deformed state of element with all nodal force variables.

It can be shown that cross-sectional forces can be obtained based on applied nodal forces and moments using equilibrium equations per Eq. (3.3.a). To include the second-order (P-δ) effects, a vector of forces due to the deformed state of the beam-column element, shown in Figure 1(c), is added to the nodal equilibrium equations:

$$\begin{bmatrix} N(x) \\ M(x) \end{bmatrix} = \begin{bmatrix} 1 & 0 & 0 \\ 0 & 1-\frac{x}{L} & \frac{x}{L} \end{bmatrix} \begin{bmatrix} N_i \\ M_i \\ M_j \end{bmatrix} + \begin{bmatrix} 0 \\ -N_i.w''(x) \end{bmatrix} \tag{3.3.a}$$

$$\underline{\boldsymbol{R}(\boldsymbol{x})} = \boldsymbol{\Omega}\,.\underline{\boldsymbol{f}} + \underline{\boldsymbol{R}''(\boldsymbol{x})} \tag{3.3.b}$$

where w”(x) is the out-of-straightness curvature of the beam-column that causes the P-δ effects. The compact format of the matrix equation, Eq. (3.3.b), indicates that ***R(x)*** and ***R”(x)*** are vectors of internal cross-sectional forces developed because of the inclusion of second-order effects. The vector ***f*** represents the applied nodal forces and moments and **Ω** is a matrix that correlates the applied nodal forces to those developed internally in the cross-section. Note that the matrix $\boldsymbol{\Omega}$ appears in both the kinematic and equilibrium equations.

In the next step, the cross-sectional strain and curvature must be related to the cross-sectional forces and moments. Eq. (3.4.a) below provides this relationship, under the assumption that the element responds elastically to nodal forces. In the compact form of Eq. (3.4.b), all vectors of $\underline{\boldsymbol{R(x)}}$ and $\underline{\boldsymbol{\gamma}}$ have been defined previously except the section stiffness, $\mathbf{k_s(x)}$.

$$\begin{bmatrix} N(x) \\ M(x) \end{bmatrix} = \begin{bmatrix} E(x)A & 0 \\ 0 & E(x)I \end{bmatrix} \begin{bmatrix} \epsilon \\ \varphi \end{bmatrix} \tag{3.4.a}$$

$$\underline{\boldsymbol{R}(\boldsymbol{x})} = \mathbf{k_s}(\mathbf{x}) \, . \underline{\boldsymbol{\gamma}} \tag{3.4.b}$$

Note that the longitudinal variation in the elastic modulus, caused by the non-uniform temperature distribution, is reflected in Eq. (3.4). This is one of the most important features of the presented framework, since a constant modulus of elasticity would imply no variation in temperature along the length. Substituting the longitudinal linear variation of elastic modulus, Eq. (3.1), into the equation representing $\mathbf{k_s(x)}$, leads to

$$\mathbf{k_s}(\mathbf{x}) = E(T_i)\left(1 + \frac{\zeta x}{L}\right) \begin{bmatrix} A & 0 \\ 0 & I \end{bmatrix} \tag{3.5}$$

Eq. (3.5) clearly indicates that the section stiffness varies along the length of element as a function of the elastic modulus.

The first-order stiffness and geometric stiffness matrices necessary for the stability analysis can be extracted from the three sets of kinematic, equilibrium, and material law equations. First, substituting the equilibrium, Eq. (3.3), and constitutive, Eq. (3.4), equations into the kinematic equation, Eq. (3.2), we obtain

$$\underline{\boldsymbol{u}} = \int_0^L \boldsymbol{\Omega}^T \mathbf{k_s}^{-1} \boldsymbol{\Omega} \underline{\boldsymbol{f}} \, dx + \int_0^L \boldsymbol{\Omega}^T \mathbf{k_s}^{\mathbf{-1}} \underline{\boldsymbol{R}"(\boldsymbol{x})} \, dx \tag{3.6}$$

Eq. (3.6) can be re-arranged based on $\underline{\boldsymbol{f}}$, leading to

$$\underline{\boldsymbol{f}} = \eta . \underline{\boldsymbol{u}} + \underline{\boldsymbol{f}}'' \tag{3.7}$$

in which,

$$\eta = \left(\int_0^L \boldsymbol{\Omega}^T \mathbf{k_s}^{-1} \boldsymbol{\Omega} \, dx \right)^{-1} \tag{3.8.a}$$

$$\underline{\boldsymbol{f}}'' = -\eta \int_0^L \boldsymbol{\Omega}^T \mathbf{k_s}^{-1} \underline{\boldsymbol{R}''(\boldsymbol{x})} \, dx \tag{3.8.b}$$

and where, η relates the vector of relative displacements and rotations, $\underline{\boldsymbol{u}}$, to the vector of applied external actions, $\underline{\boldsymbol{f}}$. In addition, $\underline{\boldsymbol{f}''}$ represents nodal actions resulting from second-order (P-δ) effects. If the $\boldsymbol{\Omega}$ and $\mathbf{k_s}^{-1}$ matrices are substituted into Eq. (3.8.a), η will become,

$$\eta = \left(\int_0^L \frac{1}{E(T_i)\left(1+\frac{\zeta x}{L}\right)} \begin{bmatrix} \frac{1}{A} & 0 & 0 \\ 0 & \frac{\left(1-\frac{x}{L}\right)^2}{I} & \frac{\left(1-\frac{x}{L}\right)\frac{x}{L}}{I} \\ 0 & \frac{\left(1-\frac{x}{L}\right)\frac{x}{L}}{I} & \frac{\left(\frac{x}{L}\right)^2}{I} \end{bmatrix} dx \right)^{-1} \tag{3.9}$$

As the final step, the vector of applied nodal forces and moments, $\underline{\boldsymbol{f}}$, and the vector of relative displacements and rotations, $\underline{\boldsymbol{u}}$, must be related to the full vector of nodal actions and deformations, F and U:

$$\underline{\boldsymbol{F}} = \begin{bmatrix} N_i & V_i & M_i & N_j & V_j & M_j \end{bmatrix}^T \tag{3.10.a}$$

$$\underline{\boldsymbol{U}} = \begin{bmatrix} u_i & w_i & \theta_i & u_j & w_j & \theta_j \end{bmatrix}^T \tag{3.10.b}$$

A transformation matrix, $\boldsymbol{\Gamma}$,

$$\boldsymbol{\Gamma} = \begin{bmatrix} 1 & 0 & 0 \\ 0 & -\frac{1}{L} & \frac{1}{L} \\ 0 & -1 & 0 \\ -1 & 0 & 0 \\ 0 & \frac{1}{L} & -\frac{1}{L} \\ 0 & 0 & 1 \end{bmatrix} \tag{3.11}$$

can be used to relate correlate $\underline{\boldsymbol{f}}$ and $\underline{\boldsymbol{u}}$ to $\underline{\boldsymbol{F}}$ and $\underline{\boldsymbol{U}}$, respectively.

$$\underline{\boldsymbol{F}} = \Gamma . \underline{\boldsymbol{f}} + \underline{\boldsymbol{F}}'' \tag{3.12.a}$$

$$\underline{\boldsymbol{u}} = \Gamma^T.\underline{\boldsymbol{U}} \tag{3.12.b}$$

Note that the magnitude of moments caused by the P-δ effects has been considered in Eq. (3.7) via vector ***f"***. Therefore, Eq. (3.12.a) includes the effects of moments; however, the developed shear forces caused by the P-δ effect are missing. Therefore, a new vector of nodal shear forces, ***F"***, is added to ***F*** as shown in Eq. (3.12.a). This new vector

$$\underline{\boldsymbol{F}}'' = \begin{bmatrix} 0 & N_i\frac{w_j-w_i}{L} & 0 & 0 & -N_i\frac{w_j-w_i}{L} & 0 \end{bmatrix}^T \tag{13}$$

considers the shear forces proportional to applied axial force caused by P-δ effects, which is constant along the length of element.

Substituting Eq.'s (3.7) and (3.12.b) into Eq (3.12.a), we obtain:

$$\underline{\boldsymbol{F}} = \Gamma.\left(\eta\underline{\boldsymbol{u}} + \underline{\boldsymbol{f}}''\right) + \underline{\boldsymbol{F}}'' = \Gamma\eta\Gamma^T\underline{\boldsymbol{U}} + \Gamma\underline{\boldsymbol{f}}'' + \underline{\boldsymbol{F}}'' \tag{3.14}$$

As can be seen from Eq. (3.14), the vector of nodal actions, ***F***, has been related to the vector of nodal deformations via the first term; therefore, the stiffness matrix of an element, **K**, with non-uniform longitudinal temperature can be defined by:

$$\mathbf{K} = \Gamma\eta\Gamma^T \tag{3.15}$$

The appearance of η in the element stiffness matrix reflects the effects of temperature variation along the length of the beam-column element. The second and third terms in Eq. (3.14) represent the geometric stiffness matrix of the element:

$$\mathbf{K_G}\underline{\boldsymbol{U}} = \Gamma\underline{\boldsymbol{f}}'' + \underline{\boldsymbol{F}}'' \tag{3.16}$$

The overall second-order elastic stiffness that can be written in the classic form: **K** = **K** + **K$_G$**

All vectors and matrices in Eq. (3.16) have been established with the exception of ***R"(x)***, which is embedded in Eq. (3.8) defining ***f"***. However, only ***w"(x)*** is needed to define ***R"(x)***, which can be obtained using the compatibility equation of the element in its deformed state. Defining ***w(x)*** in terms of nodal displacements and rotations, we arrive at ***w"(x)*** through the following steps:

$$w(x) = w_i + \theta_i x + \int_0^x \varphi(x-\tau)d\tau \tag{3.17.a}$$

$$w'(x) = w_i + \frac{w_j - w_i}{L} x \tag{3.17.b}$$

$$w''(x) = w(x) - w'(x) = \theta_i x + \frac{w_i - w_j}{L} x + \int_0^x [0 \quad x-\tau] \begin{bmatrix} \epsilon \\ \varphi \end{bmatrix} d\tau \tag{3.17.c}$$

$$w''(x) = \theta_i x + \frac{w_i - w_j}{L} x + \int_0^x \underline{\boldsymbol{\beta\gamma}}\, d\tau \tag{3.17.d}$$

$$w''(x) = \theta_i x + \frac{w_i - w_j}{L} x + \int_0^x \boldsymbol{\beta} \mathbf{k_s^{-1}} \boldsymbol{\Omega\eta\Gamma}^T \underline{\boldsymbol{U}}\, d\tau \tag{3.17.e}$$

The inclusion of matrix $\boldsymbol{\eta}$ in Eq. (3.17.e) inherently accounts for the effects of longitudinal temperature variation on the geometric stiffness matrix of the element. In summary, the stiffness and geometric stiffness matrices of a beam-column element were developed in this section to reflect non-uniform temperature variation along the length of element. The cross section is assumed to have uniform temperature.

3.4. Temperature Profiles

The introduced flexibility-based analysis framework can be used to generate both first-order stiffness and geometric stiffness matrices for a column member with uniform and/or non-uniform longitudinal temperature profiles. A uniform temperature is assumed across the W-shape steel section in accordance with design recommendation by AISC 360-10 (2010), Takagi and Deierlein (2007), and Agarwal and Varma (2011).

Both uniform and non-uniform longitudinal temperature profiles will be considered in the present study to evaluate instability of steel columns under fire following earthquake. The uniform longitudinal temperature profiles will be mainly used for validation analyses along with analysis of columns with non-uniform longitudinal temperature distributions subjected to the cascading hazard of earthquake and fire. In the present study, four various non-uniform longitudinal temperature profiles are considered as follows:

- Profile (1): 20℃ – 300℃
- Profile (2): 200℃ – 500℃
- Profile (3): 300℃ – 600℃
- Profile (4): 400℃ – 800℃

The aforementioned temperature intervals have been selected such that they capture various rates of change in temperature-dependent mechanical properties of structural steel according to Eq. (3.18) below:

$$Longitudinal\ reduction\ in\ mechanical\ properties = \frac{Prop.(T_{cooler\ end}) - Prop.(T_{hotter\ end})}{Prop.(T_{cooler\ end})} \tag{3.18}$$

This in fact includes variation in modulus of elasticity, yield stress, and proportional limit as highlighted in Figure 3.2. The modulus of elasticity in profile (1) has 20% reduction from cooler end to hotter end, while this is 33.3, 61.3, and 87.1 percent for profiles 2, 3, and 4, respectively. In the profile (1), it is noted that while modulus of elasticity drops 20% by increase in temperature along the length of column, proportional limit drops 38.7%. However, the yield stress is constant in this temperature profile as shown in Figure 3.2. In the Profile (2), modulus of elasticity, yield stress, and proportional limit drop 33.3, 22, and 55.4 percent, respectively, along the length of column. In fact, all mechanical properties have higher drop in profile (2) than those in profile (1).

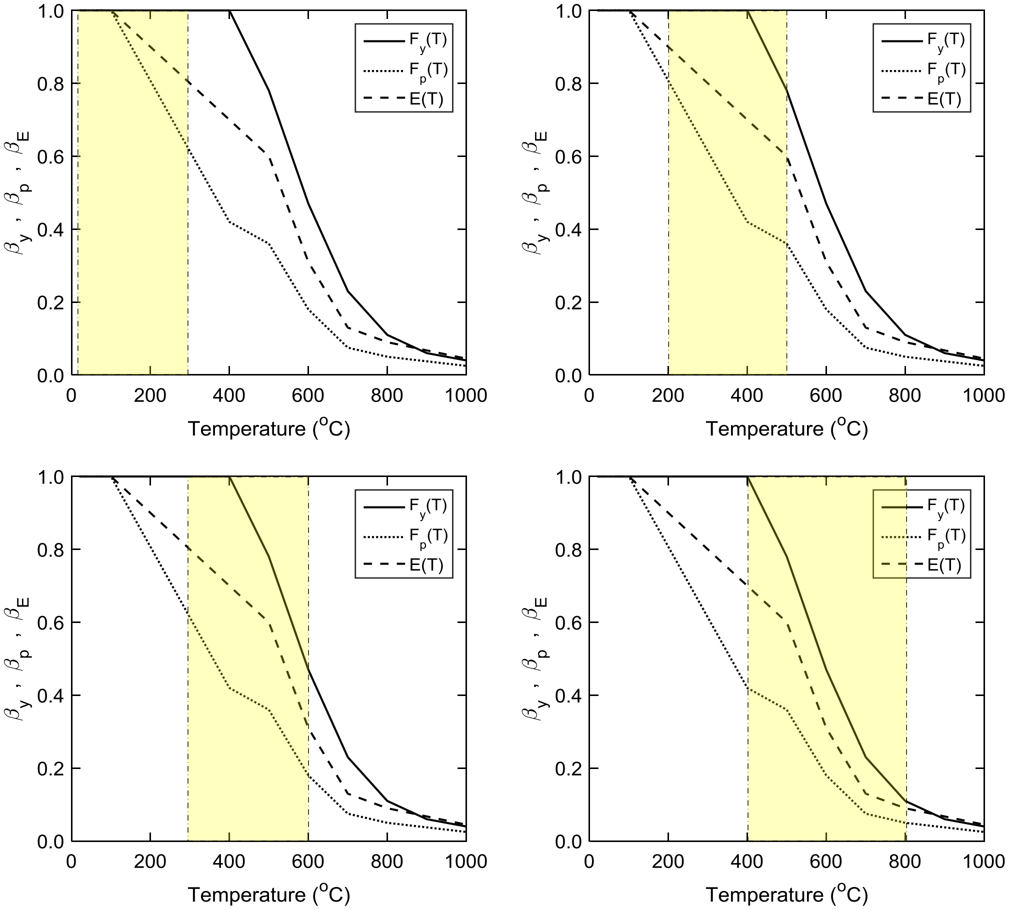

Figure 3.2 Variation of temperature-dependent mechanical properties in non-uniform longitudinal temperature profiles considered in the present study.

The longitudinal reduction in all 3 mechanical properties of structural steel, according to Eq. (3.18), is larger in profile (3) in comparison to profiles (1) and (2) and it is 61.3%, 53%, and 70.6% for modulus of elasticity, yield stress, and proportional limit, respectively. However, the largest longitudinal drop in mechanical properties is in the profile (4). This is 87.1% for modulus of elasticity, 89% for yield stress, and 88.1% for proportional limit. These four non-uniform longitudinal temperature distributions are suited for the evaluation of instability of steel columns under different levels of variation in mechanical properties of structural steel. It is emphasized that these non-uniform longitudinal temperature profiles are not the results of any heat transfer analysis. Table 3.1 summarizes longitudinal reduction of temperature-dependent mechanical properties of structural steel from the cooler end to hotter end of a steel column.

Table 3.1 Longitudinal reduction in mechanical properties of structural steel according to non-uniform temperature profiles in this study.

Profile	Modulus of elasticity	Yield stress	Proportional limit
Profile (1)	20.0%	0.0%	38.7%
Profile (2)	33.3%	22.0%	55.4%
Profile (3)	61.3%	53.0%	70.6%
Profile (4)	87.1%	89.0%	88.1%

The pattern of temperature distribution along the length of a column is also an important parameter to be considered. A quick glance into the solution of the governing 1-D Partial Differential Equation (PDE) for heat transfer through conduction, Eq. (3.19.a), shows heat distribution to follow a parabolic function along the length of steel member at time t.

$$\frac{\partial T(x,t)}{\partial t} = \alpha(T)\frac{\partial^2 T(x,t)}{\partial^2 x} \tag{3.19.a}$$

where T is temperature, x is the coordinate axis along the length of column, and $\alpha(T)$ is thermal diffusivity defined in accordance with Eq. (3.19.b) as follows:

$$\alpha = \frac{\kappa(T)}{\rho.\rho(T)} \tag{3.19.b}$$

in which, $\kappa(T)$ is thermal conduction and $\rho(T)$ is specific heat, both as a function of temperature. Hence, it is essential to evaluate instability of steel columns with parabolic distribution of temperature along their length. However, since the requirements in code provisions to solve conduction heat-transfer PDE problem and obtain parabolic distribution of temperature along the length of the member pose difficulties in real applications, a linear longitudinal distribution of temperature along the length of column will be also considered. This is to evaluate the difference in the results when using the two different distributions and assess the use of a linear distribution of the differences are within what might be considered acceptable. This will allow for understanding the difference resulting from using a simplified linear distribution on instability analysis of steel columns under fire following earthquake. The two patterns of non-uniform longitudinal temperature profiles are shown in Figure 3.3.

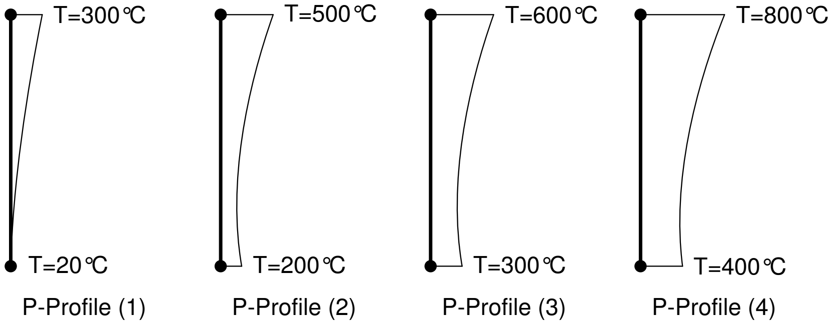

(a) Non-uniform **P**arabolic longitudinal temperature profiles

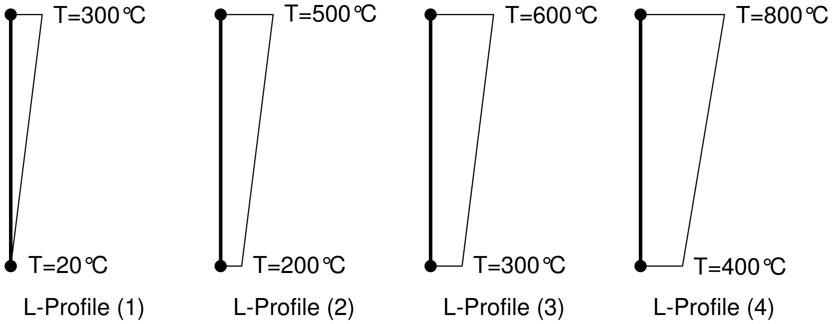

(b) Non-uniform **L**inear longitudinal temperature profiles

Figure 3.3 (a) Parabolic and (b) linear non-uniform distribution of temperature along the length of column in the present study.

Eq. (3.20) is used to calculate both parabolic and linear longitudinal distribution of temperature in steel columns;

$$T(x) = T_{cool-end}\left(1 + \frac{\psi x}{L_c}\right)^m \tag{3.20}$$

in which, x is coordinate axis along the length of column from 0 to L_c, $T_{cool\text{-}end}$ represents cooler end of column, m determines degree of polynomial such that it is 2 for parabolic and 1 for linear functions, and finally, ψ is determined using Eq. (3.21) as below:

$$\psi = \frac{T_{hot-end}}{T_{cool-end}} - 1 \tag{3.21}$$

Table 3.2 summarizes values for all 4 variables of Eq. (3.21) for all 4 linear and parabolic longitudinal temperature distributions profiles shown in Figure 3.3.

Table 3.2 Values of m and ψ for both longitudinal parabolic and linear temperature profiles.

Profile	**Longitudinal parabolic distribution**		**Longitudinal linear distribution**	
	m	**ψ**	**m**	**ψ**
Profile (1)	1	14.0	2	14
Profile (2)	1	1.5	2	1.5
Profile (3)	1	1.0	2	1.0
Profile (4)	1	1.0	2	1.0

3.5. Linear elastic analysis

This section presents details of the linear elastic finite element analysis used to obtain the Euler elastic critical stress for a column subjected to either uniform longitudinal or non-uniform temperature distribution. Figure 3.4 shows a schematic description of the finite element model of steel column under a non-uniform longitudinal distribution of temperature. All columns analyzed in this study are divided into 50 identical elements in length regardless of the longitudinal uniformity of the temperature distribution. The assemblage of stiffness matrices (elastic and geometric) of all 50 elements results in the stiffness matrix of a column.

The nodal temperature at the ends of each element is considered in generating the stiffness matrices as described in Figure 3.4(b) and (c). The modulus of elasticity, corresponding to the nodal temperatures, is adopted from Eurocode 3 (CEN, 2005) and a linear variation of modulus of elasticity is assumed along the length of elements as illustrated in Figure 3.4.

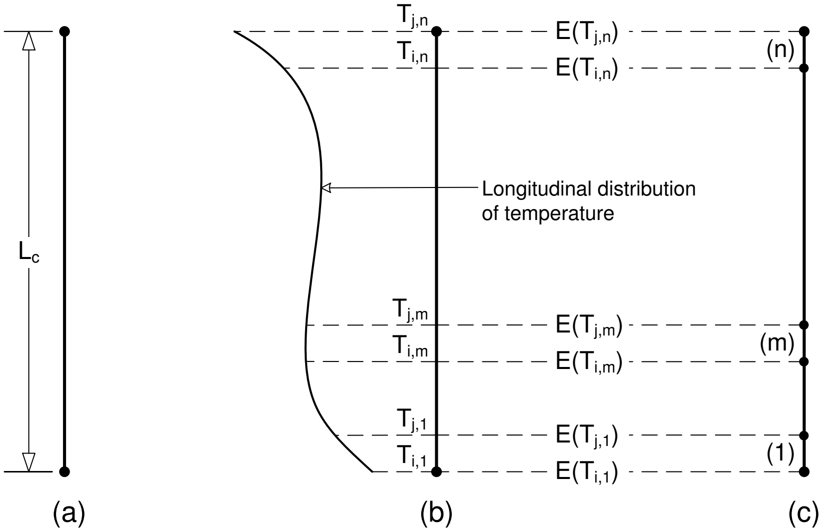

Figure 3.4 A schematic description of the finite element model of steel column under a non-uniform longitudinal distribution of temperature for linear elastic analysis.

The proposed analysis framework provides first-order stiffness and geometric stiffness matrix for a column member with sufficient number of elements. This allows modal analysis (eigenvalue analysis) to be conducted such that eigenvalues (elastic buckling force) and eigenvectors (elastic buckling mode shapes) can be obtained. Standard eigenvalue problem is defined by solving Equation 3.22 as shown below:

$$[A]\{X\} = \lambda\{X\} \tag{3.22.a}$$

$$[A - \lambda I]\{X\} = \{0\} \tag{3.22.b}$$

where λ is eigenvalue and $\{X\}$ is eigenvector. Nontrivial solution for Eq. (3.22.a) exists if and only if

$$|A - \lambda I| = 0 \tag{3.22.c}$$

To solve buckling eigenvalue problem, Eq. (3.23) needs to be considered as follow:

$$[A]\{X\} + \lambda[B]\{X\} = \lambda\{X\} \tag{3.23.a}$$

$$[A + \lambda B]\{X\} = \lambda\{X\} \tag{3.23.b}$$

where λ will return the eigenvalue and $\{X\}$ is the corresponding eigenvector. For the column elastic buckling analysis, $[A]$ is represented by stiffness matrix, $[K]$, and matrix $[B]$ is substituted by geometric stiffness matrix, $[K_G]$. Thereafter, Eq. (3.23.b) can be written in format of Eq. (3.24.a) as following:

$$[K + \lambda K_G]\{X\} = \lambda\{X\} \tag{3.24.a}$$

Nontrivial solution exists for Eq. (3.24.a) if and only if

$$|K + \lambda K_G| = 0 \tag{3.24.b}$$

The outcome of solving the eigenvalue problem is the determination of Euler elastic buckling force and mode shapes associated with instability in steel columns. Furthermore, the effective length factor of column buckling can be calculated for the 1st mode shape and higher. It is noted that temperature-dependent elastic modulus (stiffness) of structural steel will be only effective in determining Euler elastic buckling force of steel columns. In fact, temperature-dependent properties of proportional limit and/or yield stress will have no effects on Euler elastic buckling force.

It is essential to validate both stiffness matrices of a steel column by running an eigenvalue problem with known results. To do so, a uniform longitudinal temperature distribution, e.g. 300℃, is considered to obtain the Euler elastic buckling stress for a column with pinned-pinned boundary condition. This will allow for direct comparison between the results of eigenvalue problem to the equation of Euler elastic buckling stress, which is as follows:

$$F_e(T) = \frac{\pi^2 E(T)}{\left(\frac{KL}{r}\right)^2} \tag{3.25}$$

where, $F_e(T)$ is elastic buckling stress as a function of temperature, $E(T)$ is temperature-dependent modulus of elasticity, K is effective length factor, and L/r is the slenderness of column, called λ in the present study. Figure 3.5 shows that Euler elastic buckling stress about both strong and weak axes of W14X90 steel section is in excellent agreement with results of Euler equation, Eq. (3.25). This validates both first-order stiffness and geometric stiffness matrices generated based on proposed flexibility-based approach in the numerical code.

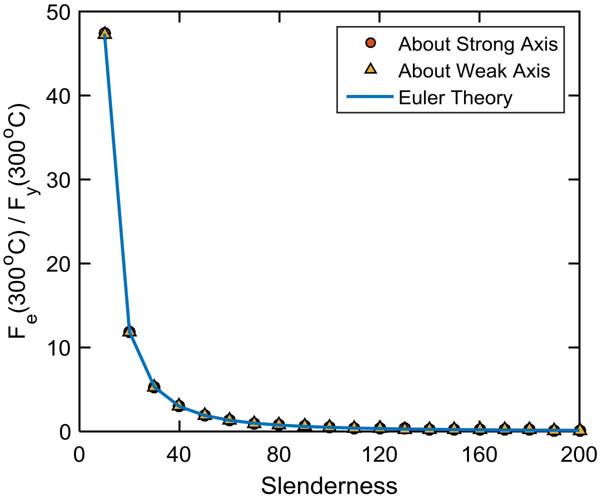

Figure 3.5 Comparison of Euler elastic buckling stress obtained by the present study and Euler equation.

In the present study, the effects of both uniform and non-uniform longitudinal temperature profiles, along with boundary conditions on elastic buckling force and mode shapes of steel columns is assessed. In the context of this study, only the first eigenvalue (Euler elastic buckling force) and the first 3 eigenvectors (mode shapes) are discussed here. The effective length factor is also calculated for the 1st mode shape of instability. In addition, an equation is proposed to predict the Euler elastic buckling stress in case of non-uniform longitudinal temperature distribution.

The first 3 mode shapes of instability of steel column with various parabolic longitudinal temperature profiles and boundary conditions are shown in Figure 3.6. It should be noted that the black dash lines show instability mode shapes when there uniform longitudinal temperature distribution is used. It is observed that non-uniform longitudinal temperature distributions change the instability mode shape of steel column although this change is insignificant in profiles (1)-(3). Table 3.1 shows that longitudinal reduction of material stiffness (elastic modulus) is up to 61.3% in profiles (1)-(3). However, profile (4) shows a significant change in mode shapes of instability in comparison to either uniform longitudinal temperature distribution or non-uniform temperature profiles (1)-(3). This can be attributed to the fact that modulus of elasticity has longitudinal variation of 87% in profile (4). This difference is larger in higher mode shapes of instability, e.g. 3rd mode shape, in accordance with Figure 3.6. In general, the 3 mode shapes indicate that maximum deflection along column length is shifted towards higher temperature zones (i.e. softer material) while naturally accounting for the effect of boundary conditions.

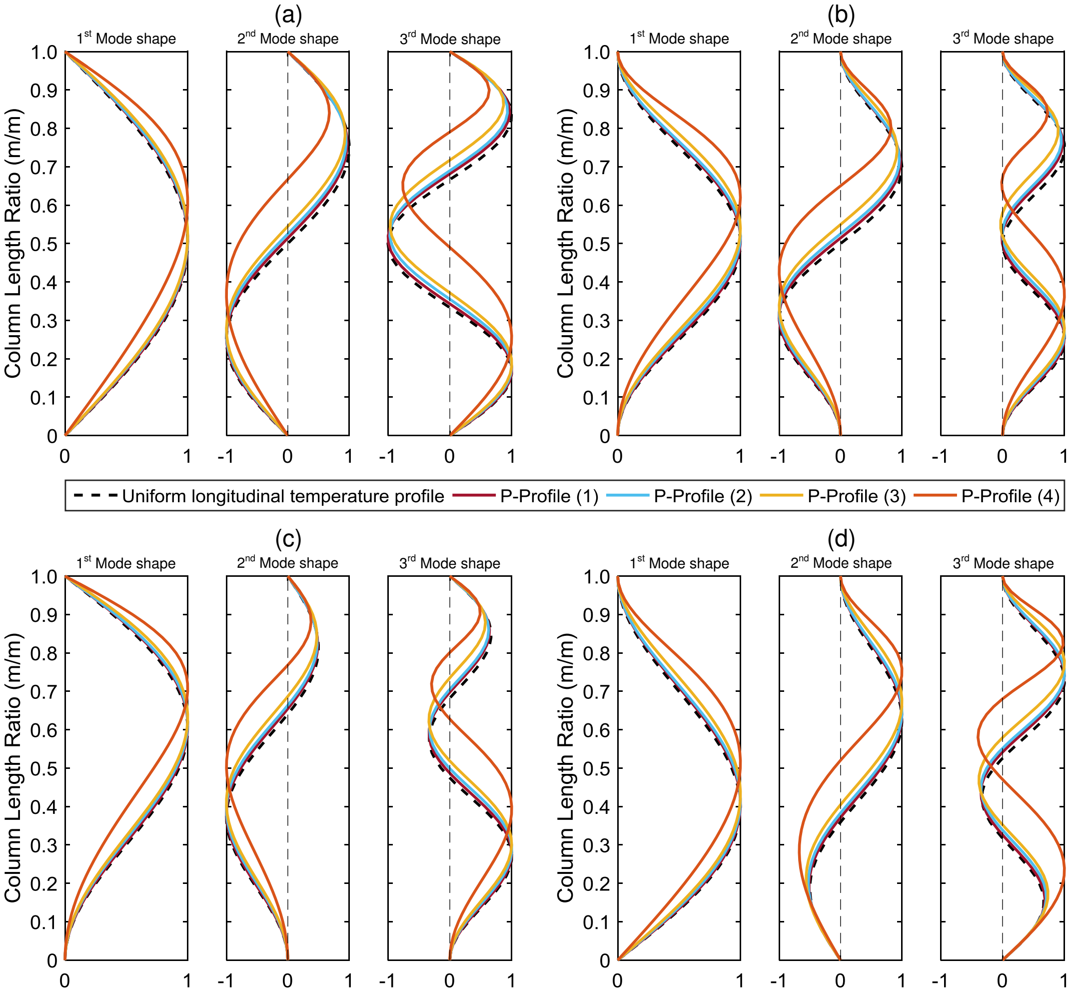

Figure 3.6 The first 3 mode shapes of instability in steel column with various parabolic longitudinal temperature distributions and (a) pinned-pinned, (b) fixed-fixed, (c) fixed-pinned, and (d) pinned-fixed boundary conditions.

It is important to assess the effects of parabolic and linear variation of temperature distribution along the length of column on the mode shapes of instability. Figure 3.7 shows mode shapes of instability for both parabolic and linear longitudinal variation of temperature for fixed-fixed and pinned-fixed boundary conditions. It is seen that there is insignificant difference between two longitudinal variations of temperature. Therefore, it can be concluded that linear elastic analysis shows minimal difference between parabolic and linear longitudinal variation of temperature although inelastic analysis can result in different conclusion since proportional limit and yield stress are effective along with modulus of elasticity in the instability of steel columns. The results of the analysis show that at least under elastic conditions, parabolic and linear longitudinal variations of temperature make no difference on mode shapes of instability. This will be further investigated in the section pertaining to non-linear inelastic analysis.

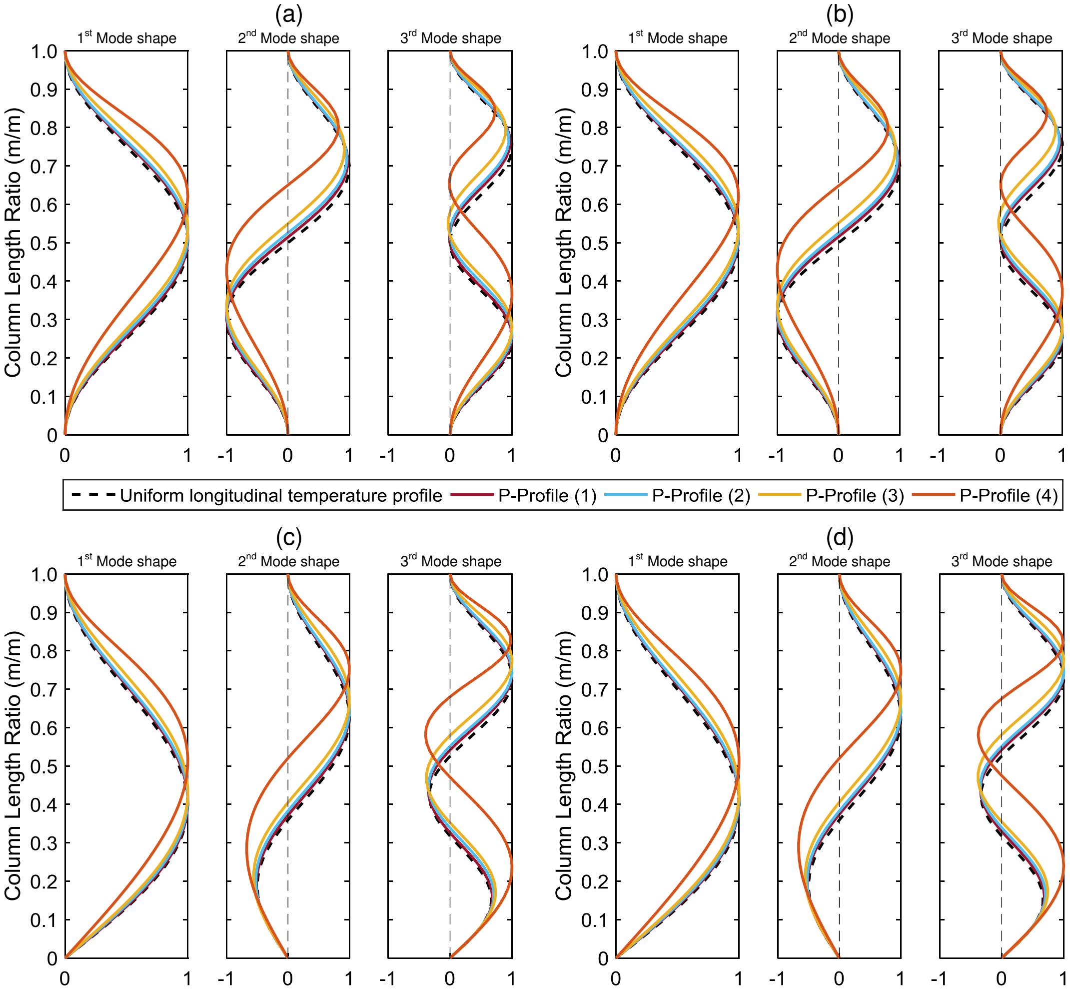

Figure 3.7 Comparison between linear (left) and parabolic (right) pattern of longitudinal temperature distributions using (a) fixed-fixed, (b) fixed-fixed, (c) pinned-fixed, and (d) pinned-fixed boundary conditions.

It is also crucial to investigate the effects of boundary conditions on elastic buckling stress. This allows correlation to be made between the elastic buckling stress and the effective length factor. This analysis is performed using profile (3) considering linear longitudinal distribution of temperature. It is shown in Figure 3.8 that pinned-pinned boundary condition results in smaller elastic buckling stress in comparison to fixed-fixed boundary condition, which has the largest elastic buckling stress. It is attributed to that fact that fixed-fixed boundary condition has smallest effective length factor in comparison to pinned-fixed or pinned-pinned boundary conditions.

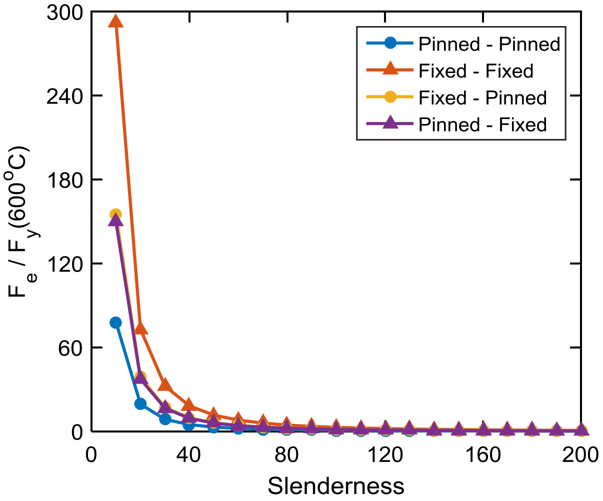

Figure 3.8 The effect of boundary conditions on the Euler elastic buckling stress.

The effective length factor for the 1st mode shape is calculated based on curvature (second derivative of deformation) change along the length of column. The results of the calculations are summarized in Table 3.3. It is noted that the effective length factors correspond to the values available in the literature for uniform longitudinal temperature profiles. However, the effective length factors change slightly in profiles (1)-(3) as expected because the change in mode shapes was minimal due to these profiles. The change in effective length factors is relatively significant in profile (4), which confirms mode shapes shown previously in Figure 3.6. The calculated effective length factors in accordance with Table 3.3 are satisfied by ratio of elastic buckling stress in fixed-fixed, fixed-pinned, and pinned-fixed to pinned-pinned boundary condition with minimal difference.

Table 3.3 The effective length factors for parabolic and linear longitudinal variation of temperature.

Profile	**Boundary conditions**							
	Pinned-Pinned		**Fixed-Fixed**		**Fixed-Pinned**		**Pinned-Fixed**	
	Parabolic	**Linear**	**Parabolic**	**Linear**	**Parabolic**	**Linear**	**Parabolic**	**Linear**
Uniform longitudinal temperature distribution	1.00		0.50		0.70		0.68	
Profile (1)	1.00	1.00	0.52	0.52	0.70	0.68	0.70	0.70
Profile (2)	1.00	1.00	0.50	0.50	0.68	0.68	0.72	0.72
Profile (3)	1.00	1.00	0.54	0.52	0.68	0.68	0.74	0.74
Profile (4)	1.00	1.00	0.48	0.46	0.56	0.56	0.80	0.80

The effects of parabolic and linear longitudinal distribution of temperature on Euler elastic buckling stress is shown in Figure 3.9. Profile (2) with fixed-fixed boundaries and profile (4) with pinned-fixed boundaries are selected to assess these effects. It is observed that parabolic and linear longitudinal temperature distributions have insignificant effect on Euler elastic buckling stress. This can be attributed to Profiles (1) and (3) since they had approximately the same mode shapes of instability as profile (2). However, there is a slight difference between parabolic and linear distributions of temperature along the length of column in profile (4). This can be attributed to the fact that longitudinal reduction of modulus of elasticity in profile (4) is larger than those in profiles (1)-(3), and parabolic versus linear longitudinal distribution of temperatures creates a slight change in longitudinal distribution of modulus of elasticity. Therefore, it can be concluded that linear longitudinal temperature distribution can be used in the elastic buckling analysis of steel columns instead of parabolic distribution, when longitudinal variation of modulus of elasticity is approximately less than 60% along the length of column.

This can be also applied to larger longitudinal reduction of modulus of elasticity (>60%) while being cautious in the level of approximation.

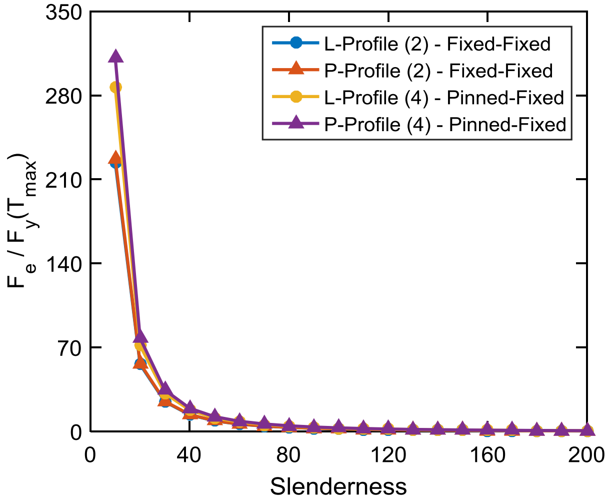

Figure 3.9 The effects of parabolic and linear longitudinal distribution of temperature on Euler elastic buckling stress.

The effects of various non-uniform longitudinal temperature profiles are also studied in order to determine an appropriate equation for the Euler elastic buckling stress. This analysis is performed using non-uniform longitudinal linear temperature profiles and pinned-pinned boundary conditions. The results shown in Figure 3.10 indicate that the Euler elastic buckling stress varies from one profile to another. The ratio of Euler elastic buckling stress to yield stress at maximum temperature increases from profile (1) with smaller high temperature at the boundaries to profile (4) with larger high temperature at the boundaries.

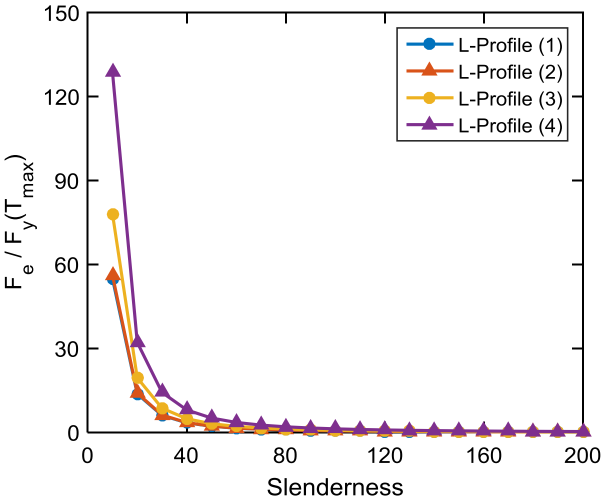

Figure 3.10 The effects of various longitudinal temperature profiles on Euler elastic buckling stress.

According to the discussions above, an equation is proposed to predict Euler elastic buckling stress in a steel W-shape column subjected to non-uniform longitudinal temperature distribution. The format of equation is assumed identical to the Euler elastic buckling equation, Eq. (3.25); however, an equivalent modulus of elasticity is considered for modulus of elasticity in case of non-uniform longitudinal temperature profiles as follow:

$$F_e(T) = \frac{\pi^2 E_{eq}}{\left(\frac{KL}{r}\right)^2} \tag{3.26.a}$$

$$E_{eq} = e^{\left(\alpha_1 . ln(E_1) + \alpha_2 . ln(E_2)\right)} \tag{3.26.b}$$

where E_1 and E_2 are modulus of elasticity at cool- and hot-end of column, respectively. α_1 and α_2 are two unknowns which should be determined using multi-linear regression analysis. Eq. (3.26.a) above can be written in a linear format, shown in Eq. (3.27), to perform a multi-linear regression analysis to obtain the unknown coefficients α_1 and α_2.

$$ln\left(F_e(T)\right) = 2ln(\pi) + ln\left(E_{eq}\right) - 2ln\left(\frac{KL}{r}\right) \tag{3.27.a}$$

$$ln\left(E_{eq}\right) = ln\left(F_e(T)\right) + 2ln\left(\frac{KL}{r}\right) - 2ln(\pi) \tag{3.27.b}$$

The multi-linear regression analysis based on both parabolic and linear longitudinal temperature distributions resulted in the following values for the α_1 and α_2 coefficients:

$$\alpha_1 = 0.4815$$

$$\alpha_2 = 0.5226$$

Therefore, the Euler elastic buckling stress can be predicted according the Eq. (3.28) below for non-uniform longitudinal temperature profiles. It is noted that the effective length factor of uniform longitudinal temperature distribution was considered in regression analysis; therefore, the K factor must be considered as ambient temperature. The plots below show the error of the proposed equation.

$$F_e(T) = \frac{\pi^2}{\left(\frac{KL}{r}\right)^2} e^{\{0.4815 ln(E_1) + 0.5226 ln(E_2)\}} \tag{3.28}$$

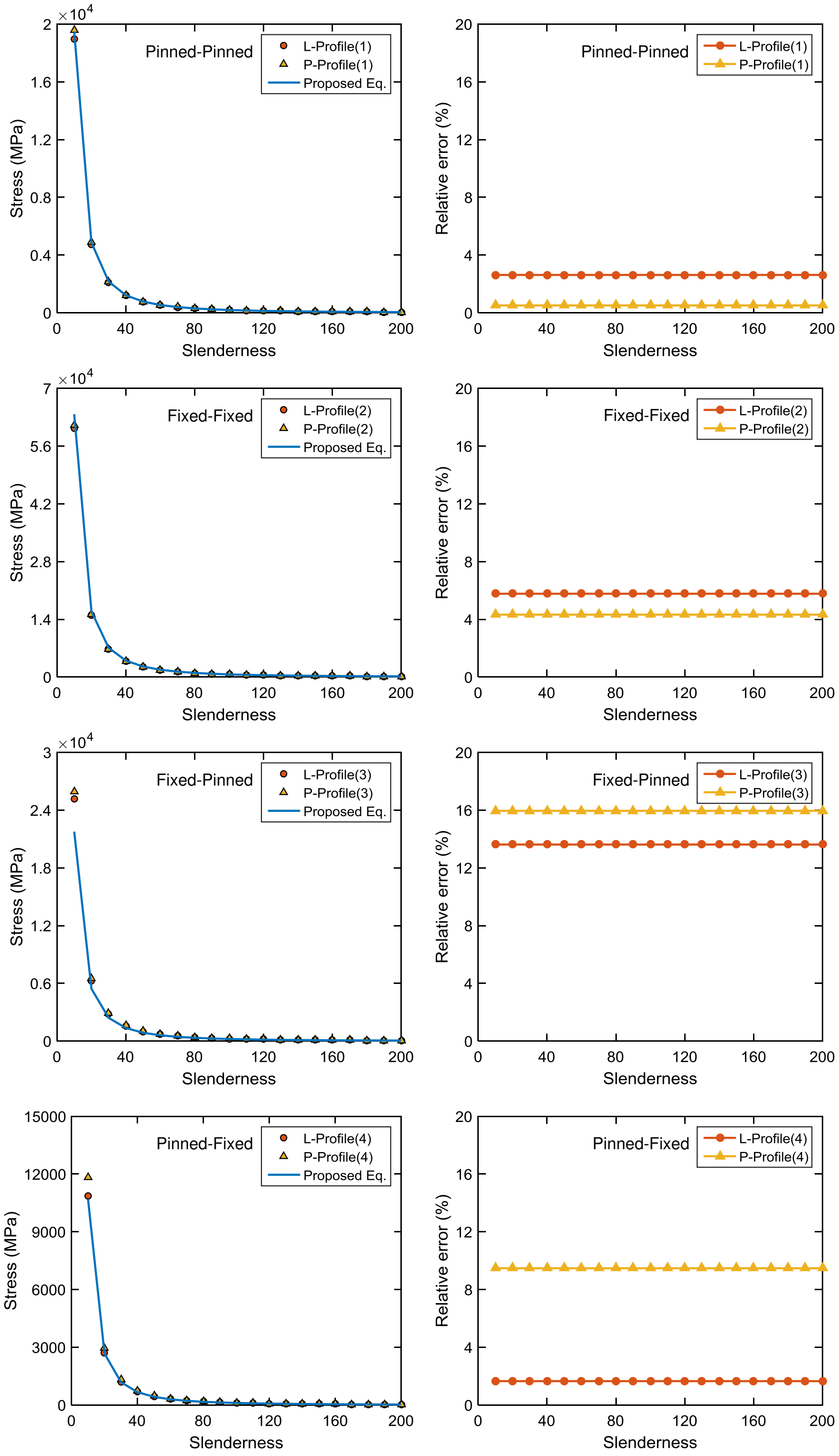

Figure 3.11 The Euler elastic buckling stress according (a) pinned-pinned boundary condition in profile (1) (b) fixed-fixed boundary condition in profile (2) (c) fixed-pinned boundary condition in profile (3) (d) pinned-fixed boundary condition in profile (4).

It should be emphasized that the proposed equation is limited to the analysis of non-uniform longitudinal temperature profiles in the present study. This equation can only provide a prediction for Euler elastic buckling stress in other cases to structural fire engineers. Further analyses should be conducted to justify the proposed equation.

3.6. Finite element framework for nonlinear inelastic analysis

This section presents details of the finite element analysis used to obtain the critical stress at instability for a column subjected to either uniform longitudinal or non-uniform temperature distribution. Figure 3.12 shows a schematic description of the finite element model of steel column under a non-uniform longitudinal distribution of temperature. All columns analyzed in this study are divided into 50 identical elements in length regardless of the longitudinal uniformity of the temperature distribution. The assemblage of stiffness matrices (elastic and geometric) of all 50 elements results in the stiffness matrix of a column, as described below.

As shown in Figure 3.12(a), sources of initial imperfection including out-of-straightness and out-of-plumbness are independently considered in the geometry of the columns analyzed. The out-of-straightness is modeled by introducing a single sinusoidal curve along the column length such that a maximum displacement of $0.001L_c$ is located at mid-height of column, where L_c is the length of column. As shown in Figure 3.12(c), the rotation angle of each element (α) in global coordinate resulting from the initial out-of-straightness is considered separately in generating the elastic and geometric stiffness matrices of the element. The transformation matrix,

$$\mathbf{T} = \begin{bmatrix} \cos\alpha & \sin\alpha & 0 & 0 & 0 & 0 \\ -\sin\alpha & \cos\alpha & 0 & 0 & 0 & 0 \\ 0 & 0 & 1 & 0 & 0 & 0 \\ 0 & 0 & 0 & \cos\alpha & \sin\alpha & 0 \\ 0 & 0 & 0 & -\sin\alpha & \cos\alpha & 0 \\ 0 & 0 & 0 & 0 & 0 & 1 \end{bmatrix} \tag{3.29}$$

is accordingly replaced by the following to obtain the stiffness matrices in accordance with the global coordinates considering the element orientation described by angle (α).

$$\mathbf{K}_{\boldsymbol{\alpha}} = \mathbf{T}^{T}\mathbf{K}\mathbf{T} \tag{3.30.a}$$

$$\mathbf{K}_{\mathbf{G},\boldsymbol{\alpha}} = \mathbf{T}^{T}\mathbf{K}_{\mathbf{G}}\mathbf{T} \tag{3.30.b}$$

where, $\mathbf{K}_{\boldsymbol{\alpha}}$ and $\mathbf{K}_{\mathbf{G},\boldsymbol{\alpha}}$ are the first-order and geometric stiffness matrices in the global coordinate system. The effect of out-of-plumbness (P-Δ) is also included explicitly in the finite element analysis. Specifically, an initial out-of-plumbness of $0.001L_c$ is assumed at the top end of the column and the lateral sway for the remaining nodes is calculated assuming a straight column. Following this step, the lateral nodal displacements are multiplied by the applied axial force to calculate the corresponding nodal moments, which are then assembled with the applied axial force to form the entire action vector on the column.

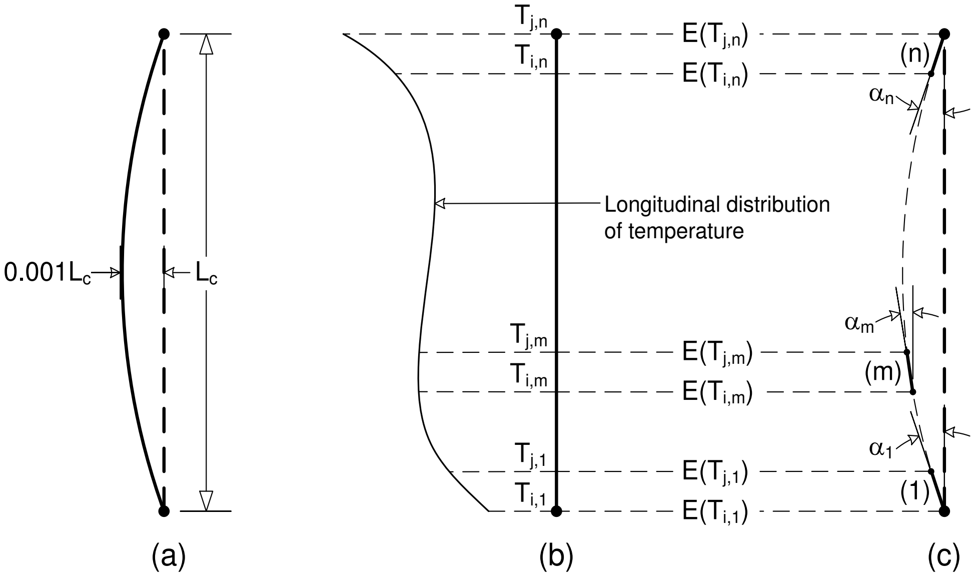

Figure 3.12 (a) The inclusion of out-of-straightness initial imperfection with a single sinusoidal curve along the length of column (b) non-uniform longitudinal distribution of temperature in column (c) schematic explanation of finite element analysis considering angle of elements as well as non-uniform longitudinal temperature distribution.

The nodal temperature at the ends of each element is also considered in generating the stiffness matrices as described in Figure 3.12(b) and 3.12(c). The modulus of elasticity, corresponding to the nodal temperatures, can be obtained from available codes, for instance Eurocode 3 (CEN, 2005) or the AISC 2010 Specification (AISC 360-10). Thereafter, a linear variation of modulus of elasticity is assumed along the length of element as explained in framework development section and in Figure 3.1(a).

To determine the critical stress causing column instability, the applied compressive force is increased incrementally until the onset of buckling in the column. A maximum loading increment (ΔP) of 2.45 kN (1 kip) is adopted in the present study. A W14X90 section, fabricated from A572-Gr50 steel, is selected for the finite element analyses.

As indicated in the *AISC Specification* (AISC 360-10), slender columns with slenderness ratio (λ=KL/r) less than $4.71\sqrt{\frac{E}{F_y}}$ at ambient temperature are susceptible to inelastic buckling, while columns with slenderness greater than $4.71\sqrt{\frac{E}{F_y}}$ buckle elastically. Therefore, it is important that this distinction be captured in the finite element analysis of the column. This is realized by defining two independent limit states. For inelastic buckling, 6 reference points (RPs) are specified over the cross section of the column, as shown in Figure 3.13(a), and the stresses developed at these 6 reference points is calculated in all elements at each loading increment using Eq. (3.31) below:

$$\sigma(n,i) = max\left(\frac{P(i)}{A} + \frac{M(n,i).y_{1:6}}{I}\right) \tag{3.31}$$

where, $\sigma(n,i)$ and $M(n,i)$ are the maximum developed compressive stress and the bending moment, respectively, at node n in increment i; P(i) is the applied axial compressive force at increment i; $y_{1:6}$ is the distance from the 6 reference points to the neutral axis of the cross section as shown in Figure 3.13(a); A and I are the cross-sectional area and moment of inertia. The onset of compressive yielding at any of these 6 reference points, based on the yield stress for the temperature at that section, is chosen as the limit state for inelastic buckling in accordance with Eq. (3.32) below:

$$\chi(i) = \frac{\sigma(n,i)}{F_y(n)} \tag{3.32}$$

where, $\chi(i)$ is the maximum ratio of developed compressive stress, $\sigma(n,i)$, to yield stress at node n, $F_y(n)$, at loading increment i. It should be noted that $F_y(n)$ is not constant, and depends on nodal temperature. Furthermore, the calculated stress in the cross section is influenced not only by the applied load but also by any residual stresses that might be present, modeled by the residual stress field shown in Figure 3.13(b). It is assumed that the maximum thermally-induced residual stresses are 70 MPa (~$0.2F_y$) at ambient temperature. The reduction factor for yield stress at elevated temperatures is also used to reduce the intensity of the residual stresses in the cross section. This assumption was also made by Takagi and Deierlein (2007).

Lastly, the buckling stress, F_{cr}, is determined using Eq. (3.33), when the value of $\chi(i)$, in one of the sections, reaches a limit of 0.99.

$$F_{cr} = \frac{P(i)}{A} \tag{3.33}$$

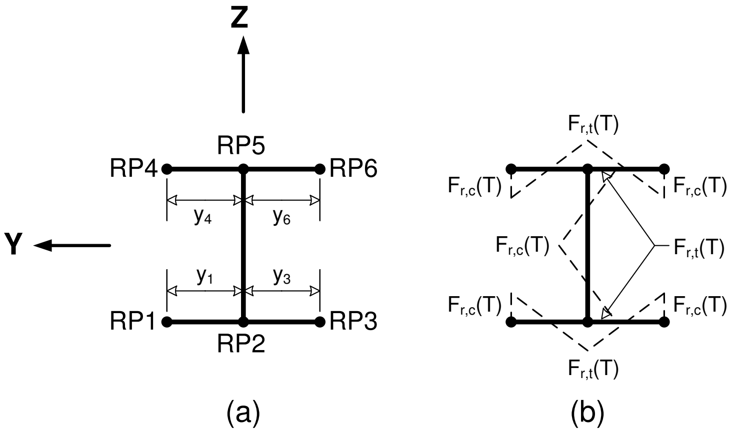

$F_r(T)=\beta_y.F_r(20°C)$

$\beta_y=F_y(T)/F_y(20°C)$

$F_r(20°C)$=Residual stresses at 20°C

$F_{r,t}(T)$: Tensile residual stress

$F_{r,c}(T)$: Compressive residual stress

Figure 3.13 (a) 6 reference points (RP's) in W-shape steel section (b) distribution of residual stresses in W-shape hot-rolled steel section.

The lateral stiffness of the steel column under the applied compressive load defines the limit state for elastic buckling. In this limit state, the applied compressive load and maximum deflection of the column are recorded at each increment. The lateral stiffness of the column is obtained in each increment using Eq. (3.34) below:

$$\kappa(i) = \frac{P(i)-P(i-1)}{d(i)-d(i-1)} \tag{3.34}$$

where, κ(i) is lateral stiffness of the column in increment i; P(i) and P(i-1) and d(i) and d(i-1)are the applied compressive forces and maximum deflections, respectively, of the column in increments i and i-1. Once the lateral stiffness of the column at a given loading increment is computed, it is then compared to the initial lateral stiffness of the column, κ(1), which is calculated based on first increment of loading. This is performed using:

$$\rho(i) = \frac{\kappa(i)}{\kappa(1)} \tag{3.35}$$

where, ρ(i) is the reduction in the column lateral stiffness in the i^{th} increment in comparison to the initial lateral stiffness, κ(1). Theoretically, Euler elastic buckling for a concentrically loaded column takes place when ρ(i) reaches zero. However, initial assessment of the developed formulation indicates that the onset of elastic buckling is reached when the column loses 96% or more of its initial lateral stiffness. Therefore, the elastic buckling is determined when ρ(i) is at 4% or less in the i^{th} increment of loading. Eq. (3.33) is also used here to calculate the elastic buckling stress, F_{cr}. Figure 3.14 shows the flowchart of finite element buckling analysis of steel column exposed to lateral and fire loads.

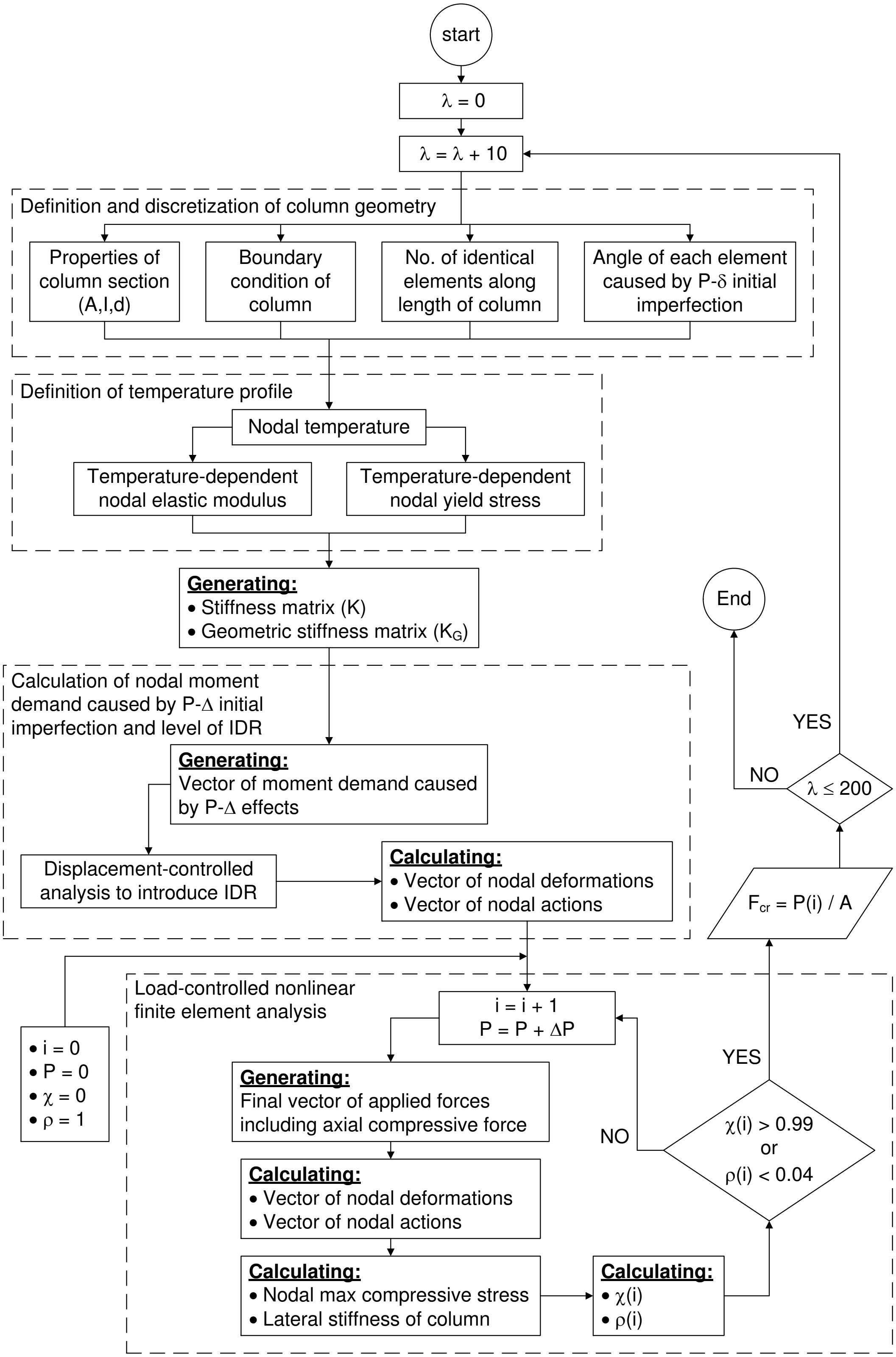

Figure 3.14 Flowchart of finite element buckling analysis of steel column exposed to lateral and fire loads.

3.7. Temperature-dependent material modeling for inelastic analysis

Four alternative steel material modeling approaches will be considered, as shown in Figure 3.15. The stress-strain curve is assumed to be elastic-perfectly plastic behavior at ambient temperature. It should be noted that the transition from elastic to inelastic material behavior utilized in the stability analysis has a significant effect on the calculated buckling stress of steel columns at elevated temperatures (Takagi and Deierlein, 2007; Agarwal and Varma 2011). There are three essential mechanical properties of structural steel that will be considered in the instability analysis of columns exposed to elevated temperatures: modulus of elasticity (E), proportional limit (F_p), and yield stress (F_y).

First, the temperature-dependent mechanical properties of structural steel are modeled exactly as in Eurocode 3 (CEN, 2005), as shown in Figure 3.15(a). This material modeling approach was implemented by Takagi and Deierlein (2007). Second, an actual curvilinear stress-strain curve of steel material at elevated temperatures is idealized with the bilinear relation shown in Figure 3.15(b). In this approach, the equivalent modulus of elasticity, Eeq(T), and yield stress, Fy,eq(T), are computed such that the two hatched areas in Figure 3.15(b) are equal. This approach has been used by Agarwal and Varma (2011). Third, a temperature-dependent elastic-perfectly plastic stress-strain curve is considered with no consideration to the effects of proportional limit (Fp), as shown in Figure 3.15(c). The elastic modulus, E(T), and yield stress, Fy(T), are both adopted from Eurocode 3 (CEN, 2005). Lastly, a trilinear stress-strain curve is implemented, as shown in Figure 5(d). In this approach, the temperature-dependent modulus of elasticity is adopted from Eurocode 3 (CEN, 2005) with no changes; however, a new effective yield stress, Fye(T), is defined such that two hatched areas in Figure 3.15(d) are identical. These four approaches will be referred to in the next sections of this article as material models (a)-(d).

The variations in E, Fp, and Fy as a function of temperature, described by β_E, β_p, and β_y, for the four different reference stress-strain curves are summarized in Table 3.4.

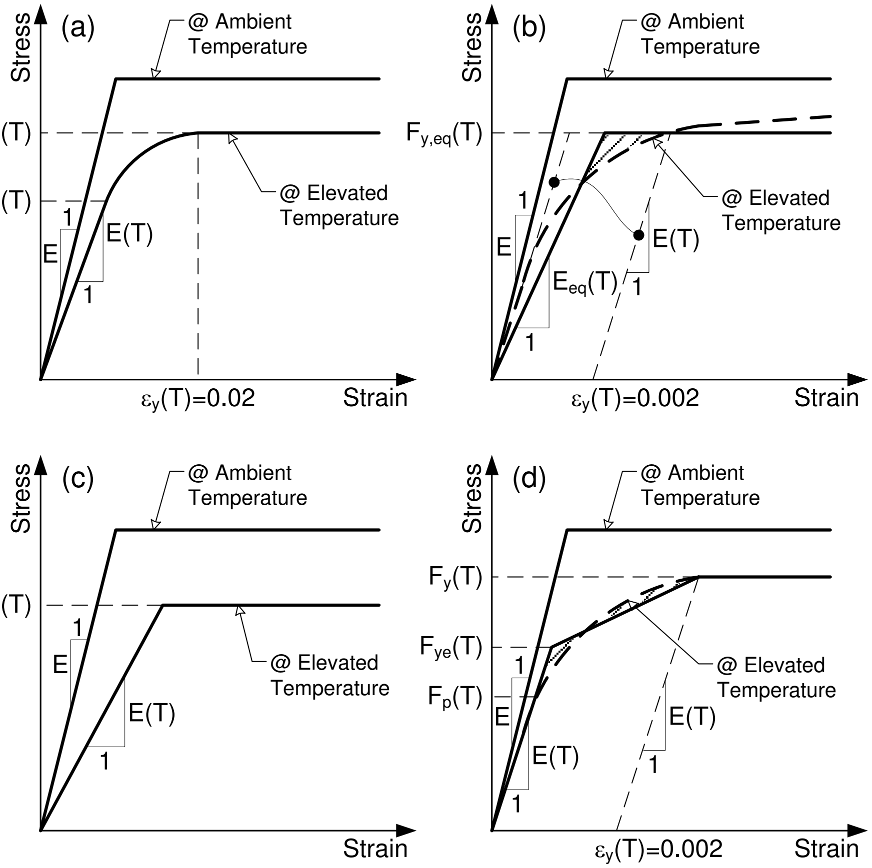

Figure 3.15 Schematic explanation of material modeling (a) Eurocode 3 (CEN, 2005), (b) Agarwal and Varma (2011), (c) elastic-perfectly plastic, (d) tri-linear equivalent model.

Table 3.4 Summary of variations in β_E, β_p, and β_y for 4 different stress-strain curves investigated.

Temp. (℃)	Material (a)			Material (b)		Material (c)		Material (d)	
	β_y	β_p	β_E	$\beta_{y,eff}$	$\beta_{E,eff}$	β_y	β_E	β_{ye}	β_E
20	1.00	1.00	1.00	1.00	1.00	1.00	1.00	1.00	1.00
100	1.00	1.00	1.00	1.00	1.00	1.00	1.00	1.00	1.00
200	1.00	0.81	0.90	0.89	0.84	1.00	0.90	0.88	0.90
300	1.00	0.61	0.80	0.79	0.68	1.00	0.80	0.77	0.80
400	1.00	0.42	0.70	0.69	0.54	1.00	0.70	0.67	0.70
500	0.78	0.36	0.60	0.56	0.47	0.78	0.60	0.54	0.60
600	0.47	0.18	0.31	0.32	0.24	0.47	0.31	0.31	0.31
700	0.23	0.08	0.13	0.15	0.10	0.23	0.13	0.14	0.13
800	0.11	0.05	0.09	---	---	0.11	0.09	0.07	0.09

3.8. Illustration of the proposed framework - verification

A set of analyses is conducted to illustrate the proposed formulation and finite element analysis approach. This includes examination of buckling of a pinned-pinned column at ambient and elevated temperatures using the W14X90 steel column considered previously. While the developed formulation can account for any restraints at the column ends, only pinned-pinned boundary conditions are used so that a direct comparison can be used against existing code provisions, which were developed using pinned-pinned boundary conditions. Details of the column evaluated are shown in Figure 3.16(a). At ambient temperature, the results of the analysis are compared to the column buckling stress, Fcr, determined with Eqs (E3 and E4 of the AISC Specification (AISC 360-10). Note that the AISC Specification (AISC 360-10) equation for column buckling is based on the assumption of elastic-perfectly plastic behavior. Therefore, the same material behavior is assumed in the verification at ambient temperature. Furthermore, while column initial out-of-straightness is considered, the P-Δ effect is neglected because it is not reflected in the AISC Specification (AISC 360-10) column curve. As shown in Figure 3.16(b), excellent agreement is observed between the buckling stress computed using the proposed formulation and that of the AISC Specification (AISC 360-10) design equation.

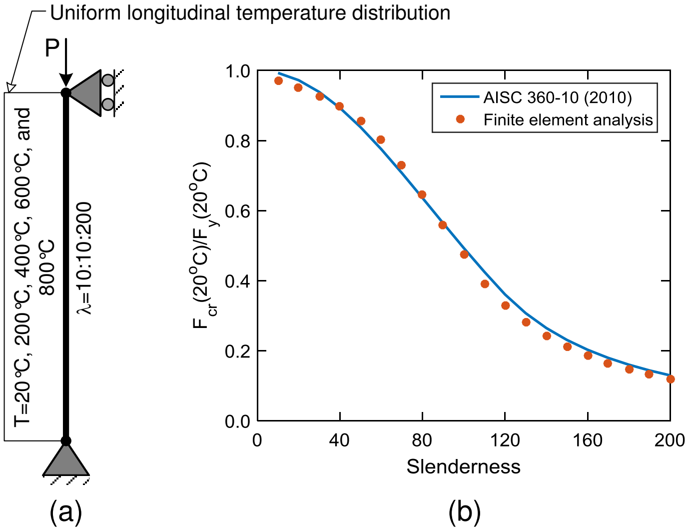

Figure 3.16 (a) Details of the evaluated column member and (b) buckling stress computed using AISC Specification (AISC 360-10, 2010) and proposed formulation in the present study.

Two additional studies are chosen for further verification of column stability at elevated temperatures, utilizing the column buckling equations at elevated temperature, proposed by Takagi and Deierlein (2007) and Agarwal and Varma (2011). In both studies, a uniform longitudinal temperature distribution in pinned-pinned columns is assumed, initial out-of-straightness and residual stresses are considered, but the initial out-of-plumbness was not taken into account. Takagi and Deierlein (2007) utilized material model (a) in accordance with Figure 3.15 while Agarwal and Varma implemented material model (b). Making the same assumptions as in the two previous studies allows for a direct comparison with the results of those studies. The comparison is conducted at four various temperatures: 200, 400, 600, 800°C. In this comparison, the proposed design equations by Takagi and Deierlein (2007) and Agarwal and Varma (2011) are plotted first for each of the above-mentioned temperatures. Then, using each of the four temperature-dependent material models discussed in the previous section (a)–(d), a nonlinear finite element analysis was conducted. Figure 3.17 shows the results of the nonlinear finite element analysis versus the proposed design equations. Good agreement was observed between the results obtained using the proposed finite element formulation and the results achieved using the equations used in the two above-mentioned studies. Specifically, good agreement is observed between the proposed design equation by Takagi and Deierlein (2007) and the results of our finite element analysis using material model (a). Similarly, implementing material (b), which was used by Agarwal and Varma (2011), resulted in very close agreement to what is obtained in this study using the proposed finite element approach. Thus, the results of the proposed methodology against previous studies which utilized commercial finite element software with shell elements, clearly demonstrates the efficiency of the proposed approach and highlights its potential as an attractive alternative to evaluate column.

As indicated by both Takagi and Deierlein (2007) and Agarwal and Varma (2011), the use of elastic-perfectly plastic temperature-dependent material behavior results in non-conservative estimates of buckling stresses. This is confirmed by this study, where the inelastic buckling stresses obtained using material (c) in Figure 3.17 are much larger than those predicted using material definitions (a) and (b). In addition, Figure 3.17 shows that the proposed trilinear temperature-dependent material behavior in the present study provides very good agreement with the previous studies, particularly with the results of Agarwal and Varma (2011). We conclude that the calculated buckling stresses using the proposed finite element framework are in good agreement with those calculated based on previous studies. Furthermore, temperature-dependent material model (c) is not a good model for evaluating column buckling at elevated temperatures. Since material models (b) (proposed by Agarwal and Varma (2011)) and (d) (proposed in this study) provide similar results, further analysis on evaluating the effect of initial lateral demand will be conducted using material (d). The results will be compared to those obtained using material (a), which was utilized by Takagi and Deierlein (2007).

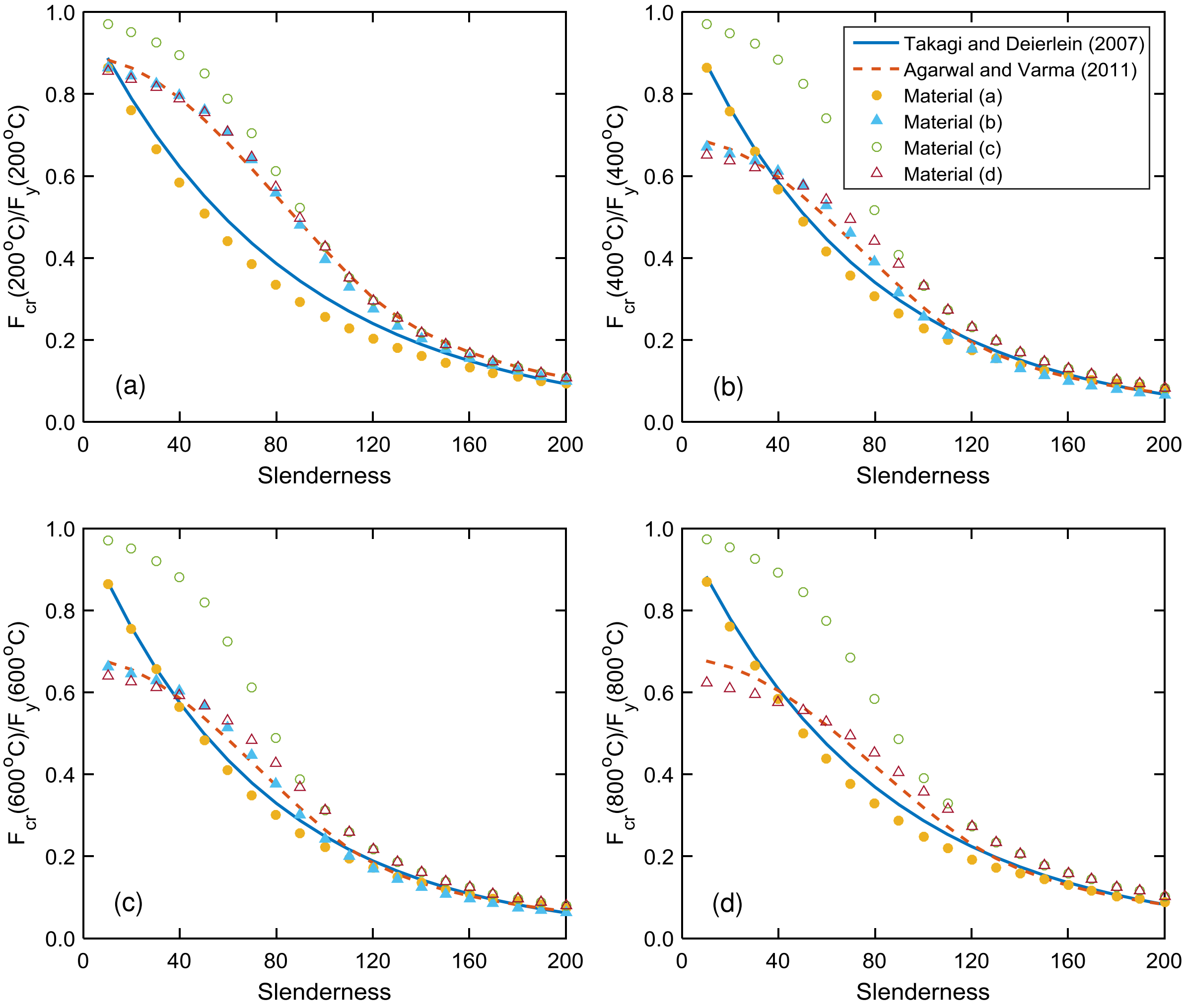

Figure 3.17 Buckling stress of steel columns subjected to uniform longitudinal temperature profiles (a) 200℃ (b) 400℃ (c) 600℃ and (d) 800℃ using nonlinear finite element analysis presented in this study versus the proposed design equations.

3.9. Case study – Effect of lateral sway followed by uniform longitudinal temperature

To emulate the multi-hazard effect of lateral demand resulting from an earthquake, followed by fire loading, an analysis is conducted to evaluate the instability of pinned-pinned columns exposed to uniform longitudinal temperature distribution with and without lateral sway. The lateral sway represents a level of residual drift that might be experienced by a column at the conclusion of an earthquake event. The analysis conducted in the present study is aimed at highlighting the capabilities of the proposed framework in addressing stability effects under combined hazards. Further studies are needed to fully assess such loading demand. For example, evaluating the response of an isolated column, with idealized pinned-pinned boundary conditions, does not provide the same level of insight that could be achieved from a frame analysis.

As shown in Figure 3.18(a), four uniform longitudinal temperatures are considered in the analysis - 200, 400, 600, and 800°C. Materials (a) and (d), in accordance with Figure 3.15, are utilized in the analysis to investigate their effects on the response of columns subjected to various levels of lateral sway and temperatures. First, the columns are analyzed with no lateral sway as shown in Figure 3.18(b). Second, two levels of lateral sway are applied to the columns: $\Delta=0.01Lc$, and $\Delta=0.02Lc$ as shown in Figure 3.18(c).

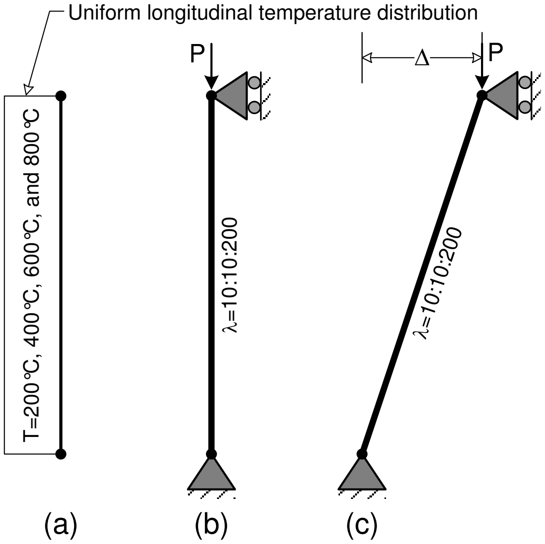

Figure 3.18 (a) Uniform longitudinal temperature distribution in the columns, (b) pinned-pinned columns with various slenderness ratios and no lateral sway (c) pinned-pinned columns with various slenderness ratios and subjected to lateral sway at two levels of $\Delta=0.01Lc$ and $\Delta=0.02Lc$.

Figure 3.19 shows the results of the analyses of the above columns. The inclusion of lateral sway causes a significant reduction in the buckling stress of pinned-pinned steel columns, as might be expected. Furthermore, material (d) generally resulted in larger buckling stresses for columns with no lateral sway in comparison to material (a) except at slenderness values, λ, smaller than 40. However, when lateral sway is included, material (d) always resulted in relatively smaller buckling stress values than those obtained using material (a).

The minimum reduction in the buckling stress in the presence of lateral sway appears to occur in the shortest steel columns, with λ=10. The reduction is 50-55% for 1% lateral sway and 65-70% for 2% lateral sway for both material models (a) and (d). The maximum reduction in buckling stress due to lateral sway occurs in columns in the slenderness range between 50 and 100 (50≤λ≤100). For 1% lateral sway, material (a) results in 70-80% reduction in the buckling stress while 80-90% reduction is seen using material (d). In addition, 80-90% reduction in the buckling stress is observed by implementing material (a) and beyond 90% is seen using material (d) at 2% of lateral sway. The reduction in the buckling stress caused by the lateral sway is minimal for slenderness ratios larger than 100 (λ>100). This reduction is approximately linear until the slenderness ratio reaches 200 (λ=200) where the reduction is 65-70% and 78-82% using material (a) at 1% and 2% level of lateral sway, respectively. Material (d) also indicates a reduction of 70-80% at 1% lateral sway and 84-90% at 2% lateral sway at slenderness ratio of 200 (λ=200).

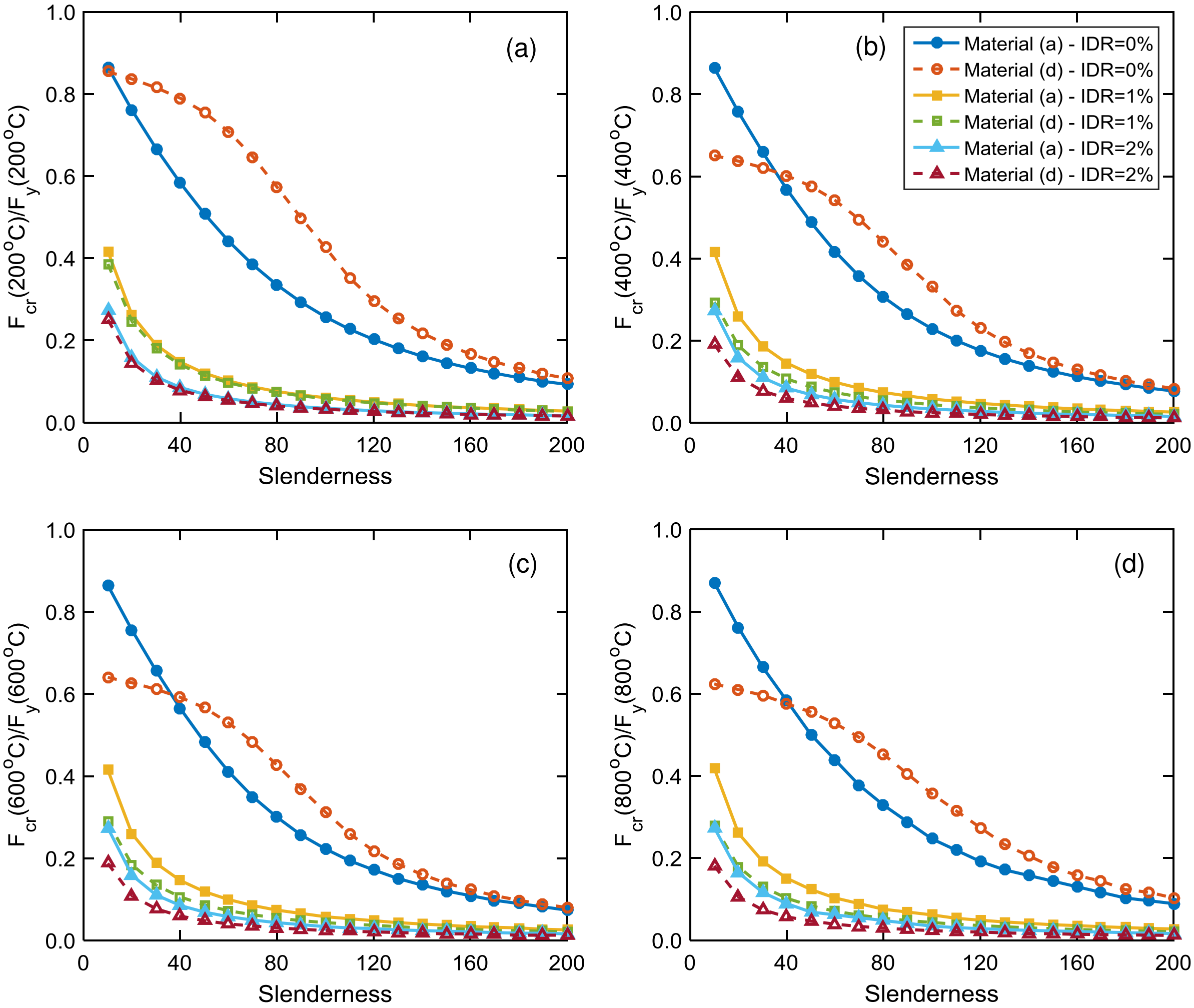

Figure 3.19 Buckling stress of steel columns subjected to uniform longitudinal temperature profiles (a) 200℃ (b) 400℃ (c) 600℃ and (d) 800℃ with and without lateral sway.

3.10. Case study – Effect of lateral sway and non-uniform longitudinal temperature

As noted previously, the proposed framework has the capability to analyze columns under non-uniform longitudinal temperature profiles. Two non-uniform longitudinal linear temperature profiles, shown in Figure 3.20(a) and (b), are chosen to illustrate this capability. Columns in this illustration of non-uniform temperature effects are analyzed without lateral sway, Figure 3.20(c), and with 1% lateral sway, $\Delta=0.01Lc$, as shown in Figure 3.20(d). The effects of material stress-strain modeling are also considered.

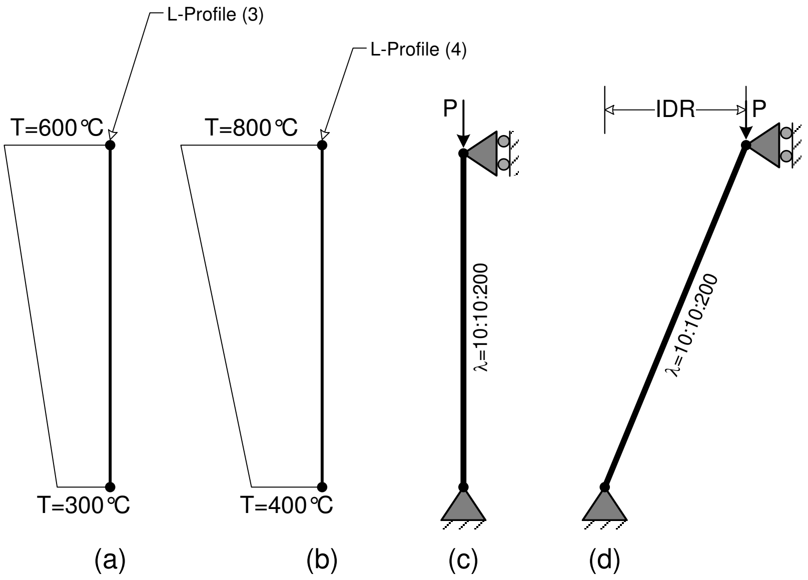

Figure 3.20 (a) Non-uniform linear longitudinal temperature profile (3), (b) non-uniform linear longitudinal temperature profile (4), (c) pinned-pinned columns with various slenderness ratios and no lateral sway (d) pinned-pinned columns subjected to inter-story drift ratio of 1%.

Columns with lateral sway have significantly smaller stresses at instability than those with no lateral sway, as shown in Figure 3.21. The results also show that the buckling stress is larger when material (d) is used, when slenderness ratios are larger than 70 for temperature profile (3) and larger than 100 for temperature profile (4), and when the columns are not subjected to lateral sway. In addition, material (a) results in a larger buckling stress than that of material (d) when the lateral sway of the columns equals 1%. For the sway cases, the analysis shows that the use of both materials lead to approximately identical reduction in buckling stress for slenderness ratios equal to or less than 60 ($\lambda \leq 60$) for each of the temperature profiles. In comparison to the non-sway case, the reduction in buckling stress when sway is included is 65-75% in columns with 1% of lateral sway and when material (a) in implemented 75-85% when material (d) is used, for slenderness ratios large than 60 ($\lambda > 60$). The maximum reduction (86%) is for columns with slenderness ratio of 100 under temperature profile (1) and slenderness ratio of 140 under temperature profile (2) using material (d).

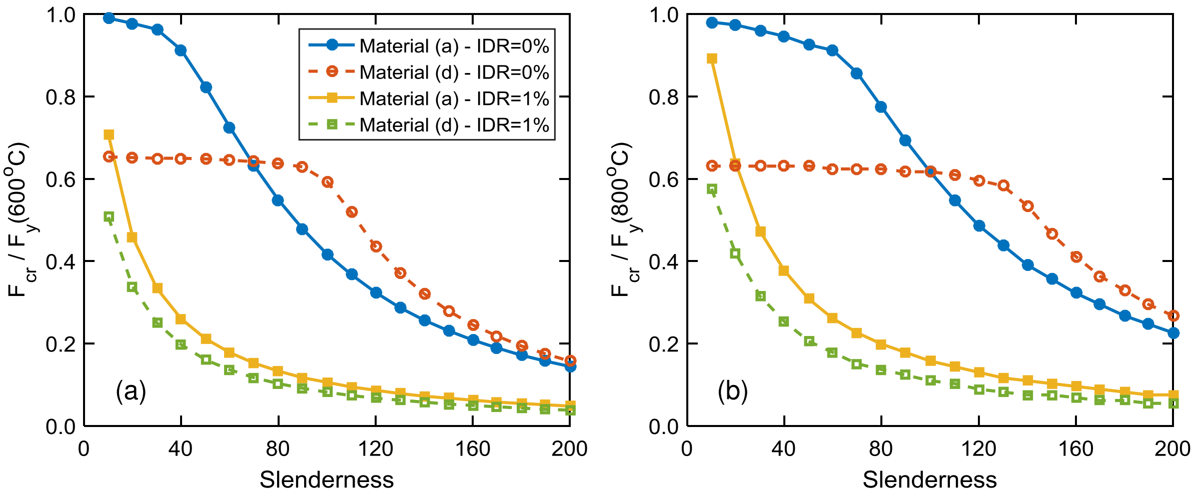

Figure 3.21 Buckling stress of steel columns subjected to non-uniform linear longitudinal temperature with and without lateral sway.

The remainder of the analysis presented below is conducted using material (a), which inherently captures creep effects. Figure 3.22 shows the buckling stress of a pinned-pinned steel column subjected to various levels of inter-story drift ratios and non-uniform longitudinal temperature profiles. This again indicates that increase in inter-story drift causes significant reduction in the inelastic buckling stress of steel columns. This reduction varies from one temperature profile to another. However, it is seen that the buckling stress for inter-story drift ratio of 5% reaches is less than 40% of its value when no inter-story-drift is present. In other words, permanent residual rotation in steel columns caused by earthquake can result in significant reduction in buckling capacity of the column.

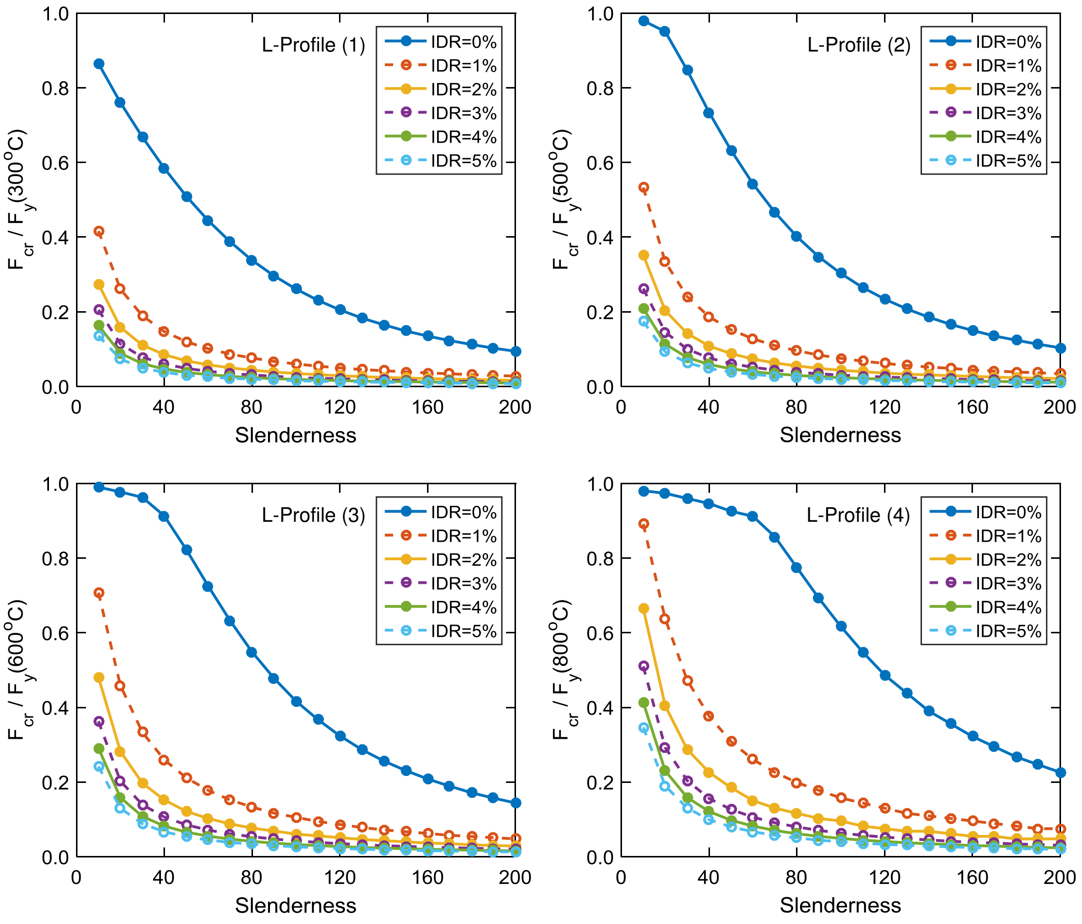

Figure 3.22 The buckling stress in the pinned-pinned column at various inter-story drift ratios and longitudinal temperature profiles.

3.11. Design equation proposal for columns under FFE

This section discusses a proposal for equations to predict the inelastic buckling stress of steel columns subjected to either uniform and/or non-uniform longitudinal temperature profiles with no lateral sway. In addition, the effects of lateral sway caused by earthquake demands will be taken into account by proposing reduction coefficients for design inelastic buckling stress in the absence of lateral sway. The results can allow structural engineers to predict nominal strength of steel columns subjected to cascading hazard of earthquake and fire along with only fire hazard.

In this section, a design equation is proposed for the case of non-uniform longitudinal temperature profiles with no inter-story drift. The equation is similar to the format of the current equation listed in the AISC Specification (AISC 360-10) proposed by Takagi and Deierlein (2007). Two coefficients, p and q, are added to the current design equation in the AISC Specification (AISC 360-10) to consider longitudinal variation of mechanical properties of structural steel as follows:

$$F_{cr} = \left[(0.42p)^{\sqrt{\left(\frac{Fy(T_{max})}{F_e}\right)^q}} \right] . F_y(T_{max}) \tag{3.36}$$

where, F_e shall be calculated according to Eq. (3.28). The two coefficients, p and q, can be determined in accordance with Tables (3.5) and (3.6) for desired limit of column slenderness as indicated below. It is noted that $E(T_{max})$ and $Fy(T_{max})$ correspond to modulus of elasticity and yield stress at the hot-end of the column, respectively.

Table 3.5 The p and q coefficients for slenderness equal or less than $4.71\sqrt{\frac{E(T_{max})}{F_y(T_{max})}}$.

Profile	**Longitudinal reduction of yield stress (%)**	**p**	**q**
L-Profile (1)	0.00	0.90	0.90
L-Profile (2)	22.00	1.05	1.50
L-Profile (3)	53.00	1.30	1.80
L-Profile (4)	89.00	1.30	2.40

Table 3.6 The p and q coefficients for slenderness greater than $4.71\sqrt{\frac{E(T_{max})}{F_y(T_{max})}}$.

Profile	Longitudinal reduction of yield stress (%)	p	q
L-Profile (1)	0.00	0.90	0.90
L-Profile (2)	22.00	0.90	0.90
L-Profile (3)	53.00	1.18	1.15
L-Profile (4)	89.00	1.20	1.50

It can be seen in Figure 3.23 that the proposed equation has a great agreement with the results of the finite element analysis. The error in the predicted inelastic buckling stress by the proposed equation relative to the results of the finite element analysis is shown in Figure 3.24, which indicates a relative error of less than 10% in all cases.

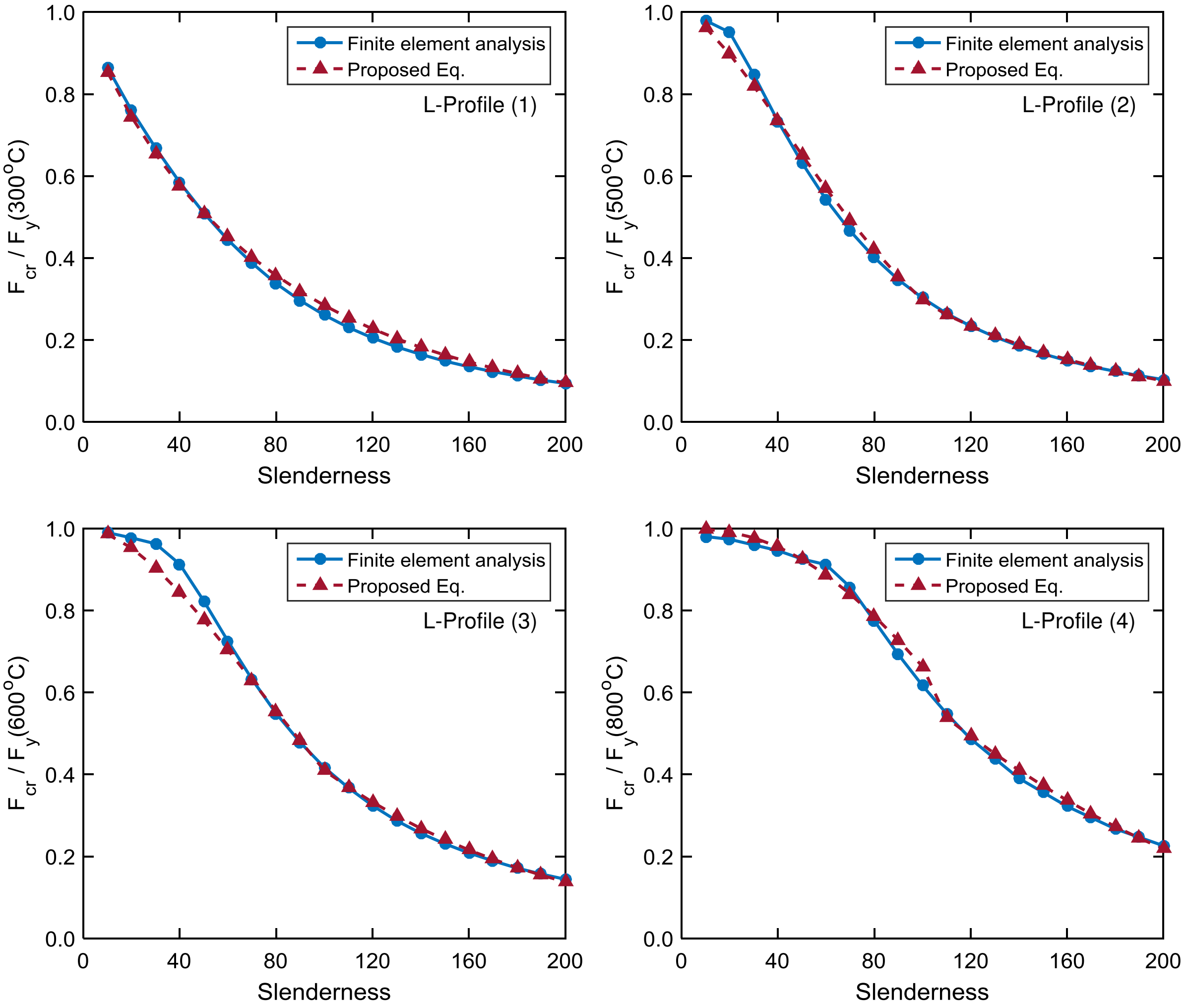

Figure 3.23 The inelastic buckling stress obtained by finite element analysis and proposed equation in the present study.

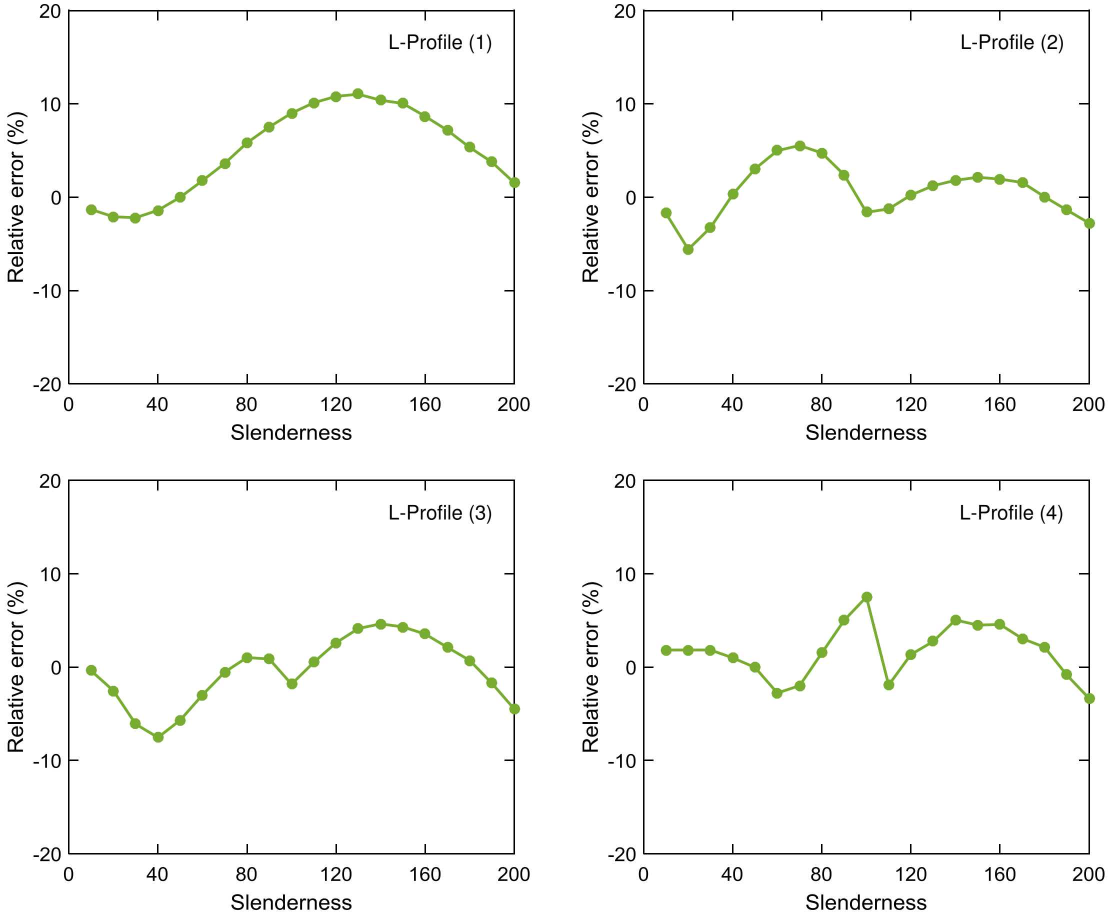

Figure 3.24 Relative error caused by the proposed equation in comparison to the results of finite element analysis.

To consider the effects of lateral sway in reducing the inelastic buckling stress of steel columns, a reduction factor, Ψ, is introduced as shown in Eq. (3.37.a) below:

$$F_{cr}^{\theta} = \Psi F_{cr} \tag{3.37.a}$$

where, F_{cr}^{θ} is design buckling stress considering rotation in column, θ, caused by lateral demands. This is also determined according to desired limit of column slenderness as follow:

For $\lambda \leq 4.71\sqrt{\frac{E(T_{max})}{F_y(T_{max})}}$

$$\Psi = (f\theta^{-g})e^{(r\lambda+s\lambda^2)} \tag{3.37.b}$$

Where, f, g, r, and s are determined according to Table 3.7.

Table 3.7 The coefficients of Eq. (3.27.b).

Profile	Longitudinal reduction of yield stress (%)	f	g	r	s	R^2 (%)
L-Profile (1)	0.00	1.514×10^{-2}	0.8257	-3.237×10^{-2}	2.220×10^{-4}	93.8
L-Profile (2)	22.00	1.686×10^{-2}	0.8280	-3.620×10^{-2}	2.584×10^{-4}	91.1
L-Profile (3)	53.00	2.870×10^{-2}	0.8191	-5.046×10^{-2}	3.682×10^{-4}	96.8
L-Profile (4)	89.00	4.189×10^{-2}	0.8076	-4.777×10^{-2}	2.897×10^{-4}	98.4

For $\lambda > 4.71\sqrt{\frac{E(T_{max})}{F_y(T_{max})}}$:

$$\Psi = (f\theta^{-g})e^{(r\lambda)} \tag{3.37.c}$$

Where, f, g, and r are determined in accordance with Table 3.8.

Table 3.8 The coefficients of Eq. (3.37.c).

Profile	Longitudinal reduction of yield stress (%)	f	g	r	R^2 (%)
L-Profile (1)	0.00	3.871×10^{-3}	0.8211	2.961×10^{-3}	95.7
L-Profile (2)	22.00	3.893×10^{-3}	0.8296	3.374×10^{-3}	95.2
L-Profile (3)	53.00	4.014×10^{-3}	0.8307	3.197×10^{-3}	96.1
L-Profile (4)	89.00	4.075×10^{-3}	0.8371	2.841×10^{-3}	88.9

Figure 3.25 shows the excellent agreement between the proposed equation and the results of the flexibility-based finite element analysis for determining the elastic buckling stress of steel columns under the combined hazards of lateral demand and fire loads. This was performed for linear longitudinal distribution of temperature as indicated in the Figure 3.25.

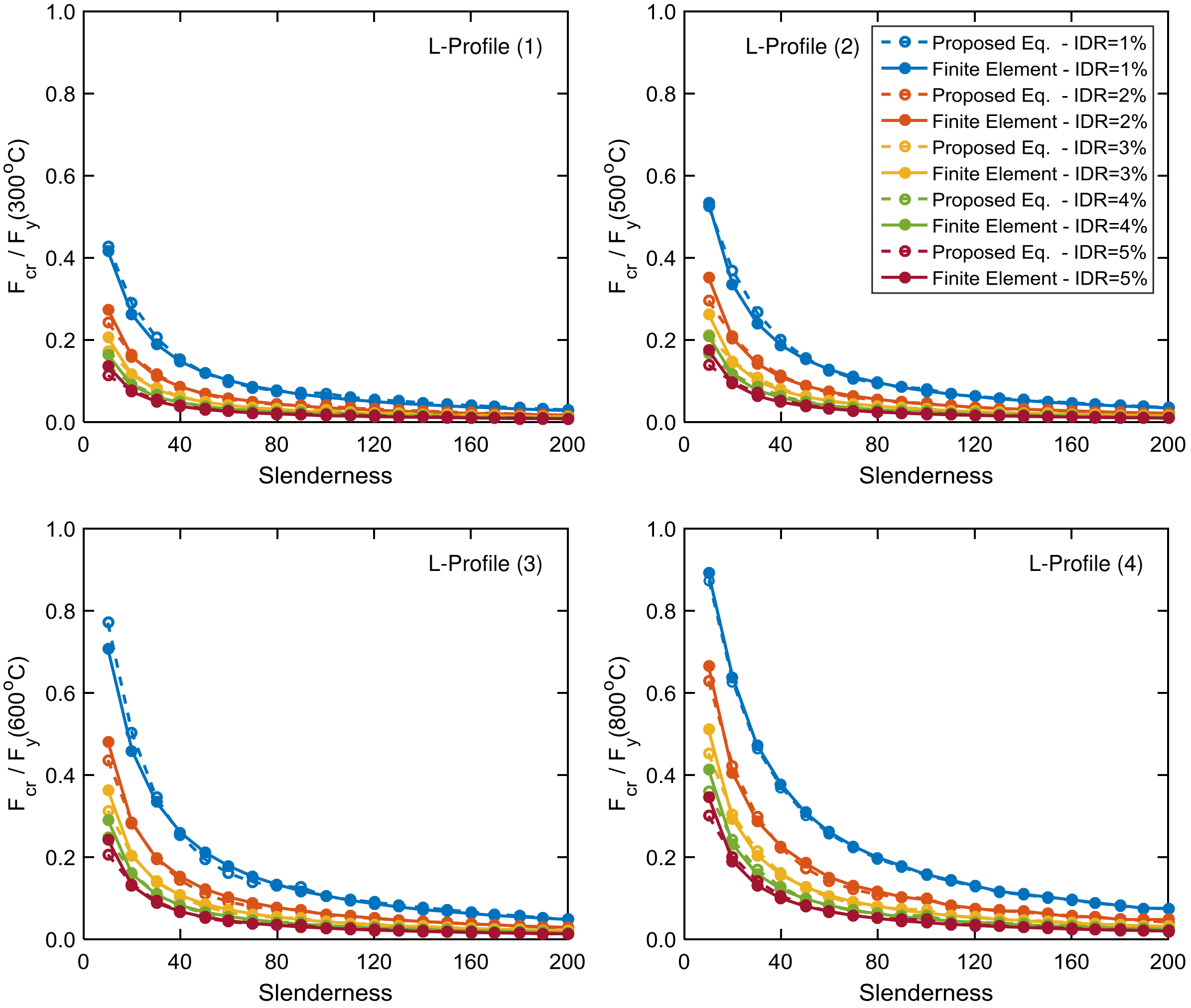

Figure 3.25 The inelastic buckling stress obtained by proposed equation in the present study and finite element analysis in presence of inter-story drift ratio.

3.12. Summary

In this chapter, a geometrically non-linear flexibility-based finite element formulation was proposed for assessing the response of steel columns under the sequential demand of earthquake and fire loadings. The proposed approach is an efficient finite element tool that can be employed to study the effects of a wide variety of variables on the buckling response of steel columns subjected to fire and fire following earthquakes. This methodology includes both P- δ and P-Δ effects, residual stresses in hot-rolled W-shape steel sections, temperature-dependent material modeling, different boundary conditions (although only pinned-pinned was evaluated), and non-uniform temperatures along the length of the column. Four various non-uniform longitudinal temperature profiles were considered to allow for capturing of various rates of change in temperature-dependent mechanical properties of structural steel including modulus of elasticity, yield stress, and proportional limit.

The following preliminary conclusions can be drawn from the linear elastic analysis:

- The Euler elastic buckling stress, calculated by the flexibility-based approach, about both strong and weak axes of W-shape steel columns was in excellent agreement with results of classical Euler elastic buckling equation. This verified both first-order stiffness and geometric stiffness matrices generated based on the proposed flexibility-based approach in the numerical code.
- It was observed that profile (4) significantly changed the instability mode shape of steel column although this change was insignificant in profiles (1)-(3). This can be attributed to the fact that modulus of elasticity has longitudinal variation of 87% in profile (4). The difference in the mode shapes is larger for higher modes of instability. The 1st mode shape indicates that maximum deflection along column length is shifted towards higher temperature zones (i.e. softer material) while naturally accounting for the effect of boundary conditions.
- The effective length factor of column buckling was calculated for the 1st mode shape of instability considering non-uniform longitudinal temperature distribution. The effective length factors showed a small change in profiles (1)-(3)

as expected because the change in mode shapes was minimal. The change in effective length factors was relatively significant in profile (4).

- It was observed that there is insignificant difference between parabolic and linear temperature profiles in the elastic response. In fact, the results of the analysis showed that under elastic conditions, parabolic and linear longitudinal variations of temperature make no difference on mode shapes of instability.
- It was concluded that linear longitudinal temperature distribution can be used in elastic buckling analysis of steel columns, instead of parabolic distribution, when longitudinal variation of modulus of elasticity is approximately less than 60% along the length of column.
- An equation was proposed to predict Euler elastic buckling stress in a steel W-shape column subjected to non-uniform longitudinal temperature distribution. The results of proposed equation indicated a good agreement with the solution of eigenvalue problem.

The following conclusions can be drawn from the inelastic analysis:

- The initial imperfections including out-of-straightness and out-of-plumbness were independently considered in the geometry of the columns analyzed. The out-of-straightness (P-δ) was modeled by introducing a single sinusoidal curve along the column length with maximum displacement of 0.001 column length located at mid-height of column. The effect of out-of-plumbness (P-Δ) was included explicitly in the finite element analysis such that 0.001 column length was assumed at the top end of the column and the lateral sway for the remaining nodes was calculated assuming a straight column.

- Good agreement was observed between results of the proposed analytical approach and available strength design equations for steel columns at ambient and elevated temperatures.
- Using Eurocode 3 (CEN, 2005) temperature-dependent material modeling, the results of the presented approach was in good agreement with the results of Takagi and Deierlein (2007), which was obtained using the same material modeling.
- This proposed approach resulted in close agreement with design equation proposed by Agarwal and Varma (2011) when implementing their material model.
- It was shown that assuming elastic-perfectly plastic temperature-dependent material modeling resulted in non-conservative buckling stress values.
- A new tri-linear temperature-dependent material modeling was shown to yield very close results to those obtained by Agarwal and Varma (2011).
- The inclusion of P-Δ effects with uniform temperature resulted in significant reduction in buckling capacity of steel columns. In addition, implementing tri-linear material – material (d) – resulted in more reduction in buckling stress in steel column under lateral sway.
- The column with slenderness ratio of 10 showed the least reduction in buckling stress caused by the P-Δ effects under uniform temperature. However, maximum reduction took place in columns with slenderness ratio between 50 and 100.
- When non-uniform longitudinal temperature is included, material (a) resulted in larger buckling stress than that of material (d) when lateral sway was introduced.

- The use of non-uniform longitudinal temperature resulted in the maximum reduction in buckling stress, caused by P-Δ effects, to be observed in columns with slenderness ratio of 100 in profile (3) and 140 in profile (4).
- A set of design equations was proposed to estimate the inelastic buckling stress of W-shape steel columns for the case of non-uniform longitudinal temperature profiles with and without inter-story drift. The proposed equations showed a good agreement with the results of nonlinear finite element analysis.

Chapter 4. Performance of steel moment resisting frames subjected to fire following earthquake

4.1. Overview

This chapter utilizes finite element simulations, using the commercial software ABAQUS (Simula, 2010) to provide insight into the effects of earthquake-initiated fires on low-, medium-, and high-rise steel moment resisting frames with reduced beam section connections, which have become common frame type in modern earthquake-resistant design following the 1994 Northridge and 1995 Kobe earthquakes. The earthquake simulations are conducted using nonlinear time-history analysis where the frames are subjected to a suite of near-field and far-field ground motions. With the state of the structure following the earthquake used as the initial condition for the fire analysis, the uncoupled thermal-mechanical analysis is performed with a specified time-temperature curve applied at the reduced beam section connections. The results of the simulations can be used by engineers to reflect on the behavior of moment frames under the combined actions of earthquake and fire.

4.2. Background

Steel moment resisting frames (MRFs) with reduced beam section (RBS) connections are common in seismically active regions. RBS connections have been extensively used in MRFs following the 1994 Northridge and 1995 Kobe earthquakes to mitigate the brittle fractures that were observed in pre-Northridge moment resisting connections. However, studies on the performance of MRFs with RBS connections under combined hazard of earthquake and fire loadings currently are lacking. This chapter investigates the performance of low-, medium-, and high-rise MRFs with RBS connections subjected to post-earthquake fire scenarios. Nonlinear dynamic time-history and thermal-mechanical analyses are implemented to simulate ground motions and post-earthquake fires, respectively. The frames considered are fireproofed; the fire is applied only to the RBS connections under the assumption that the fireproofing may spall at the connection where large inelastic demand is concentrated during the seismic events. This analysis provides a realistic representation of the expected seismic and fire demand. The buildings investigated were initially studied in the SAC– a partnership of: Structural Engineers Association of California (**S**EAoC), Applied technology Council (**A**TC), California Universities for Research in Earthquake Engineering (**C**UREE) – Steel Project (FEMA 354, 2000) and have been used subsequently in numerous studies to evaluate their seismic response. Therefore, assessing their response under fire following earthquake will provide valuable knowledge, which can improve modern performance-based design approaches for steel structures exposed to the threat of post-earthquake fires.

4.3. Configuration of moment resisting frames

A set of low-, medium-, and high-rise buildings with perimeter steel MRFs and interior gravity frames, identified in the SAC Steel Project (FEMA 354, 2000) and designed in accordance with the Uniform Building Code (UBC 94, 1994) for Los Angeles, CA for high seismicity, are analyzed in the present study. The 2-D perimeter steel MRFs were selected because they have the ability to represent the performance of steel MRFs subjected to elevated temperatures with reasonable accuracy and with less computational effort than would be required with a 3-D building model (Quiel and Garlock, 2008). In cases when a large redistribution of forces is expected, the use of a full 3-D configuration might be needed for analysis.

The perimeter MRFs of 3-, 9-, and 20-story buildings in the N-S direction are analyzed in the present chapter. Figure 4.1 shows the configuration of the frames, the story heights, the cross sections of all beams and columns, and the seismic mass. More details on the buildings are provided in FEMA-355C (2000). Unlike the original design, in this chapter, the frame connections are redesigned as RBS connections in accordance with the procedure outlined in the FEMA-350 (2000). The most reduced width of flange in all RBS connections is also provided in Figure 4.1. The cut portion of the beam flanges in the RBS connection leads to relocation of the plastic hinge to the reduced section away from the face of the column flange. Hence, the demand on the column is reduced and the potential for brittle fracture in the connection is minimized. The use of RBS connections leads to a minor reduction in the global stiffness of the buildings when compared to the original design (FEMA 355D, 2000).

The results discussed in this chapter are based on numerical simulations in which the structural system is assumed to have been built conforming to the specified deign and detailing requirements. Any deviation of such in the actual fabrication and/or construction could lead to different structural response and alterations to the conclusions made. For example, changes to the topology of the reduced beam section used will lead to different damage accumulation in the connection and consequently a change to the overall system response.

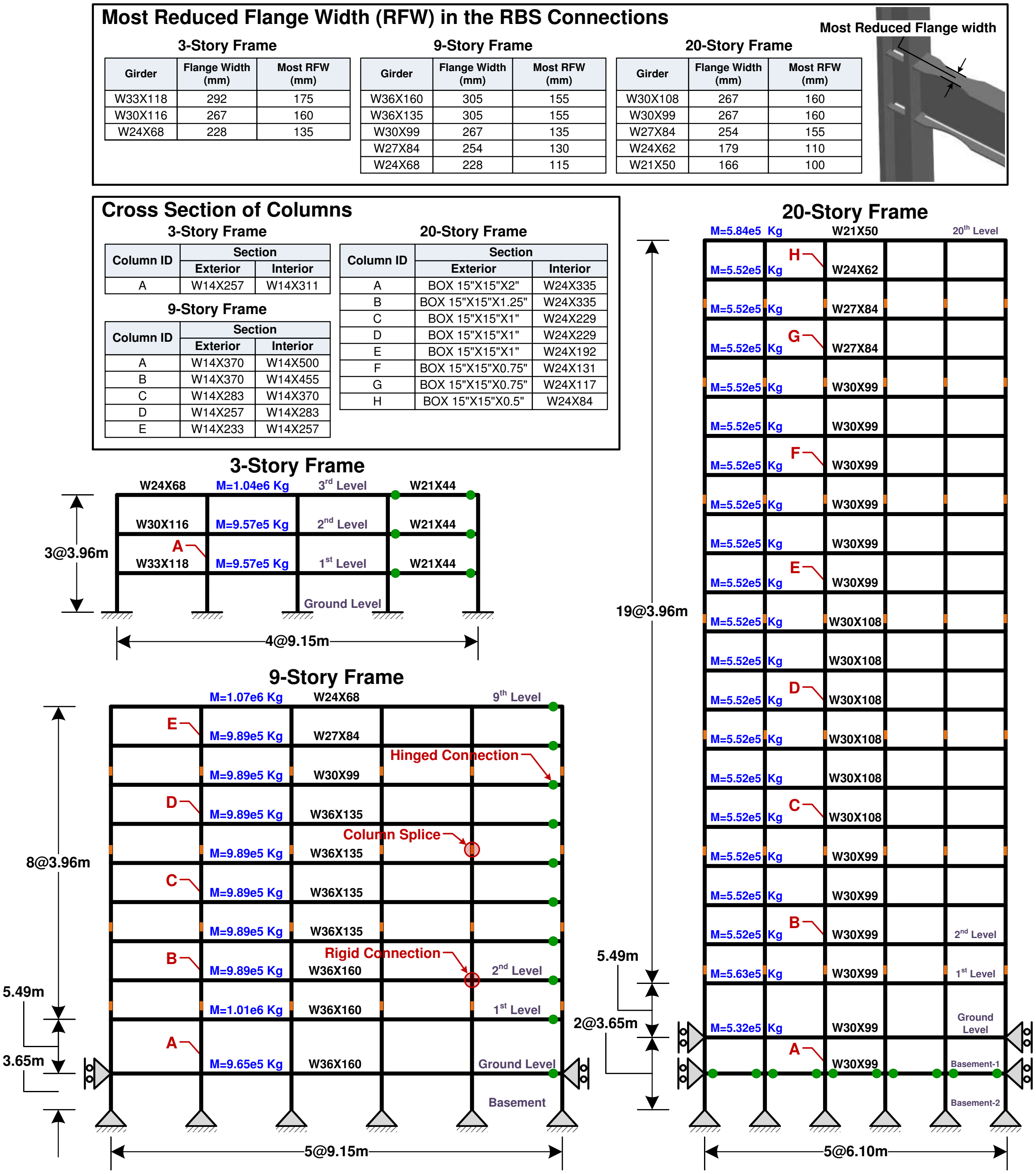

Most Reduced Flange Width (RFW) in the RBS Connections

3-Story Frame

Girder	Flange Width (mm)	Most RFW (mm)
W33X118	292	175
W30X116	267	160
W24X68	228	135

9-Story Frame

Girder	Flange Width (mm)	Most RFW (mm)
W36X160	305	155
W36X135	305	155
W30X99	267	135
W27X84	254	130
W24X68	228	115

20-Story Frame

Girder	Flange Width (mm)	Most RFW (mm)
W30X108	267	160
W30X99	267	160
W27X84	254	155
W24X62	179	110
W21X50	166	100

Cross Section of Columns

3-Story Frame

Column ID	Section	
	Exterior	Interior
A	W14X257	W14X311

9-Story Frame

Column ID	Section	
	Exterior	Interior
A	W14X370	W14X500
B	W14X370	W14X455
C	W14X283	W14X370
D	W14X257	W14X283
E	W14X233	W14X257

20-Story Frame

Column ID	Section	
	Exterior	Interior
A	BOX 15"X15"X2"	W24X335
B	BOX 15"X15"X1.25"	W24X335
C	BOX 15"X15"X1"	W24X229
D	BOX 15"X15"X1"	W24X229
E	BOX 15"X15"X1"	W24X192
F	BOX 15"X15"X0.75"	W24X131
G	BOX 15"X15"X0.75"	W24X117
H	BOX 15"X15"X0.5"	W24X84

Figure 4.1 Configuration of the studied 3-, 9-, and 20-story MRFs.

4.4. Numerical model of moment resisting frames

The finite element software ABAQUS (Simula, 2010) is utilized for the development and analysis of the building models. A 3-step analysis procedure is performed to simulate the post-earthquake fire scenarios in these MRFs. First, the frames are analyzed under gravity loads. Second, ground motion records are applied at the ground and lower levels, if any, to simulate earthquakes using dynamic time-history analysis. Third, thermal-mechanical analysis is conducted to simulate post-earthquake fires and the corresponding stresses. To perform the third step, a transient heat transfer analysis first is conducted to obtain the transient nodal temperatures followed by a mechanical analysis utilizing these nodal temperatures to determine the fire-induced actions and deformations.

As shown in Figure 4.2, using the 9-story frame for illustration, beams and columns are modeled using 1-D line elements. The 1-D line element includes a 2-node heat transfer link (DC1D2) in the transient heat transfer models and a 2-node linear beam element in plane (B21) in the mechanical models. The seismic lumped masses are distributed among the beam to column joints of the MRFs as shown in Figure 4.2. The gravity loads are divided into two parts. First, the gravity loads associated with the MRF are applied as distributed vertical forces along the beams at each story level. Second, the gravity loads associated with the interior gravity frames per tributary area are applied as concentrated loads to the leaning columns at the corresponding story levels, as shown in Figure 4.2. The representation of the gravity frames with the leaning columns is needed to account for the P-Δ effects (Gupta and Krawinkler, 2000). The leaning columns are modeled using truss elements, and are connected to the main MRF at the floor levels using multi-point constraint (MPC) links, as shown in Figures 4.2 and 4.3. These columns are axially stiff and pinned at the basement and floor levels (Figure 4.3); hence, they have no effect on the lateral stiffness of the main MRF.

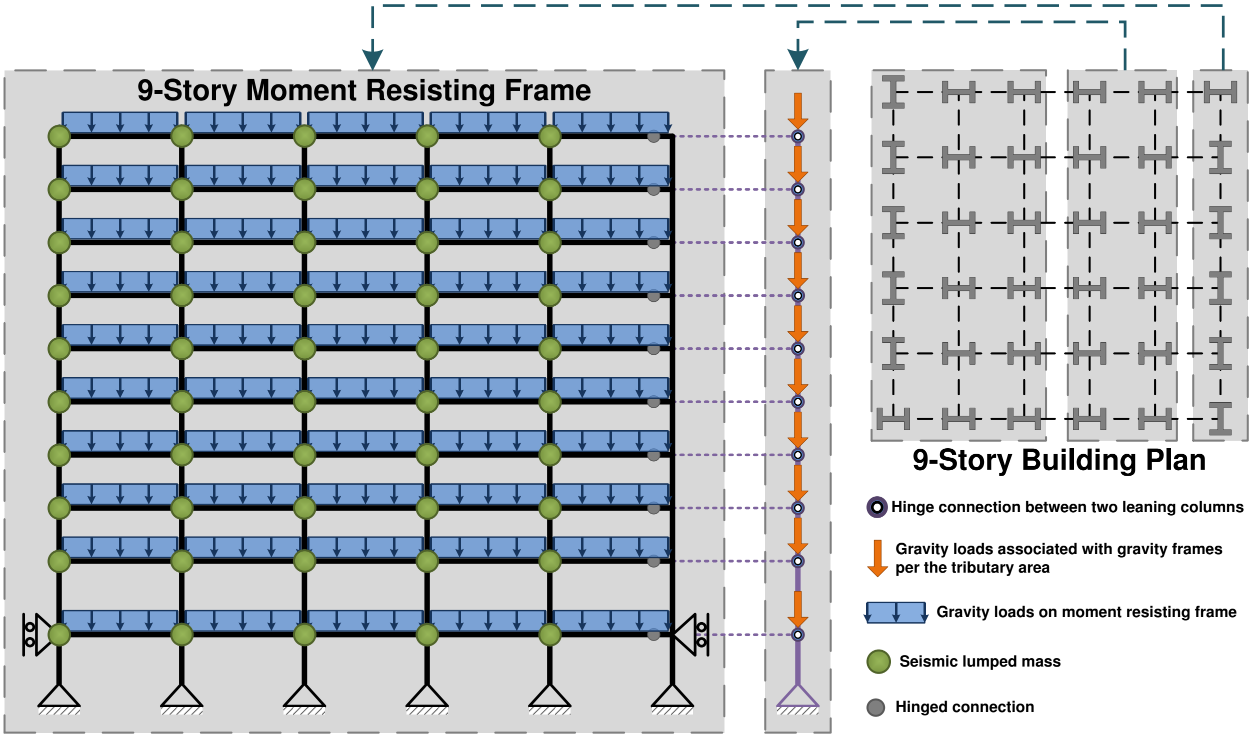

Figure 4.2 Finite element model of the steel MRFs using the 9-story frame for illustration.

Piece-wise reduced beam section connections are employed in all rigid joints of the 2-D MRFs, as shown in Figure 4.3, to create the RBS connection geometry with the proper transition in accordance with FEMA-350 (2000). The scissor model (Figure 4.3) is employed to represent the panel zone at the beam-to-column joints (Charney and Marshall, 2006). It consists of two rigid links, which are hinged at the mid-point, and tied together using a rotational spring with stiffness proportional to the beam and column sizes. The scissor model then is connected to the reminder of the frame by beam connectors, which constrain all 3 degrees of freedom of one node to an adjacent node, as shown in Figure 4.3. In this chapter, the structural steel material, A572-50, with nominal yield strength of 345 MPa is implemented, and its temperature-dependent properties are adopted in accordance with Eurocode 3 (CEN, 2005) discussed in details in chapter 2. In the dynamic analysis, Rayleigh damping is used with 5% viscous damping for the 1st and 3rd modes. In addition, damage initiation is modeled in accordance with the Johnson-Cook ductile damage model discussed in Chapter 2. The schematic temperature-dependent stress-strain curve according to Eurocode 3 (CEN, 2005) and Johnson and Cook (1985) damage model is shown in Figure 2.14.

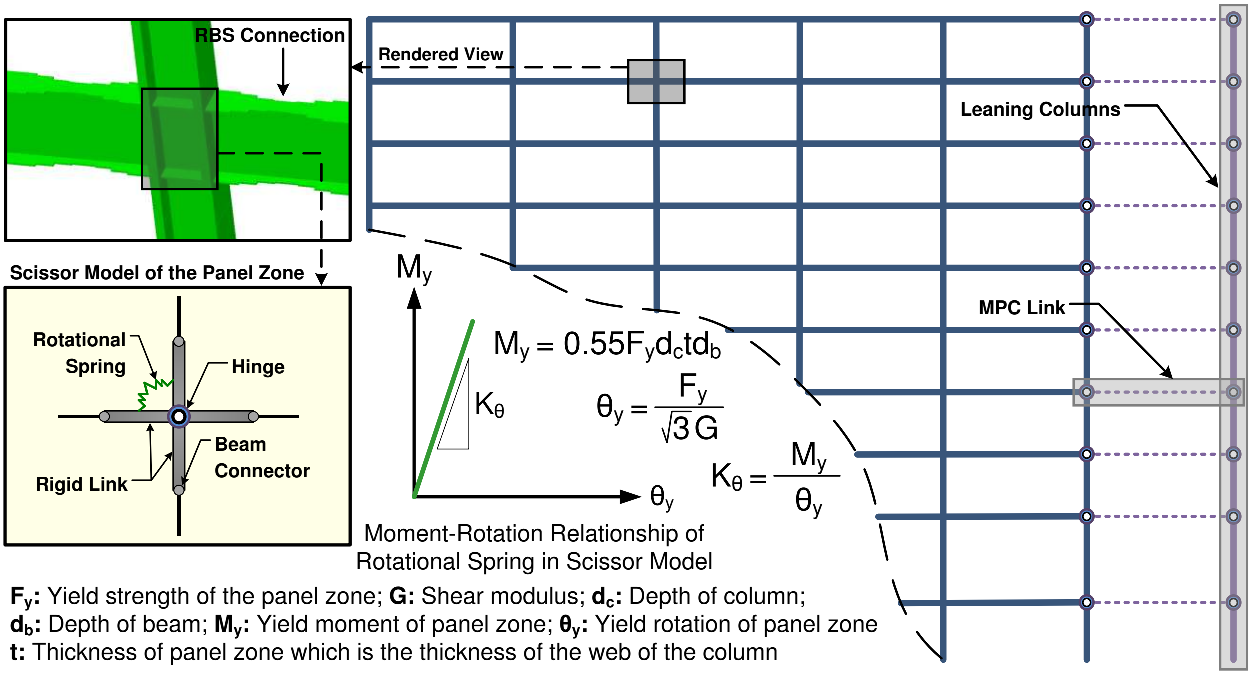

Figure 4.3 Details of the leaning columns, RBS connections, and scissor model.

4.5. Verification of numerical modeling technique

A series of verification analyses are conducted to confirm the modeling approach used in the current finite element analysis. To verify the dynamic characteristics of the studied steel MRFs, an eigenvalue analysis is performed to obtain the first 3 period of vibrations in the 3-, 9-, and 20-story frames, respectively. Table 4.1 shows the obtained periods in the present study in comparison with those obtained by Gupta and Krawinkler (Gupta and Krawinkler, 1999). The minor differences are attributable to the implementation of the RBS connections and the different panel zone model in this study.

Table 4.1 The comparison of period of vibrations for steel MRFs.

	3-Story Frame			9-Story Frame			20-Story Frame		
	1st Mode	2nd Mode	3rd Mode	1st Mode	2nd Mode	3rd Mode	1st Mode	2nd Mode	3rd Mode
Gupta and Krawinkler [24]	1.03	0.33	0.17	2.34	0.88	0.50	3.98	1.36	0.79
Present Study	1.10	0.32	0.15	2.44	0.91	0.51	4.67	1.64	0.96

To validate the thermal-mechanical analysis, a small scale steel frame is chosen (Figure 4.4), which has been previously tested at elevated temperatures by Rubert and Schaumann (1985), and was subsequently analyzed by Lien et al. (2010) and Sun et al. (2012). All structural members are made of European IPE80 I-sections. The structural members of the left bay are uniformly heated using the ISO 834 standard fire curve (CEN, 2002). The validation model included the Eurocode 3 (CEN, 2005) temperature-dependent material properties. Lateral displacements versus temperature at two rigid joints are compared to the experimental results and previous numerical studies. The comparison in Figure 4.4 shows good agreement with the previous experimental and numerical studies and confirms the approach used in this study for simulating the heat transfer and the subsequent structural performance of the steel frames.

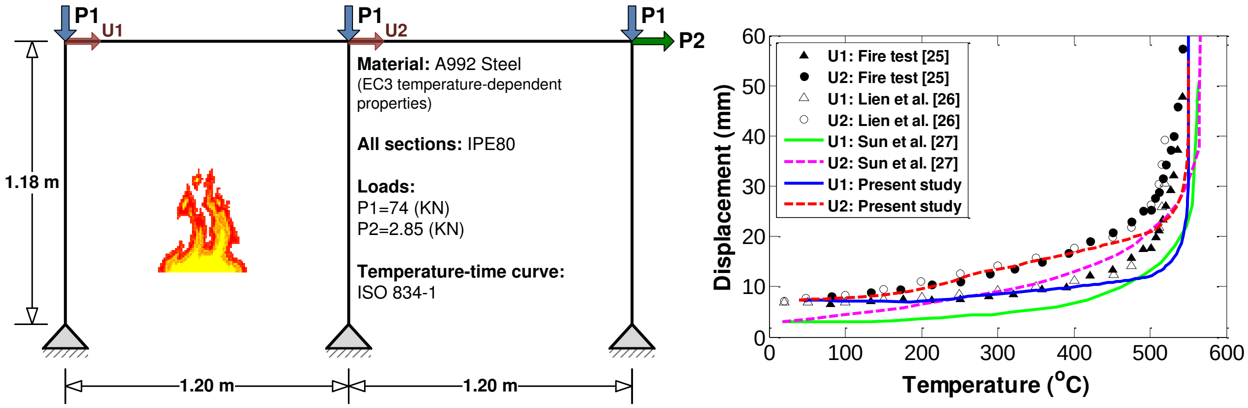

Figure 4.4 The small scale steel frame used in the verification of thermal-mechanical analysis and its corresponding results.

4.6. Earthquake simulations and results

A nonlinear time-history analysis is employed to simulate the earthquakes using a suite of ground motions (summarized in Table 4.2) including 5 near-field and 5 far-field records, selected in accordance with the criteria outlined in FEMA-P695 (2009). The earthquakes were scaled to a target spectral acceleration, Sa, associated with a given code-defined period (T) to remove the expected variability in spectral demand at that given period in the ground motions. To do so, as suggested in FEMA-P695 (2009), individual earthquake records are normalized with respect to peak ground velocity (PGV), and each set of records is collectively scaled to match the median spectral acceleration of the set to the maximum considered earthquake (MCE) response spectrum at the code-defined period of the structure. The MCE response spectrum allows the structure to be assessed based on the collapse prevention performance criterion for a seismic event with a 2% probability of being exceeded in 50 years. The MCE response spectrum, shown in Figure 4.5, is based on the structure being a standard office building located in a region near Los Angeles with site class D as shown. The response spectra of the normalized near-field and far-field earthquake records are also shown in Figure 4.5.

Table 4.2 Near- and far-field set of records used in the present study.

M_W	Year	Earthquake	Station	Distance (km)	PGA_{max} (g)	Scale Factor (-Story Frame)		
			Near Field Records			**3-**	**9-**	**20-**
7.5	1999	Kocaeli	Izmit	5.3	0.22	2.77	2.75	5.16
6.5	1979	Imperial Valley-06	Bonds Corner	6.2	0.76			
6.9	1989	Loma Prieta	Corralitos	7.2	0.51			
6.7	1992	Erzican	Erzican	9	0.49			
6.7	1994	Northridge-01	Rinaldi Receiving Sta	10.9	0.87			
			Far Field Records			**3-**	**9-**	**20-**
6.9	1989	Loma Prieta	Capitola	9.8	0.53	2.10	3.19	4.23
6.7	1994	Northridge	Canyon Country-WLC	26.5	0.48			
6.6	1971	San Fernando	LA-Hollywood Stor FF	39.5	0.21			
7.1	1999	Duzce	Bolu	41.3	0.82			
6.9	1995	Kobe	Shin-Osaka	46	0.24			

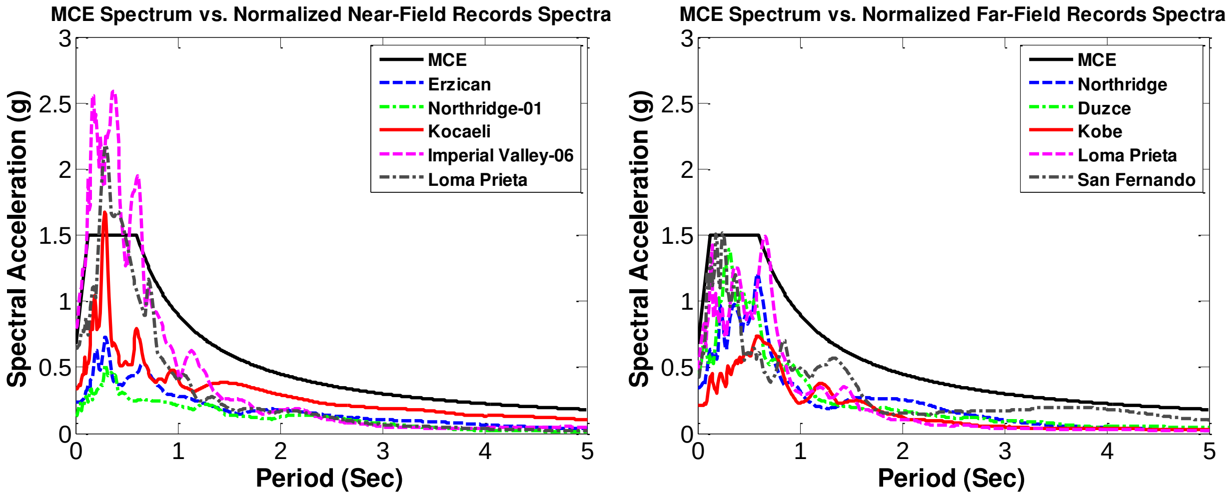

Figure 4.5 The MCE spectrum versus normalized near- and far-field record spectra.

The time-history of roof displacement of all three frames is shown in Figure 4.6 for selected near-field (left-column) and far-field (right-column) earthquake records. The roof displacement responses are characterized by residual deformation and period elongation, which is a result of the damage that is sustained throughout the frame.

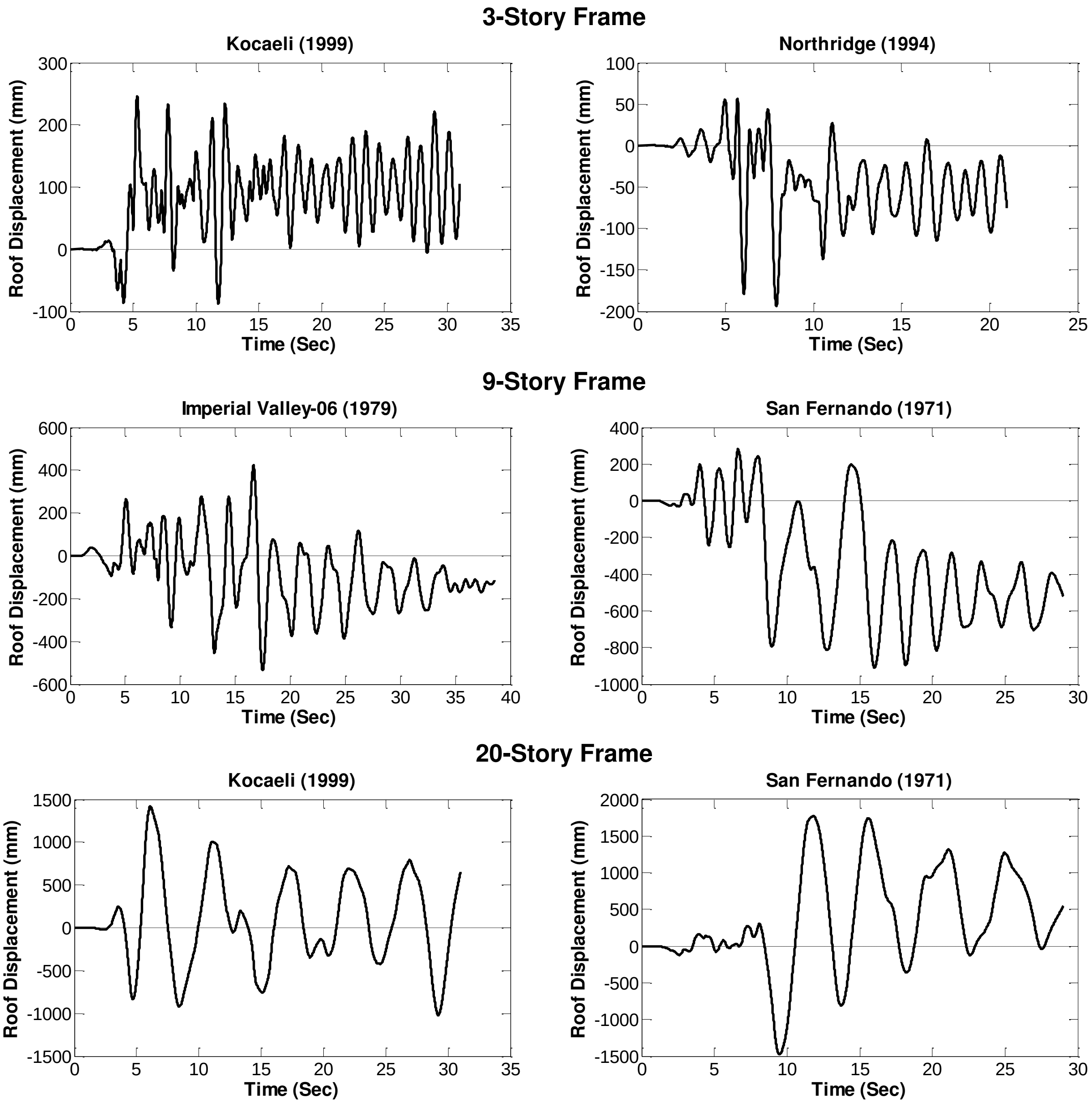

Figure 4.6 Roof displacement versus time in the selected near-field (left-column) and far-field (right-column) earthquakes.

The structural performance of the three frames is evaluated in accordance with ASCE Standard 41-06 (2007) as summarized in Table 4.3. The structural performance is tied to the inter-story drift ratio (IDR). According to ASCE Standard 41-06 (2007), the structural performance level in the steel MRFs is Immediate Occupancy (IO), Life Safety (LS), and Collapse Prevention (CP) when the IDR value is less than 0.7%, 0.7-2.5%, 2.5-5.0%, respectively. As can be seen in Table 4.3, the structural performance level of the steel MRFs is 80% LS and 20% CP. In general, the frames subjected to the near-field records experience higher IDR in comparison with their far-field counterparts.

Table 4.3 The structural performance level of the steel MRFs under 10 selected ground motions.

Ground Motions		3-Story Frame		9-Story Frame		20-Story Frame	
		Inter-story Drift Ratio (%)	Structural Performance Level	Inter-story Drift Ratio (%)	Structural Performance Level	Inter-story Drift Ratio (%)	Structural Performance Level
Near-Field Records Set	**Kocaeli**	2.68	CP	2.41	LS	2.49	LS
	Imperial Valley-06	3.43	CP	2.51	CP	2.54	CP
	Loma Prieta	1.64	LS	2.07	LS	1.77	LS
	Erzican	1.83	LS	2.32	LS	2.32	LS
	Northridge-01	1.08	LS	1.58	LS	1.66	LS
Far-Field Records Set	**Loma Prieta**	2.15	LS	2.22	LS	1.88	LS
	Northridge	1.87	LS	1.61	LS	1.54	LS
	San Fernando	2.48	LS	3.12	CP	4.39	CP
	Duzce	1.23	LS	1.74	LS	1.60	LS
	Kobe	1.73	LS	1.58	LS	1.48	LS

4.7. Post-earthquake fire simulations and results

Time-temperature curve is employed to simulate a realistic fire event in the numerical analyses. The Eurocode parametric fire curve (CEN,, 2002), shown in Figure 4.7, is used in the present study because it has the capability of representing all three different phases in a fire event including an initial heating ramp, a cooling phase, and a constant ambient temperature. As previously mentioned, the ISO 834 (CEN,, 2002) and ASTM E119 (2015) standard fire curves represent the heating phase only, in which the fuel supply is assumed to be inexhaustible. The characteristic cooling phase of Eurocode parametric fire curve (CEN,, 2002) is essential for simulating a realistic fire event since the cooling phase can give rise to large strains. The details of Eurocode parametric fire curve (CEN,, 2002) has been discussed in details in Chapter 2.

Strong ground motions can result in numerous simultaneous post-earthquake ignitions, damage to active and passive fire protection systems within a building, and impaired transportation, water supply, and communication systems, which hinder or prevent professional firefighters in responding promptly in early stages of post-earthquake fires. The combination of some or all of these issues can lead to a catastrophic situation where the post-earthquake fires could grow rapidly and spread to adjacent bays and/or upper/lower stories in buildings.

Current seismic design approaches permit inelastic deformations in the structural elements, which often results in damage to the passive fire protection system and an increase in the vulnerability of the system to fire loading. The tests conducted by Braxtan and Pessiki (2011) indicated that the earthquake-induced damages in the passive fire protection system are concentrated in the beams where plastic hinges are formed at both ends. Therefore, passive fire protection material bonded to the RBS connections where the plastic hinges may form are most vulnerable to earthquake-induced damage. Accordingly, it is assumed that all structural members are fully covered by passive fire protection material, and that the post-earthquake fire penetrates only at the location of the RBS connections at both ends of the beams. This is based on a conservative assumption that all fire protection material at the RBS connections is damaged during the earthquakes.

In accordance with the above discussion, two post-earthquake fire scenarios are considered. These two fire scenarios are applied at one-third and two-thirds the height of the three MRFs starting from the ground level, as shown in Figure 4.7, and are denoted as FFE-1/3H and FFE-2/3H, where FFE is the acronym for Fire Following Earthquake. As shown in Figure 4.7, the FFE-1/3H fire scenario includes the 1st, 1st - 3rd, and 1st - 7th levels in the 3-, 9-, and 20-story MRFs, respectively, while the FFE-2/3H fire scenario includes the 1st - 2nd, 1st - 6th, and 1st - 14th levels in the 3-, 9-, and 20-story MRFs. The fire is applied to all spans of a given story level only at the location of the RBS connections, as noted above. It is believed that the assumed fire scenarios in this study are conservative and were selected to evaluate the performance of steel MRFs subjected to worst case scenario post-earthquake fires. Further analyses on response of steel MRFs to the post-earthquake fires in which asymmetrical distribution of fire should be considered.

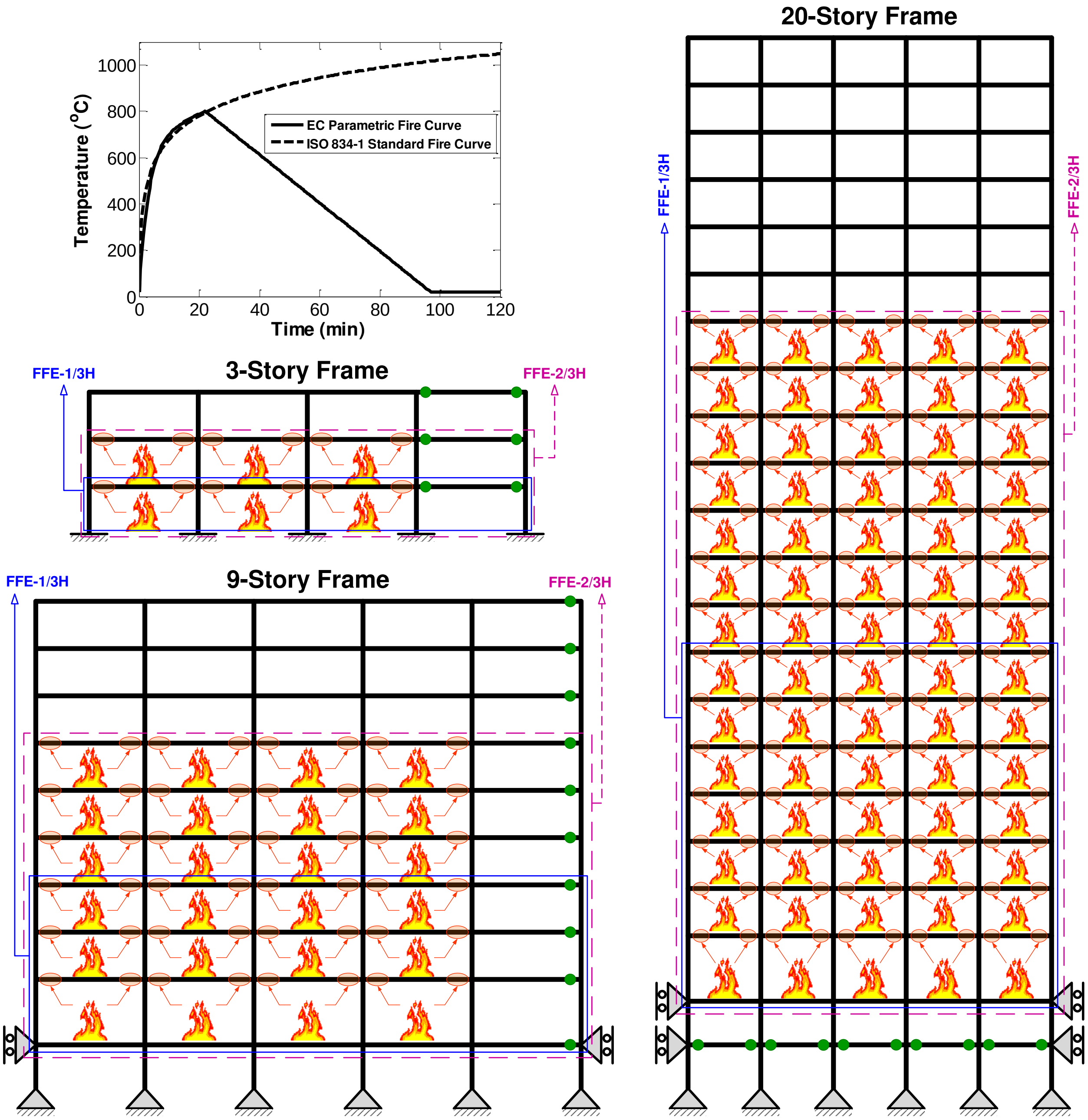

Figure 4.7 The Eurocode parametric fire curve and post-earthquake fire scenarios in all MRFs.

The mechanical effects of the concrete slabs are neglected in the thermal-mechanical analysis based on the findings of Quiel and Garlock (2008), who argued that the slab can be neglected in 2-D stress analysis of frames. Under the assumption of fully composite action between the steel girders and the concrete slabs, the rapid thermal expansion in the steel girders induces large tensile forces in the concrete slabs which cause the concrete to crack. Thus, minimal stresses are carried out by the concrete slabs, and their structural effects become negligible under fire (Quiel and Garlock, 2008).

4.8. Global response of moment resisting frames

The global response of the MRFs is evaluated in terms of the changes in the inter-story drift ratio (IDR). The IDR is selected as an indication of the global stability of the steel frames under earthquakes and two post-earthquake fires. The average of the IDRs at each story level for near-field and far-field records set is calculated and plotted in Figure 4.8. The total average of the IDRs at each story level caused by earthquake records and both post-earthquake fires is plotted next to the corresponding records set, also shown in Figure 4.8. From the figure, it can be concluded that the characteristic of the record, being near-field or far-field, has minimal effect on the resulting IDRs. Another important observation to highlight is that both post-earthquake fire scenarios usually result in smaller IDR when compared to those resulting from the earthquakes. In all stories starting from the second above the highest story subjected to fire, the reduction in the average of the IDRs is largest (60-90%) in all MRFs. In contrast, the change in the average of the IDRs is smallest at the 1st story levels and at one story level above the highest story subjected to the post-earthquake fire. This can be attributed to the fact that the bottom stories are stiffer and their resistance to deformation is larger. Figure 4.8 also shows that stories at which the fire is applied expand and contract together, while the story levels above them do not. Therefore, a significant difference in IDR is developed at the story level above the last story level subjected to the post-earthquake fire.

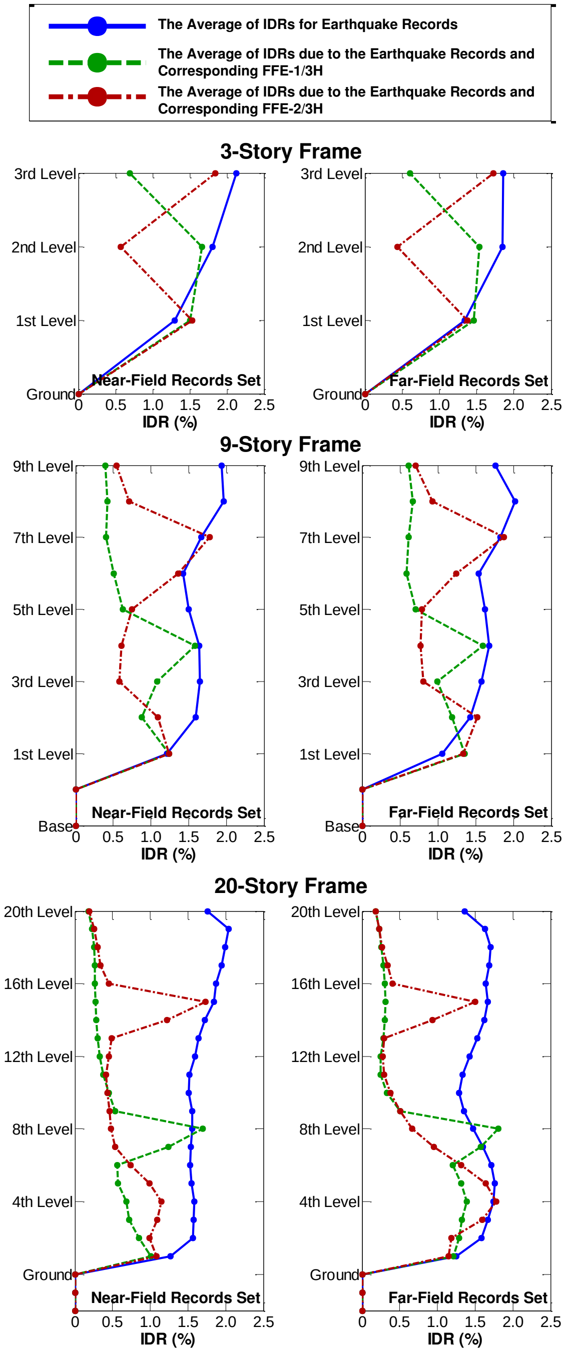

Figure 4.8 The average of IDRs for all near- and far-field sets of records, and their corresponding post-earthquake fires.

The structural performance level of the buildings under the individual earthquakes and both post-earthquake fire scenarios (measured in terms of IDR) is summarized in Figure 4.9.

With few exceptions, the structural performance level of the MRFs under the earthquakes is not affected by the post-earthquake fires. In general, it can be concluded that the global structural performance of the all three buildings is not affected by post-earthquake fire scenarios similar to those implemented in this study, and the potential for systems collapse does not appear to be imminent as a result of these applied post-earthquake fires. However, scenarios which result in asymmetric heating of the frame may give rise to excessive P-Δ effects, leading to the possibility of collapse. Moreover, a localized event such as a failure of a connection, which may trigger a disproportionate collapse, will be briefly investigated in the following sections of this chapter using multi-resolution modeling technique.

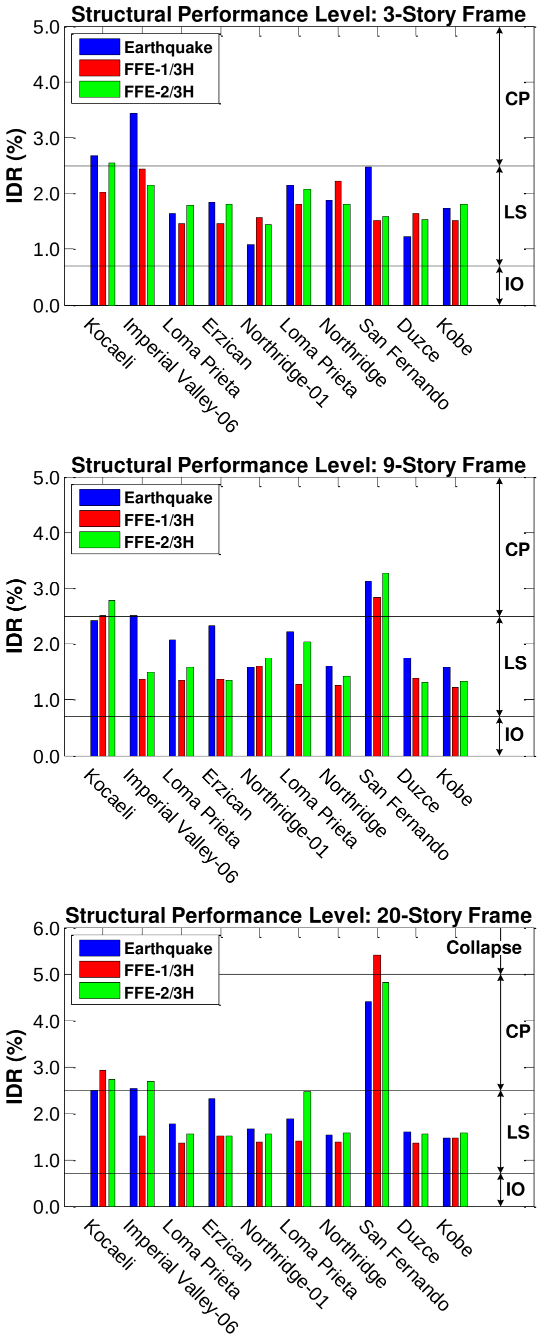

Figure 4.9 The structural performance level of the studied MRFs under the earthquakes and both post-earthquake fire scenarios.

4.9. Response of beams and columns

Large axial forces are developed in the beams during the heating phase and the axial expansion resulted in large moment demands on the columns at both ends of the beams.

Therefore, it is essential to examine the axial force-bending moment interaction for the beams and columns to evaluate their performance during the post-earthquake fires. The axial force-bending moment interaction equation, Eq. 4.1, from Section H of the AISC Specification (AISC, 2010), is applied to selected beams and columns in the MRFs.

$$\frac{P_r(T)}{2P_n(T)} + \frac{M_r(T)}{M_n(T)} \leq 1.0 \quad for \ \frac{P_r(T)}{P_n(T)} < 0.2$$

(4.1)

$$\frac{P_r(T)}{P_n(T)} + \frac{8}{9}\frac{M_r(T)}{M_n(T)} \leq 1.0 \quad for \ \frac{P_r(T)}{P_n(T)} \geq 0.2$$

where, $P_n(T)$ is the nominal compressive or tension strength as a function of temperature, and $M_n(T)$ is the nominal flexural strength. Details on the calculation of $P_n(T)$ and $M_n(T)$ can be found in AISC Specification (AISC, 2010). Moreover, $P_r(T)$ and $M_r(T)$ are the required axial compressive or tension force and bending moment, respectively, in the structural members as a function of temperature.

The most critical interaction points for the highlighted beams in the MRFs are plotted for the two post-earthquake fires as shown in Figures 4.10-4.12. The most critical interaction points are identified along the length of the highlighted beams with the highest axial force-bending moment interaction value. Since the beams are subjected to both compressive and tension forces during the post-earthquake fires, both tension axial force-bending moment (T-M), and compressive axial force-bending moment (C-M) interactions are considered separately, as shown on the Y-axes of Figures 4.10-4.12. Several important conclusions can be drawn from these plots. First, most of the interaction points coincide with each other regardless of their prior near-field or far-field earthquake history. Second, most of the T-M interaction points satisfy Eq. (4.1) and only a limited number are located slightly outside the interaction curve. This shows that the tension forces developed during the cooling phase are insignificant with respect to beam behavior.

On the other hand, the C-M interaction points vary depending on the fire scenario and frame height. As can be seen in Figures 4.10-4.12, under the FFE-1/3H scenario, the C-M interaction points of the selected beams are not within the boundaries of the interaction equation for all frames. However, in the FFE-2/3H scenario, all interaction points fall within the interaction equation limit in the 9- and 20-story MRFs (Figures 4.11 and 4.12), but not for the 3-story MRF (Figure 4.10). This is because the relative stiffness of the low-rise 3-story frame is relatively larger than that of the medium- and high-rise MRFs, which results in large axial forces. Therefore, in this low-rise frame, the C-M interaction points fall outside of the interaction equation limit and appear to be independent of the post-earthquake fire scenarios.

It should be noted that the selected beams in the three MRFs where the C-M interaction is investigated are located at the top story level subjected to the FFE-H1/3 scenario. The RBS connections of these beams are directly exposed to the elevated temperatures in both post-earthquake fires. However, the story above the selected beams is not exposed to fire in the FFE-1/3H scenario. In such cases, the temperature difference between the story level of the selected beam and one story level above resulted in large axial compressive forces in the beam. In contrast, in the FFE-2/3H scenario, the selected beams are directly exposed to fire and the story level of the selected beam and one story level above and underneath are expanding and contracting together; as a result, only insignificant axial compressive forces were developed in the selected beam. Finally, in most cases the behavior of beams is dominated more by the axial compressive force than by tensile force. In other words, the analysis and design of the beams subjected to the post-earthquake fires can be performed based on the axial compressive forces-bending moment interaction developed in the beams in accordance with the AISC Specification (AISC, 2010).

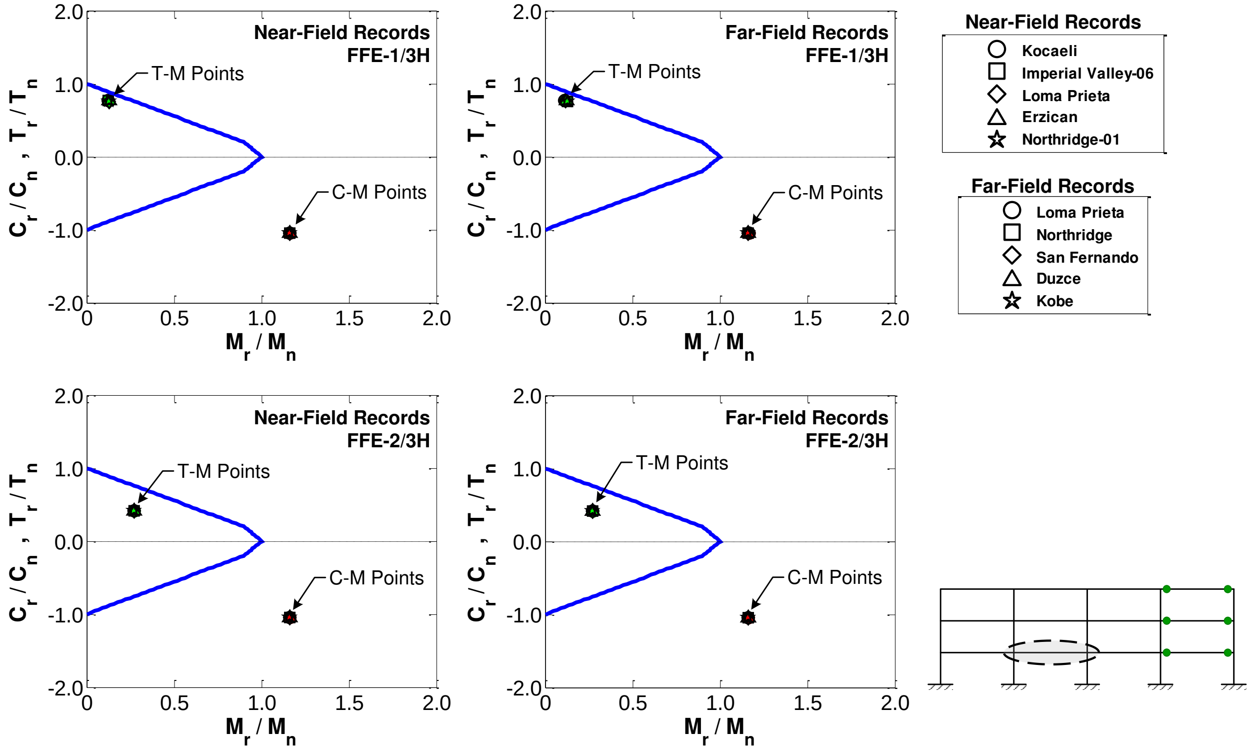

Figure 4.10 The most critical interaction points for the highlighted beam in the 3-story MRF.

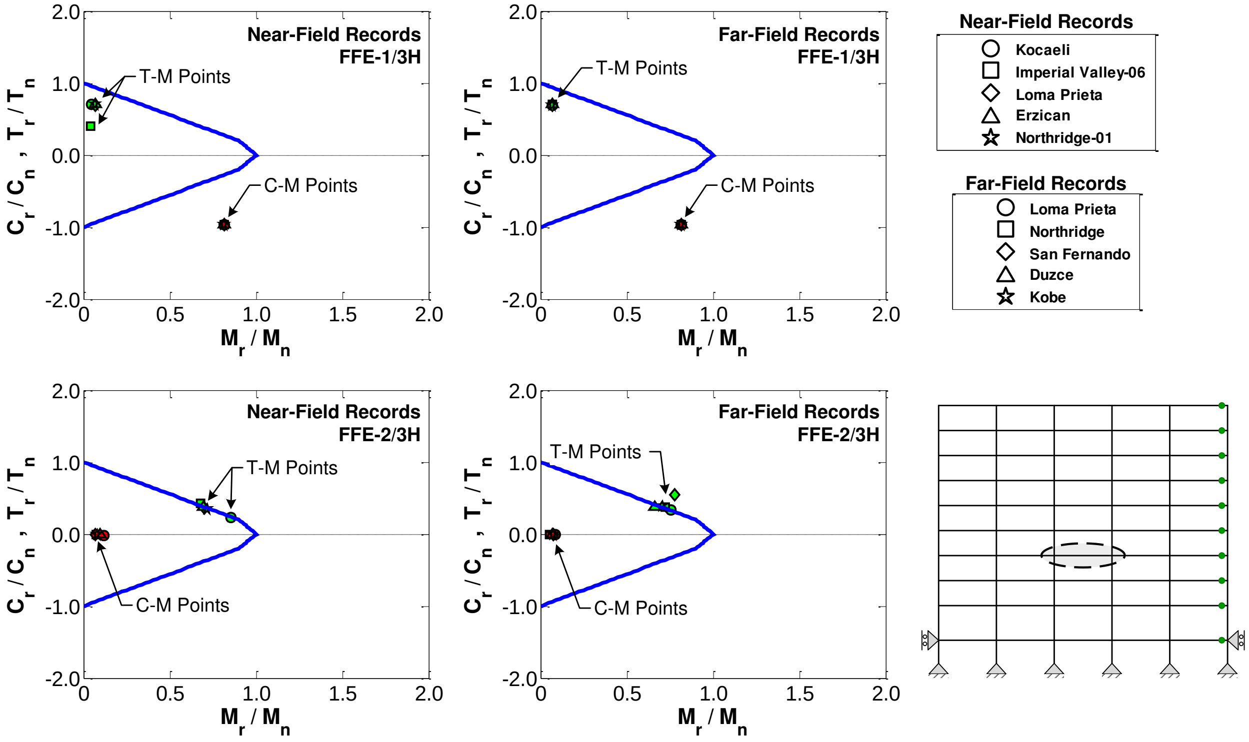

Figure 4.11 The most critical interaction points for the highlighted beam in the 9-story MRF.

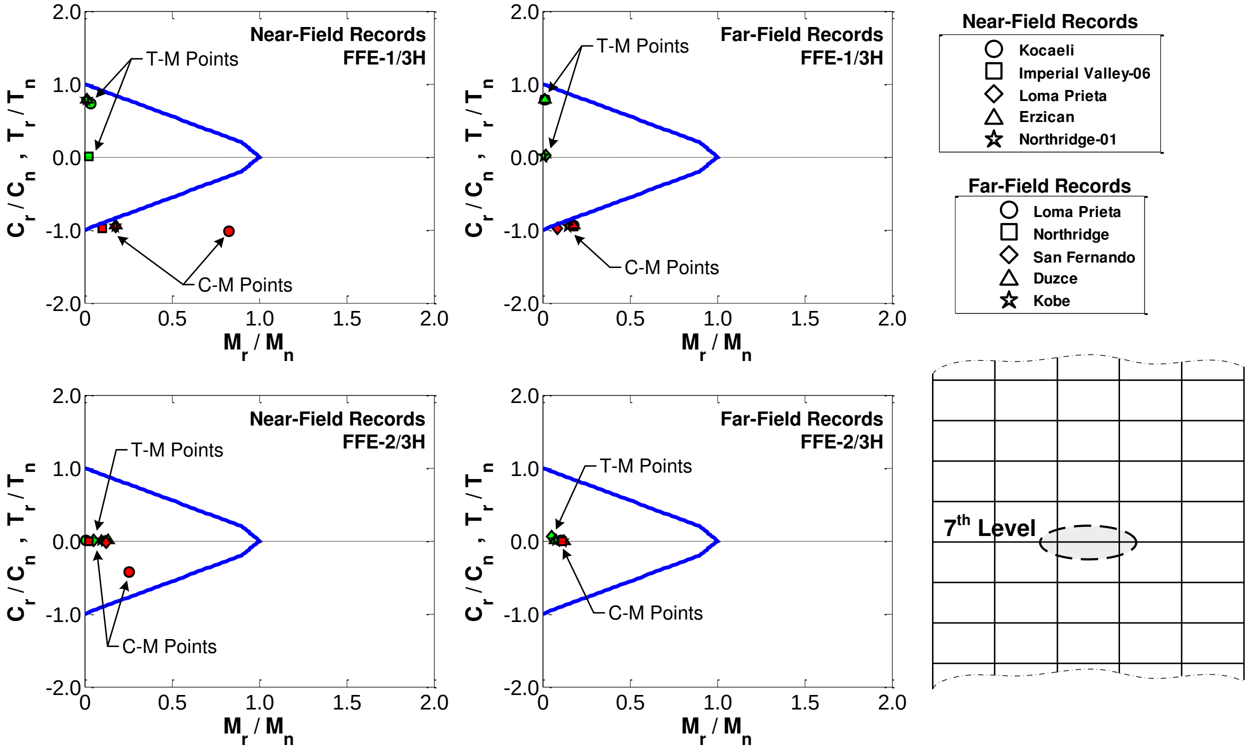

Figure 4.12 The most critical interaction points for the highlighted beam in the 20-story MRF.

The interaction points for several highlighted columns in the steel MRFs are shown in Figures 4.13-4.15. These plots include the most critical interaction points under near-field and far-field records, and both post-earthquake fires. The columns are selected because they have the largest compressive axial force due to gravity load and are also directly subjected to the post-earthquake fires. In some cases, the interaction points do not fall within the limit of the interaction equation during the earthquakes for the 3- and 20-story MRFs, as shown in Figure 4.13 and 4.15, respectively.

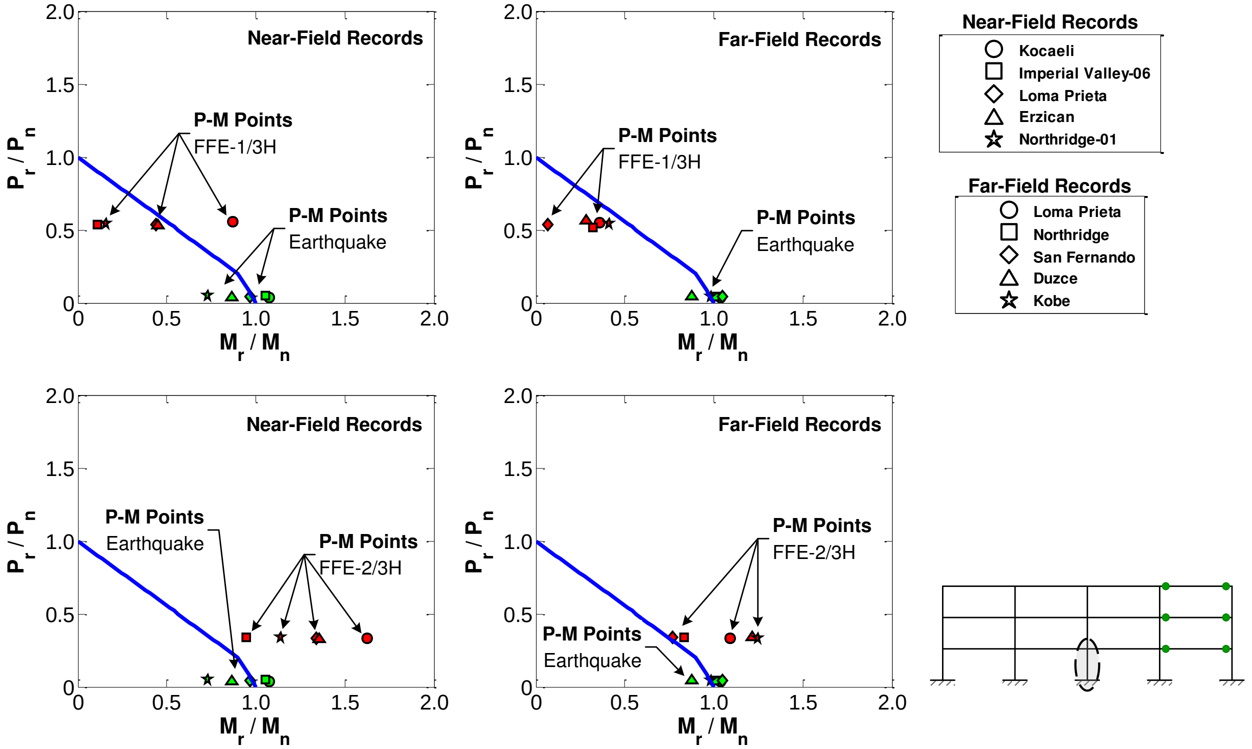

Figure 4.13 The most critical interaction points for the highlighted column in the 3-story MRF.

In general, the bending moment rather than the axial force, dominates the behavior of these columns during the earthquakes. In most cases, the interaction points in both post-earthquake fires lie significantly outside the interaction equation limit, especially the points for the 9- and 20-story MRFs, as shown in Figure 4.14 and 4.15. This is a result of an increase in the axial compressive force and bending moment experienced by the columns. For the 3-story frame, the increase in the bending moment is less than that of the 9- and 20-story MRFs because the lateral deformations developed in the 3-story MRF during both post-earthquake fires is relatively small.

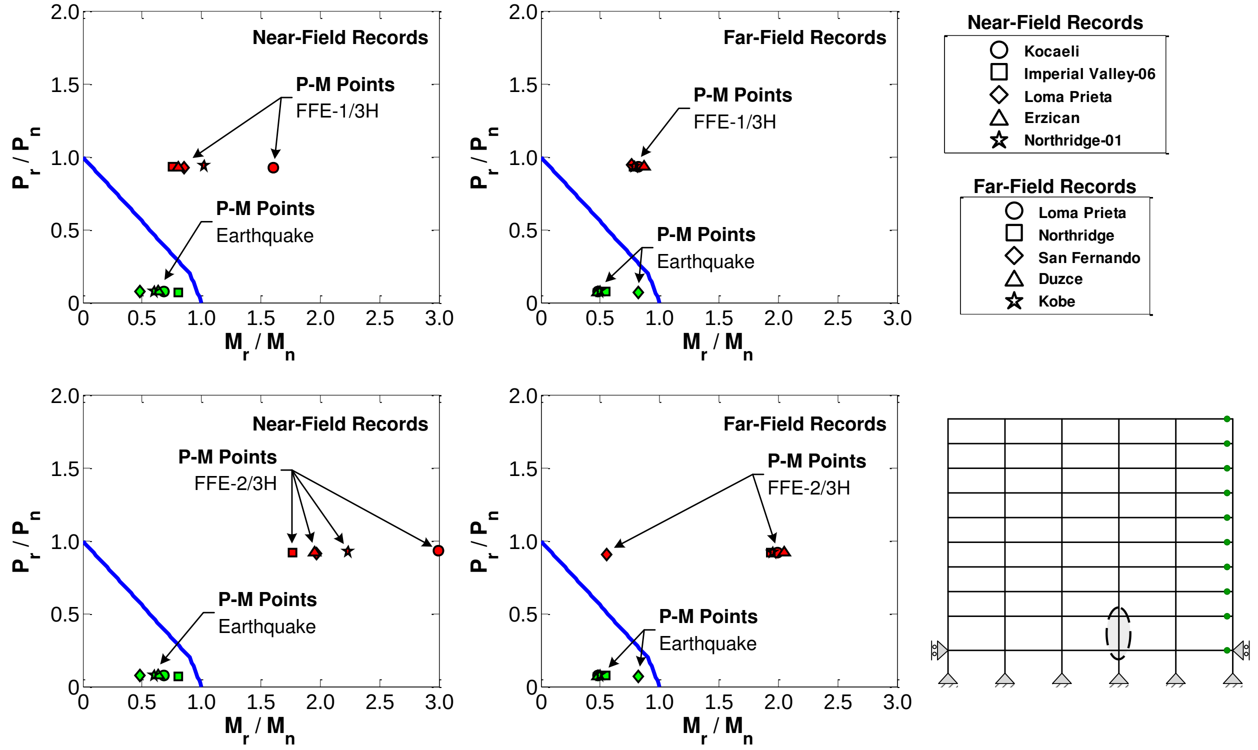

Figure 4.14 The most critical interaction points for the highlighted column in the 9-story MRF.

Most of the critical interaction points are horizontally spread in the plots of Figures 4.13-4.15 (except two points in both post-earthquake fires followed by the Kocaeli earthquake in the 20-story frame), suggesting that the axial compressive forces developed in the columns during the post-earthquake fires are independent of the earthquake history. On the other hand, the horizontal distribution of the critical points shows that the bending moments developed in the columns depend on the earthquakes history. Therefore, it can be concluded that, in columns, the different earthquake histories result in different responses to the post-earthquake fires.

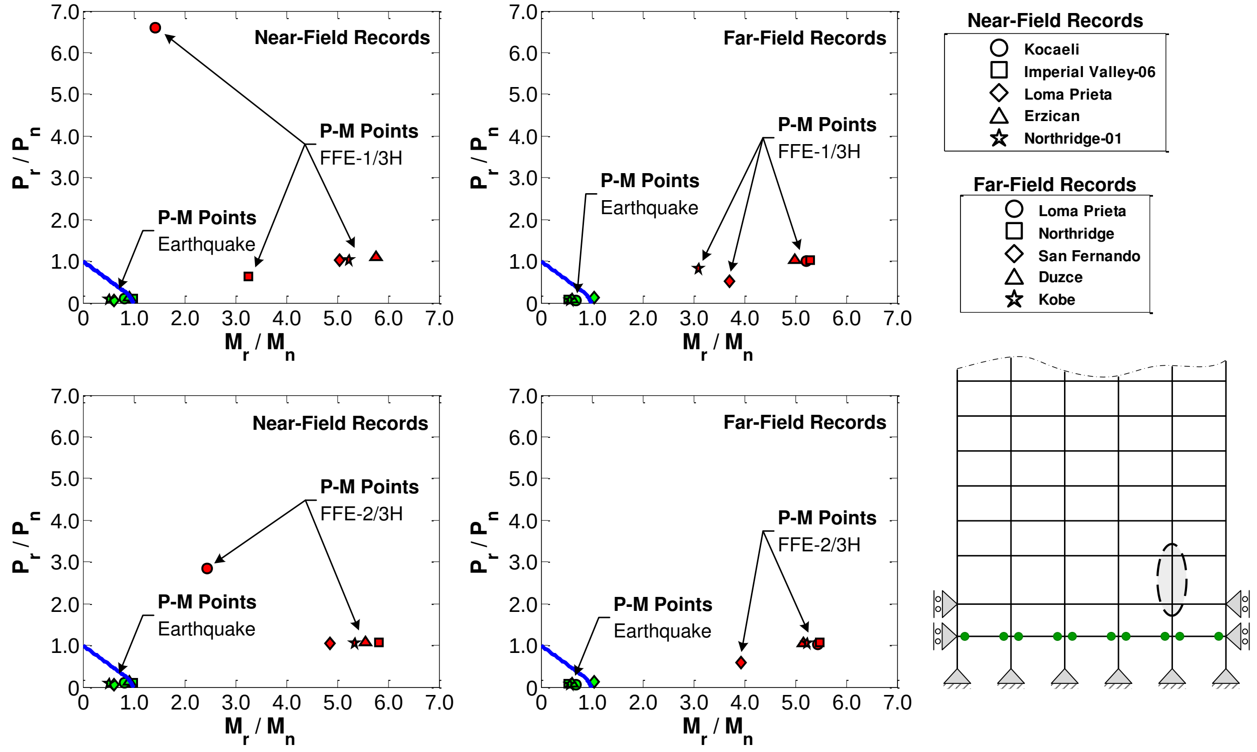

Figure 4.15 The most critical interaction points for the highlighted column in the 20-story MRF.

4.10. Response of reduced beam section connection to post-earthquake fire

The Reduced Beam Section (RBS) connection is a post-Northridge earthquake connection extensively designed and constructed in the moment-resisting frames in seismically active areas. The cut portion of the beam flange results in the formation of plastic hinge at the location of reduced section under seismic loads, where is far from the face of column flange. Thereafter, lower demand develops in the beam-to-column complete joint penetration weld (CJP) connection. Although extensive experimental tests have indicated that welded RBS connections have acceptable performance under large inelastic loads; however, performance of this type of connection has not been fairly well addressed under fire loading in the past. Furthermore, it is essential to assess their response under fire loads after residual damages caused by earthquake loads. Reduction in the load-carrying capacity, unpredicted lateral-torsional buckling, and local buckling in the reduced section under combined high rotational and axial demands are a part of the uncertainties. In the present section, an exterior connection at the 1st level of the 3-story and the ground level of the 9- and 20-strory frames is analyzed in details under a post-earthquake fire scenario to evaluate their local behavior. The details of geometry and dimensions of the selected RBS connections have been shown in Figure 4.16.

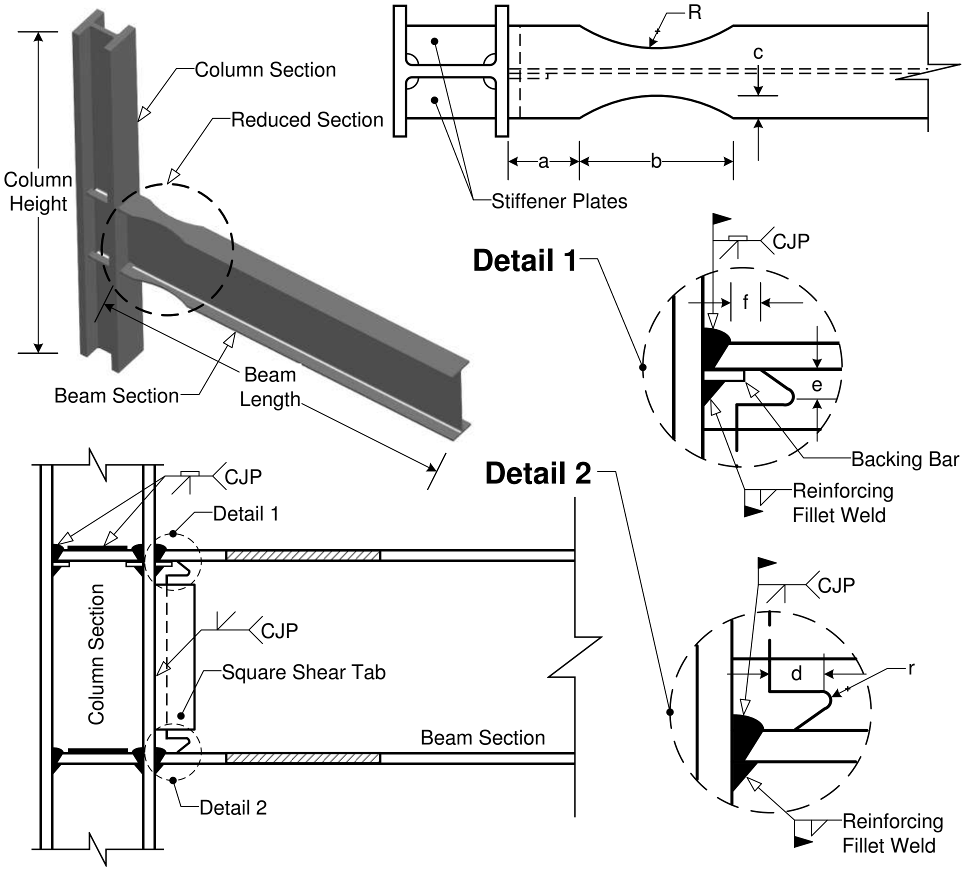

Dimensions of the Studied RBS Connections*

Frame	Beam Section	Column Section	a	b	c	R	d	e	f	r
3-story	W33X118	W14X257	175	704	58	1088	69	19	28	13
9-Story	W36X160	W14X370	183	686	76	810	76	26	26	9
20-Story	W30X99	BOX15X15X2	160	569	53	785	51	17	17	13

***All Dimensions are in mm.**

Figure 4.16 The details of geometry of selected RBS connections.

To evaluate the local behavior of the selected RBS connections under earthquake loads and also capture stiffness and strength degradation of the surrounding frame due to post-earthquake fire loads, a multi-resolution numerical model of the MRF systems is created as illustrated in Figure 4.17. The selected RBS connections are modeled using solid elements while the remainder of the frames is modeled by line elements. This allows for the natural inclusion of the effect of the surrounding structure on the response of RBS connections under post-earthquake fire loads. The 3-D connections are extended to the mid-span and mid-height of the corresponding beam and column, respectively. In the transient heat transfer analysis, 8-node linear continuum heat transfer elements (DC3D8) are applied to the 3-D solid elements of RBS connections from ABAQUS elements library (Simula, 2010). In the mechanical analysis, 8-node linear continuum reduced integration elements (C3D8R) are employed for 3-D solid elements. Furthermore, MPC connector, type TIE, is used to connect the thermal degree of freedom (NT11) in the line elements to the solid elements in the transient heat transfer model. In the mechanical model, MPC constraint, type BEAM, is implemented to constraint all transitional and rotational degrees of freedom in the line elements to the solid elements. The remainder of the MRFs has the same geometry and details as explained in the line element models. The identical temperature-dependent material properties and damage model are also employed in the 3-D model of the RBS connections.

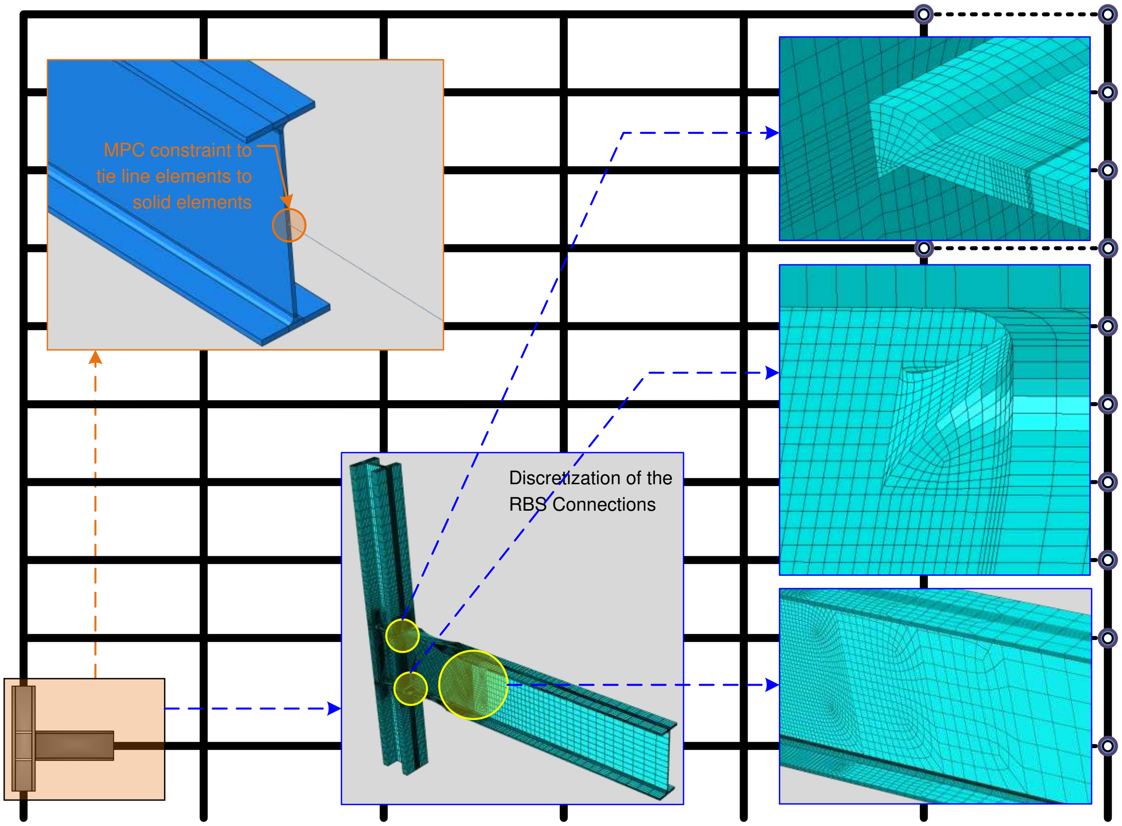

Figure 4.17 The details of multi-resolution modeling technique.

A mesh convergence study is performed on the 3-D RBS connections to satisfactorily balance in accuracy and computational intensity of the models regarding the critical zones, i.e. complete joint penetration (CJP) welds, welding access holes, and reduced portion of the beam. The mesh size is also gradually increased as the distance from the critical zones increases using various mesh techniques available in ABAQUS. The multi-resolution numerical configuration of the studied frames and some details of the finite element models are shown in Figure 4.17 using 9-story frame for illustration.

The 3-D RBS connection is required to be braced to prevent out of plane rotation, particularly under inelastic behavior, in accordance with the AISC Seismic Provision (AISC 341-10, 2010). The effect of the concrete slab on the lateral bracing of the top flange in the 3-D beam is considered, and appropriate out of plane boundary conditions are applied to restraint lateral-torsional buckling in the bottom flange with respect to the AISC 341-10 (AISC 341-10, 2010).

The multi-resolution MRFs are subjected to two selected earthquake records to determine the residual damage state of the RBS connections at the end of the earthquakes. At the conclusion of the seismic analysis, the fire load is applied on both top and bottom flanges of the reduced portion of the beam according to the analogy discussed earlier in this chapter, which assumes earthquake-induced damage to passive fire protections in the reduced section leaves the bare body of steel material exposed to elevated temperatures. The residual deformations and stresses at the end of the two selected earthquake records in the RBS connections of the 3-, 9-, and 20-story MRFs are shown in Figures 4.18-4.20, which are the initial state of connections prior to the post-earthquake fire simulations. The temperature, deformation and von Mises stress distribution along the RBS connections of all MRFs at peak and end of post-earthquake fire curve are also shown in Figures 4.18-4.20.

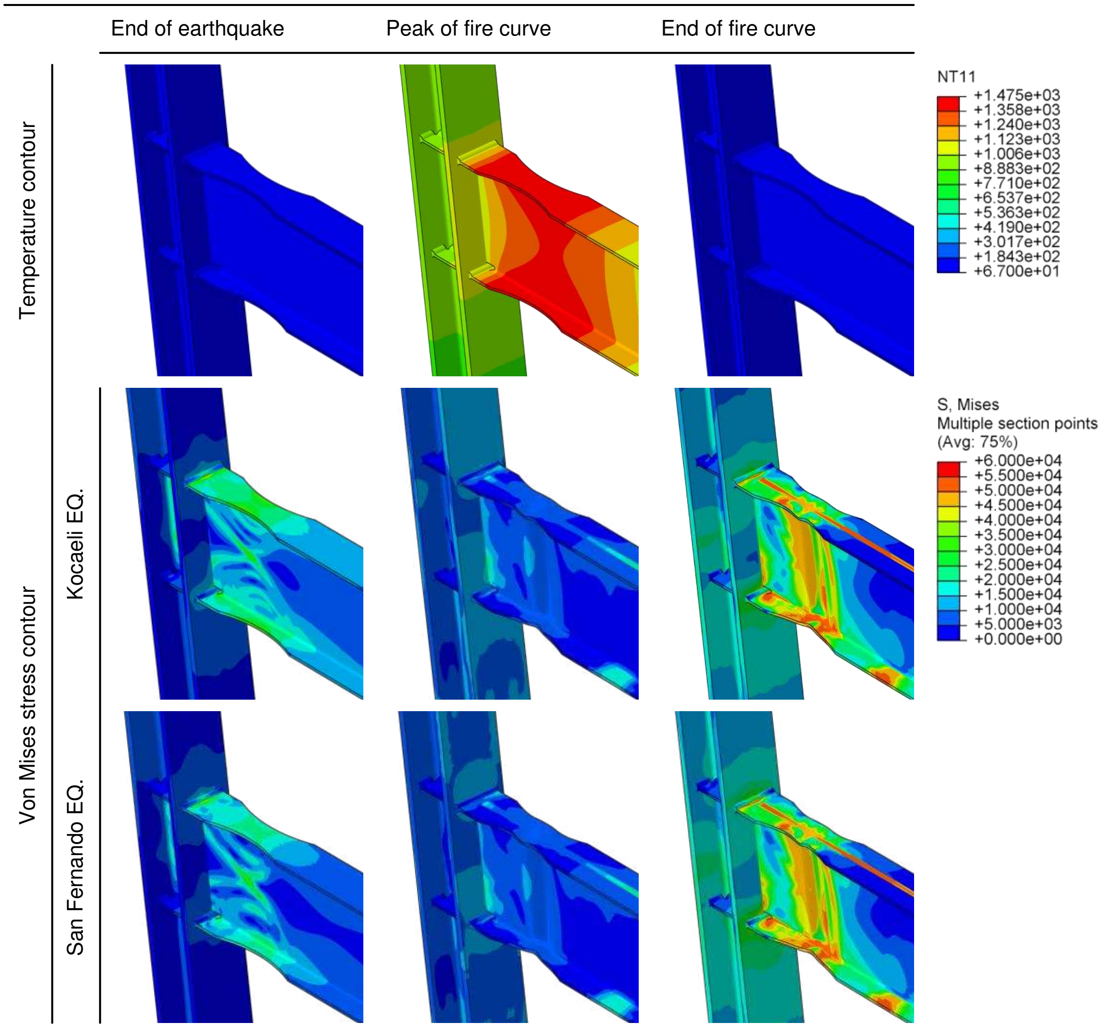

Figure 4.18 The deformation and von Mises stress distributions in the RBS connection of 3-story frame.

As shown in Figures 4.18-4.20, the residual deformations and stress history resulting from the earthquake has significant effects on the response of RBS connections to post-earthquake fire loads. In the RBS connection of the 3-story MRF, the residual deformation and stress under both Kocaeli and San Fernando earthquakes are very similar according to Figure 4.18. Therefore, the local behavior of the connection regarding stress distribution and deformation is almost identical at peak and end of the post-earthquake fire load.

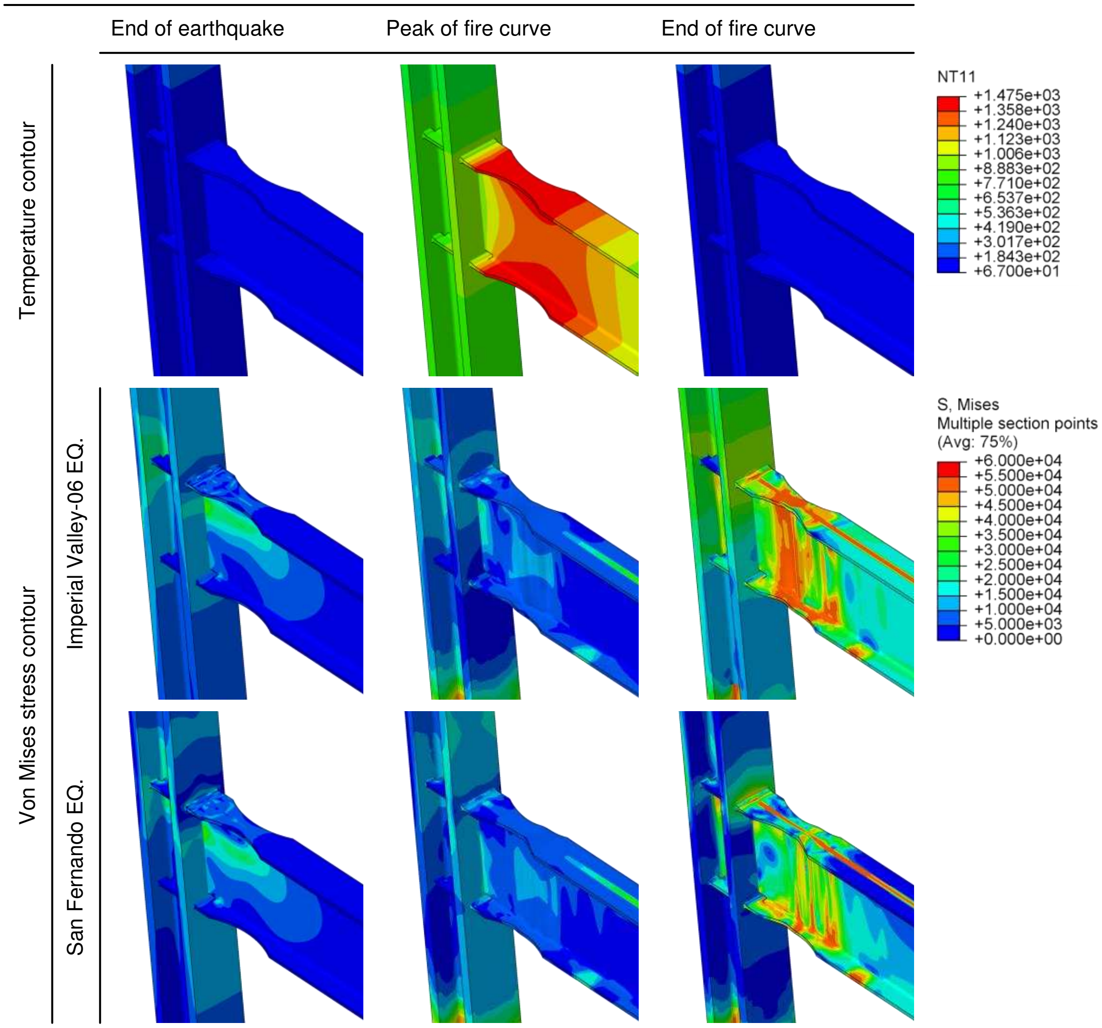

Figure 4.19 The deformation and von Mises stress distributions in the RBS connection of 9-story frame.

The residual deformation and stress distribution in the RBS connections of the 9- and 20-story MRFs is not similar at the end of the earthquake simulations. Hence, completely different local behavior is observed at peak and end of the post-earthquake fire load. Furthermore, Figures 4.19-4.20 show that significant local buckling occurs in both top and bottom reduced flanges along with web at their location under post-earthquake fire load. This can be attributed to the fact that large compressive axial forces are developed in the beams during post-earthquake fire. In addition, very high von Mises stress is concentrated in the flanges and web at the location of reduced section.

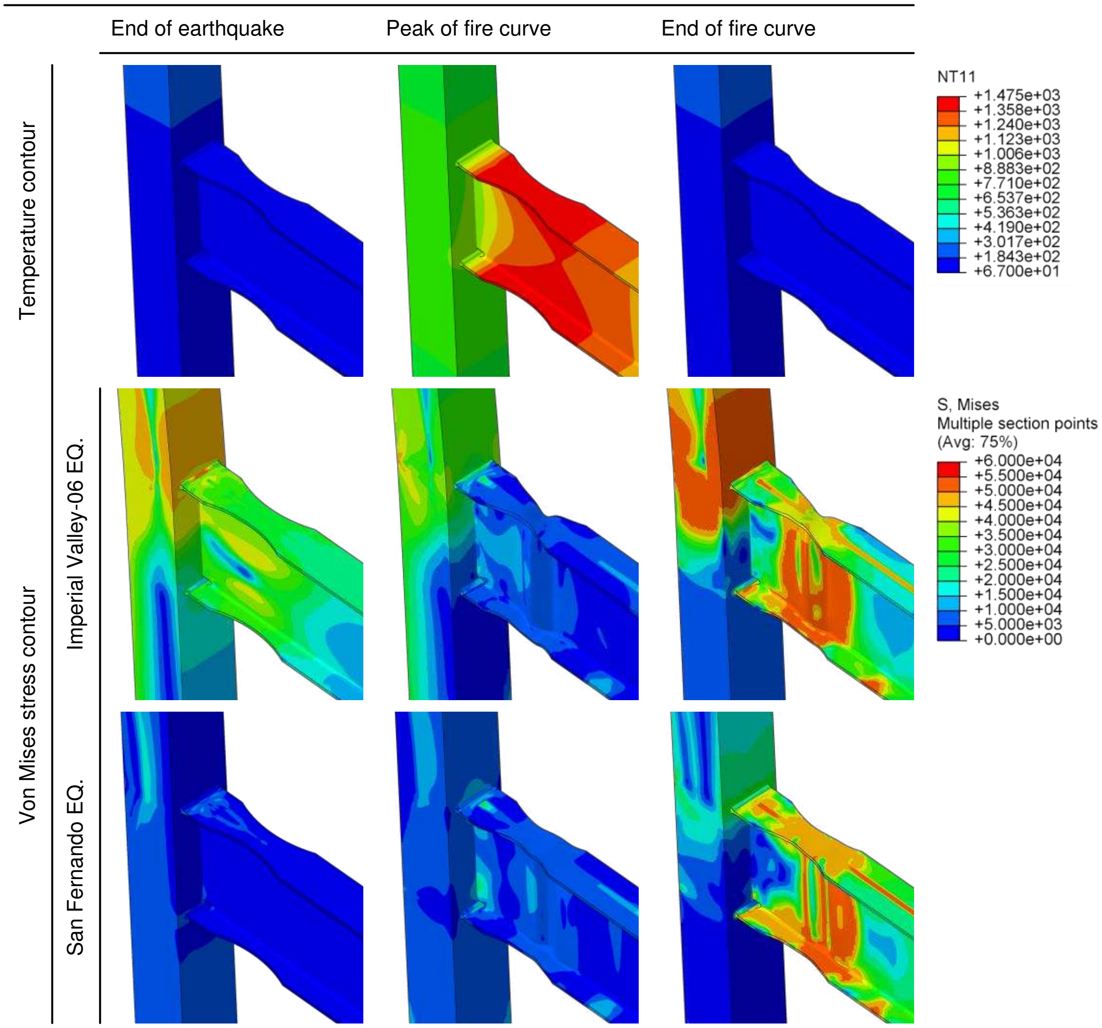

Figure 4.20 The deformation and von Mises stress distributions in the RBS connection of 20-story frame.

It is also observed in Figures 4.18-4.20 that large von Mises stresses are also developed at the location of top and bottom complete joint penetration (CJP) welds in flanges, the interface of beam web and column face, and welding access holes. Figure 4.21 shows all of these critical points in the RBS connection with their corresponding abbreviation. A simple analysis indicates that history of residual stresses caused by earthquake loads affects the response of the RBS connection under post-earthquake fire load. This is illustrated in Figures 4.22-4.24 for 3-, 9-, and 20-story MRFs, respectively, showing residual von Mises stresses at the end of earthquake, its maximum at some point during the fire load, and at the end of the fire curve for the critical details.

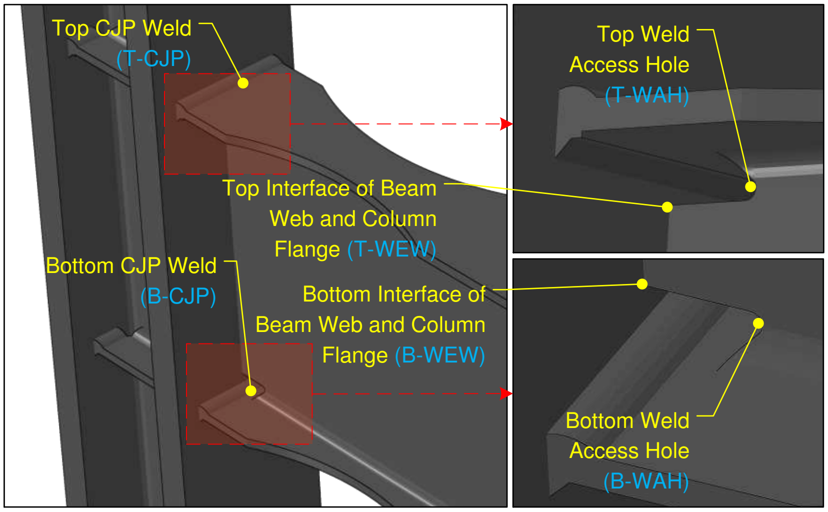

Figure 4.21 The critical spots of RBS connection.

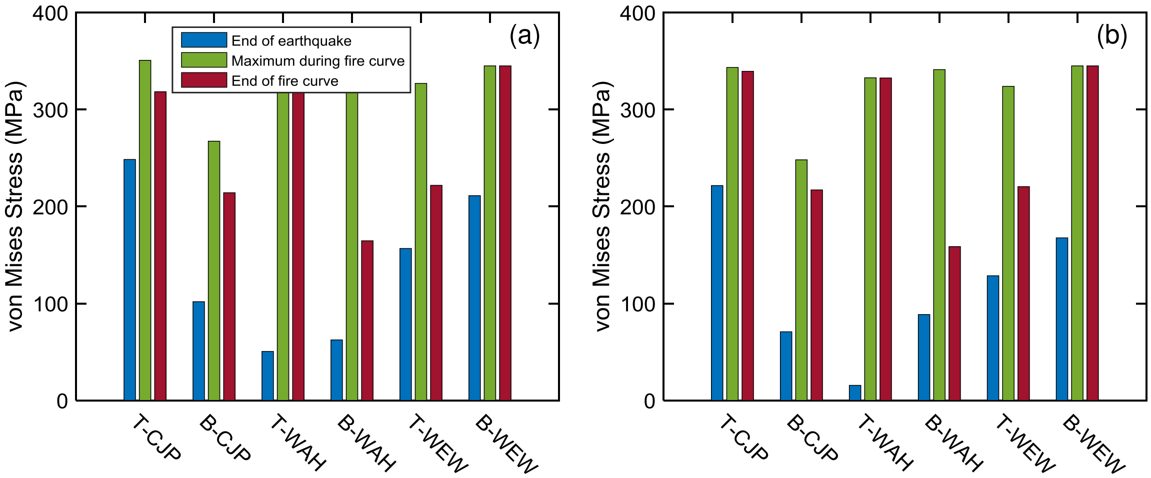

Figure 4.22 The history of von Mises stress in critical spots of RBS connection in the 3-story MRFs following (a) Kocaeli (b) San Fernando earthquakes.

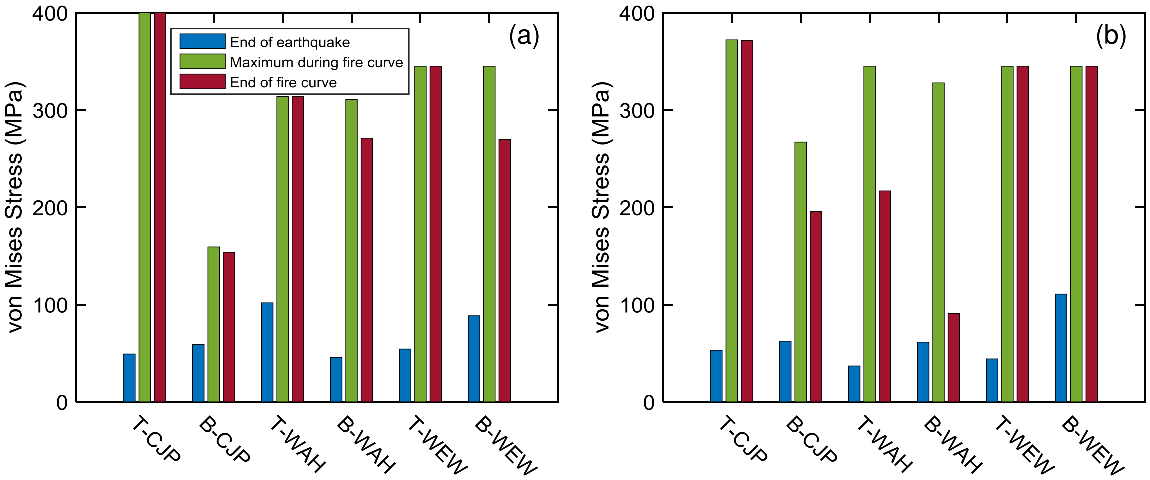

Figure 4.23 The history of von Mises stress in critical spots of RBS connection in the 9-story MRF following (a) Imperial Valley-06 (b) San Fernando earthquakes.

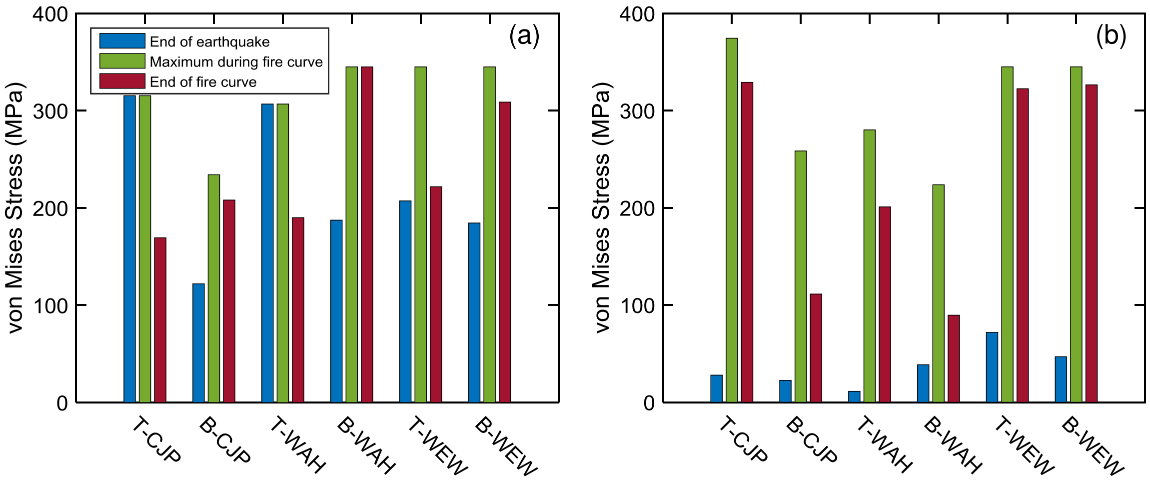

Figure 4.24 The history of von Mises stress in critical spots of RBS connection in the 20-story MRF following (a) Imperial Valley-06 (b) San Fernando earthquakes.

4.11. Summary

This chapter summarizes an investigation of the performance of low-, medium-, and high-rise steel MRFs with RBS connections subjected to fire following earthquake scenarios, providing insight on the performance of steel moment resisting frames with RBS connections under the combined hazards of earthquake and fire. Examination of previous studies on MRFs under earthquake provides a good opportunity to extend the early findings on the seismic response of these frames to include post-earthquake fire behavior. The analysis in this study under fire following earthquake was conducted using nonlinear dynamic time-history analysis followed by a sequentially uncoupled thermal-mechanical analysis. Temperature-dependent mechanical, deformational, and thermal properties were taken into account in accordance with Eurocode 3 (CEN, 2005). The Eurocode parametric fire curve was implemented to simulate post-earthquake fire loading. The fires were applied to the RBS connections under the assumption that the fireproofing was damaged during the earthquakes because of the large concentration of inelastic demands in the connections. Failure was defined in terms of the ASCE Standard 41-06 performance limits; however, failures in the connections were not considered. Although the analysis provided valuable insight on the behavior under the combined hazards, limitations in the analysis are in the inability to capture all possible failure modes in the actual structural components including for example local buckling due to the use of 1-D line elements. Moreover, complete damage to the passive fire protection system, due to the earthquake excitations, was assumed in this study, which would lead to overestimated demands on the steel elements. Therefore, the authors recommend further studies on earthquake-induced damages of structural members and passive fire protection system for the development of more representative numerical models.

The following conclusions can be drawn from the analyses:

Global Response:

- The nonlinear dynamic time-history analysis resulted in LS structural performance level in 80% and CP performance level in 20% of the ground motions in all steel MRFs.

- Both post-earthquake fires mostly resulted in smaller IDRs when compared to those resulting from the earthquakes.
- In general, the global structural performance level of the all three MRFs is not affected by post-earthquake fire scenarios similar to those considered in this study, regardless of the characteristic of the record, being near-field or far-field for the given fire scenarios.
- In all stories starting from the second above the highest story subjected to fire, the reduction in the average of the IDRs is largest in all MRFs.
- The change in the average of the IDRs is smallest at the 1st story levels and at the story level immediately above the highest story subjected to the post-earthquake fire.

Local Behavior:

- The axial force-moment interaction points for the selected beams coincide with each other regardless of the prior earthquake, except for a limited number of interaction points.
- The tension forces developed in the highlighted beams during the cooling phase of fires were insignificant.
- In the selected beams of all MRF, the C-M interaction points are outside the interaction equation limit under FFE-1/3H.
- In the highlighted beams of all MRF, the C-M interaction points mostly fall within the interaction equation limit for the medium- and high-rise frames, but not for the low-rise frame under FFE-2/3H.

- The behavior of the highlighted beams was dominated by the axial compressive forces as opposed to the tensile force.
- The design of the beams subjected to the post-earthquake fires can be performed based on the axial compressive forces-bending moment interaction developed in accordance with the AISC Specification.
- The interaction points for the selected columns in both post-earthquake fires are mostly located outside the interaction equation limit.
- The axial compressive forces developed in the highlighted columns during the post-earthquake fires are independent from the earthquake history.
- The response of the selected columns is mostly dominated by the bending moments and the response during the post-earthquake fires depends on the earthquake history.
- The residual deformations and stress history resulting from the earthquake had significant effects on the response of RBS connections to post-earthquake fire loads.
- Significant local buckling occurred in both top and bottom reduced flanges along with web at their location under post-earthquake fire load.

Chapter 5. Probabilistic performance-based fire following earthquake analysis

5.1. Overview

Performance-based fire design is one of the earliest fields, dating back to the 70s, in which performance-based design has been applied. The developed approaches, however, focused primarily on fire safety through the evaluation of various parameters including for example influence of combustible material, interior finish, zone dimensions, and openings as well as the performance of smoke detection devices, alarm system, and sprinklers. While performance-based fire design has been well-established, development in the area of performance-based fire engineering has been very limited. For structural fire design, current codes mainly focus on prescriptive approaches with the primary quantitative measure being through specifying appropriate thickness of insulation for all steel structural members to achieve certain level of fire resistance. More precisely, current codes focus on achieving prescribed fire ratings, which are based on standard fire test and bear little connection to what is required for fire safety. These prescriptive design approaches do not provide sufficient information regarding performance of the structural members or systems under elevated temperatures. They also provide no indication of the level of reliability of the structural member or system considering important uncertainties associated with the hazard of interest.

Standard furnace tests are conducted to determine the structural fire resistance over the past 60 years. These tests are required as a part of controlling systems because of their invaluable data on the performance of materials and small-scale assemblies in fire. However, the main issue with prescriptive fire-resistance ratings is the reliance on the assumption that a furnace test of a structural element or subassembly can be the basis for design of a full structural system where continuity, alternative load paths, and restraints play a significant role in performance of the entire system (Rini and Lamont, 2008). Employing performance-based design in fire engineering could for example result in fireproofing being specified at selected locations to meet specific performance objective, which could result in substantial savings. Therefore, it is imperative to move towards performance-based engineering not only due to the need for quantifying structural reliability for given performance objectives, but also to ensure more economical design and an advantage for steel structures in a competitive market place.

This chapter proposes a probabilistic framework to assess fragility of steel structural members and systems subjected to cascading hazard of earthquake and fire given uncertainties associated with earthquake hazard, fire hazard, applied gravity loads, passive fire protection system. The proposed performance-based fire following earthquake (PBFFE) engineering approach is constructed based on performance-based earthquake engineering established by Pacific Earthquake Engineering Research (PEER) center (http://peer.berkeley.edu/). The stochastic variables, assumed in this study, for structural fire engineering are identified as those associated with 1) fire loads, 2) post-flashover fire condition, 3) spray-applied fire resistive material (SFRM), and 4) applied dead and live loads. Monte Carlo simulation technique is implemented to quantify fragility of steel structural members and systems subjected to fire following earthquake. The outlined framework is intended to allow structural earthquake and fire engineers to assess performance of structural members and systems under the multiple hazards of earthquake and fire to meet the required performance objectives. Scenario-based Monte Carlo simulation is also employed to obtain fragility of steel structural systems.

5.2. Background

The current prescriptive fire design of steel structures does not address performance of structural systems under fire hazard. The current fire design method is highly prescriptive and conservative. Recently, structural reliability has been implemented in performance-based fire engineering (PBFE) to quantify load and resistance factors in fire design of structural members and systems (Iqbal and Harichandran, 2010). This work was motivated mainly by the high level of uncertainties observed in the past fire events. A probabilistic performance-based analysis allows structural fire engineers to understand variabilities in loads and resistance under fire and can lead to a better risk-informed design process. Since fire resistance rating (FRR) of steel structural members highly depends on passive fire protection and its thickness according to the current prescriptive design approaches, large variability in fire insulation, can significantly change the performance of steel structural members at elevated temperatures. These variations can result from various sources including for example type of material, method of application of material on the structural members, bonding between the material and the member, and durability.

Iqbal and Harichandran (2010) proposed a reliability-based framework to determine resistance and load factors in fire design of structural members. The study discusses the statistics of effective stochastic variables in fire design of structural members. It was concluded that significant uncertainties exist in fire design parameters of structural members compared to design parameters at ambient temperature design. The effects of an active fire protection system were incorporated in capacity reduction and fire load factors according to a preselected target reliability index. Guo et al. (2012) developed a probabilistic framework to assess the fire resistance of structural members considering uncertainties associated with fire load and structural resistance parameters. Statistical data was specified for random variables, and a large set of deterministic thermal-mechanical analyses was conducted using Monte Carlo simulation technique. The proposed framework was demonstrated by analyzing a protected steel beam in order to determine probability of failure at a given level of uncertainty in natural fire event.

Guo and Jeffers (2014) conducted a study to determine reliability of protected steel column subjected to natural fire load. First- and second-order reliability methods were utilized to quantify reliability of steel columns exposed to uniform elevated temperatures along the member length. The lateral deflection of the columns was defined as a failure criterion for member. The results of the analytical reliability methods were compared to the results of numerical Monte Carlo simulations. It was concluded that the analytical reliability methods led to sufficient accuracy along with significant reduction in computational cost when compared to Monte Carlo simulations. Lange et al. (2014) established application of performance-based earthquake engineering framework, developed by the Pacific Earthquake Engineering Research (PEER) center (http://peer.berkeley.edu/), in structural fire engineering. The study redefined hazard, structural system, and loss domains in accordance with structural fire engineering. This methodology was illustrated using a composite steel beam subjected to fire loads. The results designated a successful application of the PEER performance-based earthquake engineering in structural fire engineering. Khorasani et al. (2014) conducted a survey on probabilistic models of fire load densities available in the literature. A Bayesian probability approach was then used to predict the fire load density in office buildings. The proposed models showed a good correlation with available data, and provided better fit than those in Eurocode 1 (CEN, 2002) and NFPA 557 (2012). In addition, the proposed models for fire load density were used to obtain probabilistic models for maximum gas temperature in a compartment. It was concluded that the later proposed models for maximum gas temperature exhibits well correlation with test data.

This chapter introduces a probabilistic framework to assess performance of steel structural members and systems subjected to combined hazard of earthquake and fire given uncertainties in both hazards, material properties, and applied loads. The framework can provide means by which structural design engineers could assess alternative design scenarios and select the preferred design option based on a desired probability of failure. Monte Carlo simulations are implemented to obtain fragility of steel structural members and systems subjected to the multi-hazard loading scenario of fire following earthquake.

5.3. Performance-based Engineering

Performance-based engineering, which has been widely used in earthquake engineering, provides an opportunity to structural engineers to devise optimal and robust solutions for the design of structures under earthquake loads given all existing constraints. Performance-based earthquake engineering (PBEE) address performance of structures on a system-level based on probabilistic assessment of collapse. The PBEE framework proposed by PEER allows quantitative assessment of performance of structural systems subjected to ground motions based on three main steps (Lange et al., 2014):

- Define objectives of the design process
- Evaluate various alternative designs to meet the objectives
- Assess reliability and risk of various alternatives to choose the most efficient solution

The objective of PBEE is to achieve a structural system which satisfies the needs of the user, stated in terms of performance levels at different hazard levels. The resulting outcome is the development of probability distributions of the different performance levels during a period of interest, typically the service life of the structure. Figure 5.1 illustrates the PBEE methodology. In summary, this framework includes 4 domains:

- Hazard domain: The hazard analysis results in a curve, which shows annual rate of exceeding various levels of the hazard. The fault characteristics near the location of structure, recurrence rate of particular magnitude of ground motion, site conditions, site distance, and mechanism of fault are considered in the seismic hazard analysis.
- System domain: A numerical model of structural system is analyzed to determine uncertainties in the structural response considering an engineering demand parameter (EDP) given a particular level of seismic excitation.
- Damage domain: The engineering demand parameter is used to create fragility functions, which model probability of various levels of damage (DM). Fragility function provides the probability of various levels of damage in structural member or system given various intensity measures.
- Loss domain: the probabilistic estimation of performance given various damage levels is estimated. Decision-making variables are used to estimate the seismic performance of the structure in terms of interest of stakeholders, e.g. cost in dollar, downtime, and deaths.

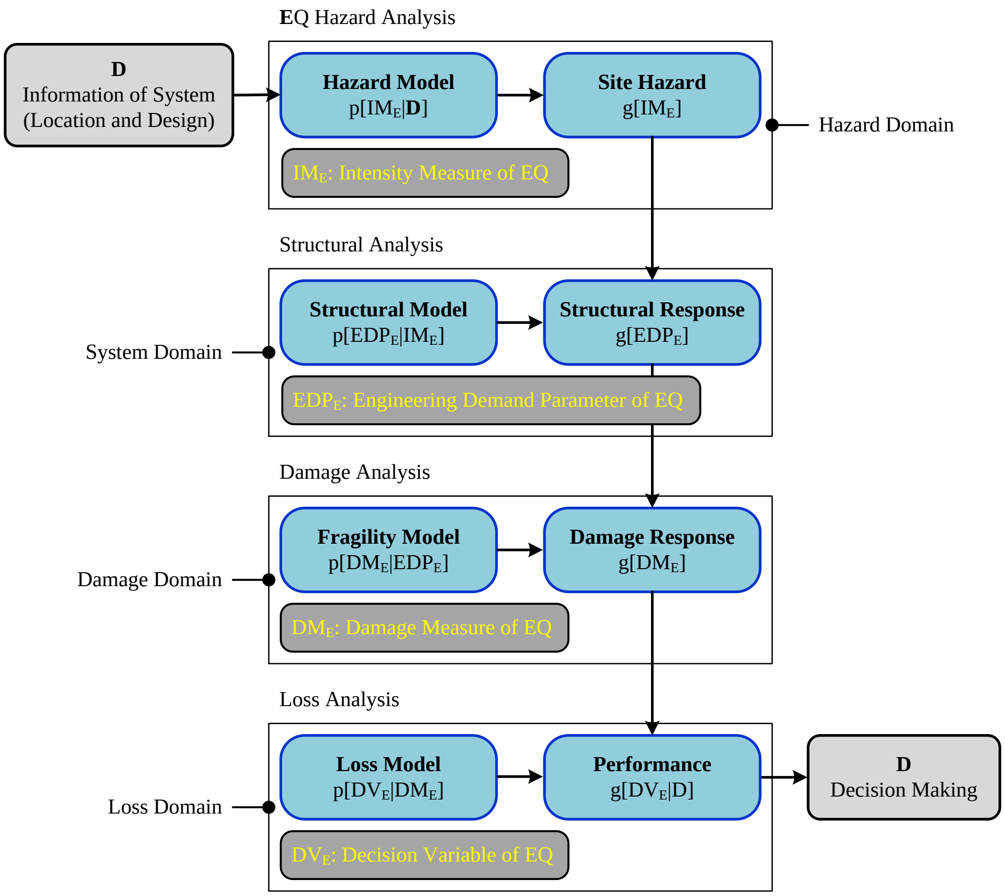

Figure 5.1 The PEER performance-based earthquake engineering framework (Bozorgnia and Bertero, 2004).

Eq. (5.1) is a mathematical expression of PEER's performance-based earthquake engineering outlined in Figure 5.1, where *g* indicates the annual rate of an event; *p* denotes the complimentary cumulative distribution function of an event. The subscript of *E*, in $\mathrm{DV_E}$ and $\mathrm{EDP_E}$, denotes earthquake hazard. *IM* is intensity measure of earthquake, e.g. spectral acceleration, *EDP* is engineering demand parameter, e.g. inter-story drift ratio, *DM* is damage measure, e.g. 5% inter-story drift ratio for collapse limit state in steel buildings, and *DV* is decision variable, e.g. cost in dollar.

$$g(DV_E|D) = \iiint p(DV_E|DM_E).p(DM_E|EDP_E).p(EDP_E|IM_E).g(IM_E|D).d(IM_E)d(EDP_E)d(DM_E) \tag{5.1}$$

Buildings are required to satisfy a desired level of resistance to fire loads in terms of *insulation, integrity, and stability* (Lange et al., 2014). It is worth noting that since this study is concerned with the multiple hazards of earthquake and fire, stability will be the primary focus in the developed framework as discussed later. Insulation and integrity can be satisfied by non-bearing elements of building and stability can be provided by structural members and system as a whole such that two objectives are met; 1) safe evacuation of occupants and 2) protection of property (Lange et al., 2014). The current prescriptive fire design of steel structures under fire loads is typically limited to specifying thickness of insulation materials for specific duration of fire. The assumption made here is that the fire will be put down prior to the consumption of the insulation material. In the case when active fire protections are used, it is assumed that the water supply will not be an issue and that the fire will be extinguished prior to flashover. While these prescriptive methods provide some level of safety, they do not take into account the probability of failure for the active or passive fire systems and the subsequent impact on integrity and stability of structural members and systems as a whole.

The PEER performance-based earthquake engineering can be adopted in structural fire engineering as shown in Figure 5.2 (Lange et al., 2014). Although this adoption is straightforward in concept; however, the definition of variables involved in the framework, e.g. intensity measure, engineering demand parameter, and damage measure, remains quite challenging due to the complex nature and extreme variability in both fire loading and in determining performance levels in comparison of that of an earthquake. For example, all engineers and researchers agree on inter-story drift ratio as an EDP in PBEE. In structural fire engineering, there has been no agreement on EDPs. This could primarily be because complete structural collapse under fire occurred only once in the case of World Trade Center 7 (WTC7).

Therefore, performance based fire engineering is likely to be concerned with functionality of exit doors and windows to allow for the occupants to escape and for fire fighters to enter the building. The functionality of these non-structural elements is very difficult to quantify, particularly since they are linked with the performance of the structural elements. Eq. (5.2) shows the mathematical expression of performance-based fire engineering outlined by Lange et al. (2014). The subscript of F implied fire hazard.

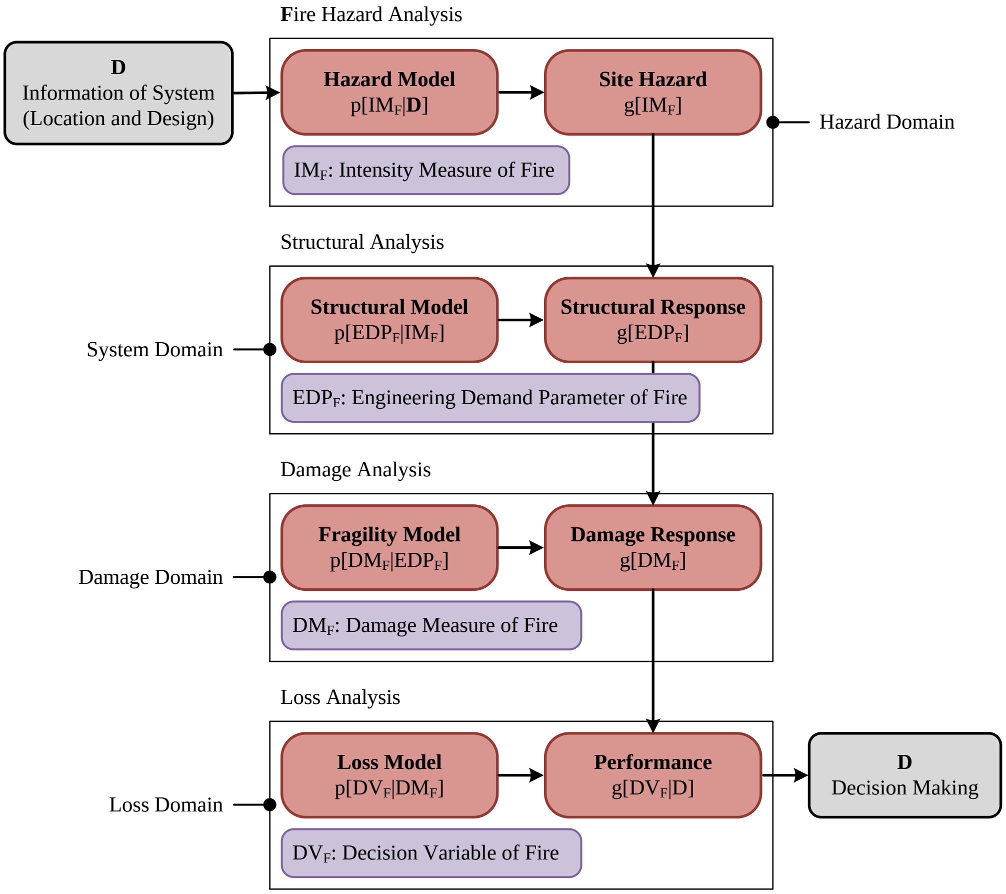

Figure 5.2 The PEER framework adopted in performance-based fire engineering (Lange et al., 2014).

$$g(DV_F|D) = \iiint p(DV_F|DM_F).p(DM_F|EDP_F).p(EDP_F|IM_F).g(IM_F|D).d(IM_F)d(EDP_F)d(DM_F) \quad (5.2.a)$$

$$g(IM_F|D) = \iint p(IM_F|Flashover).p(Flashover|Ignition).g(Ignition).d(Ignition)d(Flashover)$$

(5.2.b)

In this study, efforts are placed on investigating the first 3 domains (hazard, system, and damage domains) in PBFE framework in order to identify an appropriate variable for each of them. The hazard analysis results in identifying intensity measure of fire hazard. The intensity measure not only is used to define the intensity of an event but also is used to determine the mean annual probability of exceedance of particular intensity. The intensity measure is illustrated by hazard curve defined by frequency of exceeding an intensity measure. Several parameters have been considered as intensity measure of fire in the past studies, e.g. maximum gas temperature, duration of fire, peak temperature in a compartment, heat flux, among others. While these parameters are a viable option to serve as an intensity measure, *fire load density*, which is used in this study, could perhaps be the most suited parameter as an intensity measure for performance-based fire engineering. This is because it can be an adequate indicator of fire intensity measure considering all previously used parameters. A detailed discussion on this is provided in the next section.

The system domain enforces the selection of an appropriate engineering demand parameter for performance-based fire engineering. There has been a wide variety of selections for engineering demand parameter in the previous studies, e.g. in plane deflection of beams, lateral deformation in columns, axial force in beams and columns, maximum temperature in steel material, and time of failure. In this study, vertical stability of steel frames is chosen as the focus for the performance evaluation. This is because in this study emphasis is placed on fire following earthquakes in which vertical stability, as oppose to lateral, under fire is of concern. This of course assumes that the permanent residual inter-story drift resulting from the earthquake is below the collapse limit state. In addition, previous fire events demonstrated the potential for partial or complete vertical instability of the buildings as opposed to lateral instability. The use of vertical stability allows for meeting one out of three parameters – insulation, integrity, and stability – required to satisfy a desired level of structural performance under fire loads. The other two terms – insulation and integrity – are related to non-bearing elements of buildings. In addition, previous studies have demonstrated that axial forces are the dominant demand parameter in steel structural members under elevated temperatures (Memari and Mahmoud, 2014, Mahmoud et al., 2015). The combination of axial forces in members and the subsequent effect on vertical stability of structures could be utilized as an appropriate engineering demand parameter for performance-based fire engineering.

A key step in probabilistic analysis is to define appropriate damage measures. The damage measure equation in classical reliability analysis can be written as

$$g(X) = R_f(X) - S_f(X) \tag{5.3}$$

where, X denotes a vector contains all stochastic variables. Failure occurs when the demand $S_f(X)$ is greater than capacity $R_f(X)$ of the system. The probability of failure is then defined as

$$P_f = P[g(X) < 0] \tag{5.4}$$

Calculating the probability of failure requires the identification of a damage measure. In this study, the onset of instability in vertical structural members (columns) is defined as damage measure under fire conditions. Therefore, the capacity of columns is determined based on inelastic buckling stress and demand is evaluated according to the applied mechanical and thermal loads. In summary, the damage measure is defined as follows in the present study:

$$g(X) = \frac{S_f(X)}{R_f(X)} \geq 1.0 \tag{5.5}$$

where, $S_f(X)$ is applied demand on steel column and $R_f(X)$ is capacity of column according to the inelastic buckling stress.

In the next step, a performance-based engineering framework is needed to be defined for the cascading hazards of earthquake and fire by combining both PEER framework for earthquake and the adopted framework for fire. The developed framework for the combined hazards is outlined in Figure 5.3 below. This framework is devised based upon the concept of no correlation between the intensity measure of earthquake such as spectral acceleration and the intensity measure of fire such as fire load density. This is because although fire ignition after an earthquake highly depends on the intensity of the earthquake (as shown in Chapter 2), the fire growth to flashover condition is completely independent of the earthquake intensity and is rather dependent on available fuel load and ventilation conditions of fire compartments. Therefore, these two hazards can be assessed independently up to the step where the damage caused by earthquake has significant effects on the response of the structural member or system to fire loads.

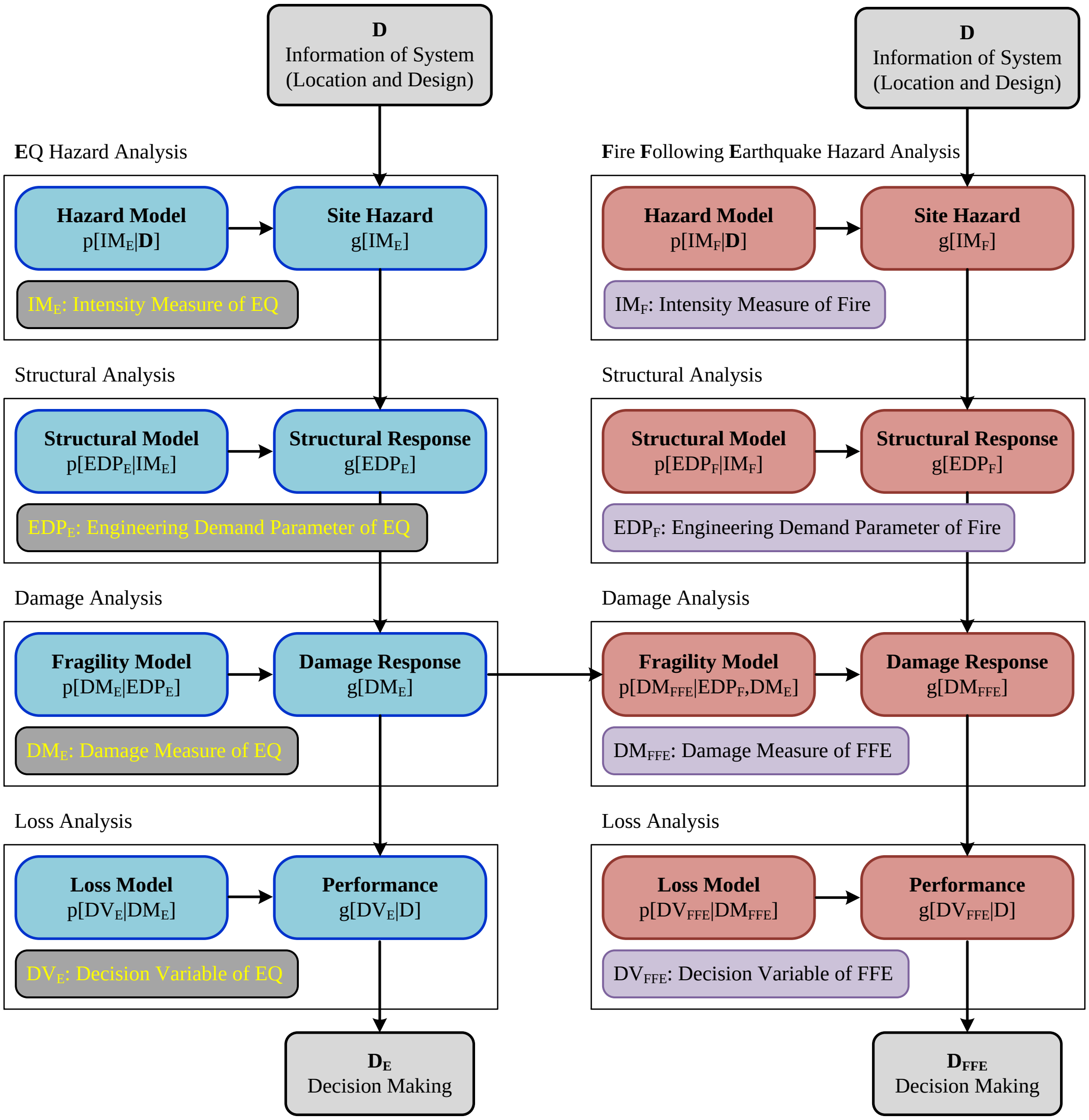

Figure 5.3 The proposed framework for performance-based fire following earthquake engineering.

As previously shown in Chapter 3, inter-story drift ratio in steel columns caused by earthquake demands resulted in significant reduction in the inelastic buckling capacity of columns at elevated temperatures. The damage measure in fire following earthquake, defined as the onset of instability in steel columns, depends on the level of inter-story drift ratio and engineering demand parameter in fire, defined as axial force. This results in correlation between earthquake and fire hazards, which has been addressed in the damage domain of the framework for performance-based fire following earthquake shown in Figure 5.3 as follow:

$$p(DM_{FFE}|EDP_F, DM_E) \tag{5.6}$$

where, DM_{FFE} is damage measure in fire following earthquake defined as the onset of instability in column. EDP_F is engineering demand parameter in fire defined as axial force, and DM_E is damage measure in earthquake determined as inter-story-drift ratio. The equation of performance-based fire following earthquake can therefore be written as shown below:

$$g(DV_{FFE}|D) = \int\int\int\int\int\int \begin{matrix} p(DV_{FFE}|DM_{FFE}).\, p(DM_{FFE}|EDP_F, DM_E).\, p(EDP_F|IM_F). \\ g(IM_F|D).\, p(DM_E|EDP_E).\, p(EDP_E|IM_E).\, g(IM_E|D). \\ d(IM_E)d(EDP_E)d(DM_E)d(IM_F)d(EDP_F)d(DM_{FFE}) \end{matrix}$$

(5.7.a)

All variables in Eq. (5.7) were previously defined. In summary, the performance-based framework introduced above forms the basis for the probabilistic analysis conducted to assess fragility of steel columns and systems at onset of instability as a damage measure.

5.4. Monte Carlo Simulation

Monte Carlo simulation technique has been widely used in engineering problems involving random behavior (Ang and Tang, 2006, Au et al., 2007 Aslani and Miranda, 2005.). This technique has also been used in previously proposed PBFE frameworks to identify uncertainty and reliability of structural members and systems under fire loads (Hamilton, 2011). Monte Carlo simulation technique is a process, which is based on random sampling of stochastic variables where the samples are generated in accordance with their probabilistic distribution, mean, and coefficient of variation. Following the sampling, a set of deterministic analyses is run based on a random combination of stochastic variables. Once all deterministic analyses are completed, probabilistic analysis can be performed based on results of all analyses where the probability of failure p_f is defined as a ratio of number of simulations in which the response exceeds a given failure criterion to total number of simulations, as shown below:

$$P_f = \frac{N_f}{N} \tag{5.8}$$

where, N_f is number of simulations in which the system/member fails based on a defined damage measure, and N is total number of simulations. Monte Carlo simulation is known as a computationally intensive method because of large number of sampling often required to achieve a desired level of accuracy. A wide range of algorithms is available for sampling stochastic variables from different types of probability distributions. There are few methods to reduce computational intensity of Monte Carlo simulation such as Latin Hypercube Sampling (LHS). The LHS method uses a technique known as "stratified sampling without replacement", because once a sample is taken from an interval it is not sampled from it again. This is because its value is already represented in the samples set. The key in LHS is to divide the cumulative distribution function into equal intervals on cumulative distribution scale from 0 to 1. Following this division, a sample is randomly chosen from each interval of cumulative distribution function. Samples are then forced to represent values in each interval as shown in Figure 5.4. The number of intervals of the cumulative distribution is equal to the number of iterations performed in Monte Carlo simulation. In fact, values of the input probability distribution are reflected more accurately using LHS method. In the present study, LHS method is used for sampling of stochastic variables.

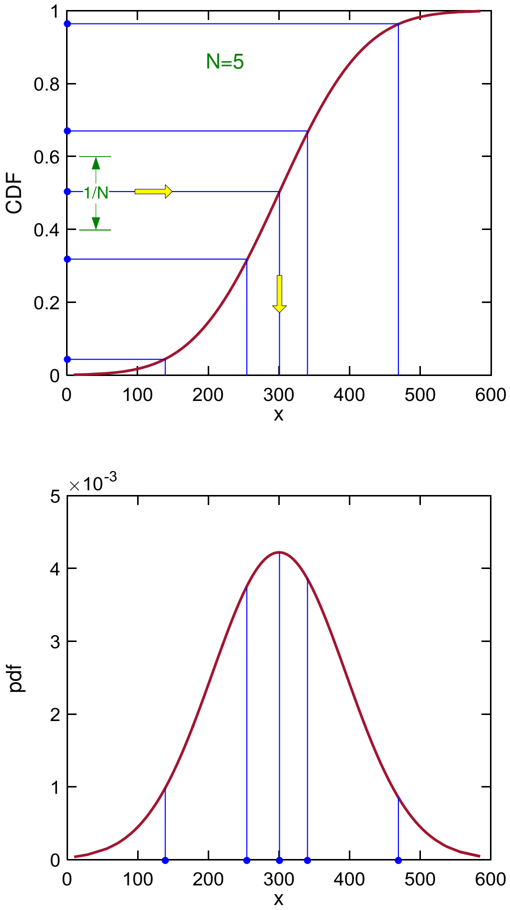

Figure 5.4 The scheme of Latin Hypercube Sampling (LHS).

5.5. Stochastic Modeling

The most important parameters in fire design of steel structural members are chosen as random variables for stochastic analysis. This includes random variables associated with post-flashover condition of fire following earthquake event, properties of spray-applied fire resistance material (SFRM) in the fire compartment, and applied mechanical loads.

Although ignition is the onset of a fire event, it has no effect on severity of fire. The most effective parameters in fire severity include fire load density, compartment ventilation, compartment geometry, and thermal characteristics of surrounding surfaces. The fire load density depends on amount, type, distribution, and characteristics of surfaces in boundaries of the compartment according to NIST (2010) and SFPE (2004). The gas temperature of fire (T_f) in the compartment varies in time (t) considering energy equilibrium, opening factor, fire load density, and thermal properties of material in compartment enclosures (SFPE, 2004). The aforementioned parameters are defined as following in accordance with SFPE (2004):

- Fire load density (WM/A_t): is a measure of energy released by combustibles in the compartment. A_t is the total area (m^2) of enclosure including walls, ceiling, floor, and openings. M is total mass (Kg) of combustible materials in the compartment, and W is the effective heat of combustibles (MJ/Kg).
- Ventilation parameter ($A_o\sqrt{h}$): is a measure of available oxygen in the compartment. A_o is total area (m^2) of vertical openings on the walls, e.g. windows and doors, and h is weighted average of window heights on the walls (m).
- Opening factor ($A_o \frac{\sqrt{h}}{A_t}$): controls the rate of combustion in the compartment. All associated variables were defined above.
- Thermal absorptivity ($\sqrt{\kappa\rho c_p}$): which is a measure of heat absorption by materials in boundaries of fire compartment. κ, ρ, and c_p are thermal conductivity, density, and specific heat of materials in the boundaries of enclosure.

5.5.1. Fire load density ($q_{t,d}$)

The fire load density is a measure of the total energy released in a fire event by quantity and type of available combustible materials per unit area in the fire compartment. Although fire load density is a random variable in intensity and spatial distribution; however, it is usually considered as spatially uniformly distributed. There is a wide variety of statistical data reported in literature for fire load density that vary according to occupancy as listed in Table 5.1, which were obtained based on building surveys that reflects fire load density at an arbitrary point in time. Culver (1976) conducted a statistical survey on fire load density in 23 typical U.S. office buildings. The results indicated a mean of 564 MJ/m2 and coefficient of variation of 0.62 with Gumbel distribution, which is shown in Figure 5.5(a). The ECCS (2001) reports the same type of distribution as Culver (1976) for fire load density with mean of 420 (MJ/m2) for office buildings (Figure 5.5(b)) and coefficient of variation of 0.3 for all occupancies. This is substantially less than the coefficient of variation reported by Culver (1976). The ECCS (2001) also recommends that the design fire load can be taken at the 80th percentile. In addition, design fire loads vary during the lifetime of a building since its occupancy classification may change at some point, much like other types of loads (Phan et al., 2010).

Table 5.1 Summary of statistical data for fire load density (MJ/m^2).

Occupancy	Mean	Standard Deviation	80% fractile	90% fractile
CIB W14 (1983 and 1986)				
Offices	420	309	680	740
Dwellings (bedroom)	640	135	750	810
Hotels	345	92	420	472
Schools	285	79	360	415
Culver (1976)				
General/clerical offices	598	358	898	1046
Conference rooms	425	425	714	969
File, storage rooms	1112	1020	1968	2400
ECCS (2001)				
Office	420	126	511	584
Dwelling	780	234	948	1085
Hotel	310	93	377	431
Shopping center	600	180	730	835
School	285	86	347	397
Hospital	230	69	280	320
Theater	300	90	365	420

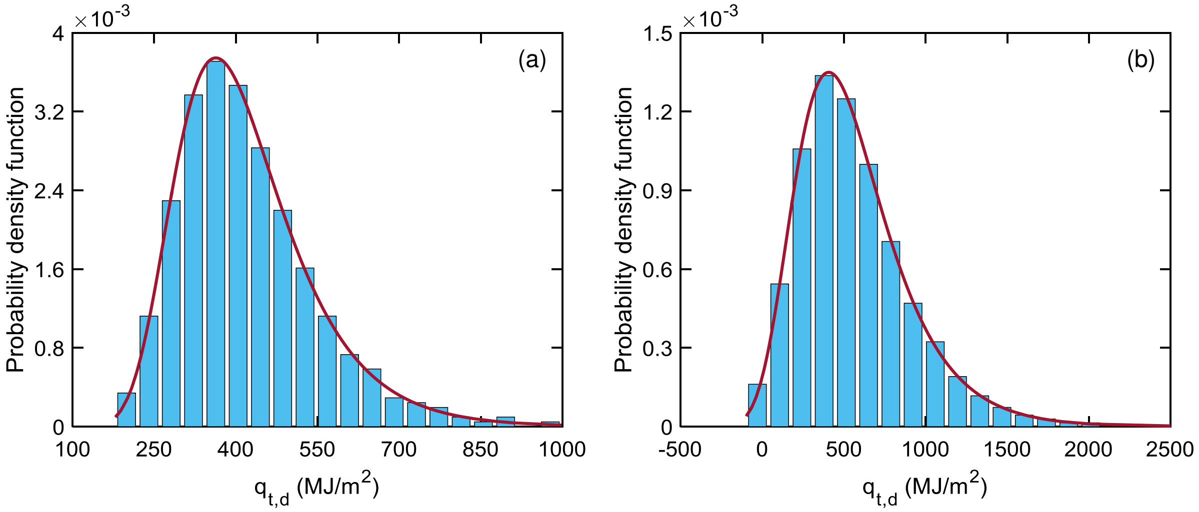

Figure 5.5 The probability distribution function of fire load density (a) Culver (1976) (b) ECCS (2001).

5.5.2. Opening Factor (O)

The fire compartment in a building usually contains vertical openings, e.g. windows and doors. It is assumed that glasses of windows are shattered during and/or immediately after an earthquake. The opening factor can be modelled using a random variable ζ in accordance with the part 2 of the recommendation of the Joint Committee on Structural Safety (JCSS, 2001) as following:

$$O = O_{max}(1 - \zeta) \tag{5.9}$$

where, O_{max} is the maximum opening factor equal to 0.20 $m^{0.5}$ according to Eurocode 1 (CEN, 2002). ζ is a random variable with truncated lognormal distribution. The lognormal distribution should be such that $\zeta<1$ to avoid negative values for the opening factor. The mean and standard deviation of ζ are 0.2 and 0.2, respectively, in accordance with JCSS (2001) Part 2. Figure 5.6 shows the probability distribution function for the opening factor.

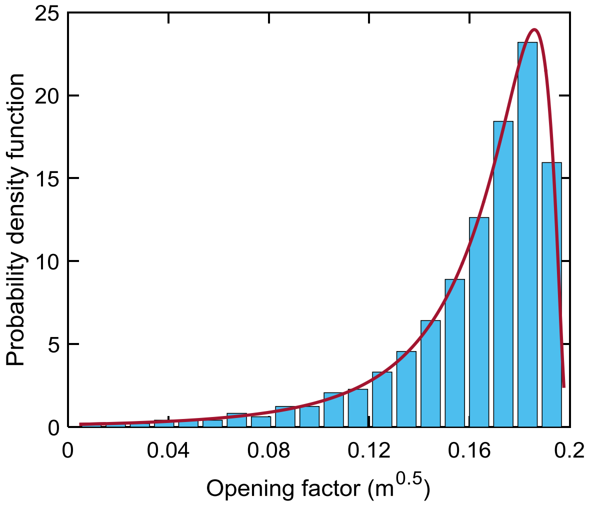

Figure 5.6 The probability distribution function of opening factor.

5.5.3. Thermal Absorptivity (b)

The thermal absorptivity is a measure of heat absorption by materials in boundaries of fire compartment. This is obtained by Eq. (5.10) below:

$$b = \sqrt{\kappa \rho c_p} \tag{5.10}$$

where, κ, ρ, and c_p are thermal conductivity, density, and specific heat of materials in boundaries of enclosure. Since the aforementioned parameters depend on temperature, therefore thermal absorptivity is considered as temperature-dependent property. However, Eurocode 1 (CEN 2002) allows the use of ambient temperature properties for design purposes. This was also confirmed by analysis conducted by Iqbal and Harichandran (2010). The review of literature indicates that limited information is available for thermal properties of some materials used in boundaries of enclosure, e.g. gypsum board and normal weight concrete (Iqbal and Harichandran, 2010). In this study, normal weight concrete is statistically represented with Normal distribution with mean of 1830 $Ws^{0.5}/m^2K$ and coefficient of variation equal to 0.094, which has been sued by both

Buchanan (2001) and Iqbal and Harichandran (2010). Figure 5.7 shows the probability distribution function for thermal absorptivity of normal weight concrete.

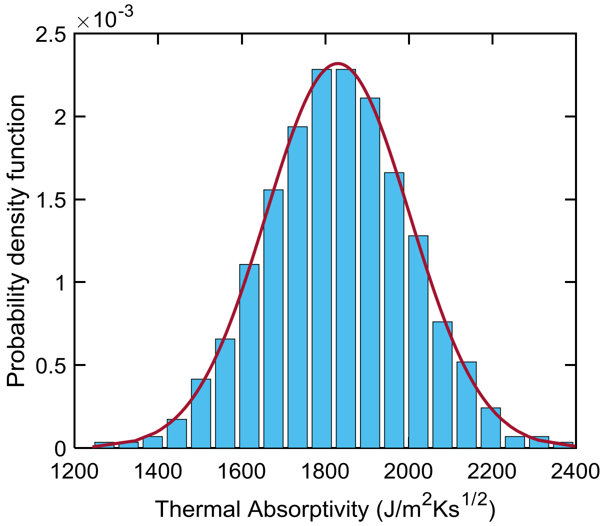

Figure 5.7 The probability distribution function of thermal absorptivity of normal weight concrete.

A fire curve can be determined based on a set of conditions, e.g. fuel supply, ventilation condition, and thermal properties of surrounding enclosure. It is reasonable to assume that thermal conditions are homogenous throughout the compartment, the fire is ventilation-controlled, and no combustion takes place outside the fire compartment for a post-flashover fire. The ASTM E119 and ISO 834 fire curves are indicative of long duration-moderately severe post-flashover fires. These two standard fire curves do not have the ability to consider variation of random parameters in post-flashover fire development as discussed in Chapter 2. The Eurocode parametric fire curve (CEN, 2002) considers the above-discussed random variables (fire load density, opening factor, and thermal absorptivity of surrounding compartment) in developing fire curve. Therefore, the Eurocode parametric fire curve is used to generate time-temperature curves for probabilistic analysis. For instance, Figure 5.8 (a) and (b) show how a set of fire curves can be generated for a constant value of fire load density – 500 (MJ/m2) and 1000 (MJ/m2), respectively – using LHS of opening factor and thermal absorptivity of compartment according to their corresponding statistical data discussed previously. This allows the evaluation of steel structural members and systems under constant fire load density since it is an indicator for intensity measure of fire.

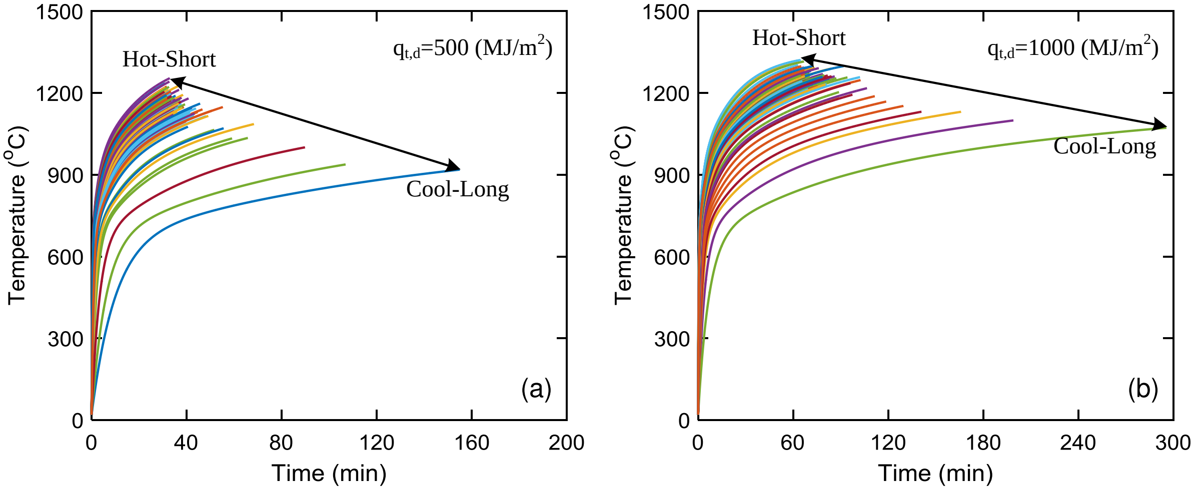

Figure 5.8 A set of fire curves with constant fire load density (a) 500 MJ/m^2 (b) 1000 (MJ/m^2).

Table 5.2 Summary of statistical data post-flashover fire conditions.

Random Parameter	Mean	C.O.V	Distribution	Reference
Fire load density, $q_{t,d}$ (MJ/m^2)	564	0.62	Gumbel	Iqbal and Harchandran (2010)
Opening factor, ζ (m$^{0.5}$) *	0.2	1.0	Trun. Lognormal	JCSS, Part 2 (2001)
Thermal absorptivity, b (J/m^{2}s$^{0.5}$K)	1830	0.094	Normal	Iqbal and Harchandran (2010)

* $O=O_{max}(1-\zeta)$

Steel structural members are usually protected against elevated temperatures using spray-applied fire resistive materials (SFRMs). This, so called "passive" fire protection system, results in avoiding exposure of bare steel material to elevated temperatures. In fact, passive fire protection system improves performance of steel structural members and systems in two ways: lower temperature in the body of steel material in comparison to gas temperature and delay in elevating temperature in the body of steel. This causes delay in temperature rise in the body of steel, which results in delay in stiffness and strength degradation of steel. Table 5.3 shows properties of various passive fire protection materials.

Table 5.3 Thermal properties of common fire protection material (ECCS, 1995).

Material	**Density (kg/m^3)**	**Moisture content (%)**	**Thermal conductivity (W/mK)**	**Specific heat (J/kgK)**
Sprays				
Mineral fibre	300	1	0.12	1200
Vermiculite cement	350	15	0.12	1200
Perlite	350	15	0.12	1200
High-density sprays				
Vermiculite (or perlite) and cement	550	15	0.12	1100
Vermiculite (or perlite) and gypsum	650	15	0.12	1100
Boards				
Vermiculite (or perlite) and cement	800	15	0.20	1200
Fibre-silicate or fibre-calcium-silicate	600	3	0.15	1200
Fibre-cement	800	5	0.15	1200
Gypsum board	800	20	0.20	1700
Compressed fiber boards				
Fibre-silicate, material- wool, stone-wool	150	2	0.20	1200
Others				
Concrete	2300	4	1.60	1000
Lightweight concrete	1600	5	0.80	840
Concrete bricks	2200	8	1.00	1200
Bricks with holes	1000	---	0.40	1200
Solid bricks	2000	---	1.20	1200

5.5.4. Thickness of Spray-Applied Fire Resistive Material (SFRM)

Thickness of spray-applied fire resistive material can be considered as one of the most important parameters in design of passive fire protection. Iqbal and Harichandran (2010), based on some literature review, indicated that the average thickness of SFRM is usually higher than the design value, and assumed a mean SFRM thickness of 1.6 mm greater than that of the design value. The thickness of SFRM follows lognormal distribution in accordance with Iqbal and Harichandran (2010). Furthermore, a small coefficient of variation of 0.20 was chosen for the thickness of SFRM since it is applied on the surface of steel members under controlled conditions. Figure 5.9 shows the probability distribution function for the SFRM thickness equal to 11.1 mm for 1-hr fire resistance ratings (FRR).

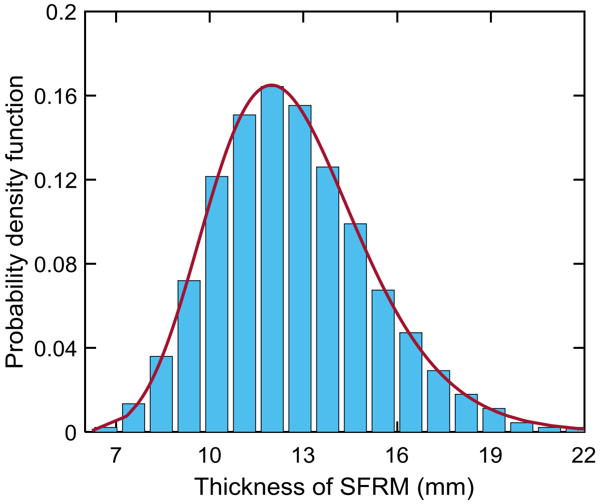

Figure 5.9 The probability distribution function for thickness of SFRM.

5.5.5. Thermal Conductivity of SFRM

Fire protection materials prevent direct penetration of temperature into the body of steel. Common fire resistive materials prevent heat penetration through one or more of the following mechanisms:

- High heat capacity
- Low thermal conductivity
- Backward radiation
- Intumescence
- Heat absorbing physical reactions

Nowadays, spray-applied fire resistive materials (SFRM's) are the most popular type of fire protections in steel structures. European Convention for Constructional Steelwork (ECCS, 1995) provides a list of popular fire protection materials with their thermal properties as shown in Table 5.3. These properties vary with temperature; however, the ECCS (1995) recommends values at ambient temperature for simple heat transfer analysis. Cementitious SFRM are usually a mix of Portland cement and aggregates. Cementitious SFRMs are classified as low-, medium-, and high-density products. In the present study, a normal weight concrete (medium-density) is considered as fire protection material. Iqbal and Harichandran (2010) reported Lognormal distribution for this spray-applied fire resistive material with mean of 0.187 W/m.K and coefficient of variation of 0.24. They also recommended Normal distribution for density of SFRM with mean of 307 kg/m^3 and coefficient of variation of 0.29. The specific heat for normal weight concrete is assumed constant at ambient temperature.

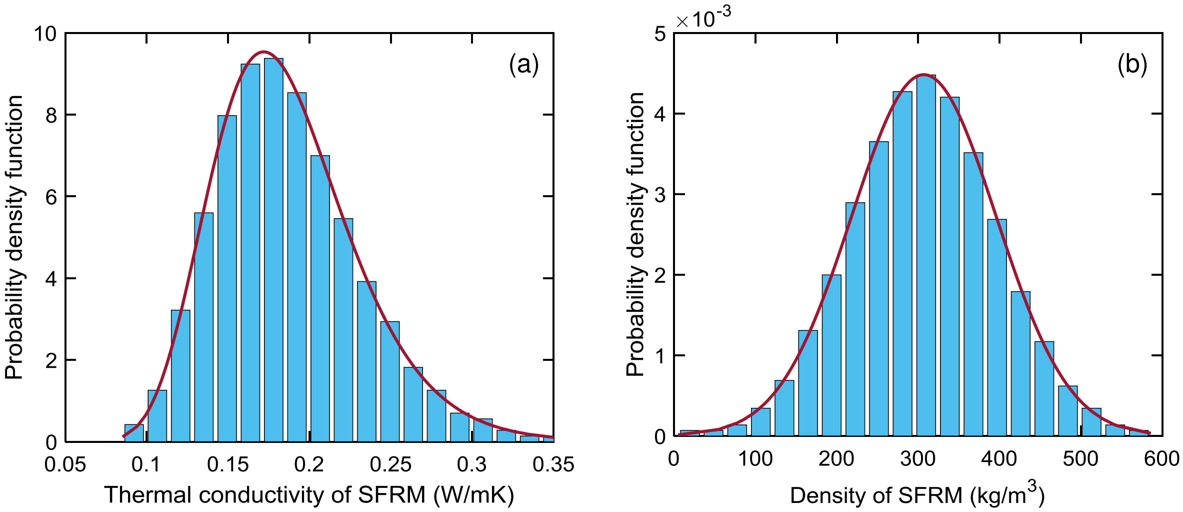

Figure 5.10 The probability distribution function for thermal conductivity and density of SFRM.

Table 5.4 Summary of statistical data for a normal weight concrete.

Random Parameter	Mean	C.O.V	Distribution	Reference
Thickness, d_p (mm)	Nominal+1.6	0.2	Lognormal	Iqbal and Harchandran (2010)
Thermal conductivity, k_p (W/mK)	0.187	0.24	Lognormal	Iqbal and Harchandran (2010)
Specific heat, c_p (J/kgK)	1200	Unknown	Unknown	---
Density, ρ_p (kg/m^3)	307	0.29	Normal	Iqbal and Harchandran (2010)

The next step is to obtain the temperature in the body of the steel material considering a passive fire protection as shown in Figure 5.11. It is assumed that temperature is uniformly distributed across the cross-section of a steel member at any time of fire in a simplified heat transfer analysis (Phan et al., 2010). This assumption is reasonable for an unprotected steel member as well as steel members with uniform protection from all sides when they are uniformly subjected to fire load from all sides.

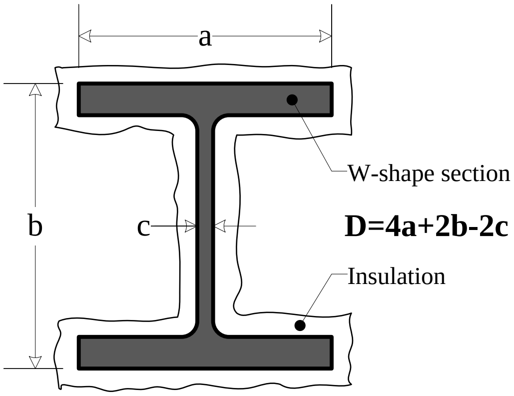

Figure 5.11 Perimeter D for steel column sections (Phan et al., 2010).

A simple heat transfer equation shown in Eq. (5.11) (AISC, 2010) approximately returns the temperature in body of steel material considering above-mentioned assumption of uniform temperature distribution across the section of steel member subjected to fire. It is also assumed that the thermal properties of protection material are temperature-independent, although temperature-dependent properties can also be used in this simplified equation.

$$\Delta T_s = \frac{k_p}{d_p}\left[\frac{T_f - T_s}{c_s\frac{W}{D} + \frac{c_p \rho_p d_p}{2}}\right]\Delta t \qquad (5.11)$$

where,

ΔT_s: Temperature rise in steel (℃)

D: Inner perimeter of fire protection, as defined in Figure 5.11.

W: Steel section weight per unit length (Kg/m)

c_s: Specific heat of steel (J/kg.C)

T_f: Fire temperature

T_s: Steel temperature

Δt: Time increment

k_p: Thermal conductivity of the protection material (W/mC)

c_p: Specific heat of the protection material (J/Kg.m)

ρ_p: Density of the protection material (W/mC)

d_p: Protection thickness (m)

The Eq. (5.12) can be solved using finite difference method considering a short time increments based on convergence criterion of Forward Euler discretization of time. According to Forward Euler time-marching scheme used here, Eq. (5.11) is discretized as follows:

$$T_s^{n+1} - T_s^n = \frac{k_p}{d_p}\left[\frac{T_f^{n+1} - T_s^n}{c_s\frac{W}{D} + \frac{c_p\rho_p d_p}{2}}\right][t^{n+1} - t^n] \tag{5.12}$$

Eq. (5.12) allows for the calculation of temperature history in the body of steel given gas temperature based on fire curve. Therefore, the set of fire curves shown in Figure 5.8 can be converted to the new time-temperature curves, based on Eq. (5.12). Figure 5.12 shows a set of time-temperature curves based on fire load density of 1000 (MJ/m^2) for spray-applied fire resistive material thickness of 11.1 mm for 1-hr fire resistive rate. This figure indicates that using protective material results in reduction of the effective temperature on the body of steel material in comparison with Figure 5.8(b). It is also noted that random numbers for insulation material properties were inserted in Eq. (5.12). Mean, coefficient of variation, and distribution of these properties were discussed previously.

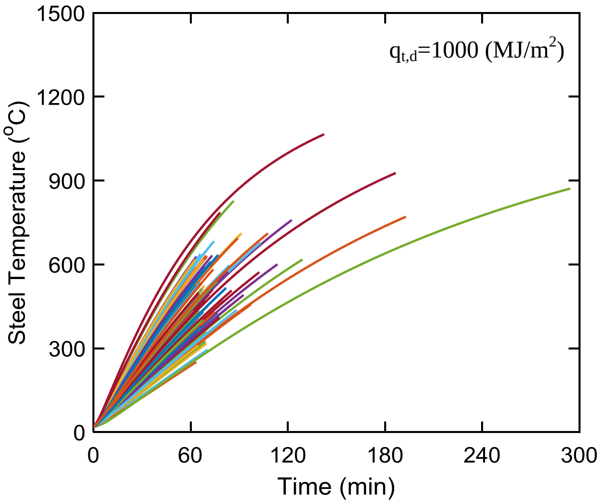

Figure 5.12 The time-temperature curve applied to the body of steel material.

5.5.6. Mechanical loads

Ellingwood (2005) showed that the probability of simultaneous application of fire loads with design dead and live loads, wind, snow, and earthquake loads is minimal. It was also indicated that fraction of the design loads were present on the structure when fire occurs. Ellingwood (2005) recommended using a combination of partial dead load and arbitrary-point-in-time live load for probabilistic-based analysis of members or structures subjected to fire as follows:

$$w = w_{DL} + w_{LL,apt} \tag{5.13}$$

where, w_{DL} and $w_{LL,apt}$ are random variables reflect dead and arbitrary-point-in-time live load. The recommended statistical properties of w_{DL}, $w_{LL,apt}$ are shown in Table 5.5.

Table 5.5 Summary of statistical properties of mechanical loads and associated coefficients.

Random Parameter	Mean	C.O.V	Distribution	Reference
Dead load, wDL	1.05×nominal	0.1	Normal	Ellingwood (2005)
Live load, wLL	0.24×nominal	0.8	Gamma	Ellingwood (2005)

5.6. Member-level probabilistic analysis

The member-level probabilistic analysis is conducted on steel columns in the preset study by considering their instability under cascading hazards of earthquake and fire. As discussed previously, axial force developed in the steel columns under specific inter-story drift ratio and elevated temperatures is selected as predominant response of steel columns under fire following earthquake. Therefore, the combination of axial and moment (P-Δ) demands control the response of steel column in such cascading load scenario. The damage measure is defined when the combined demands exceeds the axial inelastic buckling capacity of the steel column. The longitudinal temperature distribution is needed to calculate thermal demand on steel columns along with determining their capacity. To do so, the conduction partial differential equation (PDE), Eq. (5.14), must be solved considering the time-temperature curves generated for the body of steel columns.

$$\frac{\partial T(x,t)}{\partial t} = \alpha(T)\frac{\partial^2 T(x,t)}{\partial x^2} \tag{5.14}$$

where, T(x,t) represents temperature in space and time and α(T) is thermal diffusivity. To solve the above-mentioned conduction partial differential equation, 3-point central in space discretization and backward Euler time marching scheme is used according to finite difference method. The 3-point central in-space discretization scheme results in discretization of the second derivative of temperature with respect to space in the right hand side of the Eq. (5.14) as following:

$$\frac{\partial^2 T(x,t)}{\partial x^2} = \frac{T_{j-1}-2T_j+T_{j+1}}{\Delta x^2} + \frac{\Delta x^2}{12}\frac{\partial^4 T}{\partial x^4} \tag{5.15.a}$$

$$\frac{\partial^2 T(x,t)}{\partial x^2} = \frac{T_{j-1}-2T_j+T_{j+1}}{\Delta x^2} + O(\Delta x^2) \tag{5.15.b}$$

It is seen that the truncated error is from second order. The backward Euler time marching scheme results in

$$\frac{\partial T(x,t)}{\partial t} = \frac{T^{n+1}-T^{n}}{\Delta t} + \frac{\Delta t}{2}\frac{\partial^2 T}{\partial t^2} \tag{5.16.a}$$

$$\frac{\partial T(x,t)}{\partial t} = \frac{T^{n+1}-T^{n}}{\Delta t} + O(\Delta t) \tag{5.16.b}$$

$$\frac{T^{n+1}-T^{n}}{\Delta t} = \lambda T^{n+1} \tag{5.16.c}$$

In summary, the discretization of conduction partial differential equation, Eq. (5.14), yields Eq. (5.17) using 3-point central in space and backward Euler in time (CS-BT) discretization schemes.

$$\frac{T_j^{n+1}-T_j^{n}}{\Delta t} = \alpha(T)\frac{T_{j-1}^{n+1}-2T_j^{n+1}+T_{j+1}^{n+1}}{\Delta x^2} \tag{5.17.a}$$

The Eq. (5.17) is organized such that temperature in different time steps (n and n+1) is located in two sides of the equation as shown in Eq. (5.17.b). This equation can be written in a matrix form considering all nodes along the length of steel column.

$$T_j^{n} = -S_x T_{j-1}^{n+1} + (1+2S_x)T_j^{n+1} - S_x T_{j+1}^{n+1} \tag{5.17.b}$$

where,

$$S_x = \frac{\alpha(T).\Delta t}{\Delta x^2} \tag{5.17.c}$$

The boundary conditions are as follows:

- The temperature in node 1 is equal to the user-defined input; then, K(1,1)=1
- The temperature in the end point (node 51 in the present study) will be

$$T_j^{n} = -S_x T_{j-1}^{n+1} + (1+S_x)T_j^{n+1} \tag{5.11.d}$$

It is noted that temperature-dependent thermal properties of steel are used in solving this PDE, including thermal conduction and specific heat. The density of steel is however temperature-independent and constant. Thereafter, thermal diffusivity α(T) is a temperature-dependent variable in solution process of conduction PDE.

Once conduction transient heat transfer analysis is performed, the demand on the column and its capacity under non-uniform longitudinal temperature distribution should be determined. The capacity is calculated using the flexibility-based formulation developed in Chapter 3. As previously demonstrated, the flexibility-based formation allows for the evaluation of buckling stress of steel columns at any inter-story drift ratio and arbitrary longitudinal temperature profile. The demand on steel columns is assessed based on three various sources: (1) applied mechanical axial dead and arbitrary-point-in-time live loads mainly due to gravity weights; (2) the moment demand on steel column caused by earthquake loads if it is a member of a moment-resisting system, otherwise it will be negligible; and (3) thermal loads due to post-earthquake fire. Case (1) must be calculated according to the tributary area of a column in the structural system using statistical data for load combination discussed previously. Case (2) can be estimated according to rotational stiffness provided by beams and columns connected to the column of interest at its both ends and the inter-story-drift demand caused by earthquake. It is important to note that uniform temperature is assumed in beams and columns connected to the top and bottom of the steel column. Case (3) is calculated according to the Eq. (5.18) assuming uniform longitudinal temperature distribution in connected columns in upper and lower stories:

$$\sum_i^n \left[\int_0^L \left(\frac{Pdx}{E(x).A} + \alpha(T).\Delta T(x)dx\right) + \left(\frac{PL}{E.A}\right)_{c,top} + \left(\frac{PL}{E.A}\right)_{c,bot}\right] = 0 \tag{5.18}$$

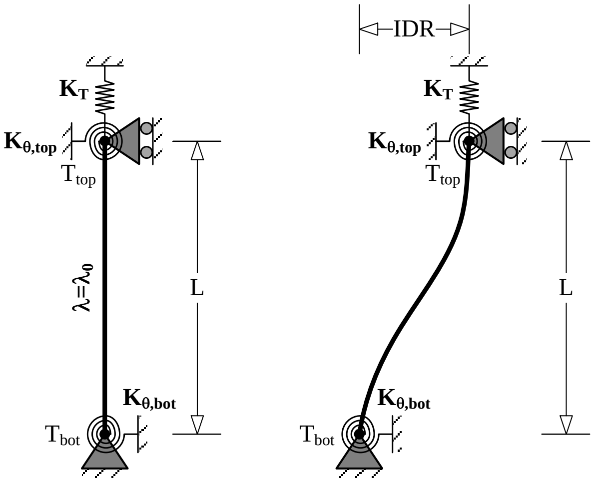

Figure 5.13 The mechanical model of steel column under fire following earthquake.

The solution of Eq. (5.18) will result in the axial force demand on a non-uniformly heated column along its length. The geometry of steel column embedded in a steel frame is considered as Figure 5.13 in the numerical analysis. To run member-level probabilistic analysis, a Monte Carlo simulation is conducted according to the flowchart shown in Figure 5.14 using LHS method. To conduct the analysis, first a numerical model with the geometrical representation of the column is developed. A displacement-controlled analysis is performed to apply a determined level of inter-story drift as an earthquake demand on column. This is performed similar to a nonlinear static pushover analysis where the column deformation at the end of conclusion of the lateral displacement analysis is considered an initial condition for post-earthquake fire loads.

A set of “N” fire curves at certain level of fire load density is generated using Latin Hypercube sampling of the related stochastic variables. This results in N fire curves that are converted to time-temperature curves in the body of the steel column considering samples of passive fire protection material described previously. A set of N axial demand forces is also generated according to stochastic variation of mechanical loads. The finite difference method is employed to obtain non-uniform longitudinal temperature profiles in the steel column for each of

N time-temperature curves. In this study, for each random variable, 100 samples are produced. In summary, prior to calculating the load demand on a column the available information would include the deformed state of a column at a certain level of inter-story drift along with longitudinal distribution of temperature and applied mechanical loads.

In the next step, N (100) analyses are conducted to obtain the ultimate interaction demand of axial force and moment on a column. The demand caused by inter-story drift and applied axial forces are calculated using the flexibility-based formulation with minimal modifications. The demand caused by the thermal loads is calculated using uncoupled thermal-mechanical analysis per Eq. (5.18) as previously explained. The capacity is also determined using the flexibility-based framework developed in Chapter 3 for all N (100) combinations of fire load and axial force demands. At this step, the developed axial and moment demands in the column caused by earthquake and fire in all cases (N=100) is compared to column capacity to determine the damage measure of the column under each case. Therefore, the probability of failure can be calculated by dividing the number of failed samples (N_f) by the total number of samples (N). The repeat of this process for all levels of inter-story drift ratios and fire load density will result in fragility surface of column of interest as shown in Figure 5.14.

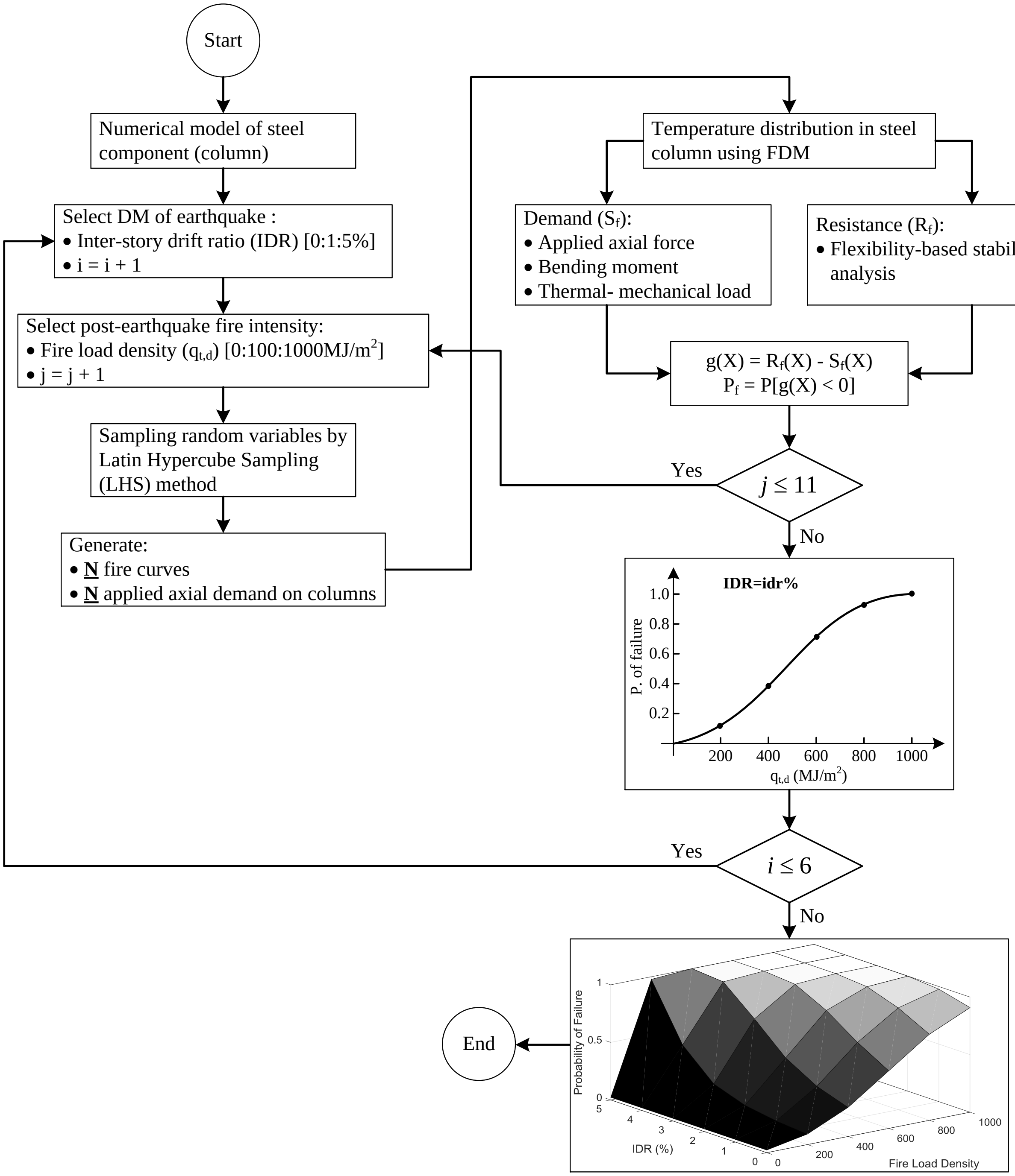

Figure 5.14 The flowchart of Monte Carlo simulation for member-level analysis.

To explain the process of aforementioned member-level probabilistic analysis, an interior column is selected in the 2^{nd} story level of 3-story moment-resisting frame, which was analyzed in Chapter 4, as highlighted in Figure 5.15. It is assumed that post-earthquake fire occurs in the second (from left) bay of this story. The W14X311 section and 3.96 m long column is numerically modeled using the procedure outlined in Figure 5.13. The design dead and live loads are obtained based on tributary area of the selected column according to FEMA-355C (2000) shown in Figure 5.15.

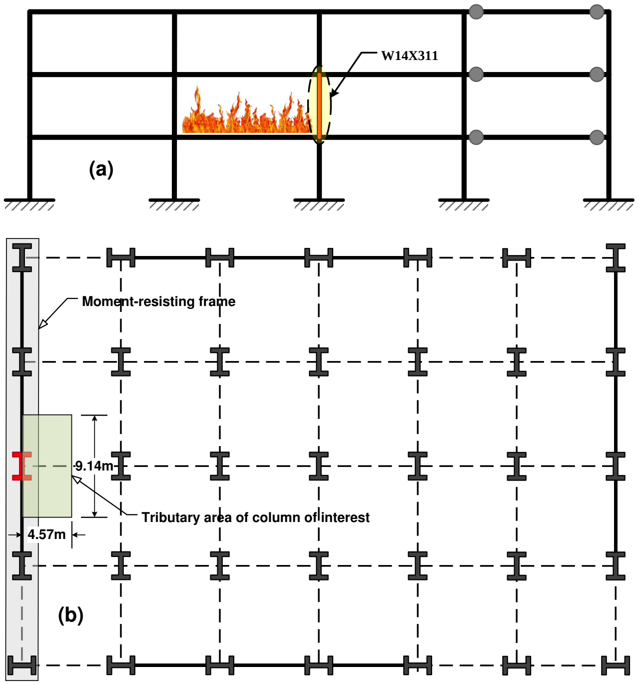

Figure 5.15 (a) The elevation view of 3-story frame along with heated column (b) The plan view of the 3-story building along tributary area of heated column.

The results of the Monte Carlo simulation for 3% inter-story drift ratio are shown in Figure 5.16. In this figure, each set of markers – associated with a particular fire load density – shows the values of damage function, g(x), for a set of fire curves (N=100). If fire curves are labeled from 1 to N (100), the values of damage function associated with each fire curve (say fire curve “i”) are connected to each other with solid color lines. The horizontal solid black line indicates the damage limit state, g(x)=1, when demand and resistance are equal. Markers located above the solid black line are an indication of failure, and those under the black line imply no failure. The same plot can be generated for the other inter-story drift ratios.

Figure 5.16 shows that the number of failed cases increases as the fire load density increase. For instance, there is no failed case for fire load intensity of 100 (MJ/m^2), while failure is shown for all cases at load intensity of 1000 (MJ/m^2). In addition, the higher positive slope rate of the curves implies that the value of damage function, g(x), rises by increase in fire load density. This is more significant for fire load density of 500 (MJ/m^2) and larger, which slope of color lines is substantially higher than those for fire load densities less than 500 (MJ/m^2). Moreover, the damage function varies between 0 and 1 for fire load density of 100 (MJ/m^2), while its variation falls between 1 and 15 for fire load density of 1000 (MJ/m^2).

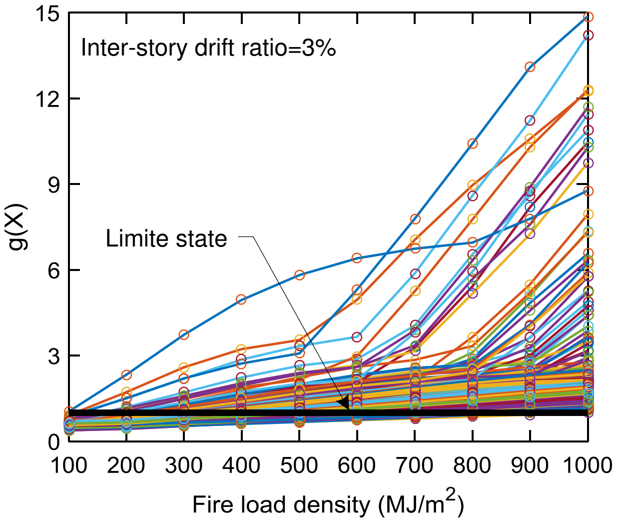

Figure 5.16 The damage state of selected steel column versus fire load density in 3% inter-story drift ratio.

The probability of exceedance for 3% inter-story drift ratio along with the rest of inter-story drifts is plotted in Figure 5.17. It is seen that the probability of failure increases by increase in fire load density and inter-story drift ratio. For instance, the probability of failure given 5% inter-story drift ratio is approximately 100% for all range of fire load densities. This implies that the probability of failure in a column with 5% inter-story drift is 100% with or without fire loads. The probability of failure in the steel column with 4% inter-story drift with no fire load is about

30% and is 100% at fire load density of 500 (MJ/m^2) and greater. In case of 2% inter-story drift ratio, the probability of exceedance reaches 84% for a maximum fire load density of 1000 (MJ/m^2). The probability of failure given 0 and 1% of inter-story drift ratio is 0.10 and 0.15, respectively, for fire load density of 1000 (MJ/m^2) as shown in Figure 5.17.

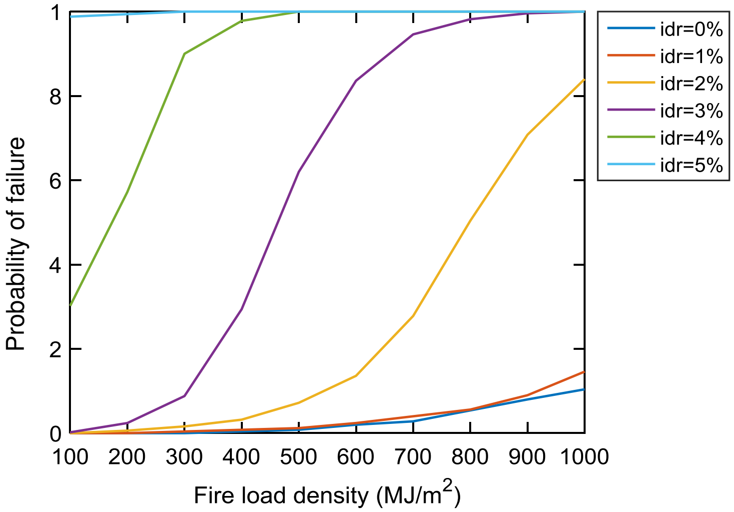

Figure 5.17 The probability of exceedance in selected steel column given inter-story drift ratio and fire load density.

Figure 5.17 is re-plotted in a 3-D form in Figure 5.18 to show the probability of exceedance given inter-story drift ratio and fire load density, which is essentially a fragility surface in this case. In fact, Figure 5.18 expresses the probability of exceedance for multiple-hazard of fire following earthquake given intensity measure of earthquake (inter-story drift ratio) and intensity measure of fire (fire load density).

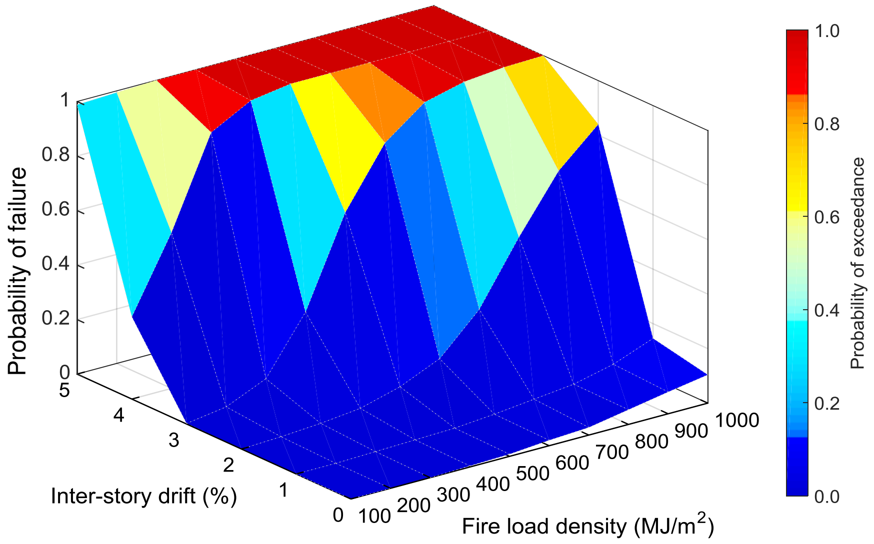

Figure 5.18 The 3-D fragility surface of the selected steel column given inter-story drift ratio and fire load density.

5.7. System-level probabilistic analysis

The system-level probabilistic performance-based analysis of steel structures under fire following earthquake is introduced in this section. This analysis is constructed on basis of member-level probabilistic analysis that provides probability of exceedance in a steel column given a certain level of inter-story drift ratio caused by earthquake and the subsequent fire. Since it is assumed that post-flashover of fire occurs at the end of an earthquake event, the permanent inter-story drift ratio is considered in all columns at the conclusion of an earthquake time-history based simulation. Table 5.6 summarizes this permanent deformation in all columns of the 3-story frame caused by the 10 earthquake records introduced in Chapter 4 according to the IDR labels for each column as shown in Figure 5.19. The number in parenthesis is the label of columns in the 3-story frame as shown in Figure 5.19. These sets of IDRs will be considered as 10 sets of randomly uncorrelated numbers in the system-level probabilistic analysis. This is because the IDRs in the columns of structure subjected to a specific earthquake record are correlated to each other. Therefore, randomly generating inter-story drifts for the columns in a structure with no correlation will not address the problem properly. In this analysis, the permanent inter-story drift ratios under the 10 earthquake records provide 10 sets of uncorrelated IDRs, which can be used as sets of random IDRs for the system-level Monte Carlo simulation. In addition, since the response of structural systems is different to near- and far-field earthquake records, separate fragility analysis is conducted for each type of earthquake records.

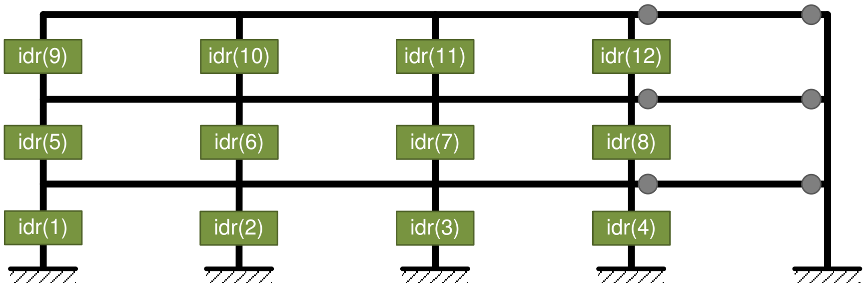

Figure 5.19 The label of columns in steel structures indicates permanent inter-story drift ratio at the end of earthquake event.

As shown in Table 5.6, the maximum permanent IDRs is 1.06% for all columns under all earthquake records. According to the results of member-level analysis, small probability of failure would be associated with this level of IDR. Since all IDRs for all columns are equal to or less than 1%, it was decided to assume the same fragility for all columns of the 3-story frame.

Table 5.6 The permanent IDRs (%) in all columns of 3-story frame caused by 10 earthquake records.

	Number of column											
Earthquake	**(1)**	**(2)**	**(3)**	**(4)**	**(5)**	**(6)**	**(7)**	**(8)**	**(9)**	**(10)**	**(11)**	**(12)**
Duzce	0.0299	0.0316	0.0321	0.0312	0.0589	0.0586	0.0596	0.0625	0.0822	0.0746	0.0680	0.0608
Erzican	0.00036	0.00057	0.00007	0.00071	0.0934	0.0923	0.0922	0.0932	0.242	0.240	0.234	0.225
Imperial Valley-06	0.790	0.783	0.785	0.788	0.947	0.979	0.978	0.965	0.778	0.753	0.764	0.797
Kobe	0.268	0.276	0.277	0.272	0.417	0.411	0.410	0.415	0.463	0.457	0.452	0.449
Kocaeli	0.674	0.681	0.681	0.675	0.933	0.927	0.927	0.934	1.06	1.06	1.05	1.05
Loma Prieta-NF	0.100	0.104	0.105	0.104	0.211	0.208	0.207	0.209	0.288	0.283	0.278	0.274
Loma Prieta	0.164	0.166	0.167	0.168	0.121	0.119	0.118	0.118	0.194	0.187	0.181	0.176
Northridge-01	0.0601	0.0608	0.0615	0.0623	0.0699	0.0708	0.0712	0.0714	0.0522	0.0442	0.0373	0.0298
Northridge	0.428	0.435	0.433	0.423	0.703	0.696	0.699	0.712	0.780	0.786	0.793	0.800
San Fernando	0.0514	0.0472	0.0452	0.0458	0.194	0.197	0.198	0.198	0.193	0.195	0.202	0.207

A set of post-earthquake fire scenarios needs to be defined for the system-level probabilistic analysis. The different scenarios imply different possible post-earthquake fire event in bays and stories of the structure. For example, Figure 5.20 shows a possible post-earthquake fire scenario in the 3-story frame where two bays in the 1st floor and one bay in the 2nd and 3rd stories are subjected to fire. Since the 3-story frame has total of 9 bays in moment-resisting frame, the post-earthquake fire event may occur in one or more bays. In a given fire scenario, the bays subjected to fire are labeled as one, and bays with no fire will be labeled as zero. This is shown in Figure 5.21 by circles with red color for the given fire scenario in Figure 5.20. Moreover, if a bay is exposed to a fire event, its two adjacent columns are also labeled with one; otherwise the columns are labeled with zero – i.e. no exposure to fire. The squares with blue color on top of columns in Figure 5.21 show how columns are labeled for the example fire scenario in accordance with Figure 5.20. For instance, in the first story all columns are subjected to post-earthquake fire according to the fire events in this story; however, only two columns are exposed to post-earthquake fire based on Figures 5.20 and 5.21.

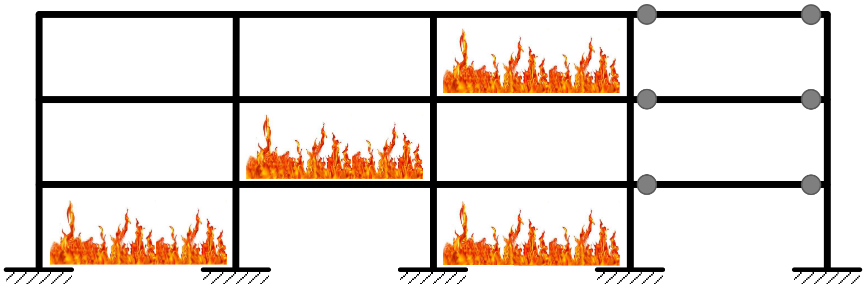

Figure 5.20 An example of post-earthquake fire scenario.

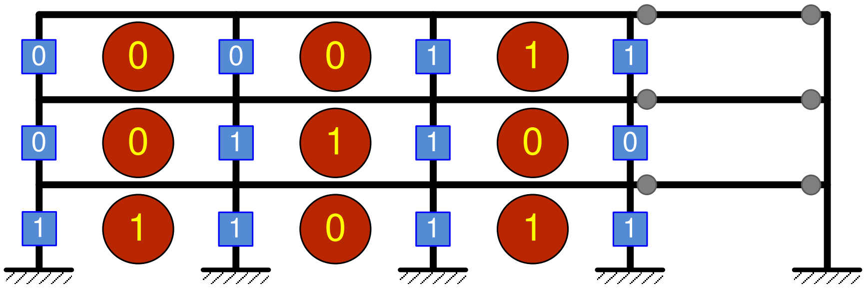

Figure 5.21 The label of bays and columns with one and zero given fire event and no fire event, respectively.

For columns given inter-story drift ratio and subjected to fire loads, it is possible to calculate the probability of exceedance according to member-level analysis (Figure 5.22). In the next step, random numbers between 0 and 1 with uniform distribution is generated for a given scenario (N = 5000 in this study) and available probability of exceedance according to Figure 5.22. These random numbers are compared to the calculated probability of exceedance in each of columns subjected to post-earthquake fire. If the randomly generated probability of exceedance is less than the available probability of failure for a given column, then the columns is assumed to have "failed", otherwise not. Again, this process in performed for N (5000) fire scenarios given permanent inter-story drift at the end of specific earthquake record and fire load. For a given fire load, this process is repeated 5 times for each type of earthquake records since 5 sets of IDRs exist at the end of each type of earthquake records considered in this study. This results in 50,000 fire following earthquake scenarios in total. The repeat of this process for all range of fire load densities from 100 to 1000 (MJ/m^2) allows the system response to be obtained under the applied fire following earthquake scenarios.

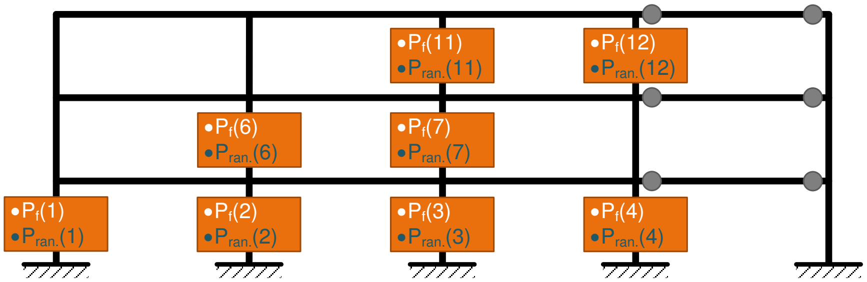

Figure 5.22 The probability of exceedance along with randomly generated probabilities for columns under post-earthquake fire accordance with scenario assumed in Figures 5.20-21.

In the next step, 4 various damage measures associated with stability of the 3-story frame are defined. It is noted that these damage measures are only considered for this case study and can be redefined for any other structure as desired. These damage measures are as following:

- Damage Measure 1 (DM-1): The onset of instability in one column or more in a story
- Damage Measure (DM-2): The onset of instability in two columns or more in a story
- Damage Measure 3 (DM-3): The onset of instability in three columns or more in a story
- Damage Measure 4 (DM-4): The onset of instability in four column or more in a story

This results in system-level fragility for a given fire load density of post–earthquake fire. This is shown in Figure 5.23 for both near- and far-field earthquake records at all defined damage measures above. It is seen that almost the same fragility curve is obtained for near- and far-field earthquake records. In addition, it is observed that the probability of exceedance for damage measures 3 and 4 is approximately zero. This means than the probability of instability in 3 or more columns in one story is approximately zero. However, the probability of instability in one or more columns at maximum fire load density is 60%. This fragility analysis provides insights into the performance of steel columns, as the most important member of the structural system, which control the stability. There is a need for further analysis to realize the consequence of instability in one or more columns on system performance as a whole.

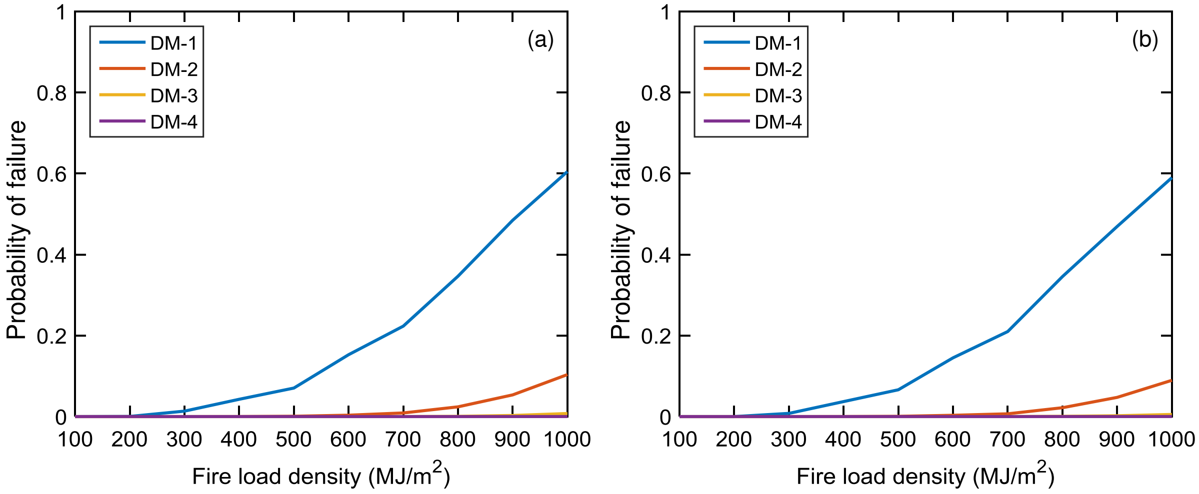

Figure 5.23 The fragility of 3-story frame subjected to fire following (a) near-field (b) far-field earthquake records.

The system-level probabilistic analysis does not take into account propagation of post-earthquake fire either from one bay to another or story to story. Since the elevated temperatures propagate relatively fast in the steel material, there is a high chance of heat penetration into adjacent beams and columns – which has not been considered here. The current system-level probabilistic analysis also does not consider explicitly the response of beams on the performance of the moment-resisting frame. The above-mentioned topics are recommended for future studies in order to promote the understanding performance of steel structural systems under cascading hazard of earthquake and fire.

5.8. Summary

This chapter proposed a probabilistic framework to assess performance of steel structural members and systems subjected to multiple hazards of earthquake and fire. Uncertainties associated with earthquake hazard, fire hazard, applied gravity loads, and passive fire protection system were considered. The proposed performance-based fire following earthquake (PBFFE) engineering framework was inspired by previous developments and study on performance-based earthquake engineering. Monte Carlo simulations were employed to develop fragilities of steel structural members subjected to fire following earthquake. The outlined framework was devised to allow structural earthquake and fire engineers to assess the performance of structural members under the multi-hazard of earthquake and fire to meet the specified performance objectives. Scenario-based Monte Carlo simulation was also implemented to obtain fragility of steel structural systems. The framework can provide means by which structural design engineers could assess alternative design scenarios and select the preferred design option based on a desired probability of failure. A summary of the steps undertaken in developing the performance-based fire following earthquake framework is provided below:

- Performance-based earthquake engineering, developed by PEER, was discussed. Four domains of hazard, system, damage, and loss were inferred according to earthquake engineering.
- Performance-based fire engineering was adopted from earthquake engineering. Detailed discussion was performed on all domains in the performance-based fire engineering, and suggestions made for appropriate variables to quantify each domain.

- The fire load density was recommended for the intensity measure in the performance-based fire engineering. Axial force was suggested as an appropriate engineering demand parameter. The onset of instability in vertical structural members (columns) in the load-bearing mechanism of the system was chosen as damage measure in performance-based fire engineering.
- Performance-based fire following earthquake engineering was outlined to consider the cascading effects of earthquake and fire on structural members (columns). A detailed discussion was executed on developing the proposed framework.
- Monte Carlo simulation technique was briefly introduced as a tool for conducting numerical probabilistic analysis. Afterward, Latin Hypercube Sampling method discussed as an approach to reduce the number of sampling without losing desired level of accuracy in the numerical probabilistic analysis.
- Stochastic modeling of the most important parameters in fire design of structural members was identified. The statistical data were presented and appropriate type of probability distribution, mean, and coefficient of variation were chosen for the probabilistic analysis. This included parameters associated with fire load density, post-flashover fire condition, spray-applied fire resistive material, and applied dead and live loads.
- A framework was outlined to run Monte Carlo simulation on the member-level (column) analysis. In this framework, finite difference method was employed to determine temperature-distribution along the length of column given specified fire curve. 3-point central in space and backward Euler time marching scheme were

implemented in finite difference analysis. Finite element method, developed in chapter 3, was used to determine the capacity and mechanical demands on the structural member.

- A scenario-based Monte Carlo simulation was also outlined to assess the performance of structural systems subjected to fire following earthquake.

The following conclusions can be drawn from the analyses;

- To clarify the process of member-level probabilistic analysis, an interior column was selected in the 2nd story level of 3-story moment-resisting frame. It was assumed that post-earthquake fire occurs in the second (from left) bay of this story.
- It was observed that the number of failed cases increased as the fire load density increased. The value of damage function, g(x), raised by increase in fire load density. This was more significant for fire load density of 500 (MJ/m^2) and larger. The damage function varies between 0 and 1 for fire load density of 100 (MJ/m^2), while its variation fell between 1 and 15 for fire load density of 1000 (MJ/m^2).
- It was shown that the probability of failure increased by increase in fire load density and inter-story drift ratio. It was also shown that the probability of failure in a column with 5% inter-story drift was 1.0 with or without fire loads. The probability of failure in the steel column with 4% inter-story drift with no fire load was about 30% and was 100% at fire load density of 500 (MJ/m^2) and greater. In case of 2% inter-story drift ratio, the probability of exceedance reached 84% for a maximum fire load density of 1000 (MJ/m^2). The probability of failure

given 0 and 1% of inter-story drift ratio was 0.10 and 0.15, respectively, for fire load density of 1000 (MJ/m^2).

- Permanent inter-story drift ratio was considered in all columns at the conclusion of an earthquake time-history based simulation. These sets of IDRs were considered as 10 sets of randomly correlated numbers in the system-level probabilistic analysis. A maximum permanent IDRs of 1.06% were recorded for all columns under all earthquake records. According to the results of member-level analysis, small probability of failure would be associated with this level of IDR.
- Four various damage states associated with stability of the 3-story frame were defined. It was observed that the probability of exceedance for instability of 3 and 4 is approximately zero. The probability of instability in one or more columns at maximum fire load density of 1000 (MJ/m^2) was 60%.

Chapter 6. Conclusions and future studies

6.1. Summary of current research

This dissertation is dedicated to assess the performance of steel structured-buildings subjected to fire following earthquakes. The analyses utilize both deterministic and probabilistic tools for evaluating steel structural members (columns) and systems (moment-resisting frames). The elastic and inelastic responses of hot-rolled W-shape steel columns are investigated under combined effects of earthquake and fire demands. The performance of three low-, medium-, and high-rise steel moment-resisting frames is studied on both the global and local scales under the cascading hazards of earthquake and fire. A new performance-based analysis framework is proposed to assess the performance of steel structural members and systems under fire following earthquake. This is realized by conducting probabilistic analyses to obtain fragility of steel columns and systems subjected to fire following earthquake.

The deterministic member-level analysis includes stability assessment of hot-rolled W-shape steel columns subjected to lateral deformations – caused by the earthquake – followed by fire loads. The analytical formulation considers a wide variety of variables in the stability analysis of steel columns subjected to the lateral and fire loads; e.g. uniform/non-uniform longitudinal distribution of temperature, inter-story drift ratio, initial imperfections, and boundary conditions. A set of equations is proposed to predict the elastic and inelastic buckling stresses in the steel columns exposed to the fire following earthquake in accordance with the results of finite element analysis.

The system-level analysis consists of evaluating the performance of 3-, 9-, and 20-story steel moment-resisting frames under multi-story fires following a suite of earthquake records. A nonlinear dynamic time-history analysis is conducted to determine the damage state of steel frames at the end of earthquake records – considering material and geometrical nonlinearities. An uncoupled thermal-mechanical analysis is then performed to simulate the post-earthquake fire scenarios. The performance of moment-resisting frames is assessed on global and local scales. The response of beams and columns is investigated to evaluate the system-level performance under fire following earthquake. Multi-resolution modeling technique is employed to simulate the detailed response of reduced beam section connections to fire following earthquake loading scenario.

A performance-based analysis framework is proposed for probabilistic assessment of steel structural members and systems under fire following earthquake. This framework ties the probability of exceedance to damages caused by the earthquake in form of inter-story drift ratio and axial force demand due to post-earthquake fire loads. Monte Carlo simulation technique is employed to perform probabilistic analysis. Random numbers of the effective stochastic variables are generated according to their corresponding probability distribution, mean, and coefficient of variation using Latin Hypercube Sampling method.

The proposed performance-based analysis framework is demonstrated on the member-level using a column in the 2nd floor of the 3-story moment-resisting frame. This probabilistic analysis results in developing fragility surface for steel column subjected to inter-story drift ratio and following fire loads. A scenario-based system-level probabilistic analysis is also conducted to clarify the application of proposed performance-based analysis framework. Four damage states are defined according to instability concerns in steel frames. The fragility of steel column – based on member-level probabilistic analysis – combined with permanent residual inter-story drift ratios – using nonlinear dynamic time-history analysis – are applied to generate fragilities of steel structural system under post-earthquake fire loads.

6.2. Summary of findings

6.2.1. Member-level deterministic analysis

A geometrically non-linear flexibility-based finite element formulation was proposed for assessing the response of steel columns under the sequential demand of earthquake and fire loadings. The proposed approach is a tool that can be employed to investigate the effects of a wide variety of variables on the buckling response of steel columns subjected to fire and fire following earthquakes. This methodology includes both P- δ and P-Δ effects, residual stresses in hot-rolled W-shape steel sections, temperature-dependent material modeling, different boundary conditions (although only pinned-pinned was evaluated), and non-uniform temperatures along the length of the column.

The Euler elastic buckling stress and mode shapes were determined by solving an eigenvalue problem. It is observed that profile (4) – with 87% reduction in modulus of elasticity along the length of column – significantly changed the instability mode shape of steel column while this change was insignificant in profiles (1)-(3). The 1st mode shape showed that maximum deflection along column length is shifted towards higher temperature zones (i.e. softer material) while naturally accounting for the effect of boundary conditions. The effective length factors showed a small change in profiles (1)-(3) as expected because the change in mode shapes was minimal. The change in effective length factors was relatively significant in profile (4).

The results of the analyses showed that under elastic conditions, parabolic and linear longitudinal variations of temperature make no difference on mode shapes of instability. It was concluded that linear longitudinal temperature distribution can be used in elastic buckling analysis of steel columns instead of parabolic distribution, when longitudinal variation of modulus of elasticity is approximately less than 60% along the length of column. An equation was proposed to predict Euler elastic buckling stress in a steel W-shape column subjected to non-uniform longitudinal temperature distribution. The results of proposed equation indicated a good agreement with the solution of eigenvalue problem.

The initial imperfections, including out-of-straightness and out-of-plumbness, were independently considered in the geometry of the columns analyzed. A good agreement was observed between results of the proposed analytical approach and available strength design equations for steel columns at ambient and elevated temperatures. Using Eurocode 3 (CEN, 2005) temperature-dependent material modeling, the results of the presented approach was in good agreement with the results of Takagi and Deierlein (2007) which was obtained using the same material modeling. This proposed approach resulted in close agreement with design equation proposed by Agarwal and Varma (2011) when implementing their material model. It was shown that assuming elastic-perfectly plastic temperature-dependent material modeling results in non-conservative buckling stress values. A new tri-linear temperature-dependent material modeling was shown to yield very close results to those obtained by Agarwal and Verma (2011).

The column with slenderness ratio of 10 showed the least reduction in buckling stress caused by the P-Δ effects under uniform temperature. However, maximum reduction took place in columns with slenderness ratio between 50 and 100. When non-uniform longitudinal temperature is included, material (a) resulted in larger buckling stress than that of material (d) when lateral sway was introduced. A set of design equations was proposed to estimate the inelastic buckling stress of W-shape steel columns for the case of non-uniform longitudinal temperature profiles with and without inter-story drift. The proposed equations showed good agreement with the results of nonlinear finite element analysis.

6.2.2. System-level deterministic analysis

The evaluation of studied MRFs under post-earthquake fires provides a good opportunity to extend previous studies on seismic response of these frames to include the post-earthquake fire. The fires were applied to the RBS connections under the assumption that the fireproofing was damaged during the earthquakes due to large concentration of inelastic demands in the connections. Failure was defined in terms of the ASCE Standard 41-06 performance limits; failures in the connections were not considered. Furthermore, the post-earthquake damage in the structural systems was captured by taking into account the material and geometrical damage modeling.

The nonlinear dynamic time-history analysis resulted in LS structural performance level in 80% and CP performance level in 20% of the ground motions in all steel MRFs. Both post-earthquake fires mostly resulted in smaller IDRs when compared to those resulting from the earthquakes. In general, the global structural performance level of the all three MRFs is not affected by post-earthquake fire scenarios similar to those considered in this study, regardless of the characteristic of the record, being near-field or far-field for the given fire scenarios. In all stories starting from the second above the highest story subjected to fire, the reduction in the average of the IDRs is largest in all MRFs. The change in the average of the IDRs is smallest at the 1st story levels and at the story level immediately above the highest story subjected to the post-earthquake fire. The potential of system collapse was not imminent as a result of applied post-earthquake fires.

The interaction points for the selected beams coincide with each other regardless of their earthquake history, except for a limited number of interaction points. The tension forces developed in the highlighted beams during the cooling phase of fires were insignificant. In the selected beams of all MRF, the C-M interaction points are outside the interaction equation limit under FFE-1/3H. In the highlighted beams of all MRF, the C-M interaction points mostly fall within the interaction equation limit for the medium- and high-rise frames, but not for the low-rise frame under FFE-2/3H. The behavior of the highlighted beams was dominated by the axial compressive forces as opposed to the tensile force. The design of the beams subjected to the post-earthquake fires can be performed based on the axial compressive forces-bending moment interaction developed in accordance with the AISC Specification.

The interaction points for the selected columns in both post-earthquake fires are mostly located outside the interaction equation limit. The axial compressive forces developed in the highlighted columns during the post-earthquake fires are independent from the earthquake history. The response of the selected columns is mostly dominated by the bending moments and the response during the post-earthquake fires depends on the earthquake history. The residual deformations and stress history resulting from the earthquake had significant effects on the response of RBS connections to post-earthquake fire loads. Significant local buckling occurred in both top and bottom reduced flanges along with web at their location under post-earthquake fire load.

6.2.3. Performance-based fire following earthquake framework

A probabilistic framework was proposed to assess performance of steel structural members and systems subjected to multiple hazards of earthquake and fire. Uncertainties associated with earthquake hazard, fire hazard, applied gravity loads, and passive fire protection system were considered. The outlined framework is envisioned to allow structural earthquake and fire engineers to assess performance of structural members under the multi-hazard of earthquake and fire to meet the specified performance objectives. Scenario-based Monte Carlo simulation is also implemented to obtain fragility of steel structural systems. The framework can provide means by which structural design engineers could assess alternative design scenarios and select the preferred design option based on a desired probability of failure.

6.2.4. Member-level probabilistic analysis

The fire load density was recommended for the intensity measure in the performance-based fire engineering. Axial force was suggested as an appropriate engineering demand parameter. The onset of instability in the vertical structural members (columns) in the load-bearing mechanism of the system was chosen as damage measure in performance-based fire engineering. Monte Carlo simulation technique is employed to quantify fragility of steel structural members subjected to fire following earthquake. Latin Hypercube Sampling method discussed as an approach to reduce the number of sampling without losing desired level of accuracy in the numerical probabilistic analysis.

The statistical data were presented and appropriate type of probability distribution, mean, and coefficient of variation were chosen for the probabilistic analysis. This included parameters associated with fire load density, post-flashover fire condition, spray-applied fire resistive material, and applied dead and live loads. Finite difference method was employed to determine temperature-distribution along the length of column given specified fire curve. Finite element method, developed in chapter 3, was used to determine the capacity and mechanical demands on the structural member.

To clarify the process of member-level probabilistic analysis, an interior column is selected in the 2nd story level of 3-story moment-resisting frame. It is assumed that post-earthquake fire occurs in the second (from left) bay of this story. It was observed that number of failed cases increases as the fire load density increase. The value of damage function, g(x), rises by increase in fire load density. This is more significant for fire load density of 500 (MJ/m^2) and larger. The damage function varies between 0 and 1 for fire load density of 100 (MJ/m^2), while its variation falls in between 1 and 15 for fire load density of 1000 (MJ/m^2). The damage function adopts values between two aforementioned extreme cases for the rest of fire load densities.

It was shown that the probability of failure increases by increase in fire load density and inter-story drift ratio. This was recognized that the probability of failure in a column with 5% inter-story drift is 1.0 with or without fire loads. The probability of failure in the steel column with 4% inter-story drift with no fire load is about 30% and is 100% at fire load density of 500 (MJ/m^2) and greater. In case of 2% inter-story drift ratio, the probability of exceedance reaches 84% for a maximum fire load density of 1000 (MJ/m^2). The probability of failure given 0 and 1% of inter-story drift ratio arrives at 0.10 and 0.15, respectively, for fire load density of 1000 (MJ/m^2).

6.2.5. System-level probabilistic analysis

Scenario-based Monte Carlo simulation was also implemented to obtain fragility of steel structural systems. The permanent inter-story drift ratio was considered in all columns at the conclusion of an earthquake time-history based simulation. These sets of IDRs were considered as 10 sets of randomly correlated numbers in the system-level probabilistic analysis. The maximum permanent IDRs of 1.06% were observed for all columns under all earthquake records. Four various damage states associated with stability of the 3-story frame were defined. It was observed that the probability of exceedance for instability of 3 and 4 is approximately zero. The probability of instability in one or more columns at maximum fire load density of 1000 (MJ/m^2) was 60%. This fragility analysis provided insights into the performance of steel columns, as the most important member of the structural system, which control the stability. There is a need for further analysis to realize the consequence of instability in one or more columns on the system performance.

6.3. Recommendations for future studies

The present study investigated the performance of steel structural members and systems under fire following earthquake considering deterministic and probabilistic analyses. The results of the study indicated that the residual deformations and stresses – caused by earthquake prior to fire loads – can significantly change the performance of steel structural members and system exposed to additional loads of post-earthquake fire exposure. Although this study provided some insights on the performance of steel framed buildings subjected to multiple hazards of earthquake and fire; however, future research directions can include the followings;

- The line element model had capability to consider a wide variety of variables in the instability analysis of W-shape steel columns under applied lateral drift and elevated temperatures. Detailed finite element analysis is needed using either shell or solid elements to confirm the effects of local and global imperfections, residual stresses, and boundary conditions on the response of steel columns under sequential applied inter-story drift and fire loads. In addition, Experimental testing can be employed to validate the results of the present study. It will be essential to consider realistic boundary conditions in the experimental assessment of column response to the lateral drift and elevated temperatures.

- Only four non-uniform longitudinal distributions of temperature were considered in the present study. It is suggested that a wide range of non-uniform longitudinal temperature profiles is considered in fire and fire following earthquake analyses. The results can be used to improve the precision of the proposed equations to estimate the inelastic buckling stress of steel columns subjected to inter-story drift and fire loads.
- The present study evaluated the response of low-, medium, and high-rise steel moment-resisting frames subjected to fire following earthquake. A symmetric fire load was applied to reduced beam section connections in the steel frames. It is recommended to consider asymmetric post-earthquake fire scenarios in the collapse performance evaluation. A disproportionate progressive collapse can be expected in the case of asymmetric post-earthquake fire loads.
- The present study focused on performance of moment-resisting frames under fire following earthquake. It is suggested that a wide variety of steel framing systems e.g. gravity frames and braced frames, be investigated under the considered multiple hazards. Furthermore, analysis of 3-D geometry of steel structural systems can provide valuable insights in the response of the entire system including redundancy and load path. The effects of concrete slabs can be also considered in 3-D modeling of the system.
- This study performed member-level probabilistic analysis on W-shape steel columns. For complete assessment of steel elements used in building constructions,

probabilistic analysis of steel beams and connections are recommended. In addition, the results of member-level probabilistic analysis can be employed to determine load and resistance factors in design of structural members for combination of earthquake and fire loads. This can also lead to the development of new design methodologies for structural systems subjected to the cascading hazards of earthquake and fire.

- The member-level analysis – both deterministic and probabilistic – did not consider the effects of strain and stress histories caused by earthquake on the post-earthquake fire response. It is recommended that the history, characterized by strength and stiffness degradation of material and connections, be accounted for in the member-level analysis.
- The present study examined the effects of multi-hazard fire following earthquakes on the structural member- and system-levels. The extension of the results and the impact on various building archetypes can provide substantial information the expected structural damage and could allow for the assessment of the post-damage functionality, recovery, and resiliency of the community.

References

Agarwal, A., Choe, L. and Varma, A.H. (2014). “Fire design of steel columns: Effects of thermal gradients.” Journal of Constructional Steel Research, 93, 107-118.

Agarwal, A. and Varma, A.H. (2011). “Design of steel columns at elevated temperatures due to fire: effects of rotational restraints.” Engineering Journal, 4th quarter, 297-314.

AISC 341-10. (2010). “Seismic provisions for structural steel buildings.” American Institute of Steel Construction, Chicago, IL.

AISC 360-10. (2010). “Specifications for structural steel buildings.” American Institute of Steel Construction, Chicago, Illinois.

Ali, F. and O’Connor, D. (2001). “Structural performance of rotationally restrained steel columns in fire.” Fire Safety Journal, 36, 679-691.

Ang, A.H. and Tang W.H. (2006). “Probability concepts in engineering: emphasis on applications to civil and environmental engineering.” John Wiley & Sons, Inc., Wiley, New York, NY.

AS 1530.4. (2005). “Fire resistance tests of elements of structure.” Standards Australia.

ASCE. (1992). “Structural fire protection.” ASCE Committee on Fire Protection, Manual of Practice No. 78, American Society of Civil Engineers, Reston, VA.

ASCE/SEI 07-10 (2010). “Minimum design loads for buildings and other structures.” American Society of Civil Engineers/Structural Engineering Institute, Reston, VA.

ASCE/SEI 41-06 (2007). “Seismic rehabilitation of existing buildings.” American Society of Civil Engineers/Structural Engineering Institute, Reston, VA.

ASCE/SEI/SFPE 29-05 (2007). “Standard calculation methods for structural fire protection.” American Society of Civil Engineers/Structural Engineering Institute/Society of Fire Protection Engineers, Reston, VA.

Aslani, H. and Miranda, E. (2005). “Probabilistic earthquake loss estimation and loss disaggregation in buildings.” The John A. Blume Earthquake Engineering Center, Report No. 157, Stanford University.

ASTM E119-16 (2016). “Standard test methods for fire tests of building construction and materials.” American Society for Testing and Materials, West Conshohocken, PA.

Au, S.K., Wang, Z.H. and Lo, S.M. (2007). “Compartment fire risk analysis by advanced Monte Carlo simulation.” Engineering Structures, 29, 2381-2390.

Beitel, J. and Iwankiw, N. (2002). “Analysis of needs and existing capabilities for full-scale fire resistance testing.” National Institute of Standards and Technology, NIST GCR 02-843, Gaithersburg, MD.

Bozorgnia, Y. and Bertero, V.V. (2004). “Earthquake engineering: From engineering seismology to performance-based engineering.” CRC Press.

Braxtan, N.L. and Pessiki, P.S. (2011). “Postearthquake fire performance of sprayed fire-resistive material on steel moment frames.” Journal of Structural Engineering, 137(9), pp. 946-953.

BS 476. (1987). “Fire tests on building materials and structures.” British Standard Institution, UK.

Buchanan, A.H. (2001). “Structural design for fire safety.” John Wiley & Sons, Inc., Wiley, New York, NY.

Carol, I. and Murcia, J. (1989). "Nonlinear time-dependent analysis of planar frames using an exact formulation – I. Theory." Computers and Structures, 33(1), pp. 79-87.

CEN. (2002). "Eurocode 1: Actions on Structures – Part 1-2: General actions – Actions on structures exposed to fire." European Committee for Standardization.

CEN. (2004). "Eurocode 2: Design of concrete structures – Part 1-2: General rules – Structural fire design." European Committee for Standardization.

CEN. (2005). "Eurocode 3: Design of steel structures – Part 1-2: General rules – Structural fire design." European Committee for Standardization.

Charney, F. and Marshall, J. (2006). "A comparison of the Krawinkler and scissor models for including beam-column joint deformations in the analysis of moment-resisting steel frames." Engineering Journal, 43(1), pp.31-48.

CIB W14. (1983). "A conceptual approach towards a probability-based design guide on structural fire safety." Fire Safety Journal, 6(1), pp. 1-79.

CIB W14. (1986). "Design guide for structural fire safety." Fire Safety Journal, 10(2), pp. 81-137.

Culver, C.G. (1976). "Survey results for fire loads and live loads in office buildings." Building Science Series No. 85, National Bureau of Standards, Washington, DC.

Della Corte, G., Faggiano, G. and Mazzolani, F.M. (2005). "On the structural effects of fire following earthquake." COST C12 Final Conference Proceedings 2005, Innsbruck, Austria.

Della Corte, G., Landolfo, R. and Mazzolani, F.M. (2003). "Post-earthquake fire resistance of moment resisting steel frames." Fire Safety Journal, 38(7), pp. 593-612.

ECCS. (1995). "Fire resistance of steel structures." Publication No. 111, Technical Committee 3, European Convention for Constructional Steelwork, Brussels, Belgium.

ECCS. (2001). “Model code on fire engineering.” Publication No. 89, Technical Committee 3, European Convention for Constructional Steelwork, Brussels, Belgium.

Eidinger, J.M. (2004). “Fire following earthquake.” Revision 11.

Ellingwood, B.R. (2005). “Load combination requirements for fire-resistant structural design.” Journal of Fire Protection Engineering, 15(1), 43-61.

Ellingwood, B.R. and Corotis, R.B. (1991). “Load combinations for buildings exposed to fire.” Engineering Journal, 28(1), pp. 37-44.

Faggiano, B., Esposto, M. and Mazzolani, F.M. (2008). “Risk assessment of steel structures under fire.” The 14th World Conference on Earthquake Engineering 2008, Beijing, China.

Faggiano, B., Esposto, M., Mazzolani, F.M. and Landolfo, R. (2007). “Fire analysis on steel portal frames damaged after earthquake according to performance based design.” Proceedings Workshop Urban Habitat Construction under Catastrophic Events (COST C26 Action) 2007, Prague, Czech Republic.

Faggiano, B., De Gregorio, D. and Mazzolani, F.M. (2010). “Assessment of the robustness of structures subjected to fire following earthquake through a performance-based approach.” Proceedings International Conference Urban Habitat Construction under Catastrophic Events (COST C26 Action) 2010, Naples, Italy.

FEMA. (1999). “HAZUS99 MR4 technical manual.” Department of Homeland Security/Federal Emergency Management Agency/National Institute of Building Sciences. Washington, DC.

FEMA 350. (2000). “Recommended seismic design criteria for new steel moment-frame buildings.” Federal Emergency Management Agency, Washington, DC.

FEMA 354. (2000). “A policy guide to steel moment frame construction.” Federal Emergency Management Agency, Washington, DC.

FEMA 355C. (2000). “State of the art report on systems performance of steel moment frames subject to earthquake ground shaking.” Federal Emergency Management Agency, Washington, DC.

FEMA 355D. (2000). “State of the art report on connection performance.” Federal Emergency Management Agency, Washington, DC.

FEMA 356. (2000). “Guidelines for seismic rehabilitation of building.” Federal Emergency Management Agency, Washington, DC.

FEMA 403. (2002). “World Trade Center building performance study: data collection, preliminary observations, and recommendations.” Federal Emergency Management Agency, Washington, DC.

FEMA P695. (2009). “Quantification of building seismic performance factors.” Federal Emergency Management Agency, Washington, DC.

Franssen, J. M., Talamona, D., Kruppa, J. and Cajot, L. G. (1998). “Stability of steel columns in case of fire: experimental evaluation.” Journal of Structural Engineering, 124(2), pp. 158-163.

Franssen, J.M., Kodur, V.K.R. and Mason, J. (2002). “User’s manual for SAFIR 2001 free – A computer program for analysis of structures submitted to the fire”, Department of Civil Engineering, University of Liege, Belgium.

Guo, Q., Shi, K., Jia, Z. and Jeffers, A. (2013). “Probabilistic evaluation of structural fire resistance.” Fire Technology, 49(3), pp. 793-811.

Guo, Q. and Jeffers, A. (2015). “Finite-element reliability analysis of structures subjected to fire.” Journal of Structural Engineering, 141(4): 04014129.

Gupta, A. and Krawinkler, H. (2000). “Dynamic P-delta effects for flexible inelastic steel structures.” Journal of Structural Engineering, 126(1), pp.145-154.

Gupta, A. and Krawinkler, H. (1999). “Seismic demands for performance evaluation of steel moment resisting frame structures.” John A. Blume Earthquake Engineering Center, Report No. 132, Stanford University.

Hamilton, S.R. (2011). “Performance-based fire engineering for steel framed structures: a probabilistic methodology.” Stanford University.

Iqbal, S. and harichandran, R.S. (2010). “Capacity reduction and fire load factors for design of steel members exposed to fire.” Journal of Structural Engineering, 136(12), pp. 1554-1562.

JCSS. (2001). “JCSS probabilistic model code, Part 2: Load models”, Joint Committee on Structural Safety, Denmark.

Johnson, G.R. and Cook, W.H. (1985). “Fracture characteristics of three metals subjected to various strains, strain Rates, temperatures and pressures.” Engineering Fracture Mechanics, 21(1), pp. 31-48.

Keller, W.J. and Pessiki, P.S. (2012). “Effect of earthquake-induced damage to spray-applied fire-resistive insulation on the response of steel moment-frame beam-column connections during fire exposure.” Journal of Fire Protection Engineering, 22(4), pp. 271-299.

Khorasani, N., Garlock, M. and Gardoni, P. (2014). “Fire load: survey data, recent standards, and probabilistic models for office buildings.” Engineering Structures, 58, pp. 152-165.

Lange, D., Devaney, S. and Usmani, A. (2014). “An application of the PEER performance based earthquake engineering framework to structures in fire.” Engineering Structures, 66, pp. 100-115.

Lee, S., Davidson, R., Ohnishi, N. and Scawthorn, C. (2008). “Fire following earthquake – reviewing the state-of-the-art of modeling.” Earthquake Spectra, 24(4), pp. 933-967.

Lien, K.H., Chiou, Y.J., Wang, R.Z. and Hsiao, P.A. (2010). “Vector form intrinsic finite element analysis of nonlinear behavior of steel structures exposed to fire.” Engineering Structures, 32(1), pp. 80-92.

Mahmoud, H., Ellingwood, B., Turbert, C. and Memari, M. (2016). “Response of steel reduced beam section connections exposed to fire”, Journal of Structural engineering, 142(1): 04015076.

Memari, M. and Attarnejad, R. (2010). “An innovative Timoshenko beam element”. Proceedings of 10th International Conference on Computational Structures Technology, Valencia, Spain.

Memari, M. and Mahmoud, H. (2014). “Performance of steel moment resisting frames with RBS connections under fire loading.” Engineering Structures, 75, 126-138.

Memari, M., Mahmoud, H. and Ellingwood, B. (2014). “Post-earthquake fire performance of moment resisting frames with reduced beam section connections.” Journal of Constructional Steel Research, 103, 215-229.

NFPA 251. (2006). “Standard methods of tests of fire endurance of building construction and materials.” National Fire Protection Association, Quincy, MA.

NFPA 557. (2012). “Standard for determination of fire load for use in structural fire protection design.” National Fire Protection Association, Quincy, MA.

Phan, L.T., McAllister, T.P., Gross, J.L. and Hurley, M.J. (2010). “Best practice guidelines for structural fire resistance design of concrete and steel buildings.” National Institute of Standards and Technology, NIST Technical Note 1681, Gaithersburg, MD.

Pucinotti, R., Bursi, O.S. and Demonceau, J.F. (2011a). “Post-earthquake fire and seismic performance of welded steel–concrete composite beam-to-column joints.” Journal of Constructional Steel Research, 67(9), pp. 1358-1375.

Pucinotti, R., Bursi, O.S., Franssen, J.M. and Lennon, T. (2011b). “Seismic-induced fire resistance of composite welded beam-to-column joints with concrete-filled tubes.” Fire Safety Journal, 46(6), pp. 335-347.

Quiel, S.E. and Garlock, M.E. (2008). “Modeling high-rise steel framed buildings under fire.” ASCE Structures Congress: Crossing Borders, Vancouver, Canada.

Ren, A. and Xie, X. (2004). “The simulation of post-earthquake fire-prone area based on GIS.” Journal of Fire Sciences, 22(5), pp. 421-439.

Rini, D. and Lamont, S. (2008). “performance based structural fire engineering for modern building design.” ASCE Structures Congress: Crossing Borders, Vancouver, Canada.

Rubert, A. and Schaumann, P. (1985). “Tragverhalten stahlerner rahmensysteme bei randbeanspruchung.” Stahlbau, 9, pp. 280–287.

Scawthorn, C., Eidinger, J.M. and Schiff, A.J. (2005). “Fire following earthquake.” American Society of Civil Engineers, Technical Council on Lifeline Earthquake Engineering Monograph No. 26, Reston, VA.

Scawthorn, C.R. (2008). “Fire following earthquake.” United States Geological Survey/California Geological Survey.

Scawthorn, C., Yamada, Y. and Iemura, H. (1981). “A model for urban post-earthquake fire hazard.” Disasters, 5(2), pp. 125-132.

Scawthorn, C. (1986). “Simulation modeling of fire following earthquake.” 3rd National Conference for Earthquake Engineering, Charleston, SC, pp. 676-685.

Scawthorn, C., O'Rourke, T. and Blackburn, F. (2006). "The 1906 San Francisco earthquake and fire – Enduring lessons for fire protection and water supply." Earthquake Spectra, 22(S2), pp. 135-158.

SEAoC. (1995). "Performance-based seismic engineering of buildings." Structural Engineering Association of California, Vision 2000 Committee.

SFPE. (2004). "Engineering guide: fire exposures to structural elements." Society of Fire Protection Engineers, Bethesda, MD.

Simula. (2005). "Abaqus analysis user's manual." Abaqus v6.5 Documentation, Hibbitt, Karlsson & Sorensen, Inc., Pawtucket, RI.

Simula. (2010). "Abaqus analysis user's manual." Abaqus v6.10 Documentation, Hibbitt, Karlsson & Sorensen, Inc., Pawtucket, RI.

Sun, R., Huang, Z. and Burgess, I.W. (2012). "Progressive collapse analysis of steel structures under fire conditions." Engineering Structures, 34, pp. 400-413.

Takagi, J. and Deierlein, G.G. (2007). "Strength design criteria for steel members at elevated temperatures." Journal of Constructional Steel Research. 63(8),1036-1050.

Tan, K.H. and Yuan, W.F. (2009). "Inelastic buckling of pin-ended steel columns under longitudinal non-uniform temperature distribution." Journal of Constructional Steel Research, 65(1), 132-141.

Twilt, L. (1991). "Stress-strain relationships of structural steel at elevated temperatures: analysis of various options and European proposal – Part F: mechanical properties." TNO Report No. B1-91-015, Delft, Netherlands.

UBC 94. (1994). "Uniform Building Code." International Code Council.

UL 263. (2003). “Standards for fire tests of building construction and materials.” Underwriters Laboratories Inc., Northbrook, IL.

Vandamme, M. and Janss, J. (1981). “Buckling of axially loaded steel columns in fire conditions.” IABSE Proceedings, P-43/81, IABSE Periodica 3/1981, pp. 81–95.

Wen, H. and Mahmoud, H. (2015a). “New Model for Ductile Fracture of Metal Alloys. I: Monotonic Loading.” Journal of Engineering Mechanics, 142(2): 04015088.

Wen, H. and Mahmoud, H. (2015b). “New Model for Ductile Fracture of Metal Alloys. II: Reverse Loading.” Journal of Engineering Mechanics, 142(2): 04015089.

Zhao, S., Xiong, L. and Ren, A. (2006). “A spatial-temporal stochastic simulation of fire out-breaks following earthquake based on GIS.” Journal of Fire Sciences, 24, pp. 313-339.